Plasmonic III-V Lasers and Waveguide Bragg Gratings

by
Shayan Saeidi

Thesis submitted to the University of Ottawa
in partial Fulfillment of the requirements for the

Doctor of Philosophy

School of Electrical Engineering and Computer Science
Faculty of Engineering
University of Ottawa

to Salar

Examining Committee

The examining committee for this thesis consisted of the following members:

Supervisor:

Professor Pierre Berini
School of Electrical Engineering and Computer Science, and Department of Physics
University of Ottawa

External Examiner:

Professor Amr S. Helmy
Department of Electrical and Computer engineering
University of Toronto

Internal Examiners:

Professor Karin Hinzer
School of Electrical Engineering and Computer Science, and Department of Physics
University of Ottawa

Professor Ksenia Dolgaleva
School of Electrical Engineering and Computer Science, and Department of Physics
University of Ottawa

Professor Steven McGarry
Department of Electronics
Carleton University

Abstract

This thesis investigates two building-blocks of integrated photonics, hybrid plasmonic–semiconductor lasers and waveguide Bragg gratings (WBGs), with the goal of improving tunability, sensing performance, and grating design. The first part examines plasmonic–III-V integration as a platform for tunable lasers aimed at data-center applications, using loss-based mode control to enable wavelength tuning. I also explore the use of hybrid plasmonic–semiconductor laser in biosensing and additionally, design an electrically driven LED refractometer as a compact sensing device. The second part of the thesis focuses on WBGs, reviewing weak and strong grating regimes with established simulation techniques. I introduce a new class of gratings, Dirac gratings, whose spectral response remains unchanged with grating order. Finally, I develop an efficient analysis tool based coupled-mode theory for design and optimization of distributed-feedback lasers and reflectors.

Acknowledgment

Foremost, I would like to thank my family, Mom, Dad, Salar, and Negar to whom I owe all that I have achieved. Secondly, I would like to thank my thesis supervisor, Prof. Pierre Berini, whose guidance was indispensable throughout my studies, and who gave me the freedom to explore the topics truly interesting for me.

I'd like to thank my colleagues with whom I worked directly in my projects: Deepthi Sekhar, who played a key role in fabrication of proposed devices; Sina Aghili, for delving into the mathematical foundations of waveguide gratings; and the NanoFab staff at the uOttawa, who provided assistance throughout my projects. I'm also grateful to Dr. Pavel Cheben and Dr. Jens Schmid for their constructive feedback on various projects. I also would like to thank Dr. Fang Wu and her team at Banyan Photonics Inc. for hosting me during the first year of my PhD and for always being willing to assist whenever I needed help with my research.

I'd also like to thank people, both within and outside academia, who influenced or supported me in different ways – Zaila, Mae, Yury, and others. While I can't name everyone individually, I am grateful to all who played a part in this journey.

Contents

List of Figures[1]

[1] Note that this thesis is by article; the figures within the individual articles are not included in this list.

List of Tables[2]

[2] Note that this thesis is by article; the tables within the individual articles are not included in this list.

Chapter 1

Introduction

1.1 Motivation

The main motivation of this thesis was to explore new ways of achieving tunability in semiconductor lasers, mainly for datacom and telecom applications. InP-based platforms are well established in industry, so most of the work naturally focuses on these structures. As the project progressed, some of the concepts developed showed strong potential for sensing. This expanded the scope of the thesis from communication lasers to sensing lasers as well.

In parallel, studying tunable lasers led to new findings about waveguide Bragg gratings and their modeling, which were also included in the thesis. Overall, the chapters follow this progression: starting with background and existing technologies, then introducing the new tuning concept, then moving to sensing applications, and finally presenting the grating studies and numerical methods. A detailed chapter-by-chapter summary is given in Section 1.3.

1.2 Background

The emergence of semiconductor diode lasers in the 60s [1] marked the birth of the integrated photonics industry. This field leverages light for applications traditionally dominated by integrated electronics, which had gained prominence over a decade earlier. Since then, photonic integrated circuits have advanced significantly, becoming a key technology in niche markets namely communication, where they enable high-speed data transmission and reception, and biotechnology, where they are integral to a variety of sensing and diagnostic applications.

Unlike electronic circuits, which rely on generic elements like resistors, transistors, and capacitors, photonics lacks such universal components. Instead, photonic elements vary greatly and are often tailored to specific applications. Moreover, the materials used in photonics are far more diverse compared to electronics, where silicon remains the dominant material of choice. For fiber-optic communication bands, such as the O-band and C-band, III-V semiconductor compounds (composed of group III and group V elements from the periodic table) are widely utilized, particularly ternary and quaternary compounds that are lattice-matched to indium phosphide InP and gallium arsenide GaAs substrates. Despite this diversity in materials and device structures, several key concepts find applications across nearly all

areas of photonics. These principles underpin a wide range of applications, enabling the design and optimization of photonic circuits. In the following, I review several key concepts which are significant for my thesis: Waveguiding, Active Photonics, Plasmonics, and Gratings.

In Sections 1.2.1 and 1.2.2, a basic review of Waveguiding and Active Photonics will be given, respectively. Active photonics generally refers to the branch of photonics concerned with the emission and detection of light. In the context of lasers, which are the focus of this thesis, the active layer(s) denotes the region of the device where electron-hole recombination occurs, resulting in the generation and emission of light. Waveguiding in active photonics has a dual meaning. The cladding layers that surround the active region possess both a lower refractive index and a higher bandgap energy compared to the active layer. The refractive index contrast confines the optical mode near the active layer, and simultaneously, the bandgap difference confines electrons and holes within the active layer. The former forms an optical waveguide, whereas the latter promotes efficient carrier recombination.

Plasmonics involves the coupled confinement of electron oscillations and optical waves, which occurs not within the core of a dielectric waveguide, but at the interface between a metal and a dielectric. The inherent absorption of light by the metal makes the propagating wave very lossy. However, this loss can be partially compensated by placing the structure adjacent to a gain medium. When the metal is sufficiently thin, the coupled fields remain strongly localized to its interfaces, and the high sensitivity of the propagating wave to the material covering the metal makes structures that are excellent for sensing applications. In Section 1.2.3, an introduction to Plasmonics will be given.

Section 1.2.4 describes the basics of waveguide Bragg gratings. These are diffraction gratings embedded within a waveguide and form the basis of distributed-feedback (DFB) or distributed Bragg reflector (DBR) lasers by providing the distributed reflection and spectral filtering necessary to form an optical cavity and sustain oscillation. Such lasers offer a highly stable output, making them critically important to data and telecom infrastructure. Therefore, ongoing research into the design, fabrication, and optimization of Bragg gratings is essential for photonic systems.

1.2.1 Waveguiding

Waveguides, just like wires guiding electrical currents, guide light using the principle of total internal reflection. They are fundamental to integrated photonics, serving as the primary means of connecting components on a chip. A waveguide confines light within a high-refractive-index core, surrounded by lower-refractive-index claddings, enabling controlled propagation. Most practical waveguides achieve two-dimensional confinement, restricting light expansion in two dimensions while allowing it to propagate along the third.

Optical waveguides are categorized by their geometries. The simplest type, the symmetric slab waveguide, consists of a core sandwiched between identical lower-index claddings, providing 1D light confinement. Waveguides with 2D confinement come in various forms, such as rib, ridge, and embedded strip geometries, as illustrated in Fig. 1.1.

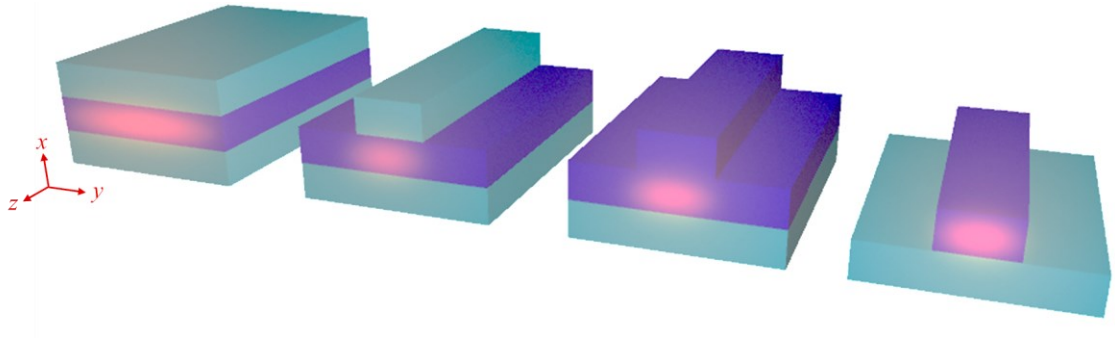

Fig. 1.1 Examples of different waveguide types. Shown from left to right: slab, strip-loaded, rib, ridge waveguides. Darker shades in the figure indicated higher refractive index and bright regions represent areas of light confinement.

A fundamental concept in integrated photonics is understanding how modes propagate within a waveguide. From the perspective of classical ray optics, wave propagation can be explained using Snell's law, where light remains confined within the waveguide as long as the conditions for total internal reflection are met. However, a more precise approach involves electromagnetic optics, which is particularly useful for analyzing complex structures commonly found in integrated photonic circuits. In the following, I will provide a brief overview of this approach.

To begin, we express Maxwell's equations under the assumption of a linear medium with no free currents or free charges [2]:

$$\nabla.(\epsilon \boldsymbol{E}) = 0 \tag{1-1}$$
$$\nabla.\boldsymbol{H} = 0 \tag{1-2}$$
$$\nabla \times \boldsymbol{E} = j\omega\mu_0 \boldsymbol{H} \tag{1-3}$$
$$\nabla \times \boldsymbol{H} = -j\omega\epsilon \boldsymbol{E} \tag{1-4}$$

where $\boldsymbol{E}(x, y, z)$ and $\boldsymbol{H}(x, y, z)$ are electric and magnetic field vectors, respectively, ϵ denotes the permittivity, and μ_0 is the vacuum permeability. In the case of an inhomogeneous medium, where $\nabla\epsilon \neq 0$, all three components of E_x, E_y, and E_z are coupled, as are H_x, H_y, and H_z. This case arises in waveguides, which consist of multiple layers with varying permittivity. When evaluating a waveguide, it is easier to write the equations separately for each region of constant permittivity to derive homogeneous differential equations. Using all four Maxwell equations and the vector identity $\nabla \times (\nabla \times \boldsymbol{A}) = \nabla(\nabla.\boldsymbol{A}) - \nabla^2\boldsymbol{A}$, the field can be expressed by:

$$\nabla^2 \boldsymbol{E} + k^2 \boldsymbol{E} = 0 \tag{1-5}$$

where $k^2 = \omega^2\mu_0\epsilon = n^2\omega^2/c^2$, and n is the refractive index. The modes of the waveguide are the electric and magnetic fields, which can be expressed in the following form:

$$\boldsymbol{E}(x,y,z) = \sum_m E^{(m)}(x,y,z)e^{j\beta_m z} \tag{1-6}$$

These equations can also be written for $\boldsymbol{H}$. A time dependence of exp $(-j\omega t)$ is assumed. The integer m represents the mode number and β_m being their corresponding propagation constant, with an infinite number of modes contributing to power transfer within the waveguide. However, most of these modes are radiative and not confined, making their contribution negligible. Therefore, we consider only the fundamental mode ($m = 0$) and omit the summation over higher-order modes. The electric field $\boldsymbol{E}$ can then be expressed in terms of its components as follows:

$$\boldsymbol{E^{(0)}} = \hat{\imath}E_x + \hat{\jmath}E_y + \hat{k}E_z \tag{1-7}$$

Using (1-5) to (1-7), we can write

$$\frac{\partial^2\boldsymbol{E^{(0)}}}{\partial z^2} + 2i\beta_0\frac{\partial\boldsymbol{E^{(0)}}}{\partial z} - {\beta_0}^2\boldsymbol{E^{(0)}} + \frac{\partial^2\boldsymbol{E^{(0)}}}{\partial x^2} + \frac{\partial^2\boldsymbol{E^{(0)}}}{\partial y^2} + k^2\boldsymbol{E^{(0)}} = 0 \tag{1-8}$$

For a straight waveguide, $\boldsymbol{E^{(0)}}$ remains constant along the propagation direction, thus $\partial/\partial z$ terms vanish:

$$\frac{\partial^2 E^{(0)}}{\partial x^2} + \frac{\partial^2 E^{(0)}}{\partial y^2} + (k^2 - {\beta_0}^2)E^{(0)} = 0 \tag{1-9}$$

Considering (1-7), we derive three wave equations for $\boldsymbol{E}$. Solving these equations for β_0 and the components E_x, E_y, and E_z provides the characteristics of the propagating mode. Similarly, wave equations can be derived for $\boldsymbol{H}$. However, it is not necessary to solve all the wave equations, as the transverse components can be determined from equations (1-3) and (1-4). Specifically, the following equations can be obtained from the curl equations:

$$\frac{\partial E_z}{\partial y} - j\beta E_y = j\omega\mu_0 H_x, \quad j\beta E_x - \frac{\partial E_z}{\partial x} = j\omega\mu_0 H_y, \quad \frac{\partial E_y}{\partial x} - \frac{\partial E_x}{\partial y} = j\omega\mu_0 H_z \tag{1-10}$$

$$\frac{\partial H_z}{\partial y} - j\beta H_y = -j\omega\epsilon E_x, \quad j\beta H_x - \frac{\partial H_z}{\partial x} = -j\omega\epsilon E_y, \quad \frac{\partial H_y}{\partial x} - \frac{\partial H_x}{\partial y} = -j\omega\epsilon E_z \tag{1-11}$$

In general, a mode with a longitudinal electric field component $E_z = 0$ is called a transverse-electric (TE) mode, while a mode with a longitudinal magnetic field component $H_z = 0$ is referred to as a transverse-magnetic (TM) mode. Such modes can occur in waveguides where the refractive index n varies only in one direction, as in a planar waveguide. This is because the lack of variation in the other transverse direction decouples the Maxwell's equations, allowing the transverse electric and magnetic fields to be solved independently of the longitudinal components. For instance, if $\partial/\partial y = 0$, then for a TE mode ($E_z = 0$), E_x and

H_y are also zero. Similarly, for a TM mode ($H_z = 0$), H_z and E_y vanish. As a result, a simplified equation for the TE mode emerges, independent of the other components:

$$\frac{\partial^2 E_y}{\partial x^2} + (k^2 - {\beta_0}^2)E_y = 0 \tag{1-12}$$

This simplification is not possible if the refractive index n varies in both the x and y directions, as the transverse wave equations are no longer decoupled. Instead, they become interdependent due to the material properties and interface boundary conditions. To elaborate this, consider equation (1-1) for a non-planar waveguide. If we assume $Ez = 0$, we will have:

$$\frac{\partial E_x}{\partial x} + \frac{\partial E_y}{\partial y} = 0 \tag{1-13}$$

From the wave equations and similarly from equation (1-10), we know that the components E_x and E_y (and their derivatives) are coupled to the variation in $n(x, y)$. That means E_x and E_y vary in both x and y directions and cannot independently satisfy the divergence condition unless their variations precisely cancel out. Unless the geometrical specification of waveguide brings such a scenario, the modes in two-dimensional confinement are generally hybrid, with some component of $\boldsymbol{E}$ and $\boldsymbol{H}$ in transverse or propagation direction (*i.e.*, E_z and H_z are nonzero). Numerical finite-element methods are a popular approach to solving such equations. In this thesis, we will primarily use the commercial Lumerical Mode Solver [3] for mode solving, unless otherwise stated.

1.2.2 Active Photonics

Active components, unlike passive components, contain a gain medium that facilitates the amplification of light. This amplification is achieved through the generation of photons in the gain medium. Active devices operate based on the principles of absorption or emission, leading to the creation of components such as photodetectors, modulators, and lasers. Since this thesis primarily focuses on lasers, I will briefly discuss the principles of semiconductor diode lasers in this section.

Diode lasers consist of a gain medium housed within a resonant cavity, which typically takes the form of a waveguide bounded by mirrors. These mirrors facilitate resonance of the traveling electromagnetic wave. It is already evident that the design of the waveguide plays a critical role in the operation of the laser. The gain medium absorbs electromagnetic waves over a range of wavelengths, making the selection of materials critical to match the desired operating wavelength of the laser. When the material is pumped, typically by an electrical current, electrons are excited to higher energy states, enabling the generation of new photons as they return to lower energy states. This process, known as recombination, results in the amplification of the incident wave, a phenomenon that will be discussed in more detail later in this section. The mirrors at the ends of the cavity provide feedback, allowing the light to be reflected back through the gain medium, where it can be further amplified. Once the traveling wave gains enough energy to compensate for the losses it experiences in the cavity (such as propagation loss or loss from the mirrors), the laser reaches its threshold. At this point, the

cavity supports specific wavelengths where the traveling waves form constructive interference. These wavelengths are referred to as cavity modes or standing waves.

The wavelengths of these cavity modes are directly related to the cavity length. Specifically, the cavity length must be an integer multiple of half the wavelength to support standing waves. This can be shown as follow: a standing wave results from the constructive interference of two waves traveling in opposite directions, which means that the wave must have a node at each mirror. As such, boundary conditions are applied at the mirrors, where the amplitudes of the waves must be zero. Let us assume that forward and backward propagating waves are $R\exp(j\beta_0 z)$ and $S\exp(-j\beta_0 z)$, respectively, where z is the propagation direction. For the total wave $\varphi(z)$ to be zero at $z = 0$, we have:

$$\varphi(0) = R + S = 0 \tag{1-14}$$

Second boundary condition requires zero amplitude at $z = L$ (L is the cavity length)

$$\varphi(L) = R(\exp(j\beta_0 L) - \exp(-j\beta_0 L) = 2jR\sin(\beta_0 L) = 0 \tag{1-15}$$

With β_0 being the mode's propagation constant and n_{eff} being its effective index, we can write

$$\frac{2\pi n_{eff} L}{\lambda} = N\pi \tag{1-16}$$

Where N is an integer. Therefore:

$$L = \frac{N\lambda}{2n_{eff}} \tag{1-17}$$

So, L satisfies the resonance condition if it is an integer multiple of half the wavelength within the medium. Similarly, the resonant wavelength for each cavity mode N can be determined using the relation $\lambda_N = 2n_{eff}L/N$.

Fig. 1.2 illustrates a longitudinal cross-section of a laser cavity along with the spectral characteristics of the gain medium and cavity modes. The gain spectrum is typically very broad, covering multiple cavity modes. Among these modes, the one that aligns with the peak of the gain spectrum experiences the highest amplification and becomes the primary lasing mode. Although, neighboring modes also experience significant amplification, leading to competition with the dominant mode. This competition can result in laser instability. Therefore, a single mode laser is preferred. To achieve single-mode operation, filtering techniques are employed to isolate a specific cavity mode. A widely used filtering method involves the use of optical gratings, which will be discussed later.

The most important aspect of studying an active medium is understanding how gain is achieved. For that, it is important to understand how the band structure forms in a semiconductor crystal. From quantum mechanics, specifically the Schrödinger equation, we

know that an electron in an isolated atom can occupy discrete energy levels. When two atoms are brought close together, the outermost electrons interact. Since each electron has a wavefunction surrounding it, these wavefunctions can interfere constructively or destructively, leading to a splitting of energy levels. This concept can be explained by starting with the Schrödinger equation [4]:

$$\hat{H}\psi = E\psi \tag{1-18}$$

In this equation, ψ represents the wavefunction of the outermost electron of the atom, E is the energy eigenvalue of the orbital, and H is the Hamiltonian operator, which accounts for the sum of kinetic and potential energy. Let us first assume that these electrons belong to the same type of atom (*i.e.*, their energy levels E are identical). Since the Hamiltonian is a linear operator, when atoms a and b are brought closer together, we can use the Linear Combination of Atomic Orbitals (LCAO) approach [5] to express the total wavefunction as:

$$\psi = c_{\mathrm{a}}\psi_{\mathrm{a}} + c_{\mathrm{b}}\psi_{\mathrm{b}} \tag{1-19}$$

so

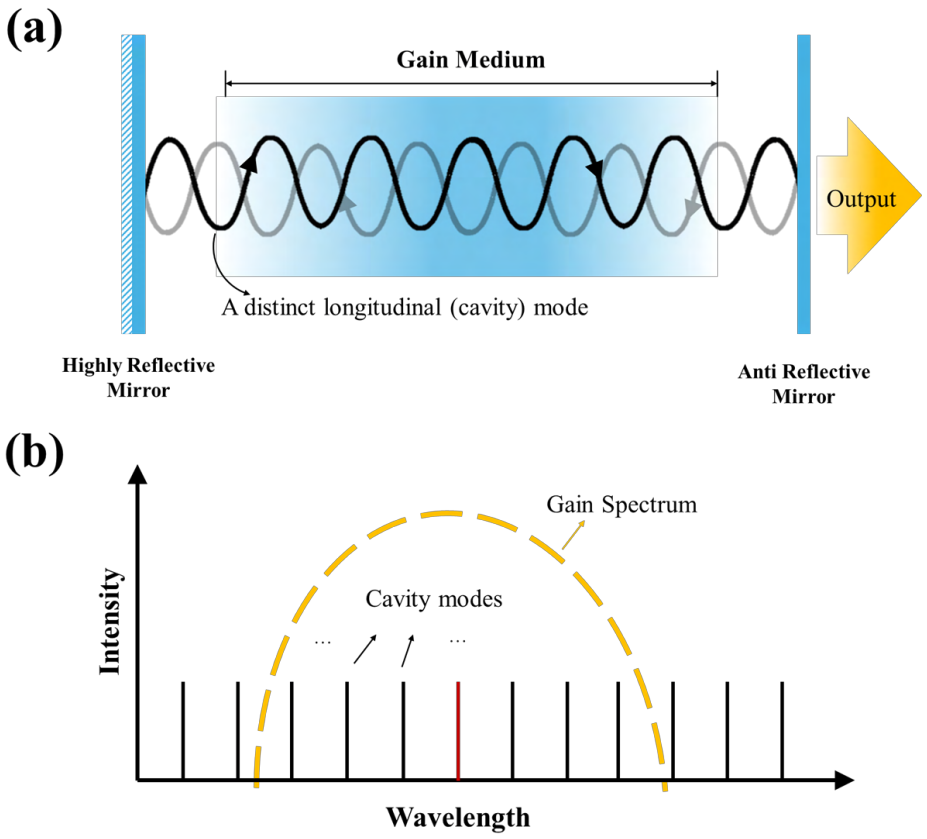

Fig. 1.2 (a) A schematic of the longitudinal cross-section of a laser, highlighting key components required for wave propagation: the cavity, gain medium, and facet mirrors. The output light is typically monitored from the facet with lower reflectivity. (b) The spectral characteristics of a laser, illustrating cavity modes and the gain spectrum. The lasing mode corresponds to the cavity mode with the highest gain (indicated in red).

$$c_{\mathrm{a}}\hat{H}\psi_{\mathrm{a}} + c_{\mathrm{b}}\hat{H}\psi_{\mathrm{b}} = c_{\mathrm{a}}E\psi_{\mathrm{a}} + c_{\mathrm{b}}E\psi_{\mathrm{b}} \tag{1-20}$$

where c_{a} and c_{b} are weighting coefficients. By multiplying each side of the equation by ${\psi_{\mathrm{a}}}^*$ and ${\psi_{\mathrm{b}}}^*$ and then integrating over the entire volume, we can define both the energy of each electron orbital and the energy exchange between them (note that $\int \psi\psi^* dV = 1$):

$$c_{\mathrm{a}}H_{aa} + c_{\mathrm{b}}H_{ab} = c_{\mathrm{a}}E + c_{\mathrm{b}}ES \tag{1-21}$$
$$c_{\mathrm{a}}H_{ba} + c_{\mathrm{b}}H_{bb} = c_{\mathrm{a}}E + c_{\mathrm{b}}ES \tag{1-22}$$

where

$$H_{aa,bb} = \int {\psi_{\mathrm{a,b}}}^* \hat{H}\psi_{\mathrm{a,b}} dV \tag{1-23a}$$
$$H_{ab} = H_{ba} = \int {\psi_{\mathrm{a}}}^* \hat{H}\psi_{\mathrm{b}} dV \tag{1-23b}$$
$$S = \int {\psi_{\mathrm{a}}}^* \psi_{\mathrm{b}} dV \tag{1-23c}$$

Here, H_{aa} and H_{bb} are the energy of the atomic orbital ψ_{a} and ψ_{b}, respectively, $H_{ab} = H_{ba} = H_0$ is the coupling energy between two orbitals, and S is the overlap integral between two orbitals. We can write the system of equations above in matrix form:

$$\begin{bmatrix} H_{aa} - E & H_0 - ES \\ H_0 - ES & H_{bb} - E \end{bmatrix} \begin{bmatrix} c_{\mathrm{a}} \\ c_{\mathrm{b}} \end{bmatrix} = 0 \tag{1-24}$$

For any non-trivial solution, the determinant of the first matrix should be zero. For simplicity, let us assume there is no overlap between the orbitals, *i.e.*, $S = 0$. Therefore:

$$E_{\pm} = \frac{H_{aa} + H_{bb}}{2} \pm \sqrt{(\frac{H_{aa} - H_{bb}}{2})^2 + {H_0}^2} \tag{1-25}$$

When two atoms are brought close to each other, it becomes evident that two solutions exist for their molecular orbital energy E. One solution corresponds to a lower energy level E_-, resulting from the constructive interference of the wavefunctions, and is referred to as the bonding molecular orbital. The other solution corresponds to a higher energy level E_+, caused by destructive interference, and is known as the antibonding molecular orbital. The two electrons from the atoms will occupy the lower energy level, as it is more stable, leaving the higher energy level unoccupied.

When a third atom is introduced, solving for the molecular orbital energy E results in a cubic equation, yielding three energy states: bonding, antibonding, and an intermediate state. Similarly, for a system of N atoms, N molecular orbitals are formed, which are closely spaced to create a continuous energy band. The lowest energy state corresponds to the bonding level, while the highest energy state represents the antibonding level. According to the Pauli

Exclusion Principle and the spin degeneracy of electrons, at temperature $T = 0$ K, the lower half of the energy band becomes filled with electrons, leaving the upper half empty. At higher temperatures, the electron occupancy follows the Fermi-Dirac distribution [2]

$$f(E) = \frac{1}{e^{(E-E_f)/kT} + 1}, \tag{1-26}$$

meaning that the probability of an electron occupying an energy level E greater than E_f becomes non-zero, and some energy levels below E_f become unoccupied. The Fermi level E_f is the energy at which $f(E) = 0.5$, and k is the Boltzmann constant.

If the material has multiple types of orbitals (*e.g.*, *s* and *p*), the interaction between these orbitals can result in gaps between energy bands, where no solutions to the Schrödinger equation exist for electron energies in that range. The band containing the energy levels associated with bonding states, or states predominantly occupied by electrons, is called the valence band. The conduction band consists of higher-energy, unoccupied states, often associated with antibonding configurations. The band gap refers to the energy difference between the top of the valence band and the bottom of the conduction band. In semiconductors, the band gap is typically around 1 eV, whereas insulators have a much larger band gap, and metals exhibit a very small or nonexistent band gap.

When the system is excited by some form of energy injection, such as thermal, electrical, or optical energy, electrons in the valence band can be promoted to the conduction band. This excitation creates holes in the valence band and electrons in the conduction band. These transitions occur only for very limited electron-hole pairs, the ones that share the same momentum, as this is required for momentum conservation. This selective transition simplifies the calculation of optical gain, as the process can be modeled by considering the interaction of a single electron-hole pair. For further details, refer to [6].

This electron transition occurs in several forms. Fig. 1.3 illustrates key transitions involving the absorption and emission of photons. The two-level energy diagram represents the top of

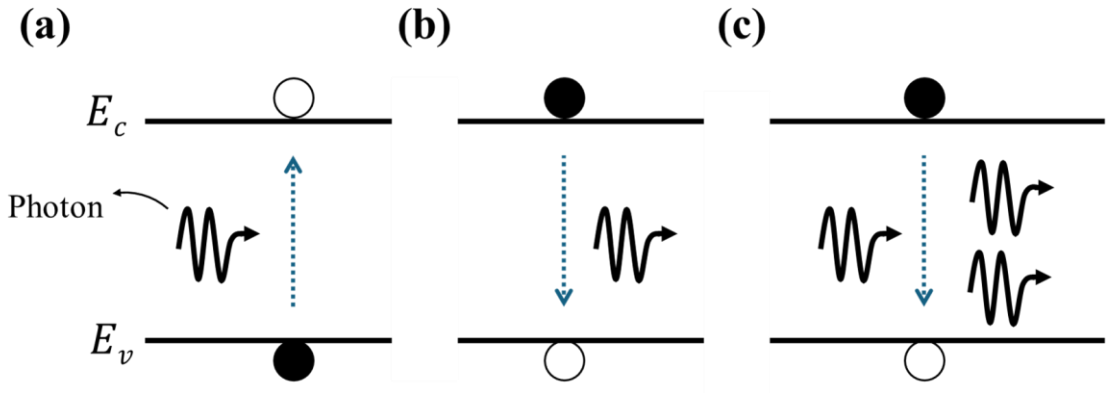

Fig. 1.3 Key electronic transitions between the valence and conduction bands: (a) generation of an electron-hole pair via light absorption, (b) recombination of an electron with a hole, resulting in spontaneous photon emission, and (c) stimulated photon emission.

the valence band $E_{v,}$ and the bottom of the conduction band E_c. Solid circles represent electrons, while open circles are holes. These carriers are shown at the energy levels because their densities are highest near the band edges, meaning most transitions occur in this region. Since the energy difference between E_v and E_c is approximately equal to the band gap energy E_g, the photon energy required for these transitions is also equal to E_g. Below, we qualitatively discuss such transitions.

The first case shows the absorption of the light (stimulated generation), where a photon with energy of E_g is efficiently absorbed by material and excites an electron from E_v to E_c, creating an electron hole pair near the band edges. The generation of charge carriers through this mechanism forms the basis of photovoltaic applications, where light energy is converted into electrical energy.

Next two steps show the recombination processes, in which energy is released in the form of heat or light. Recombination is the reverse of the generation process: an electron loses energy and transitions back to the valence band, recombining with a previously generated hole. When this energy is released as a photon, the process is referred to as spontaneous emission. In the third case, an incoming photon interacts with an excited electron, stimulating its recombination with a hole and simultaneously generating a new photon. This phenomenon is known as stimulated emission and is the fundamental principle behind laser operation. There are other significant non-radiative transitions to consider when studying gain, such as Auger recombination and defect-related transitions. While these mechanisms are not discussed in detail here, they are extensively studied in the literature. For further information, I refer you to [6].

In a laser, the net gain experienced by the incident radiation field is determined by the net combination of stimulated emission and photon absorption. The laser's efficiency in producing gain depends heavily on the recombination and generation rates, which are directly linked to the photon and carrier densities in the active region. A critical parameter is the threshold carrier density, which must be reached for stimulated emission to dominate over absorption. Accurate gain calculation is essential for laser design, as it depends on various material properties. To facilitate this, I have utilized the Lumerical MQW Solver [3] throughout this thesis as the tool for modeling and analyzing the gain spectrum.

1.2.3 Plasmonics

When a radiation field interacts with a metal-dielectric interface, the free electrons in the metal oscillate at the same frequency as the incident field. This oscillation leads to the periodic formation of regions with net negative and positive surface charge on the metal, alternating over each half-cycle of the field. These coherent electron oscillations, coupled with the electromagnetic field at the interface, are known as surface plasmon polaritons (SPPs) [7]. The energy from the incident light that drives the charge oscillations is partially absorbed by the metal, giving off the energy mainly as heat due to ohmic losses of the material. Additionally,

the confinement of the electromagnetic field near the interface and the buildup of surface charges enhances the local electric field intensity, which can further amplify absorption as the wave propagates along the interface.

From a waveguiding perspective, the presence of a metallic layer in the waveguide structure introduces a complex permittivity in Maxwell's equations (1-1) and (1-2) due to the inherent losses in metals, resulting in a complex refractive index. Applying the same analysis as outlined in Section 1.1, the mode's propagation constant becomes $\beta = \beta_r + j\beta_i$. The real part, β_r, corresponds to the effective index of the propagating mode. For a waveguide where the core dielectric is covered by a metal layer, the fundamental TM mode typically exhibits an effective index much higher than the core's refractive index, indicating that the mode is not confined to the core but is instead guided along the metal-dielectric interface. This mode is a SPP and is strongly localized at the interface.

The imaginary part, β_i, represents the propagation loss of the SPP mode. This can be understood by expressing an electric field propagating in a medium with a complex propagation constant:

$$\boldsymbol{E} = E_0 e^{j(\beta_r + j\beta_i)z}, \tag{1-26}$$

The power of the propagating wave is proportional to the square of the field amplitude:

$$P \propto |\boldsymbol{E}|^2 = |E_0|^2 e^{-2\beta_i z}, \tag{1-27}$$

The rate at which the power decreases is defined as the propagation loss, given by

$$\alpha_{\text{propagation}} = 2\beta_i \tag{1-28}$$

The inherent propagation loss of plasmonic waves limits their practical applications. To mitigate this, an alternative wave mode known as Long-Range Surface Plasmon Polaritons (LR-SPPs) has been introduced [8]. LR-SPPs exhibit a more symmetric distribution of the electromagnetic field across the metal-dielectric interface, significantly reducing ohmic losses in the metal and allowing for much longer propagation distances compared to conventional SPPs. However, their attenuation remains too high for widespread adoption in the telecom and datacom industries.

Despite this, plasmonic has found applications in other fields. For example, biosensing is a technology dominated by plasmonic, due to the extremely high sensitivity of the propagating mode to changes in the surrounding material [9-11]. In this thesis, the aim is to evaluate the performance of plasmonic components integrated with III-V dielectric lasers for telecom and biosensing applications, with the motive of compensating their inherent losses using the high gain of III-V semiconductor compounds.

1.2.4 Waveguide Bragg Gratings

An optical grating, in general terms, is a periodic structure that diffracts incident radiation into different directions. In this thesis, I specifically focus on waveguide Bragg gratings (WBGs), a type of grating where periodic structures are embedded within a waveguide. These gratings interact with the waveguide mode propagating along the same direction as the periodic pattern.

WBGs selectively reflect specific wavelengths of light, determined by the grating's periodicity. This selective reflection arises from the principle of constructive interference, where light reflected from different planes within the grating, spaced periodically by a distance Λ, reinforces at certain wavelengths. The behavior can be described mathematically using ray optics [12]. The Bragg wavelength condition is satisfied by

$$N\lambda_{\mathrm{B}} = 2n_{\mathrm{eff}}\Lambda, \tag{1-29}$$

where λ_{B} is the Bragg wavelength (center wavelength of reflection), and N is the order of the grating. As evident from the definition of WBGs, two types of waves propagate within the grating: forward- and backward-propagating waves. To understand the behavior of WBGs more comprehensively—such as the evolution of these waves, their coupling mechanisms, and their emission spectra—a theoretical framework called Coupled-Mode Theory (CMT) is employed [13]. This method involves two coupled equations that describe the interaction between the counter-propagating waves within the WBG. In the following, I will derive these equations using an improved version of CMT, first elaborated by Streifer *et al.* [14]. Let us begin by recalling Maxwell's equations:

$$\nabla^2\boldsymbol{E} + (\epsilon(x) + \Delta\epsilon(x,z))k_0^2\boldsymbol{E} = 0 \tag{1-30}$$

where $\Delta\epsilon$ is the permittivity perturbation along the propagation axis, z (refer to Fig. 1) and $k_0 = 2\pi/\lambda_{\mathrm{B}}$. The structure is assumed to be uniform in the y-direction. Let us consider a TE mode, where the only nonzero electric field component is Ey:

$$\frac{\partial^2 E_y}{\partial z^2} + \frac{\partial^2 E_y}{\partial x^2} + \left(\tilde{n}_0{}^2 + \sum_{\substack{q=-\infty \\ q\neq 0}}^{\infty} A_q(x) exp\left(\frac{i2\pi qz}{\Lambda}\right) \right) k_0^2 E_y = 0, \tag{1-31}$$

in which A_q represents the Fourier coefficients that describe the periodic structure, and

$$\tilde{n}_0{}^2 = (n_0(x) - i\frac{\tilde{\alpha}(x)}{k_0})^2, \tag{1-32}$$

where n_0 is the average refractive index within each layer of the waveguide stack, and $\tilde{\alpha}$ is gain (> 0) or loss (< 0) as a result of perturbation effects. E_y, in principle, is a superposition of an infinite number of modes. To solve (1-31), we assume:

$$E_y(x,z) = \sum_m E_y^{(m)}(x,z)e^{i\beta_m z} \tag{1-33}$$

where $\beta_m = \beta_0 + 2\pi m/\Lambda$, and each $E_y^{(m)}$ represents a partial wave. $m = 0$ refers to the waveguide mode in absence of gratings. Substituting (1-33) into (1-31), for each m, we have:

$$\frac{\partial^2 E_y^{(m)}}{\partial z^2} + 2i\beta_m \frac{\delta E_y^{(m)}}{\delta z} + \frac{\partial^2 E_y^{(m)}}{\partial x^2} + \left({k_0}^2 \tilde{n}_0{}^2 - {\beta_m}^2\right)E_y^{(m)} = -{k_0}^2 \sum_{\substack{q=-\infty \\ q\neq 0}}^{\infty} A_q(x) E_y^{(m-q)}, \forall m \tag{1-34}$$

Under the resonant condition $p = -N$, the grating couples the forward mode $E_y^{(0)}(x,z)$ and its backward-propagating counterpart $E_y^{(p)}(x,z)$. Both modes share the same transverse profile $\varepsilon_0(x)$ with their amplitudes $R(z)$ and $S(z)$ varying along the propagation direction z

$$E_y^{(0)}(x,z) = R(z)\varepsilon_0(x) \tag{1-35a}$$

$$E_y^{(p)}(x,z) = S(z)\varepsilon_0(x) \tag{1-35b}$$

Substituting (1-35) into (1-34) for $m = 0$ and $m = p$ (given that $\beta_p = -\beta_0$ and second z-derivative term is much smaller than other terms):

$$2i\beta_0\varepsilon_0(x)\frac{\delta R(z)}{\delta z} + R(z)\left[\frac{\partial^2 \varepsilon_0(x)}{\partial x^2} + \left({k_0}^2 \tilde{n}_0{}^2 - {\beta_0}^2\right)\varepsilon_0(x)\right] = -{k_0}^2 \sum_{\substack{q=-\infty \\ q\neq 0}}^{\infty} A_q(x) E_y^{(-q)} \tag{1-36a}$$

$$-2i\beta_0\varepsilon_0(x)\frac{\delta S(z)}{\delta z} + S(z)\left[\frac{\partial^2 \varepsilon_0(x)}{\partial x^2} + \left({k_0}^2 \tilde{n}_0{}^2 - {\beta_0}^2\right)\varepsilon_0(x)\right] = -{k_0}^2 \sum_{\substack{q=-\infty \\ q\neq 0}}^{\infty} A_q(x) E_y^{(p-q)} \tag{1-36b}$$

In transverse direction, $\varepsilon_0(x)$ satisfies:

$$\frac{\partial^2 \varepsilon_0(x)}{\partial x^2} + \left({k_0}^2 n_0{}^2 - \beta^2\right)\varepsilon_0(x) = 0 \tag{1-37}$$

Therefore, by Multiplying sides by $\varepsilon_0(x)$ and integrating from $-\infty$ to ∞, (1-36) becomes:

$$R' - (\alpha + i\delta)R = i\kappa_{-p}S + \frac{i{k_0}^2}{2\beta_0 P} \sum_{\substack{q=-\infty \\ q\neq 0,-p}}^{\infty} \int_0^g A_q(x)\varepsilon_0(x) E_y^{(-q)} \tag{1-38a}$$

$$-S' - (\alpha + i\delta)R = i\kappa_p S + \frac{i{k_0}^2}{2\beta_0 P} \sum_{\substack{q=-\infty \\ q\neq 0,p}}^{\infty} \int_0^g A_q(x)\varepsilon_0(x) E_y^{(p-q)} \tag{1-38b}$$

where:

$$\alpha = \frac{{k_0}^2}{2\beta_0 P}\int_{-\infty}^{\infty} n_0(x)\tilde{\alpha}(x)\varepsilon_0^2(x)dx, \qquad \kappa_p = \frac{{k_0}^2}{2\beta_0 P}\int_0^g A_p(x)\varepsilon_0^2(x)dx, \tag{1-39}$$
$$P = \int_{-\infty}^{\infty}\varepsilon_0^2(x)dx, \qquad \delta = \beta - \beta_0$$

To solve (1-38), $E_y^{(m)}$ must be determined using (1-34). We make the following assumptions: the z-derivatives in (1-34) are much smaller than other terms and only the modes $m = 0, p$ contribute to generating $E_y^{(m)}$. Therefore, (1-34) becomes:

$$\frac{\partial^2 E_y^{(m)}(x,z)}{\partial x^2} + \left({k_0}^2{n_0}^2 - {\beta_m}^2\right)E_y^{(m)}(x,z) = -{k_0}^2\left(A_m(x)R(z) + A_{m-p}(x)S(z)\right)\varepsilon_0(x), \ \forall m \tag{1-40}$$

in which $E_y^{(m)}$ is made of two separable terms associated with forward and backward propagating waves:

$$E_y^{(m)}(x,z) = R(z)\varepsilon_m^{(0)}(x) + S(z)\varepsilon_m^{(p)}(x), \ \forall m, m \neq 0, p \tag{1-41}$$

Thus:

$$\frac{\partial^2 \varepsilon_m^{(i)}(x)}{\partial x^2} + \left({k_0}^2{n_0}^2 - {\beta_m}^2\right)\varepsilon_m^{(i)}(x) = -{k_0}^2 A_{m-i}\varepsilon_0(x), \ \forall m, \ i \neq 0, p \tag{1-42}$$

Equation (1-42) has the first-order perturbation solution for $\varepsilon_m^{(i)}$. Without assuming the second assumption, general solution for $\varepsilon_m^{(i)}$ can be derived from:

$$\frac{\partial^2 \varepsilon_m^{(i)}(x)}{\partial x^2} + \left({k_0}^2{n_0}^2 - {\beta_m}^2\right)\varepsilon_m^{(i)}(x) = -{k_0}^2\sum_{\substack{q=-\infty \\ q\neq 0}}^{\infty} A_q(x)\varepsilon_{m-q}^{(i)}(x), \ \forall m, \ i \neq 0, p \tag{1-43}$$

In most cases, solving (1-42) provides sufficient accuracy. While solving Equation (1-43) is more precise, it is also more complex. By substituting solutions from either (1-42) or (1-43) in (1-38), we have

$$R' - (\alpha + i\delta + i\zeta_1)R = i(\kappa_{-p} + \zeta_2)S \tag{1-44a}$$
$$-S' - (\alpha + i\delta + i\zeta_3)S = i\left(\kappa_p + \zeta_4\right)R \tag{1-44b}$$

where

$$\zeta_1 = \sum_{\substack{q=-\infty \\ q\neq 0,-p}}^{\infty}\eta_{q,-q}^{(0)}, \ \zeta_2 = \sum_{\substack{q=-\infty \\ q\neq 0,-p}}^{\infty}\eta_{q,-q}^{(p)}, \ \zeta_3 = \sum_{\substack{q=-\infty \\ q\neq 0,p}}^{\infty}\eta_{q,p-q}^{(p)}, \ \zeta_4 = \sum_{\substack{q=-\infty \\ q\neq 0,p}}^{\infty}\eta_{q,p-q}^{(0)} \tag{1-45}$$
$$\eta_{r,s}^{(i)} = \frac{{k_0}^2}{2\beta_0 P}\int_0^g A_r(x)\varepsilon_0(x)\varepsilon_s^{(i)}(x)dx$$

Equations (1-44) represent the coupled-mode equations, which describe the interaction between forward- and backward-propagating waves, including any radiated components.

Other than Coupled-Mode Theory, more general approaches involve directly solving Maxwell's equations. Among these, the Finite-Difference Time-Domain (FDTD) method and Eigenmode Expansion (EME) are widely used for analyzing electromagnetic fields in structures with complex geometries [15, 16]. In this thesis, I will utilize these numerical methods to comprehensively study the behavior of WBGs.

1.3 Overview of the Thesis

This thesis originally set out to investigate the development of tunable lasers for telecommunication. Considerable research has been devoted to InP-based platforms, due to their commercial application in datacom and telecom industries. As a result, this thesis concentrates on these platforms. Chapter 2 offers a comprehensive review of tunable laser technologies developed over the past two decades.

In Chapter 3, a novel approach to achieving laser tunability through loss perturbation is introduced, harnessing the unique properties of plasmonics and III-V semiconductors. A key element of this method is the use of conductive oxides, such as indium tin oxide, which takes advantage of its epsilon-near-zero properties to induce significant alterations in the laser mode. The theoretical design principles for semiconductor lasers are thoroughly discussed in this chapter.

The scope of this project was expanded to include an application: biosensing. Building on the method presented in Chapter 3, Chapter 4 introduces a biosensor with substantial commercial potential. This chapter specifically details the design of an electrically driven InP-based Fabry-Perot biochemical sensing laser. The design incorporates an etch-free III-V stack with an integrated sensing area positioned atop the laser to modulate its characteristics, operating in a hybrid plasmonic-semiconductor lasing mode. Theoretical evaluations of the sensor's sensitivity are performed for various measurands.

Chapter 5 demonstrates an edge-emitting light-emitting diode (LED), functioning as a refractometer. We present a simple, easy to fabricate, and low-cost LED where the reflection of light off its facet is sensitive to the fluid covering them. Therefore, the characteristics of the output light changes with the fluid, enabling a refractometry mechanism.

Studying the applications of gratings in tunable lasers led to new findings worth further investigation. These results have been incorporated into this thesis. Chapter 6 examines strong Bragg waveguide gratings formed by trapezoidal grooves, a common feature in surface-etched structures. The analysis utilizes the finite-difference time-domain (FDTD) simulation method, with results validated against previously studied structures using coupled mode theory (CMT).

Chapter 7 introduces Dirac Gratings. This work focuses on WBGs where the refractive index perturbation is much smaller than a single period, making the perturbation along the waveguide resemble a Dirac function. Typically, higher-order gratings (where the period of an *M*-order grating is *M* times that of a first-order grating) exhibit a smaller coupling coefficient compared to first-order gratings. This chapter mathematically demonstrates that Dirac Gratings are order independent and provides physical justification for this behavior. Practical examples of Dirac Gratings are discussed at the end of this chapter.

Chapter 8 introduces a novel method for studying waveguide Bragg gratings (WBGs) that combines finite-difference techniques with the coupled-mode theory, referred to as Finite-Difference Coupled-Mode Theory (FD CMT). This approach is rigorously compared with FDTD and Finite-Element Method (FEM), showing significant computational advantages over all of them. Due to its numerical nature, FD CMT can handle any arbitrary grating profile, a capability that was previously beyond the reach of traditional coupled-mode theory.

Chapter 9 concludes the thesis by summarizing the key achievements and outlining potential directions for future research.

References

1. R. N. Hall, *et al*. "Coherent light emission from GaAs junctions." *Physical Review Letters* 9.9 (1962): 366.
2. G. P. Agrawal, and N. K. Dutta. *Semiconductor lasers*. New York, NY, US : Van Norstrand Reinhold (1993).
3. Lumerical is Now Part of the Ansys Family (2025), https://www.lumerical.com/
4. J. A. Pople, and D. L. Beveridge. "Molecular orbital theory." *C0., NY* (1970).
5. J. C. Slater, and G. F. Koster. "Simplified LCAO method for the periodic potential problem." *Physical review* 94.6 (1954): 1498.
6. L. A. Coldren, S W. Corzine, and M. L. Mashanovitch. *Diode lasers and photonic integrated circuits*. Chapter 4. Vol. 218. John Wiley & Sons, 2012.
7. S. A. Maier. *Plasmonics: fundamentals and applications*. Vol. 1. New York: springer, 2007.
8. P. Berini. "Long-range surface plasmon polaritons." *Advances in optics and photonics* 1.3 (2009): 484-588.
9. J. Zhang, L. Zhang, and W. Xu. "Surface plasmon polaritons: physics and applications." *Journal of Physics D: Applied Physics* 45.11 (2012): 113001.
10. A. B. González-Guerrero, *et al.* "Trends in photonic lab-on-chip interferometric biosensors for point-of-care diagnostics." *Analytical methods* 8.48 (2016): 8380-8394.
11. S. Kumar, *et al. Optical fiber-based plasmonic biosensors: trends, techniques, and applications*. CRC Press, 2022.

12. H. G. J. Moseley. "The high-frequency spectra of the elements." *The London, Edinburgh, and Dublin Philosophical Magazine and Journal of Science* 26.156 (1913): 1024-1034.
13. H. Kogelnik, and C. V. Shank. "Coupled-wave theory of distributed feedback lasers." *Journal of applied physics* 43.5 (1972): 2327-2335.
14. W. Streifer, D. Scifres, and R. Burnham. "Coupled wave analysis of DFB and DBR lasers." *IEEE Journal of Quantum Electronics* 13.4 (1977): 134-141.
15. J. Čtyroký, *et al*. "Bragg waveguide grating as a 1D photonic band gap structure: COST 268 modelling task." *Optical and Quantum Electronics* 34 (2002): 455-470.
16. Y. J. He, W. C. Hung, and Z. P. Lai. "Using finite element and eigenmode expansion methods to investigate the periodic and spectral characteristic of superstructure fiber Bragg gratings." *Sensors* 16.2 (2016): 192.

Chapter 2

Widely Tunable Semiconductor Lasers

The increasing Internet bandwidth consumption requires increasing transmit/receive capacity of optical networks. Today's bandwidth-hungry applications hugely rely on the ability to transfer a large amount of data at the lowest time and lowest cost. To fully realize the potential of emerging technologies, such as the rapidly expanding Internet of Things, the network must efficiently handle growing data transmission and bandwidth demands.

Considering the standard International Telecommunications Union (ITU) wavelength grid, there are more than 100 distinct wavelength channels depending on channel spacing (200, 100, 50, and 25 GHz). Normally, each laser device is assigned to a unique channel based on its single operating wavelength. Typically, a market requires a certain wavelength configuration to satisfy a specific application. The demands in different applications change rapidly so that it exceeds the supply's adjust rate. In a typical case, carriers will order more channels to keep up with the demand or to have backup strategies in case of device failure. This process will generate a massive non-revenue-making inventory. To efficiently handle this amount of traffic, Wavelength Division Multiplexing (WDM) systems have been introduced as a solution. As the numbers of channels increase, systems must become larger to fit in more components. Until lately, each of these components used a fixed single-frequency laser to produce signal at the desired frequency. This trend added more complexity to WDM systems and faced the telecom industry with cost problems [1, 2].

To overcome these limitations, tunable lasers emerged as a flexible and cost-effective alternative, replacing arrays of fixed-wavelength lasers in WDM systems. A single tunable laser with a tuning range of 10 nm can significantly reduce system complexity, lower inventory costs, and enhance network flexibility, making it a valuable solution for modern optical networks. However, despite their advantages, tunable lasers have not yet fully displaced traditional single-wavelength distributed feedback (DFB) lasers on performance and cost, which continue to be widely deployed and marketed.

In this chapter, a brief overview of tuning mechanisms is given. Following that, a comprehensive review on different types of tunable lasers is provided, evaluating their performance and their complexity.

2.1 Tuning Mechanisms

There are three primary methods to tune the refractive index of a semiconductor material, resulting in a shift in the peak wavelength of the wavelength selection filter section in tunable lasers. While mechanical tuning methods can also shift the wavelength by altering the cavity length or the angle of beam incidence, these approaches are outside the scope of this study due to their high cost and complexity in fabrication and packaging, making them less suitable for industrial applications. This review focuses on the three key methods.

2.1.1 Thermal Tuning

In this method, usually a metal heater is implemented on top of the wavelength selection section. As the temperature increases, the atomic vibration in both valence and conduction band increases. This effectively increases the average interatomic spacing, which reduces the semiconductor bandgap by shifting the conduction and valence band edges. Following relation shows the bandgap energy E_g as a function of temperature T [3]:

$$E_g(T) = E_g(0) - \frac{\alpha T^2}{T + \beta} \tag{2.1}$$

in which $E_g(0)$, α, and β are the fitting parameters. As the bandgap shrinks, the photon energy required to excite an electron from the valence band to the conduction band decreases. In regions of strong absorption near the band edge, the refractive index increases. Consequently, the effective index of the device changes, enabling the wavelength tuning behavior of the laser.

Thermal tuning allows simple fabrication, as it does not need a p-n junction in case of electrical tuning, and low optical loss. However, the wavelength switching speed is generally slow due to the slow thermal response of the material. The tuning speed in thermal tuning directly depends on thermal conductivity of the filter section, and between the elements on the chip-level. For example, a tuning range of around 3 nm is normally achieved by 40°C temperature change in DFB lasers at C-band wavelength range [4].

2.1.2 Carrier Injection

Electrical tuning, or current injection, is the most popular method to shift the lasing wavelength. Injecting current into the wavelength selection filter will change its refractive index and thus, controlling the wavelength peak can be achieved.

By carrier injection, unlike thermal tuning, a decrease in absorption happens as the bandgap energy increases due to the Moss-Burstein effect. In the case of n-type material, injected electrons can populate the lower bands of conduction band and thus, pushing the absorption

edge to higher energies. Similar phenomena happen for p-type material, where injected holes fill the highest bands of valence band and decrease the valence band energy level. Therefore, higher photon energy is required for absorption, and the absorption decreases. This effect is more significant for smaller effective masses. For p-type material, holes have larger effective masses and thus a higher density of states. This means that the valence band is pushed less downward for a given carrier concentration. The relation between refractive index n and absorption coefficient α is given by Kramers-Kronig equation [5]

$$n(E) = 1 + \frac{2ch}{2\pi e^2} P \int_0^\infty \frac{\alpha(E')}{E'^2 - E^2} dE' \tag{2.2}$$

in which c is the speed of light in vacuum, e is the electron charge, h is the Planck's constant, E is the photon energy, and P is the principal value of integral. Thus, any change to α directly applies to n as they are proportionally related.

Typically, tuning speed for such electrical tuning methods will be limited by carrier lifetime, which is in the scale of nanoseconds. So, fast switching can be achieved via carrier injection. However, parasitic effects such as heating due to non-radiative recombination can be a by-product of increasing tuning current. As explained previously, heating can lead to bandgap shrinkage which cancels out the Burstein effect to some extent.

2.1.3 Electro-Optic Effect

The electro-optic effect, also known as Pockels electro-optic effect, changes the refractive index of the optical medium linearly proportional to the applied DC electric field. However, not all materials can provide the Pockels effect. Let us write Taylor expansion of dielectric permittivity ϵ as a function of electrical field ε [6]:

$$\epsilon^{-1}(\omega, \varepsilon)_{ij} = \epsilon^{-1}{}_{ij}(\omega, 0) + \epsilon^{-1}{}_{ijk}(\omega, 0)\varepsilon_k + \cdots \tag{2.3}$$

The second term, which describes the action of electric field in linear approximation, represents the Pockels effect. Pockels coefficients $\epsilon^{-1}{}_{ijk}(\omega, 0)$ (also known with r_{ijk}) shape a tensor of rank three. However, the Pockels effect only occurs in materials without inversion symmetry. In crystals with inversion symmetry, a change in the sign of the applied electric field would produce an equivalent but opposite change in the dielectric permittivity, causing the Pockels coefficients to cancel out. As a result, only non-centrosymmetric crystals exhibit the Pockels effect. Examples of such materials include gallium arsenide (GaAs) and indium phosphide (InP), which are widely used in photonic integrated circuits (PICs). Since the refractive index changes almost immediately with the applied electric field, on a timescale determined by the material's electronic polarization, the Pockels effect is particularly well-suited for high-speed optical switching and tunable filters.

However, utilizing the Pockels effect is inherently complex because the refractive index change depends on both the polarization of the optical field and the orientation of the applied DC electric field. The subscripts of the Pockels coefficient r_{ijk} denote the orientations of the crystal axis, the electric field, and the optical field, requiring careful consideration of all three orientations. For indium phosphide (InP) and its alloys, the refractive index change for a wave propagating in the z-direction can be estimated as follows [7]:

$$\Delta n_x = \frac{{n_0}^3}{2} r \varepsilon_z \tag{2.4a}$$

$$\Delta n_y = -\frac{{n_0}^3}{2} r \varepsilon_z \tag{2.4b}$$

where n_0 is the unperturbed index for semiconductor in all direction, r is the Pockels coefficient, ε is the electrical field and Δn shows the index change in x or y direction. Since InP crystals belong to the zinc blende class, the Pockels coefficient r is the same for all nonzero tensor components. As the equations (2.4) show, the refractive index changes in the x- and y-directions, while it remains unchanged in the direction of the electric field. Such an effect can be used in filter sections in widely tunable lasers.

2.2 Widely Tunable Lasers

There have been many studies toward tunable lasers over the past few decades. Tunable laser technology requires certain criteria to be practical in WDM systems, such as tuning range, output power, side-mode suppression ratio (SMSR), chirp, tuning speed, and reliability. The applicability of tunable lasers depends on how well these criteria are balanced. However, achieving a commercial tunable laser presents significant challenges due to fundamental design trade-offs. For example, the conventional design of single-wavelength distributed feedback (DFB) lasers prioritizes stability at the cost of tunability. As a result, developing tunable lasers that meet both stability and performance standards remains a complex task.

Tunable lasers permit shifting output spectrum wavelength in post-fabrication. Narrowband tunability was considered in the early development of tunable lasers. In this case, an array of fixed-wavelength distributed feedback (DFB) lasers was monolithically integrated with a multimode interferometer (MMI) optical combiner to cover multiple channels in WDM systems. These techniques were used to obtain a tuning range of up to 15 nm [8]. These devices can be a good alternative to single-wavelength DFB lasers but still not an ideal solution, as the number of channels in WDM systems keeps increasing. Let us consider the equation describing the lasing wavelength λ:

$$m\lambda = 2n_{eff}L_{eff} \tag{2.5}$$

in which, n_{eff} is the effective index, L_{eff} is the effective length, and m is an integer representing the mode number. Thus, tunability in lasers can be implied by [9]:

$$\frac{\Delta\lambda}{\lambda} = \frac{\Delta n_{eff}}{n_{eff}} + \frac{\Delta L_{eff}}{L_{eff}} - \frac{\Delta m}{m} \tag{2.6}$$

where the change in lasing wavelength is related to waveguide's index change, cavity length change, and cavity mode change.

2.2.1 Sampled grating distributed Bragg reflector

One of the most commercialized tunable lasers is sampled grating distributed Bragg reflector (DBR) lasers which consists of four sections. For simplicity, let us consider a two-section DBR laser first, comprising a gain section and a mirror section. The mirror contains gratings that provide frequency-selective reflection. The refractive index of the material can be modified by injecting carriers through an applied current. Consequently, applying a bias shifts the center frequency of reflection in proportion to the change in the refractive index. Similarly, the laser gain can also be adjusted by applying bias. This allows independent control of each section, enabling manipulation of both the laser gain and the center frequency.

However, applying bias introduces undesired effects, as cavity modes shift along with changes in the refractive index. As a result, a specific axial mode may coincide with a frequency near the Bragg frequency when tuning the grating reflection spectrum. To address this issue, a third section, known as the phase section, can be added to the DBR laser device. By independently biasing the phase section, the mode comb can be shifted without altering the Bragg wavelength of the grating. Fig. 2.1 shows a schematic of spectral characteristics of mode comb, gain, and gratings (mirror) in a three-section DBR.

However, such a structure has a limited tuning range, as wavelength tunability is constrained by the achievable refractive index change. A solution to this problem is to add a

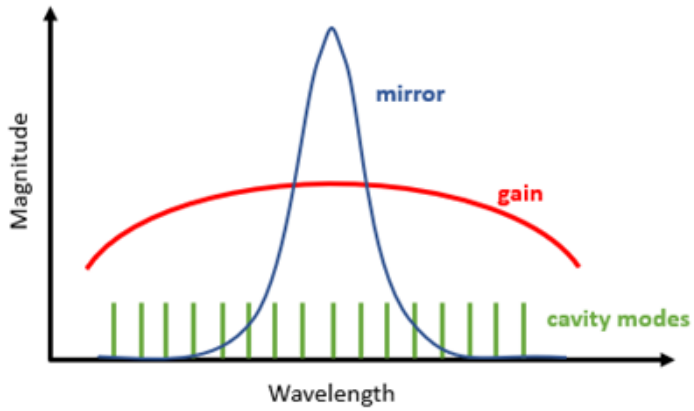

Fig. 2.1 Sketch of spectral characteristics of mode comb, gain, and mirror reflection for a three-section DBR.

second mirror to the front end of the laser structure. In this configuration, Bragg wavelength tuning is achieved by independently tuning both mirrors. This principle forms the basis of widely tunable Sampled Grating Distributed Bragg Reflector (SG-DBR) lasers.

The key feature in SG-DBR lasers is that the gratings in the front and back mirrors are periodically sampled. From Fourier analysis, we know that a continuous periodic structure produces a delta function in the frequency domain. To create a comb-like reflection spectrum with periodic maxima, the gratings are sampled by introducing blank areas between short grating patches. This periodic modulation in the spatial domain generates a periodic reflectivity spectrum in the frequency domain, enabling wide wavelength tunability. Fig. 2.2 shows an illustration of SG-DBR laser side cross-section with sampled front and back mirrors.

To realize how SG-DBR generates a comb reflection spectrum, we can start by evaluating propagating waves in a DFB structure. The electric field E can be written as the sum of two counter-propagating waves R and S:

$$E(z) = S(z)e^{-j\beta_0 z} + R(z)e^{j\beta_0 z} \tag{2.7}$$

For simplicity, I assume no radiated waves in this calculation, unlike in (1-33). Using the coupled-mode approach, we can assume the waves $R(z)$ and $S(z)$ are sufficiently slowly varying functions and their second-order derivatives can be neglected [10]. In this relation, β_0 is the propagation constant and z refers to the propagation axis. Therefore, the coupled-wave equations are as follow:

$$\frac{dR}{dz} - (j\delta)R = j\kappa S \tag{2.8a}$$

$$\frac{dS}{dz} + (j\delta)S = -j\kappa R \tag{2.8b}$$

By solving these equations, reflection spectrum for a uniform finite grating with length of L can be obtained:

$$r = -\frac{j\kappa \, tanh \, tanh \, (\gamma L)}{\gamma + j\Delta\beta tanh \, (\gamma L)} \tag{2.9}$$

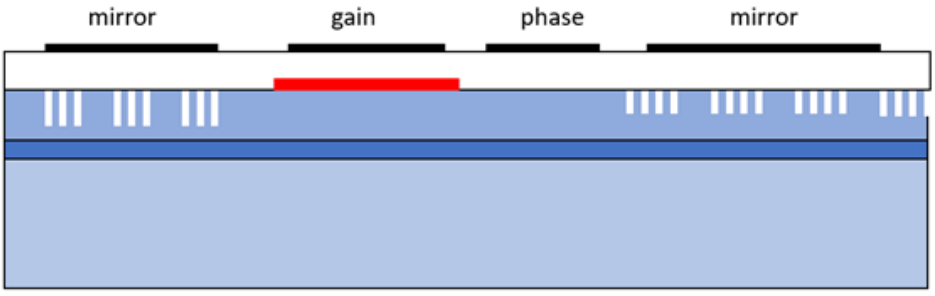

Fig. 2.2 Sampled grating DBR, consisting four sections: Two sampled grating (front and back mirrors), gain, and phase.

For a rectangular-shaped grating, the coupling coefficient $\kappa = \pi\Delta n/2\lambda$ quantifies the amount of reflection per unit of length where Δn is the average index change, and $\delta = \beta - \beta_0 = \frac{2\pi}{\lambda} n_{eff} - \frac{\pi}{\Lambda}$ where Λ is the length of period. The parameter γ is defined as $j\sqrt{\delta^2 - \kappa^2}$. Fig. 2.3 shows an example of a reflection spectrum with one peak at Bragg wavelength.

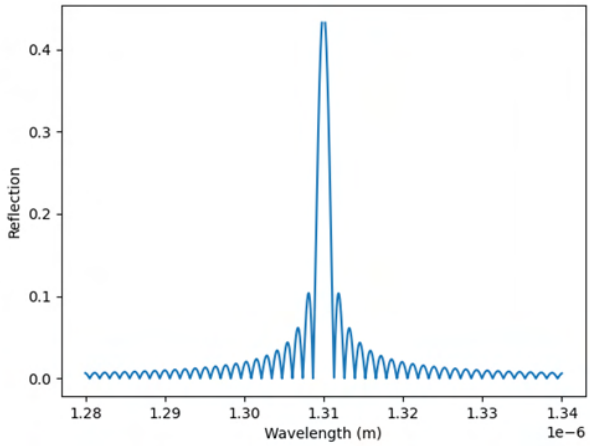

Fig. 2.3 Example of reflectivity of a first-order grating calculated using the coupled-mode approach. The grating parameters are: L=200 μm, Λ=200 nm, effective index $n_{eff} = 3.275$, and $\Delta n = 10^{-3}$ at 1310 nm.

Assuming an infinite, continuous grating, the reflection spectrum approaches the form of a Dirac delta function centered at the Bragg wavelength. Fig. 2.4(a) illustrates an approximation of this reflection spectrum. A sampled grating structure can be created by dividing the continuous grating into patches, separated by blank waveguide regions. This structure can be visualized as a finite pulse train, as shown in Fig. 2.4(b). The reflection spectrum of a sampled grating can be obtained by convolving the Dirac delta-like reflection spectrum of the continuous grating with the Fourier transform of the pulse train. This process results in a comb-like reflection spectrum, as demonstrated in Fig. 2.4(c), where the sampled grating generates distinct reflection peaks with non-uniform output power.

By designing the mirrors with different sample periods, each mirror produces a reflection spectrum with a unique wavelength periodicity. When one reflection maximum from one mirror aligns with a reflection maximum from the other mirror, the remaining maxima will be misaligned. As a result, the product of the two spectra will exhibit a single dominant reflection peak. This ensures a high side-mode suppression ratio (SMSR), which is a critical parameter in laser design. If both mirrors are tuned simultaneously to maintain alignment of their dominant peaks, the Bragg wavelength can be continuously shifted. Conversely, if only one mirror is tuned, or the mirrors are tuned independently, the entire reflection comb of that mirror shifts until a different pair of maxima aligns. This results in distinct tuning steps, often referred to as channel switching. The concept of increasing the tuning range by utilizing two comb-shaped reflection spectra is similar to the Vernier effect. Lasers leveraging the Vernier effect have become widely used in the design of tunable lasers. Various designs that employ this principle will be explored in the remainder of this chapter.

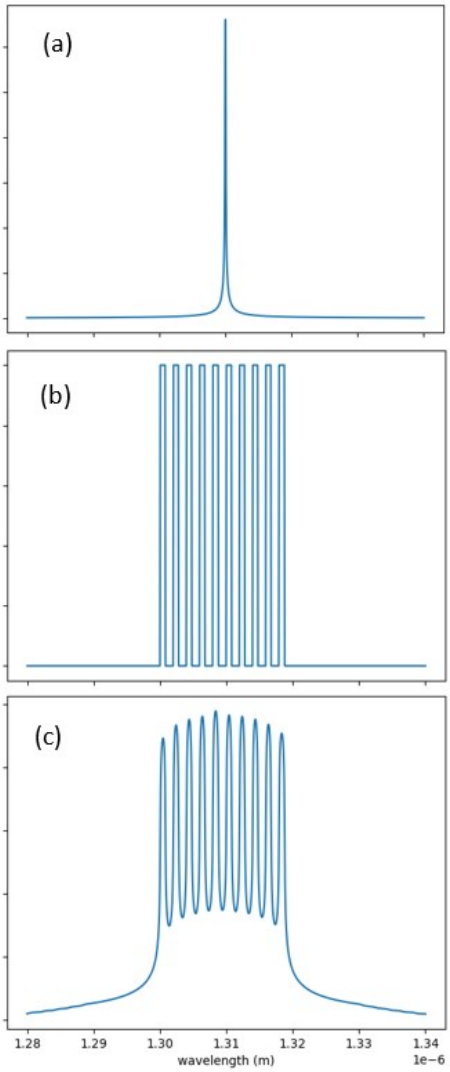

Fig. 2.4 Estimated reflection spectrum of SG structure (c) can be obtained by convolving reflection spectrum of a continuous grating (a) and sampling function (b). Sampling function parameters: 10 bursts of grating with duty cycle of 40%. Note that the vertical axis is not scaled.

2.2.2 Digital Supermode DBR

Similar to the SG-DBR, the Digital Supermode DBR (DS-DBR) consists of front and back mirrors. However, a different set of gratings is used in these mirrors. The back mirror, just like in the SG-DBR, is based on amplitude- or phase-modulated gratings and consists of grating patches separated by blank waveguide regions. With proper design, the reflection spectrum of the back mirror provides a flat, comb-shaped response with sharp peaks. The front mirror, on the other hand, is composed of a series of gratings with varying pitches, *i.e.*, a continuously chirped grating [11, 12]. This structure generates a broad reflectivity spectrum. The front

mirror is connected to several individual contact pads, which are used to bias different parts of the mirror. When no current is applied, the reflection is too low to produce lasing. By injecting current through the appropriate contact pad, the reflection at the desired wavelength is enhanced. A high SMSR can be achieved by aligning the wavelength at which reflection is enhanced in the front mirror with the corresponding reflection peak of the back mirror. By biasing different parts of the front mirror, a broad reflection peak (from the front mirror) is generated that overlaps with the center of one of the back mirror's peaks. This enables longitudinal mode selection, contributing to a wide tuning range. In this case, distinct tuning is obtained. As with SG-DBR lasers, continuous tuning is achieved by tuning both mirrors simultaneously. A schematic of DS-DBR is shown in Fig. 2.5 (a). Fig 2.5 (b) shows experimental results of reflection responses of the front mirror and back mirror [12].

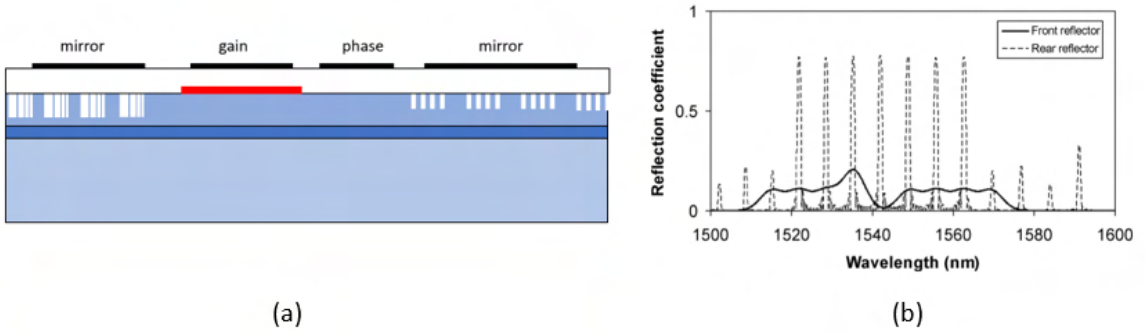

Fig. 2.5 (a) A schematic of DS-DBR with chirped sampled gratings in front mirror. (b) Diagram showing lasing wavelength selection by aligning reflection peak of front and back mirrors (© 2005 IEEE, [12]).

Like SG-DBR, the remaining sections of laser device consist of a gain section and a phase control section. By injecting current into the phase section, the location of cavity modes can be changed so that by properly aligning them with mirror peaks, a high SMSR is achieved.

2.2.3 Superstructure DBR

Structure of superstructure grating DBR (SSG-DBR) is very similar to SG-DBR. It consists of a gain section, phase section, and back and front mirrors. The main difference is that gratings used in mirrors are phase modulated. This is achieved by utilizing chirping in the gratings in SSG structure. Both mirrors produce a comb-shaped reflectivity spectrum with multiple peaks because of the periodic phase modulation in gratings. The spacing between peaks is determined by the modulation period. Since the comb separation is engineered to be slightly different in front and back mirrors, only one wavelength in which peaks are aligned can be selected as the lasing wavelength. Same concept as Vernier mechanism, by using current injection two SSG's reflection combs can shift and multiple longitudinal modes can be selected in a wide wavelength range. Depending on tuning mirrors simultaneously or

separately, continuous and distinct wavelength tuning can be obtained, respectively. Same as other DBR structures, phase section is used to align cavity modes to mirror peak reflections to ensure a high SMSR.

As mentioned earlier, the reflectivity of this structure can be calculated using coupled-mode theory. This involves analyzing the Fourier components obtained by convolving the delta-Dirac function (which represents continuous, non-modulated gratings in real space) with a comb of Fourier components (which corresponds to the sampling function in real space). Each of these Fourier components contributes to a reflection peak in the spectrum. For sampled gratings, the amplitude of the *N*-th Fourier component is proportional to $1/N$ [13], meaning the amplitude decreases as the number of reflection peaks increases. In contrast, for phase-modulated gratings, the amplitude of the Fourier component decreases according to $1/\sqrt{N}$ [14]. This difference arises due to Parseval's theorem, which states that the sum of the squares of the Fourier components equals 1 ($\sum_n |F_n|^2 = 1$). As a result, phase-modulated superstructure gratings generate a higher number of reflection peaks within the same spectral range compared to sampled gratings.

Fig. 2.6 shows the difference between reflection spectrums of SG and SSG structures. This difference arises due to the nature of the phase modulation, which spreads the energy more evenly across the spectrum. As a result, phase-modulated superstructure gratings generate more reflection peaks within the same spectral range compared to sampled gratings.

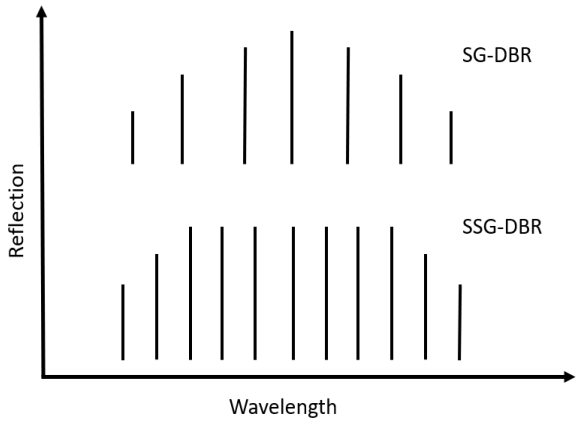

Fig. 2.6 A schematic of reflection peaks for sampled grating DBR (top) and superstructure grating DBR (bottom).

2.2.4 Modulated Grating Y-branch

Another form of use in SG-DBR is Modulated Grating Y-branch laser (MGY). Same as SG-DBR, it utilizes the Vernier mechanism to achieve a wide tuning range. MGY consists of two reflectors split by a 1x2 multimode interferometer (MMI). Each branch consists of a sampled

grating mirror which filters out certain frequencies. Then the reflected beams are added up in MMI, instead of multiplication in the case of SG-DBR. The addition of beams has the advantage of obtaining a better SMSR. However, addition is sensitive to phase difference of beams. To keep the reflected beams in phase, a differential phase section is implemented in one of the arms. Finally, a gain section is implemented to compensate the loss, and a phase section is used to align the cavity modes with the reflected peaks. The tuning mechanism stays the same, a distinct tuning can be achieved by current injection to one of the arms and a continuous tuning happens when both arms are tuned together. A schematic of MGY structure design and experimental power reflection spectra of two reflectors and their sum [15] is shown in Fig. 2.7.

One of the benefits of MGY over SG-DBR is that the beam is less exposed to potential absorption loss. In the case of (S)SG-DBR, the output beam is passed through the front gratings where significant free carrier absorption loss occurs. This can potentially lead to undesired variation of output power with tuning the wavelength. Even in the case of a long enough SSG structure, which provides a wide uniform reflection spectrum, the laser will experience a reduction in output power due to the absorption loss in the front mirror [16]. On the other hand, MGY has all the grating sections on the same side of the gain section, which makes the beam exit the cavity without experiencing much free carrier absorption.

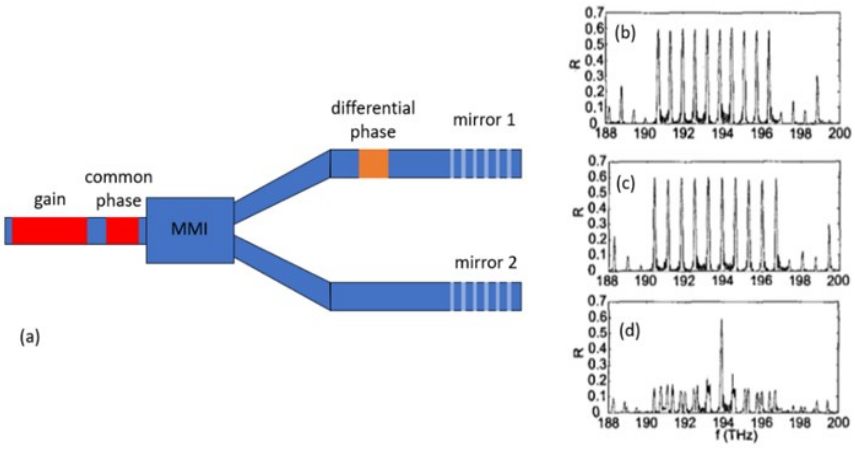

Fig. 2.7 An illustration of a typical MGY (a) and reflection spectra of (b) mirror 1 r_1 and (c) mirror 2 r_2 and (d) sum of them $|r_1 + r_2|^2/4$ (© 2002 IEEE, [15])

2.2.5 Grating-Coupled Sampled Reflector

Figure 2.8 illustrates the schematic of the Grating-Coupled Sampled Reflector (GCSR). Like the previous DBRs, it consists of four sections: a gain section, a grating coupler, a phase section, and a sampled grating mirror. The key difference between GCSR and SG DBRs is that GCSR uses two waveguide layers. In a co-directional coupler, if the two waveguides are identical and their modes have the same propagation constant, the device operates over a broad

wavelength range. However, in GCSR, where the waveguides are dissimilar, sharp wavelength filtering occurs. A significant advantage of this structure is that, with proper design and when the phase-matching condition for the two coupled modes is met, the tuning range of the Bragg grating (where $\Delta\lambda/\lambda = \Delta n/n$) is enhanced by the factor [7]

$$n_{g1}/(n_{g1} - n_{g2}) \tag{2.10}$$

where n_{g1} and n_{g2} refers to group effective index of two waveguide layers 1 and 2, respectively. Therefore, only a small index change (small tuning current) can lead to a large wavelength change.

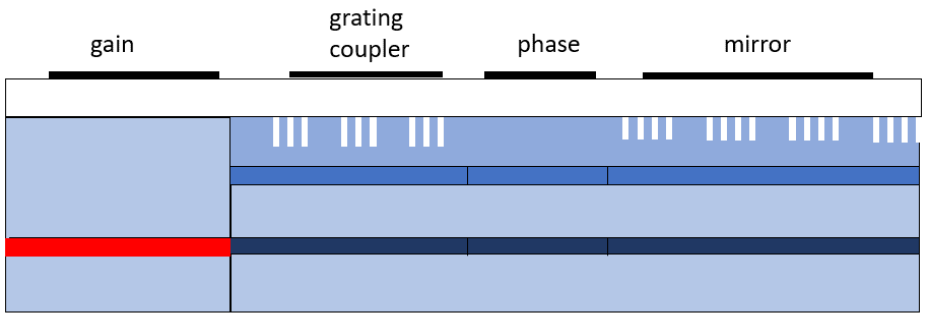

Fig. 2.8 Schematic of GCSR with back (S)SG reflector

In the GCSR laser device, the coupled beam from the lower waveguide in the gain section is directed to the upper waveguide through the grating coupler. The back reflector, which can use sampled or superstructure gratings, provides a comb-shaped reflectivity. Unlike other DBRs, the tuning mechanism in GCSR does not rely on the Vernier effect. Instead, the coupler selects a lasing wavelength from one of the peaks of the back reflector, which can be adjusted by changing the current applied to the coupler. Similar to SG and SSG DBRs, the GCSR laser has three tuning sections. The mirror section can be tuned to shift the reflection comb, and in combination with the coupler current injection, this shifts the lasing wavelength. Tuning in the phase section further refines the adjustment of cavity modes, allowing for fine, continuous tuning of the laser. Such laser has been described in detail by *Lavrova et al* [17].

Same as Y-branch laser devices, GCSR has all its tuning sections on one side of gain and therefore, the output light is less exposed to free carrier absorption loss. This will lead to low output power variation during tuning. However, the main drawbacks of this structure are first, long length of device which means very small spacing between cavity modes. This might lead to low SMSR. The other disadvantage is the complexity of fabrication process, which needs growth and regrowth steps.

2.2.6 Tunable Twin Guide

So far, the tunable laser devices presented in this section rely on three tuning currents. One of the drawbacks of such a device, is the time-consuming and complex characterization of laser. As the number of tuning sections reduce, the tuning characterization will improve in terms of complexity, cost, and tuning time. Also, more tuning sections means longer device which often lead to higher material or radiation loss and limits the output power. Amann et al. [18] reported an alternative structure, the tunable twin guide (TTG), which uses only a single tuning current. Laser wavelength tuning is achieved by adjusting the effective index of a DFB laser within a twin waveguide. This structure consists of a tuning layer, an active layer, and a grating layer stacked on top of each other. The current applied to the tuning layer shifts the Bragg wavelength. However, because only a single grating is used in this device, the tuning range of the TTG is limited.

A widely tunable laser structure can be achieved by utilizing at least two different gratings. In contrast to SG and SSG structures, the number of tuning sections corresponds to the number of gratings. This means the presence of a phase section is not necessary in the TTG approach. In (S)SG-DBR tunable lasers, a phase section is required to achieve monomodal behavior. In contrast, this TTG concept is based on a DFB structure, where a phase shift between the two gratings inherently ensures monomodal behavior. In this configuration, the TTG effectively functions as a quarter-wavelength-shifted ($\lambda/4$) DFB laser. [19]. The $\lambda/4$ shift between the two gratings is maintained over the operating range by adjusting the refractive index of the tuning layer, which preserves the phase relationship between the gratings as the effective index is varied.

Fig. 2.9 shows a schematic of TTG laser. As it can be seen, it consists of multiple semiconductor layers grown on top of each other: an active section which generates the emission, and a passive section which its role is to guide and tune the generated beam. The passive waveguide consists of at least two grating sections which can be either sampled gratings or superstructure gratings. Like (S)SG-DBR, each grating creates a comb-shaped reflectivity with separation determined by structure of grating. Using Vernier effect, lasing wavelength is the wavelength where reflection maxima of both gratings overlap perfectly. An electrode is used for each grating subsection, which is located on top of the passive tuning waveguide. Injecting current into each subsection will lead to varying the effective refractive index of gratings in passive tuning waveguide, which leads to tuning the laser wavelength. Like (S)SG-DBR, tuning two currents simultaneously will lead to continuous tuning.

Overall, this structure offers two major benefits: One is that lack of phase section in the device makes the length of chip shorter. This might be beneficial in order to minimize the propagation loss and generate high output powers. Second benefit is that TTG has only two current tunings in case of two grating sections, instead of three current tunings in a typical DBR tunable laser. This makes the characterization of laser less time consuming and costly. A disadvantage to this structure can be the complex fabrication as multiple re-growths needed to be done since the gratings are buried.

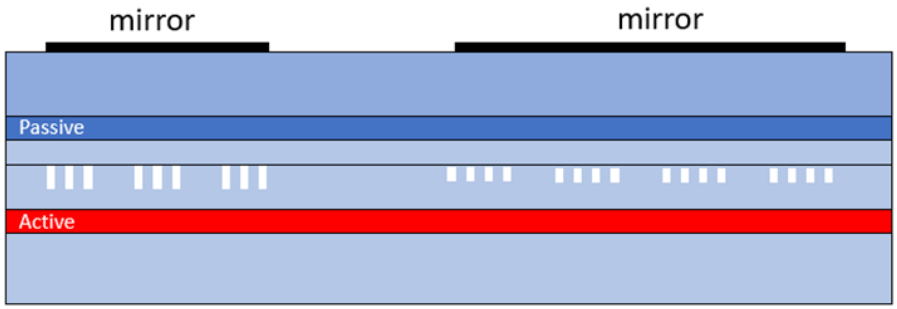

Fig. 2.9 Schematic of a TTG. Superstructure or sampled gratings can be used as mirrors.

2.2.7 Ring Resonators

So far, all the structures that have been discussed contains gratings, which is a crucial part to produce a periodic output function. The comb-shaped output form of sampled gratings or superstructure gratings is necessary in the filter sections of tunable laser. A single ring resonator also provides a similar output. Therefore, by using two different ring resonator structures, we can have two comb-shaped reflection spectra with different free spectral ranges (FSR). Using Vernier mechanism, one can achieve a widely tunable laser within a ring structure. With proper design, a dual ring resonator tunable laser can provide a narrower bandwidth and a sharper, higher Q factor resonance compared to (S)SG-DBR [20].

Fig. 2.10 (a) shows a schematic of a double ring resonator laser structure. Similar to (S)SG structures, it consists of a gain section, a phase section, and two ring resonators. In such device, the resonant wavelength, where two reflection peaks of two rings align, reflects into the gain section. So, the lasing wavelength can be modified by moving the resonant wavelength of ring resonators. Similar to GCSR, rings are located on same side of gain section. Therefore, light is less exposed to free carrier absorption and thus suffers less from output power variation [21].

Fig. 2.10 (b) shows the same concept with a different design [22]. This hybrid structure consists of two bus waveguides connecting two rings, which are used as front and rear mirrors of the laser, and a gain section. A phase section is not implemented in this device as phase tuning can be achieved by slightly tuning the pump current. Front and back mirrors produce

two comb-shaped reflection spectra. By aligning the peaks at desired wavelength, using Vernier effect, laser wavelength can be selected. Like (S)SG-DBR, tuning one mirror leads to a discrete tuning and tuning both mirrors simultaneously gives continuous tuning. In this device, two metal heaters are implemented on rings to control the reflection spectrum by thermally tuning the ring's effective refractive index.

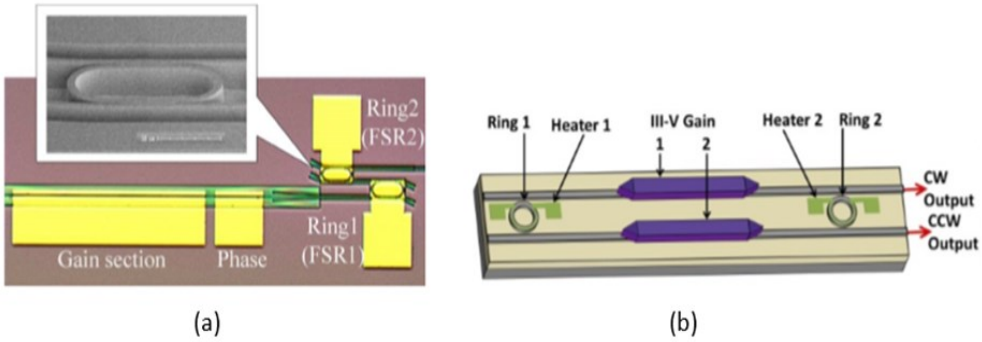

Fig. 2.10 Two different designs of widely tunable lasers using ring resonators from (a) (© 1993 IEEE, [14]) and (b) (Reprinted with permission from [22] © Optica Publishing Group America)

Fig. 2.11 shows a comparison between simulated reflection spectra of a single ring resonator and a sampled grating structure. Finite-difference time-domain (FDTD) method was used to calculate the reflection by the commercially available Lumerical software. Both structures are designed to have a peak spacing of around 4 nm at wavelength 1.55 µm. It can

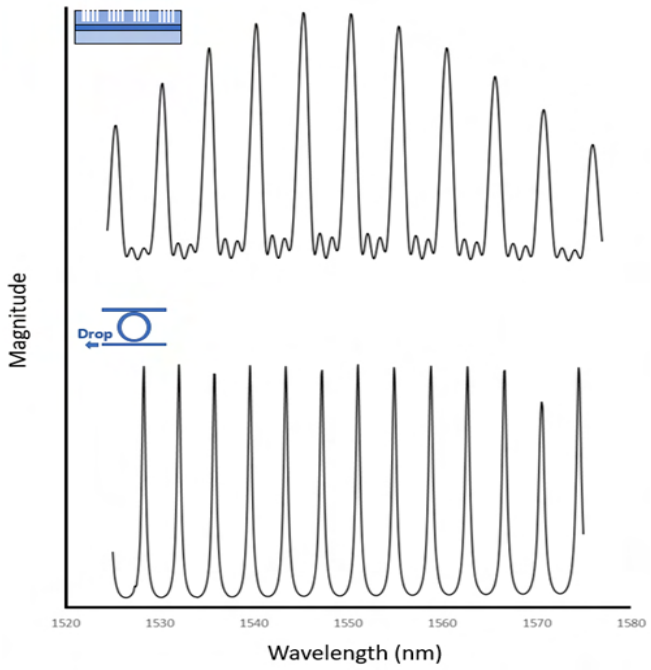

Fig. 2.11 Reflection spectrum of sampled grating (top) and output spectrum of the drop port in a ring resonator (bottom). Note that curves are not scaled. Insets show the schematic of the models used in simulations.

be clearly seen that ring resonator provides a sharper resonance with higher-Q, and narrower bandwidth compared to SG structure. The high-Q factor of a ring resonator results in a narrow resonance linewidth due to the extended photon lifetime within the cavity, and improves mode selectivity. In addition, ring resonators offer an infinite number of peaks with uniform output power, but SG only provides a limited number of peaks with power variation as wavelength changes. These characteristics make ring resonator appealing to achieve a widely tunable laser.

Complexity of fabrication of rings is one of the main disadvantages of such tunable lasers. A good and accurate process control is required to fabricate micro-ring resonators as it lacks tolerance to small fabrication and environmental changes. In most cases, a post-fabrication trimming is required to make the ring have the exact desired resonance frequency [23]. Such problems may become challenges in mass production.

2.2.8 Mach-Zehnder based tunable laser

A relatively different widely tunable laser structure is achieved by using Mach-Zehnder interferometers. A single unbalanced Mach-Zehnder, known as Asymmetric Mach-Zehnder Interferometer (AMZI), has a sinusoidal transmission function with free spectral range (FSR) proportional to $1/\Delta L$ where ΔL is the length difference between two arms. By changing the optical phase between two optical paths by 2π, AMZI filter can be tuned over one full FSR. This can be achieved by using electro-optic phase modulators in AMZI arms. Similar to other tunable laser devices, a gain section is also used. Lasing mode selection is obtained by aligning the peak of transmission spectrum with the center of gain profile. However, using a single AMZI is not enough to have a single mode operation. Fig. 2.12(a) illustrates the layout of a tunable laser structure using three AMZIs in sequence [24]. In this configuration, a combination of three AMZIs with different path-length differences improves mode selectivity. Fig. 2.12(b) shows the transmission spectrum of the three AMZIs in series alongside the gain profile, while Fig. 2.12(c) displays the same transmission spectrum along with the cavity modes over a wavelength range of 1 nm. The small spacing between the modes results from the long optical length of the device. By aligning the transmission peak with the cavity modes within a narrow wavelength range, the desired mode can be selected. For tuning, three voltage-controlled electro-optic phase modulators are employed—one for each AMZI. Additionally, to achieve a tunable laser, another phase modulator is implemented to continuously tune the cavity modes.

Such laser consists of widely used building blocks which makes it easy to transfer to any platform. In addition, it shows a very wide tuning range (~ 74 nm [24]). However, having four voltage controller sections can add complexity to performance characterization and affect tuning speed.

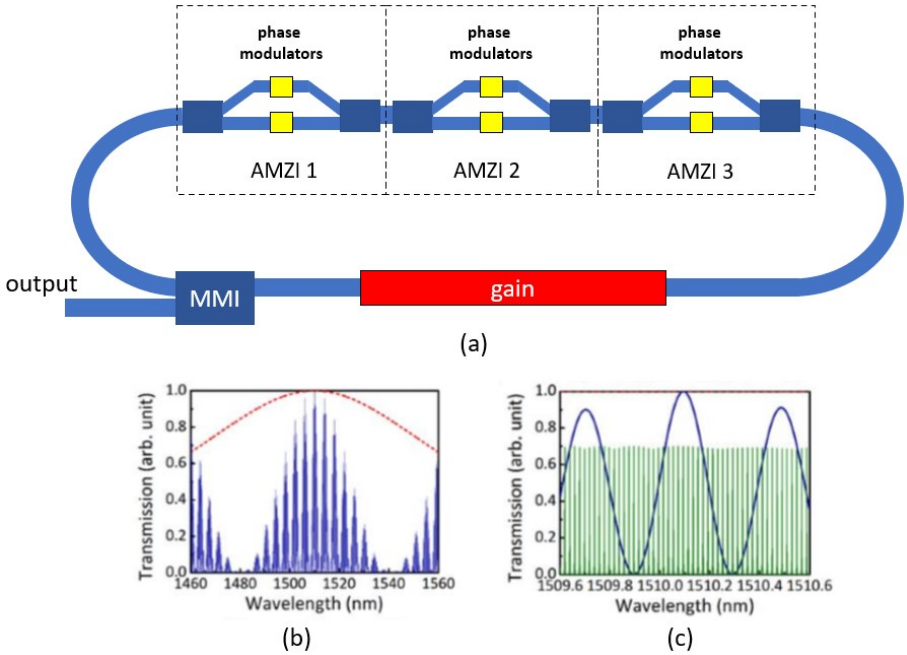

Fig. 2.12 (a) Schematic of the tunable laser based on three Mach-Zehnder Interferometers in series. Structure redrawn from (redrawn from © 2015 IEEE, [24]), (b) Transmission spectra of device in blue overlapped with gain profile in red and (c) transmission spectra of device over span of 1 nm in blue along with cavity modes in green (© 2015 IEEE, [24]).

2.2.9 Multi-Channel Interference

Another form of tunable laser which utilizes AMZI in the filter section is multi-channel interference (MCI), which is reported by [25]. In such a structure, filtering is obtained by constructive interference of eight unequal arms in a 1x8 MMI. Fig. 2.13 (a) shows an illustration of this structure. The 1x8 MMI is realized by seven cascaded 1x2 MMIs. Each of 8 arms is terminated with a multi-mode interference reflector (MIR). Therefore, reflection from each arm is added to achieve mode selection. Unlike most tunable lasers that use the Vernier effect as tuning mechanism, MCI uses constructive interference of eight arms. When all channels are in phase at desired wavelength, a strong reflection peak at that wavelength will be generated. The shape of the generated reflection spectrum relies on the arm length differences. A narrow linewidth with high SMSR can be generated through arms-length-difference optimization.

Same as other laser devices, this structure contains a gain section and a common phase section between MMIs and gain. Also, each arm uses a separate phase section. Distinct wavelength tuning can be achieved by injecting current into any of arm phase sections. Injecting current into common phase section or all arm phase sections simultaneously will lead

to continuous laser wavelength tuning. Fig. 2.13 (b) shows the experimental results of measured lasing spectra covering C-band.

In such a structure, wavelength tuning can be a challenge as there are eight phase tuning sections that need to be tuned simultaneously. This can be a complicated and time-consuming operation. The main advantage of this structure compared to grating-based devices, is avoiding expensive high-resolution processing in fabrication. MCI can benefit from standard fabrication procedures with large tolerances.

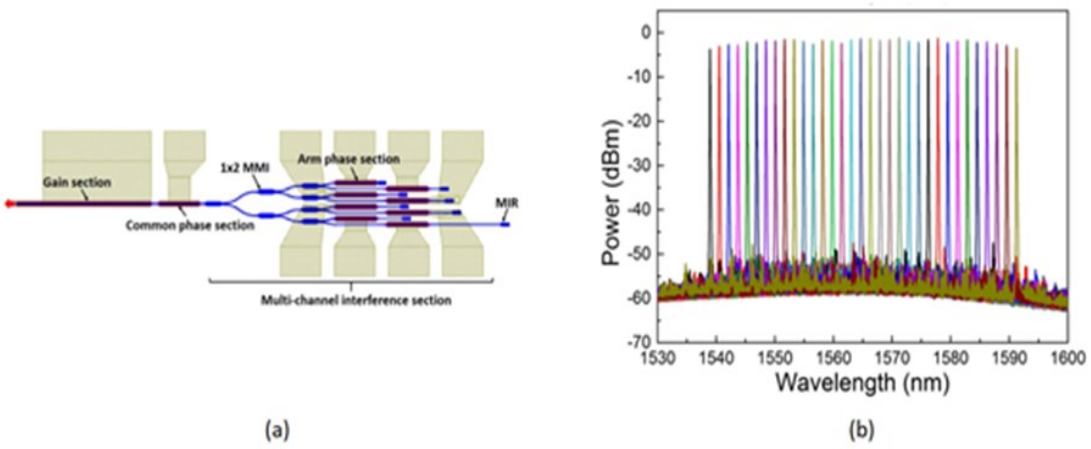

Fig. 2.13 (a) Illustration of MCI laser. (b) Superimposed measured lasing spectra over ~ 50 nm (© 2016 IEEE, [25])

2.2.10 V-Cavity Laser

V-cavity laser (VCL) mainly consists of two Fabry-Perot cavities with different lengths and a reflective half-wave coupler. Each cavity is bounded by a reflective etched facet on one side and the half-wave coupler on the other side. Half-wave coupler, *i.e.* a coupler with 180° coupling phase, plays an important role for obtaining high single mode selectivity as it produces a synchronous transfer function for two input waveguides [26]. Tuning mechanism follows the Vernier effect: each cavity produces a reflection spectrum with resonant peaks separated by a certain interval. Length of each cavity is chosen in a way so that only one peak overlaps with one peak of the other cavity. Fig. 2.14 shows the microscope image of such a structure.

All-active Fabry-Perot cavities are implemented in the device. This VCL is fabricated on multiple quantum wells (MQW) structure through the whole device. Therefore, a single epitaxial growth is sufficient. A gain electrode is used to inject current to the whole structure through a contact metal. The wavelength tuning section consists of heater electrodes on both arms. By injecting current to any of the heaters, the refractive index of waveguide changes which leads to shifting resonant peaks. In such a structure [27], a combination of four heaters is used to achieve wavelength tuning of 43 nm. However, fewer heaters can be implemented

depending on the application. As shown on Fig. 2.14 (a), two photodiodes (PD) are also implemented at both ends of the cavity for monitoring the transmitted power.

Overall, such structure benefits from a simple fabrication process and compactness. Another advantage of this device is the easy control over laser tuning because of the lack of phase section, which is due to DFB-like epitaxial layers. However, a disadvantage is the need for etched facets to provide reflectivity for laser operation. Etched facets require additional

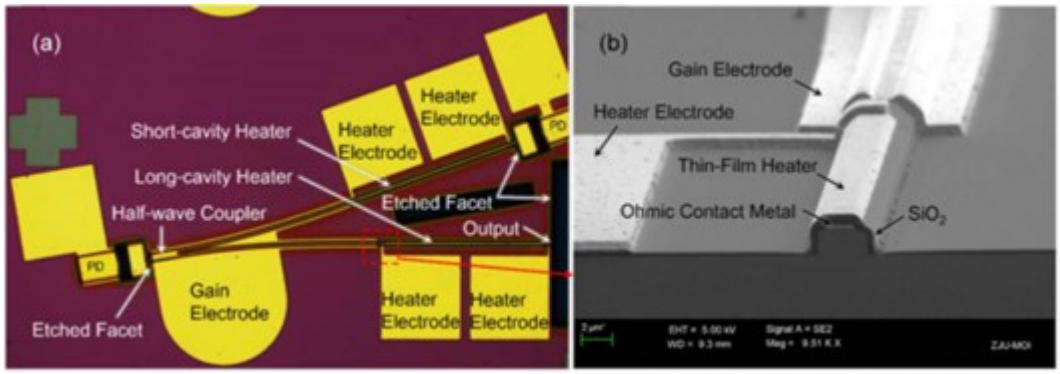

Fig. 2.14 (a) Microscope image of VCL. (b) Cross-section SEM image of heater. (© 2016 IEEE, [27]).

lithography steps, and the resulting etched regions can complicate the integration of other components on the same chip.

2.2.11 Slotted-based Tunable Laser

As discussed in previous sections, grating-based devices are well-established as widely tunable lasers. The best performance of these devices in terms of high reflection and low loss can be obtained with low order gratings. However, it is difficult to create a low order grating as it needs expensive and high-resolution fabrication procedures. Besides, to have a simple fabrication, a regrowth free structure is required which means surface grating is highly preferred to avoid high costs and complexity of fabrication. To avoid these problems, the slotted-based laser has been reported [28]. This structure is shown in Fig. 2.15. As it can be seen, the laser resembles SG-DBR with two mirrors in front and back. Each mirror can be considered as a very high order grating. In order to provide high reflectivity similar to low order gratings, each slot is etched as deep as possible. To compensate for the loss from deeply etched slots, long active sections are used. In addition, unlike SG-DBR, grating sections are also active to provide gain to make up for the loss.

Each slot is long enough to act as a short Fabry-Perot to produce resonant peaks. However, one single slot can only provide a weak reflection, so a cascade of slots is required to produce a strong reflectivity. Therefore, a group of equally spaced slots is used in front and back mirrors. Each of them has a different period to produce a periodic reflection spectrum with a certain FSR. So, Vernier effect can be used to reach a large tuning range. Similar to SG-DBR, a phase section is implemented for fine tuning.

The fabricated laser [28] provides a 55 nm wavelength tuning range with a side mode rejection ratio of at least 30 dB over the whole range. In this structure, 9 slots were used in front and back mirrors with slightly different periods: 70 µm and 76 µm for front and back mirrors, respectively. More slots can be used to make a higher reflectivity and narrower linewidth of a peak, but that would make the cavity longer. To have a simple fabrication, the

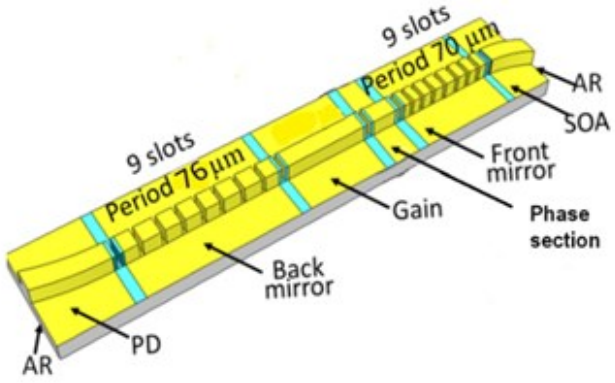

Fig. 2.15 Illustration of tunable laser based on slots (Reprinted with permission from [28] © Optica Publishing Group America).

slot width is set to 1 µm and depth is 1.8 µm, which is etched as deep as the ridge layer and just above the active layer. The results achieved within this structure are certainly competitive to existing tunable lasers on the market. However, very long (around 3 mm) cavity length can be a serious challenge in mass production as only a limited number of laser devices can be fabricated on one wafer.

2.2.12 Pockels Laser

So far, we have reviewed lasers that rely primarily on electrical or thermal injection for wavelength tuning. Here, we focus on a design that utilizes the electro-optic (Pockels) effect

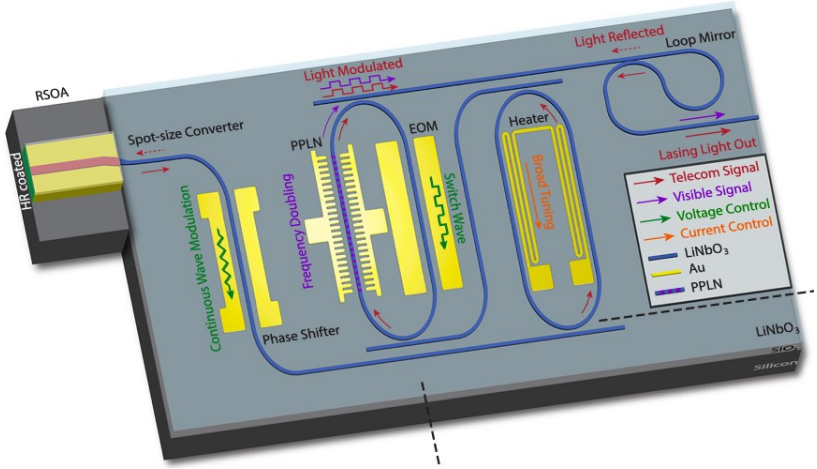

Fig. 2.16 Illustration of the integrated Pockels laser (copyright © 2022, M. Li *et al* [29]).

for high-speed tuning. This structure, reported in [29], consists of a III-V semiconductor amplifier edge-coupled to a Lithium Niobate on Insulator (LNOI) chip, combining the efficient light generation of III-V materials with the strong electro-optic properties of lithium niobate. The LNOI chip, as shown in Fig. 2.16, integrates several key components to enable precise and flexible tuning. These include a phase shifter, two racetrack resonators for generating and controlling optical mode combs, and a Sagnac loop mirror, which acts as a reflector to complete the laser cavity. Racetracks were preferred for comb generation over rings because the electro-optic modulation efficiency requires a long straight section. One of the racetrack resonators is equipped with a thermal pad for broad tuning through the thermo-optic effect, while the other employs electro-optic tuning via electrodes placed on the lithium niobate. By combining these tuning mechanisms and Vernier technique, the system achieves high mode selectivity of 50 dB and a wavelength tuning range of up to 20 nm in the C-band.

However, a disadvantage of this configuration is the requirement for mode coupling between the amplifier and the LNOI chip, which can introduce coupling loss and reduce overall efficiency. Additionally, the design requires the separate fabrication of the amplifier and the tuning chip, as they are built on different material platforms. This separation increases fabrication complexity and cost.

2.3 Comparison of Tunable Lasers

This section evaluates different methods for achieving a widely tunable laser and their corresponding design structures. Each has advantages and disadvantages, making it suitable for specific applications. To identify the most comprehensive solution that supports mass production, several factors must be considered: the complexity of growth and fabrication, device complexity, and laser performance. For fabrication feasibility, this review focuses on monolithically integrated devices in an InP-based platform due to their manufacturability and reliability. Device complexity is assessed based on the number of essential structural sections and tuning components. A greater number of components increases the complexity and time required for laser characterization. Additionally, as the number of components increases, the chip length also increases, which may introduce propagation loss. Laser performance is evaluated based on tuning range, side-mode suppression ratio (SMSR), linewidth, and tuning speed. Tuning speed (or switching time) depends on the laser's tuning mechanism and typically ranges from a few nanoseconds to a few microseconds; however, this aspect is beyond the scope of this section.

Table 1.1 shows a comparison between different types of widely tunable lasers. The values reported for each laser represent some of the highest performance metrics available in the literature. However, comparable results might have been reported by other groups.

Table 1.1: Comparison of different types of widely tunable lasers.

Structure	Number of vital sections	Tuning components	Tuning range	Threshold current (mA)	SMSR (dB)	Linewidth (kHz)	Output power (dBm)	Reference
SG-DBR	4	3	40 nm		50	70	17	*Larson et al.* [30]
DS-DBR	4	>5	45 nm		40	500	14	*Ward et al.* [12]
SSG-DBR	4	3	40 nm	12	35	400	2.5	*Ishii et al.* [31]
Y-branch	5	3	50 nm	30	40		6	*Mashanovitch et al.* [32]
GCSR	4	3	70 nm		30	10	6	*Oberg et al.* [33]
TTG	2	2	40 nm	27	35		10	*Todt et al.* [34]
Rings	4	3	56 nm	32	41		18	*Hiratani et al.* [35]
Rings	4	2	50 nm	10	50	259	10	*Ramírez et al. [36]*
Rings + MMI	4	3	70 nm	20	50	25	18	*Li et al. [37]*
AMZI	4	4	70 nm	68	30	360	4.5	*Latkowski et al.* [24]
MCI	3	9	50 nm	32	45		-1	*Chen et al. [25]*
TTG + MCI	2	4	40 nm	28	30		2	*Kabir et al [38]*
VCL	2	2	40 nm		35			*Li et al. [39]*
Slot-based	4	3	55 nm		30	>8	2	*Nawrocka et al. [28]*
Pockels	4	2	20 nm	80	50	<15	0	*Li et al. [29]*

The SMSR values reported in Table 1.1 correspond to the channel with the poorest SMSR performance, that is, the channel exhibiting the highest SMSR value among the tunable laser's operating wavelengths. Similarly, the linewidth values shown represent the widest linewidth observed. A narrow linewidth is preferred as it provides a sharper, *i.e.* lower frequency noise, resonance and higher output power. Some fields in the table are left empty because those values were not reported in the corresponding references. Although tunable lasers can operate across various bands, including the O-band, the values compiled in Table 1.1 are all from C-band devices, as these were the best reported results.

Linewidth of gratings-based lasers typically falls between a few kHz to a few MHz. Theoretically, as discussed in a previous section, rings can exhibit much sharper and higher-Q resonance, which means narrower linewidth. By optimizing the active region and minimizing the loss and using heater electrodes for tuning, sub-kHz linewidths can be achieved in a grating-based structure as reported in [30]. But on the other hand, unlike rings which provide an infinite number of reflection peaks, the number of peaks decreases by narrowing resonance in grating-based lasers.

Another important factor in the performance of tunable lasers is SMSR. Side-mode rejection over 40 dB is usually preferred in optical communication systems as the values lower than that, may lead to unavoidable intensity noise and crosstalk. Due to the lossy nature of III-V elements, a gain region or semiconductor optical amplifier (SOA) is an essential part of laser to compensate for the loss in the main mode. However, it is shown that the amplified spontaneous emission (ASE) coming from integrated SOA, severely degrade the SMSR and may affect the spectral purity, *i.e.* linewidth [40]. *Larson et al* [30] suppressed such impact by implementing a broadband tunable AMZI filter and obtained SMSR of more than 50 dB, as mentioned in Table 1.1. However, such configuration needs an extra tuning component for the tunable AMZI filter which makes laser characterization more time consuming and costly. Fig. 2.17 shows a sketch of this device. In this structure, as shown on bottom of Fig. 2.17, mirrors and phase sections are thermally isolated from substrate so that the heat generated by heaters reach less to the substrate. As a result, tuning can be achieved with much smaller power dissipation.

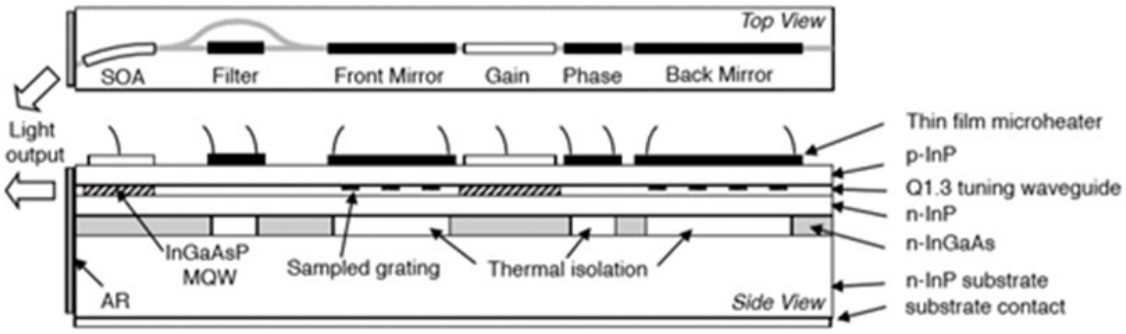

Fig. 2.17 Schematic of the SG-DBR laser with AMZI filter and SOA (Reprinted with permission from [30] © Optica Publishing Group America).

In Table 1.1, another notable device is the tunable twin guide TTG. Despite having a relatively few number of components, it exhibits competitive performance. This simplicity makes it attractive due to its compactness and lower cost. *Todt et al.* [34] reported a TTG structure with the active layer as the bottom and tuning (passive) layer as the top layer, where the gratings are defined, shown in Fig. 2.18. Tuning and active layers are electronically separated by an n-layer which allows gain and filter profiles to be tuned independently. The strength of such design is that due to the DFB-like vertical integration of passive and active layers, a phase tuning section is not needed in contrast to a typical tunable DBR laser. However, the disadvantage is that multiple regrowth steps are needed which may decrease the fabrication yield.

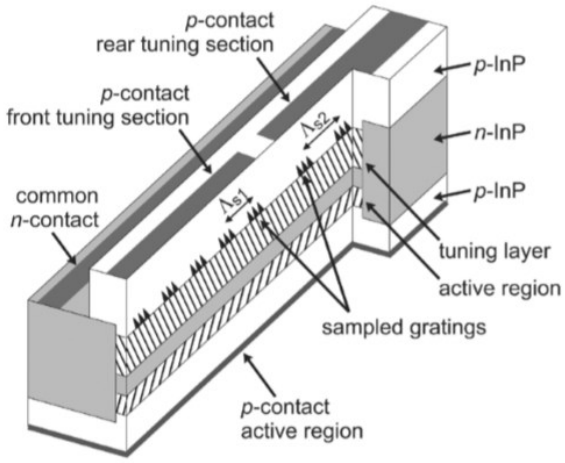

Fig. 2.18 Schematic of the TTG laser (© 2005 IEEE, [34]).

Recent approaches to tunable lasers typically combine several of the concepts discussed so far. For example, Kabir *et al*. [38] employed a twin-guide structure as the gain section within a multi-mode interference (MMI) structure consisting of four arms of varying lengths. Each arm integrates a thermo-optic phase shifter to enable wavelength tuning. Optical gain is provided by an InP-based quantum well structure, implemented using InP membrane-on-silicon technology. Fig. 2.19 shows a schematic of the twin-guide amplifier along with the overall layout of the laser.

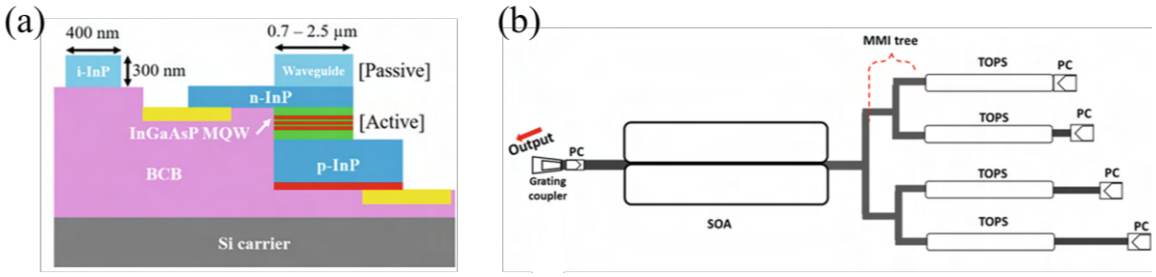

Fig. 2.19 (a) Cross-sectional illustration of the twin-guide amplifier. (b) Schematic of the layout of the laser. (*Reproduced with permission from Springer Nature* [38]).

Similarly, Li *et al*. [37] demonstrated a hybrid integration approach in which a III-V amplifier is edge-coupled to a silicon photonic chip. The silicon chip includes two ring resonators, each with thermally tunable spectra. These rings generate slightly offset spectral responses that interfere with one another and couple to the amplifier via a multi-mode interference (MMI) coupler. A common thermal phase controller is also integrated to fine-tune the output. By leveraging the Vernier effect, the interference between the ring spectra enables high spectral selectivity, wide tuning range, and low linewidth. Fig. 2.20 shows the schematic of this laser.

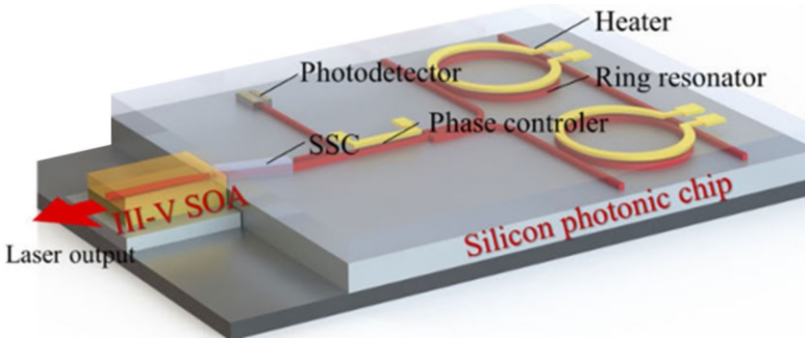

Fig. 2.20 Schematic of the widely tunable laser based on MMI and Ring Resonators (copyright ©, [37]).

Another example of III-V and silicon co-integration shown in Table 1.1, demonstrated by Ramírez *et al*. [36], features a tunable laser incorporating a Vernier filter - comprised of two thermally controlled ring resonators - positioned at one end of the laser cavity. The cavity itself is bounded by Bragg mirrors and is followed in series by an amplifier to boost the output power. The gain sections are based on InP and are wafer-bonded onto the silicon chip, which contains the rest of the photonic components.

The Y-branch laser reported by *Mashanovitch et al.* [32] demonstrates promising performance, as shown in Table 1.1. The main difference between this laser and conventional Y-branch lasers is that the two outputs are extracted from the Y-arm waveguides. A high-reflection (HR) coating is applied to the back facet of the laser, resulting in a high SMSR. Additionally, the HR coating allows the use of shorter (S)SG mirrors in the arms, as lower

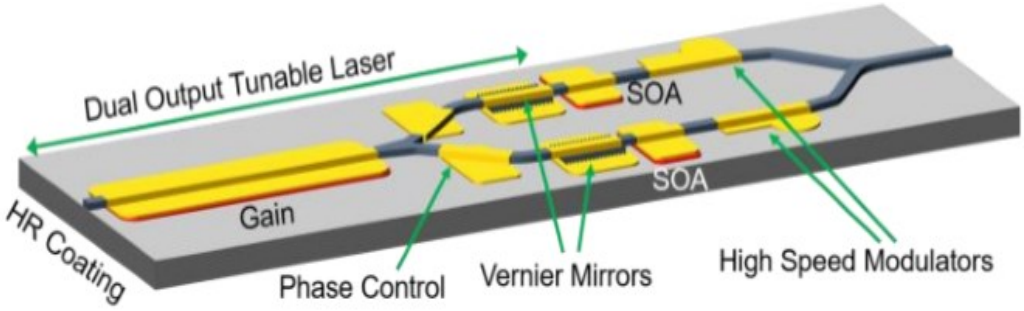

Fig. 2.21 Illustration of Y-branch tunable laser (© 2017 IEEE, [32])

reflectivity is sufficient. This configuration is beneficial for achieving a shorter device and reducing the required tuning current. Fig. 2.21 shows an illustration of such a structure.

Another interesting structure with few numbers of components is VCL. As discussed before, its simple structure makes it suitable for mass fabrication operation. This device basically consists of one short cavity and one long cavity in order to utilize Vernier effect to extend the tuning range. Deep etched facets at the end of cavities are used as mirrors. A half-wave coupler is implemented as the junction of V-shape structure to ensure high SMSR. Three electrodes for controlling gain and tuning are implemented on the device which are separated by two isolation gaps. The image of such a structure is shown on Fig. 2.22. A quasi-continuous tuning is achieved by tuning reflection combs of two cavities simultaneously through thermo-optic effect. Thermal tuning is less susceptible to free carrier absorption compared to the carrier injection method, which can result in sharper resonance. As discussed in a previous section, current injection has opposing effects on the refractive index. On one hand, it decreases the refractive index, while on the other hand, the temperature increase caused by the injection raises the refractive index. Therefore, a high tuning current is needed to overcome the effect of carrier injection on the refractive index. In thermal tuning, only the temperature increase contributes to changes in the refractive index.

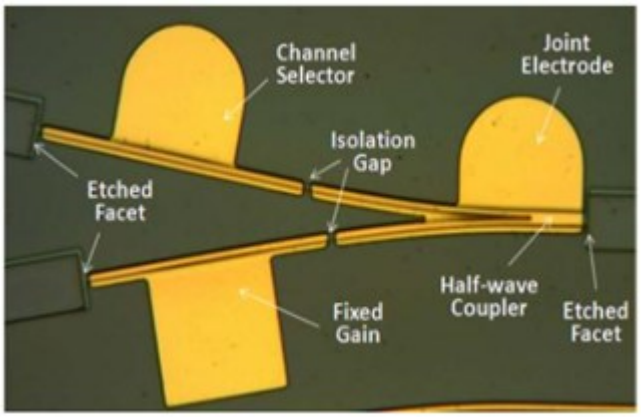

Fig. 2.22 Optical microscope image of VCL (copyright ©, [39]).

An easy-implementing method has been used by the same group to reduce the linewidth of discussed VCL. Fig. 2.23 shows an illustration of this method. The output of the laser is divided by a splitter which one path is used for linewidth measurement setup and another path is used for total reflection feedback. The end facet of the reflection path is coated with a gold film. In this method, self-injection feedback is used to reduce the frequency fluctuations without significantly affecting the SMSR and tuning range. Linewidth as narrow as 60 kHz was achieved by having a 50:50 splitting ratio at the splitter and ~5 mm length of feedback path. Details of this method are discussed in [39].

Overall, four structures discussed above along with the AMZI-based laser, which was discussed in Section 2.2.8, show the most promising widely tunable lasers.

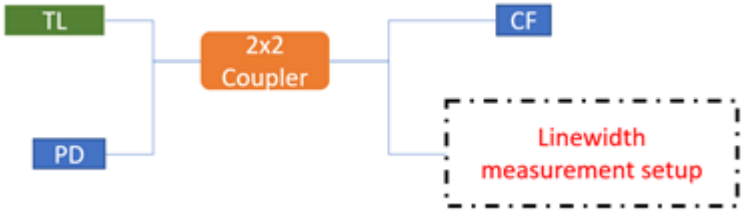

Fig. 2.23 Schematic diagram of the self-injection method for linewidth reduction. Abbreviations: TL: tunable laser; CF: coated fiber; PD: photodiode. (Redrawn with modification from © 2004 IEEE, [41])

2.4 A novel approach to achieve tunable laser based on loss perturbation

In the next chapter, I will discuss a novel concept for a tunable plasmonic semiconductor laser, which uses loss perturbation as its tuning mechanism. This design incorporates a metal oxide semiconductor (MOS) capacitor atop an edge-emitting Fabry-Perot (FP) diode laser. This arrangement supports a hybrid plasmonic TM mode, which partially overlaps with both the MOS capacitor and the semiconductor gain region, serving as the lasing mode.

This method also involves the utilization of indium tin oxide (ITO), within the MOS structure. This choice is motivated by the capability to achieve the epsilon near zero (ENZ) condition under accumulation in the conductive oxide layer. This results in a significant alteration in the imaginary part of effective index of the hybrid plasmonic TM mode, *i.e.* mode loss. The modification serves as the means to tune the lasing wavelength.

References

1. B. Pezeshki, G. Parhar, and N. Badr. "Tunable lasers." *IEEE circuits and devices magazine* 19.5 (2003): 36-40.
2. P. J. Winzer, and D. T. Neilson. "From scaling disparities to integrated parallelism: A decathlon for a decade." *Journal of Lightwave Technology* 35.5 (2017): 1099-1115.
3. B. J. Van Zeghbroeck. "Principles of semiconductor devices." (2011).
4. M. Nakazawa, K. Kikuchi, and T. Miyazaki, eds. *High spectral density optical communication technologies*. Vol. 6. Springer Science & Business Media, 2010.

5. B. R. Bennett, R. A. Soref, and J. A. Del Alamo. "Carrier-induced change in refractive index of InP, GaAs and InGaAsP." *IEEE Journal of Quantum Electronics* 26.1 (1990): 113-122.
6. P. Hertel, *Continuum Physics*. Springer Science & Business Media, 2012.
7. L. A. Coldren, S. W. Corzine, and M. L. Mashanovitch. *Diode lasers and photonic integrated circuits*. Vol. 218. John Wiley & Sons, 2012.
8. K. Kudo, *et al*. "1.55-μm wavelength-selectable microarray DFB-LD's with monolithically integrated MMI combiner, SOA, and EA-modulator." *IEEE Photonics Technology Letters* 12.3 (2000): 242-244.
9. L. A. Coldren, *et al.* "Tunable semiconductor lasers: A tutorial." *Journal of Lightwave Technology* 22.1 (2004): 193.
10. H. Kogelnik, and C. V. Shank. "Coupled-wave theory of distributed feedback lasers." *Journal of applied physics* 43.5 (1972): 2327-2335.
11. G. Busico, *et al.* "A widely tunable digital supermode DBR laser with high SMSR." *2002 28TH European Conference on Optical Communication*. Vol. 2. IEEE, 2002.
12. A. J. Ward, *et al.* "Widely tunable DS-DBR laser with monolithically integrated SOA: Design and performance." *IEEE Journal of selected topics in quantum electronics* 11.1 (2005): 149-156.
13. V. Jayaraman, Z-M. Chuang, and L. A. Coldren. "Theory, design, and performance of extended tuning range semiconductor lasers with sampled gratings." *IEEE Journal of quantum electronics* 29.6 (1993): 1824-1834.
14. H. Ishii, *et al.* "Super-structure-grating (SSG) for broadly tunable DBR lasers." *IEEE photonics technology letters* 5.4 (1993): 393-395.
15. J-O. Wesstrom, *et al.* "Design of a widely tunable modulated grating Y-branch laser using the additive Vernier effect for improved super-mode selection." *IEEE 18th International Semiconductor Laser Conference*. IEEE, 2002.
16. M. Gotoda, T. Nishimura, and Y. Tokuda. "A widely tunable SOA-integrated DBR laser by combination of sampled and superstructure gratings." *Journal of lightwave technology* 23.7 (2005): 2331-2336.
17. O. A. Lavrova, and D. J. Blumenthal. "Detailed transfer matrix method-based dynamic model for multisection widely tunable GCSR lasers." *Journal of lightwave technology* 18.9 (2000): 1274.
18. M-C. Amann, *et al*. "Tunable twin-guide laser: A novel laser diode with improved tuning performance." *Applied physics letters* 54.25 (1989): 2532-2533.
19. G. Morthier. "Widely tunable twin guide laser structure." U.S. Patent No. 7,653,093. 26 Jan. 2010.
20. B. Liu, A. Shakouri, and J. E. Bowers. "Wide tunable double ring resonator coupled lasers." *IEEE Photonics Technology Letters* 14.5 (2002): 600-602.
21. S. Matsuo, and T. Segawa. "Microring-resonator-based widely tunable lasers." *IEEE Journal of Selected Topics in Quantum Electronics* 15.3 (2009): 545-554.
22. J. C. Hulme, J. K. Doylend, and J. E. Bowers. "Widely tunable Vernier ring laser on hybrid silicon." *Optics express* 21.17 (2013): 19718-19722.

23. C. W. Holzwarth, *et al*. "Accurate resonant frequency spacing of microring filters without postfabrication trimming." *Journal of Vacuum Science & Technology B: Microelectronics and Nanometer Structures Processing, Measurement, and Phenomena* 24.6 (2006): 3244-3247.
24. S. Latkowski, *et al.* "Novel widely tunable monolithically integrated laser source." *IEEE Photonics Journal* 7.6 (2015): 1-9.
25. Q. Chen, *et al.* "Demonstration of multi-channel interference widely tunable semiconductor laser." *IEEE Photonics Technology Letters* 28.24 (2016): 2862-2865.
26. J-J. He, and D. Liu. "Wavelength switchable semiconductor laser using half-wave V-coupled cavities." *Optics express* 16.6 (2008): 3896-3911.
27. H. Deng, *et al.* "Wavelength tunable V-cavity laser employing integrated thin-film heaters." *IEEE Photonics Journal* 8.4 (2016): 1-8.
28. M. Nawrocka, *et al.* "Widely tunable six-section semiconductor laser based on etched slots." *Optics express* 22.16 (2014): 18949-18957.
29. M. Li, *et al*. "Integrated pockels laser." *Nature communications* 13.1 (2022): 5344.
30. M. C. Larson, *et al*. "Narrow linewidth sampled-grating distributed Bragg reflector laser with enhanced side-mode suppression." *Optical Fiber Communication Conference*. Optica Publishing Group, 2015.
31. H. Ishii, *et al.* "Narrow spectral linewidth under wavelength tuning in thermally tunable super-structure-grating (SSG) DBR lasers." *IEEE Journal of Selected Topics in Quantum Electronics* 1.2 (1995): 401-407.
32. M. L. Mashanovitch, *et al.* "Monolithic tunable interferometric transmitter (TunIT) in indium phosphide." *IEEE Journal of Selected Topics in Quantum Electronics* 23.6 (2017): 1-5.
33. M. Oberg, *et al.* "74 nm wavelength tuning range of an InGaAsP/InP vertical grating assisted codirectional coupler laser with rear sampled grating reflector." *IEEE Photonics Technology Letters* 5.7 (1993): 735-737.
34. R. Todt, *et al*. "Sampled grating tunable twin-guide laser diodes with over 40-nm electronic tuning range." *IEEE photonics technology letters* 17.12 (2005): 2514-2516.
35. T. Hiratani, *et al*. "III-V gain region/Si external cavity hybrid tunable lasers with InP-based two-storied ridge structure." *2021 27th International Semiconductor Laser Conference (ISLC)*. IEEE, 2021.
36. J. M. Ramírez, *et al*. "Low-threshold, high-power on-chip tunable III-V/Si lasers with integrated semiconductor optical amplifiers." *Applied Sciences* 11.23 (2021): 11096.
37. C. Li, *et al*. "High-power III–V/Si integrated wavelength tunable laser for L-band applications." *IEEE Journal of Quantum Electronics* 59.6 (2023): 1-6.
38. T. Kabir, *et al.* "Widely Tunable Laser on IMOS Platform." *European Conference on Integrated Optics*. Cham: Springer Nature Switzerland, 2024.
39. T. Li, J. Meng, and J-J. He. "40nm Quasi-Continuous Wavelength Tuning of V-cavity Semiconductor Laser." *Journal of Physics: Conference Series*. Vol. 844. No. 1. IOP Publishing, 2017.

40. B. Moeyersoon, G. Morthier, and M. Zhao. "Degradation of the mode suppression in single-mode laser diodes due to integrated optical amplifiers." *IEEE journal of quantum electronics* 40.3 (2004): 241-244.
41. X. Xiong, *et al.* "Narrow linewidth tunable V-cavity laser using self-injection method." *Optics Express* 25.26 (2017): 32957-32963.

Chapter 3

Tunable Hybrid Plasmonic Semiconductor Laser Based on Loss Perturbation

This chapter is based on the published paper titled “Tunable Hybrid Plasmonic Semiconductor Laser Based on Loss Perturbation”. First, I will discuss my contributions to the work, followed by a presentation of the paper itself. The remaining chapters of this thesis will follow a similar structure, unless otherwise noted.

3.1 Contribution Statement

The core concept of this project was developed collaboratively between myself and my supervisor, Prof. Berini. The project involves a multi-physics simulation approach, requiring both optical and electrical optimization of the laser device, along with an analysis of thermal effects. I led the initial development and execution of the optimization algorithms, conducted the simulations, and prepared the figures for the manuscript. Throughout the project, the work was refined through regular meetings with Prof. Berini. Additionally, I wrote the first draft of the paper.

Related conference publication arising from this work is listed below:

- S. Saeidi, *et al*. " Tunable Hybrid Plasmonic-Semiconductor Laser Incorporating ENZ Material." *2023 Photonics North (PN)*. IEEE, 2023.

3.2 Article

The article follows below verbatim.

IEEE JOURNAL OF QUANTUM ELECTRONICS, VOL. 59, NO. 2, APRIL 2023 1100108

Tunable Hybrid Plasmonic Semiconductor Laser Based on Loss Perturbation

Shayan Saeidi and Pierre Berini, *Fellow, IEEE*

***Abstract*— We propose a tunable plasmonic semiconductor laser that exploits loss perturbation as a tuning mechanism. A metal oxide semiconductor (MOS) capacitive structure is added on top of an edge-emitting Fabry-Perot (FP) diode laser, such that a hybrid plasmonic TM mode that overlaps partly with the MOS capacitor and the semiconductor gain region is supported as the lasing mode. We also propose the use of a layer of conductive oxide, *e.g.*, indium tin oxide (ITO), as the semiconductor of the MOS structure, because the epsilon near zero (ENZ) condition can be attained therein under accumulation, thereby producing a very large change in the effective index of the hybrid plasmonic TM mode. The change in the imaginary part of the effective index is used to tune the lasing wavelength - exploiting loss perturbation to achieve laser tuning is paradigm-shifting. The laser proposed operates at telecom wavelengths, requiring an electrical forward bias to pump the active layer, and a gate voltage to drive the MOS tuning capacitor. Simulations yield a tuning range of over 7 nm in the O-band for a 100 μm long FP laser cavity.**

***Index Terms*— Semiconductor laser, plasmonic laser, hybrid laser, epsilon-near-zero material, ITO, MOS capacitor.**

I. Introduction

In RECENT years, there have been many studies on materials with a vanishing real part of permittivity at specific wavelengths [1], [2], [3]. These materials are commonly known as epsilon-near-zero (ENZ) materials. The initial research on these materials suggested a significant increase in the electric field in the material when the real part of permittivity is zero [4], [5]. Examples of such materials, include degenerate semiconductors like tin-doped indium oxide (ITO) and aluminum-doped zinc oxide (AZO), in which the high level of doping causes them to show a dielectric behavior at visible wavelengths and a metallic behavior in the infrared. The two examples mentioned have their zero-permittivity region in the near-infrared range, suggesting applications in telecom systems.

By matching the ENZ wavelength with the operating wavelength, one can exploit the characteristics of such materials. ENZ materials have generated significant interest due to their substantial optical nonlinearity, including wave mixing, harmonic generation, and frequency conversion [6], [7]. Applications of these materials can be expanded to electro-optic components since ITO is compatible with electronics [8], [9], [10].

Various options exist to achieve optical tuning in lasers, such as modifying the laser cavity length, light propagation direction, or changing the effective index of the optical mode [11]. In principle, the latter can be produced by ITO as it exhibits a significant change in refractive index in the ENZ region. To achieve tunability via ITO, one should induce a change in the free carrier concentration of ITO, which overlaps with the propagating laser mode.

In this paper, we aim to exploit the properties of ITO by incorporating it in InP-based lasers to achieve broad tunability following a novel approach based on perturbing mode loss. The mechanism is simple yet unique and is explained as follow: First, the design of the laser's active region (gain medium) plays a vital role in our approach as the peak of the gain spectrum can blueshift or redshift (depending on the design) as a function of carrier density. In a Fabry-Perot (FP) laser, the overlap of the gain spectrum with the cavity modes determines the wavelength of the lasing modes. As the mode loss increases, a higher current (carrier density) must be injected into the active region to compensate for the loss. Therefore, by injecting different current levels, the lasing frequency changes with the frequency of the gain peak. So, a wide tuning range can be achieved if the gain medium compensates for the loss. Second, perturbation of mode loss can be achieved by perturbing the free carrier concentration in the ITO layer, which operates as the semiconductor layer in a plasmonic metal-oxide-semiconductor (MOS) capacitor that is placed in proximity to the gain region, in the optical path. The carrier refraction effect in the ITO layer within a MOS capacitor has been exploited previously to enable a beam steering device [12]. We show that a short FP cavity ($\sim$100 μm) can be tuned over 7 nm ($\sim$1.2 THz) in the O-band. Such broad tunability from a conventional edge-emitting FP laser in III-V platform has never been reported. However, since tuning relies on loss perturbation, it is clear that this mechanism comes at the expense of high power consumption.

This paper is organized as follow. In Section II, the proposed device is described. Semiconductor modeling is discussed in Section III-A, followed by the waveguide design (Section III-B), then the design of the active region including thermal effects (Section III-C). We present laser characteristics in Section III-D, followed by conclusions in Section IV.

Manuscript received 25 March 2022; revised 9 August 2022; accepted 14 February 2023. Date of publication 22 February 2023; date of current version 28 February 2023. This work was supported by the Natural Sciences and Engineering Research Council of Canada. *(Corresponding author: Shayan Saeidi.)*

Shayan Saeidi is with the Centre for Research in Photonics and the School of Electrical Engineering and Computer Science, University of Ottawa, Ottawa, ON K1N 6N5, Canada (e-mail: ssaeidi@uottawa.ca).

Pierre Berini is with the Centre for Research in Photonics, the Department of Physics, and the School of Electrical Engineering and Computer Science, University of Ottawa, Ottawa, ON K1N 6N5, Canada (e-mail: pberini@uottawa.ca).

Color versions of one or more figures in this article are available at https://doi.org/10.1109/JQE.2023.3246987.

Digital Object Identifier 10.1109/JQE.2023.3246987

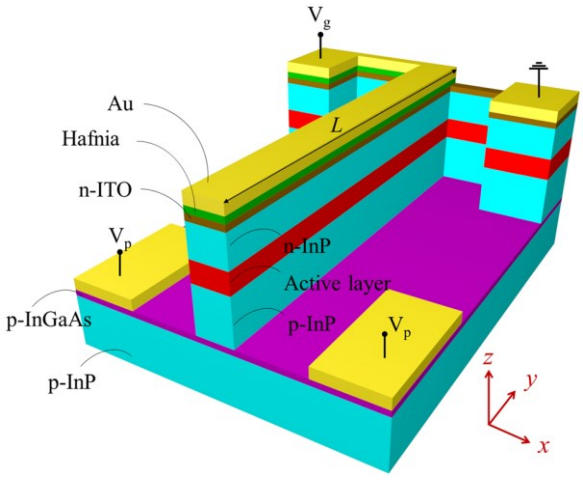

Fig. 1. 3-dimensional schematic of the proposed tunable plasmonic semiconductor laser incorporating an epsilon-near-zero material (ITO).

TABLE I
DESCRIPTION OF LAYERS IN LASER STRUCTURE

Layer	Material	Thickness (nm)	Refractive Index (1300 nm)	Doping (cm^{-3})
metal	gold	1000	0.139 + 8.49i	
oxide	hafnia	6	2.07	undoped
n-semicond.	ITO	13	1.718 + 0.045i	3×10^{20}
n-cladding	InP	350	3.205	2×10^{18}
barrier (×11)	$Al_{0.42}In_{0.58}As$	18	3.308	undoped
QW (×11)	$Al_{0.04}Ga_{0.58}In_{0.38}As$	6	3.573	undoped
barrier	$Al_{0.42}In_{0.58}As$	18	3.308	undoped
p-cladding	InP	1000	3.205	2×10^{18}
p-contact	$In_{0.53}Ga_{0.47}As$	50	3.46 + 0.09i	2×10^{19}
p-substrate	InP		3.205	1×10^{17}

II. Proposed Structure

Fig. 1 shows the proposed structure (layers not drawn to scale). The structure contains a core (active) layer bounded by p-type and n-type InP claddings, forming a p-i-n diode. The active layer consists of multiple quantum wells (MQWs) which will be discussed in detail in Section III-C. A MOS capacitor is implemented on top by using gold as the metal, hafnia as the oxide, and ITO as the semiconductor. We can exploit the carrier refraction effect in the ITO layer by operating the MOS capacitor in its accumulation regime, as will be discussed in Section III-A. The n-type ITO and the n-type InP layers provide a common ground for the MOS capacitor and the p-i-n diode.

Electrical injection to pump the active layer occurs by applying a voltage V_p to the p-InP cladding layer relative to ground. A heavily doped (2×10^{19} cm^{-3}) p-InGaAs layer is used to form an ohmic contact with the metal. The cavity is of length L which can be tailored to determine the spacing between cavity modes, as will be discussed in Section III-D. The MOS structure is biased by the voltage V_g applied to the top contact relative to ground, as shown in Fig. 1.

To exploit the properties of ITO and of the gain medium, the propagating (lasing) mode should overlap strongly with both regions. This requires forming a hybrid plasmonic mode [13] with the MOS metal contact to strongly localize fields to this region. However, there is a trade-off between the overlap of the hybrid plasmonic mode with the metal and ITO layers to exploit ENZ, and with the active layer to compensate the attenuation.

The laser structure is described in Table I (starting from the top layer). The refractive indices are given at 1300 nm. The refractive indices of gold, hafnia, and InP are extracted from [14], [15], and [16]. The refractive index of ITO is calculated from the electrostatic simulations discussed in Section III-A using the Drude model. The refractive index of InP has negligible change with doping level of $10^{17} \sim 10^{18}$ [17]. The positive sign of the imaginary part of the refractive index indicates loss (or gain when negative). The thicknesses are optimized to satisfy the loss/gain trade-off (discussed further in Section III-B). The refractive indices of the AlGaInAs layers are calculated using the methodology described in [18]. To calculate the refractive index of heavily doped InGaAs, we need to take into account carrier absorption effects. For p-type InGaAsP, the dominant absorption mechanisms involving holes is intervalence band transitions. Using the Kramers-Kronig relation gives the index change Δn associated with this absorption mechanisms [19]:

$$\Delta n = \frac{hc\alpha_0}{2\pi^2 eE}\left\{e^{-bE}\left[\gamma + \ln(bE) + \sum_{n=1}^{\infty}\frac{(bE)^n}{n!n}\right] + e^{bE}\left[-\gamma - \ln(bE) - \sum_{n=1}^{\infty}\frac{(-1)^n(bE)^n}{n!n}\right]\right\} p \quad (1)$$

where h is Planck's constant, c is the speed of light in vacuum, e is the electron charge, E is the photon energy in eV, p is the hole density in cm^{-3}, $\alpha_0 = 4.252\times10^{-20}$ m^2, $b = 3.657$ eV^{-1}, and γ is Euler's constant.

III. Simulations

The simulation results presented throughout the paper are carried out by Lumerical Photonic Software [20].

A. Electrostatic Modeling

The permittivity of ITO as a function of frequency $\varepsilon(\omega)$ can be represented at optical wavelengths by the Drude model, $\varepsilon(\omega) = \varepsilon_\infty - \omega_p^2/(\omega^2 + i\zeta\omega)$ where ε_∞ is the high-frequency permittivity and ζ is the electron damping term. The plasma frequency ω_p varies with carrier density N according to $\omega_p = \sqrt{Ne^2/(\varepsilon_0 m_n^*)}$, where e is the electron charge, ε_0 is the vacuum permittivity, and m_n^* is the effective mass of electrons for conductivity. For ITO we set $\varepsilon_\infty = 4.2345$, $\zeta = 1.75 \times 10^{14}$ rad/s, and $m_n^* = 0.35m_e$ with m_e being the free electron mass [12]. The carrier density can be tuned electrically over a thin region of ITO within a MOS capacitor,

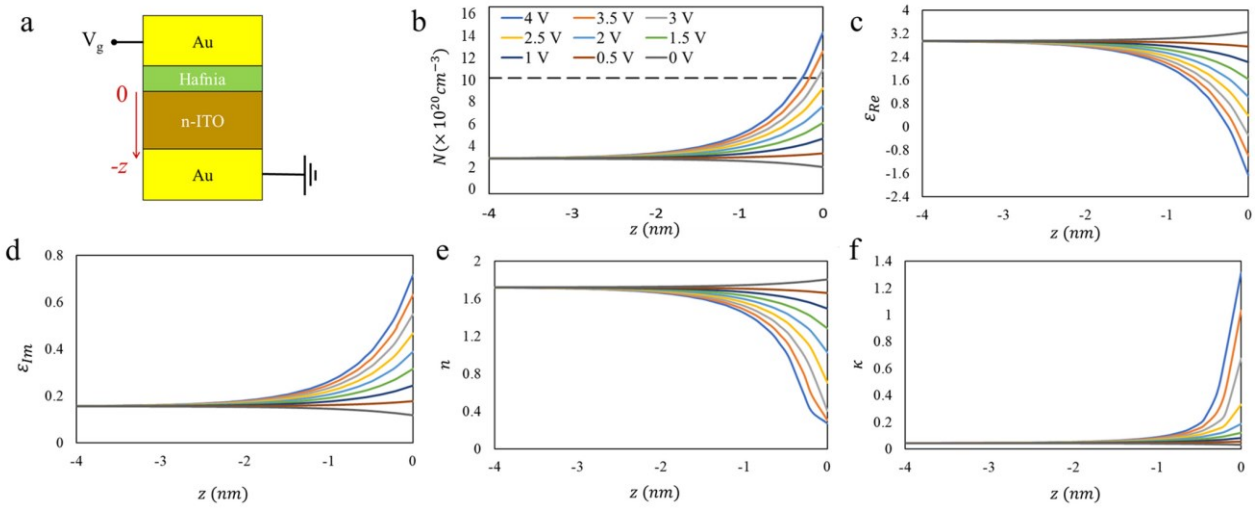

Fig. 2. (a) 1D cross-section of the MOS capacitor of interest. (b) Carrier density across the ITO layer for various V_g. Dashed black line shows the carrier density required for ITO to reach ENZ. (c), (d) Real (ε_{Re}) and imaginary (ε_{Im}) parts of relative permittivity across the ITO layer for various V_g. (e), (f) Real (n) and imaginary (κ) parts of refractive index across the ITO layer for various V_g.

where ITO is used as the semiconductor. In this subsection, we carry out electrostatic modeling to investigate our MOS structure.

Fig. 2(a) shows the 1-D cross-section of the MOS structure, where we apply a gate voltage V_g to the top contact while grounding the bottom contact. We used gold as the metal and HfO_2 as the insulator. To carry out the electrostatic simulations, we assumed for ITO: DC permittivity $\varepsilon_{DC} = 9.3$, electron mobility $\mu_e = 25$ cm^{2}V^{-1}s^{-1}, bandgap energy $E_g = 2.8$ eV, electron affinity $\chi = 4.8$ eV, hole mobility $\mu_h = 1$ cm^{2}V^{-1}s^{-1}, and hole effective mass $m_h^* = m_e$ (the hole mobility and effective mass in degenerately doped ITO are not well-known as they do not contribute significantly to transport processes) [21]. We consider the bulk charge carrier (electron) density of ITO to be 3×10^{20} cm^{-3}, such that ITO is an n-type degenerate semiconductor. We assume that the variation in doping level of ITO does not change the band-structure significantly, so the electron effective mass remains constant in our calculations. The work function of gold is taken as 5.1 eV [14]. We assume a breakdown field of $E_{bk} = 6.4$ MV/cm [22] for HfO_2 which leads to a breakdown voltage of $V_{bk} = 3.8$ V for a HfO_2 thickness of 6 nm ($V_g < V_{bk}$). We use the drift-diffusion model to compute the charge distribution in ITO [23]. However, the accuracy of the charge carrier density distribution in the accumulation regime could be improved by adopting the Schrödinger-Poisson model [24].

Fig. 2(b) shows that the carrier density in ITO increases near the HfO_2 interface as V_g increases. When no voltage is applied, the structure is slightly depleted. The flatband voltage is ~0.32 V and as V_g is increased further, the capacitor enters the accumulation regime. The carrier density that produces ENZ in the accumulation region is shown by the dashed black line. Therefore, ENZ can be reached by applying a gate voltage of ~2.9 V. In Figs. 2(c) and 2(d), we show the real and imaginary parts of the relative permittivity, ε_{Re} and ε_{Im}, calculated at 1300 nm as a function of depth into ITO, using the Drude model given above, and the charge distribution plotted in Fig. 2(b). We see that by increasing V_g, ε_{Im} increases, which signifies the metallic behavior of ITO. Figs. 2(e) and 2(f) show the real and imaginary parts of the refractive index, n and κ, as a function of depth into ITO. For unperturbed ITO we have $n_{unpert} = 1.718$ and $\kappa_{unpert} = 0.045$. Carrier accumulation is localized in ITO to within 1 ~ 2 nm of the interface with HfO_2. We use a mesh resolution of 0.1 nm at the ITO/Hafnia interface in the forthcoming optical computations (discussed in Section III-B).

B. Waveguide Modeling

It is generally known that plasmonic waveguides are subject to a trade-off between mode confinement and propagation losses due to strong absorption in metal [25]. A configuration supporting hybridized plasmonic-dielectric modes [13], [26], [27] is appropriate here, given the overall device structure. The hybrid mode used is a transverse-magnetic (TM) mode, arising from the coupling between a dielectric mode propagating in the active region sandwiched between dielectric claddings and a surface plasmon polariton (SPP) mode on the metal surface. This mode arises naturally as we place the MOS capacitor (discussed in Section III-A) on top of the III-V laser cavity, such that the hybrid mode overlaps with the ITO layer of the MOS capacitor. The fraction of mode power overlapping with the active region and the metal can be tuned by changing the thickness of the layers separating them. Tuning these thicknesses directly changes the net modal power gain (α_{net}) which is described by:

$$\alpha_{net} = \alpha_{loss} - \Gamma g_{mat} \tag{2}$$

The mode power attenuation (α_{loss}) is calculated as:

$$\alpha_{loss} = 2k\kappa_{eff} \tag{3}$$

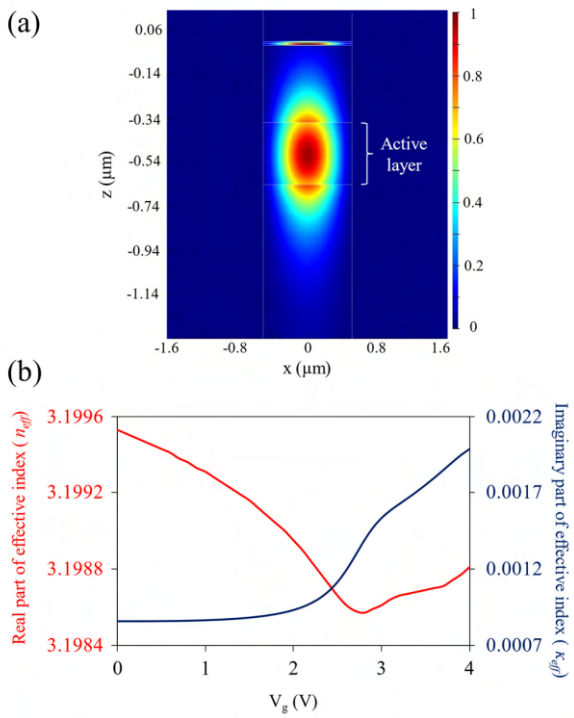

Fig. 3. (a) Electric field amplitude of the hybrid mode at the ridge of the modelled waveguide. (b) Effective index of the hybrid mode with varying V_g.

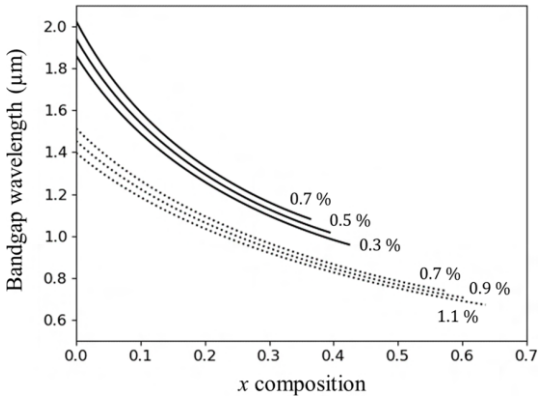

Fig. 4. Bandgap wavelength of $Al_xGa_yIn_{1-x-y}As$ vs. x for different strains (indicated in percentage). Solid curves denote compressive strain and dotted curves are tensile strain.

where k is the vacuum wavenumber and κ_{eff} is the imaginary part of the effective index of the mode. Γ is the fraction of mode power overlapping with the gain region (*i.e.*, the QWs), and g_{mat} is the power gain coefficient provided by the active material (discussed in Section III-C). The modal gain of the TM polarized hybrid mode should be higher than that of the transverse-electric (TE) polarized mode for lasing to occur in the TM mode (which also overlaps with the ITO layer).

In a conventional semiconductor laser, the TE mode is the dominant lasing mode due to lower loss compared to the TM mode and the prevalence of TE gain in QWs. We address the latter point in the next subsection, and the former by utilizing a narrow waveguide (*e.g.*, a nanowire waveguide [28]), such that the TE mode loses confinement and Γ becomes small, while the hybrid TM mode retains confinement and a large Γ - we find that a ridge width of 1 μm satisfies these requirements. Fig. 3(a) shows the electric field profile of the fundamental hybrid TM mode of the waveguide for the case where ITO is unperturbed. The overlap of the mode with the active layer is around 45%.

The effective index of the hybrid TM mode changes significantly as the MOS capacitor is driven into accumulation and the ITO is perturbed by the increased carrier density. Changes in the real part of the effective index (n_{eff}) typically contribute to the tuning, while an increase in the imaginary part of the effective index (κ_{eff}) corresponds to increasing optical losses - conventionally, the former is exploited for tuning, whereas the latter is undesired. Fig. 3(b) shows the real and imaginary parts of the effective index as we vary the applied gate voltage. We note that the real part of the effective index changes by less than 0.1%, yielding only about 0.4 nm of tuning range (estimated from the Bragg equation). But the imaginary part of the effective index, and consequently the mode loss, changes by a factor of 2.5. Our proposed laser concept exploits this latter effect as the tuning mechanism.

C. Active Region Modeling

The active region used in our model is an InP-based laser diode designed to provide TM gain, as required for lasing in the hybrid TM mode of interest. Previous studies show that tensile-strained AlGaInAs quantum wells provide higher TM gain than TE gain [29], [30]. Therefore, we establish our active layer based on tensile-strained AlGaInAs MQWs.

We want the transition wavelength to correspond to a wavelength in O-band. However, the transition wavelength is a function of the well and barrier thickness and composition. The choice of these parameters is non-trivial. To find the right material composition, we start by considering the bandgap wavelength of $Al_xGa_yIn_{1-x-y}As$ for several cases of tensile and compressive strain for barriers and wells, respectively. Fig. 4 shows the bandgap wavelength as a function of x, with tensile strain (dotted lines) varying from 0.7% to 1.1% and compressive strain (solid lines) varying from 0.3% to 0.7%. It is desirable for the tensile strain in the wells to be as high as possible to achieve a high TM gain. Consequently, the required compressive strain in the barriers must increase to compensate at least partially the tension in the wells. On the other hand, our simulations show that the gain for the TE mode increases with compression in wells/barriers, which is undesirable. For the target transition wavelength to be in O-band, we need a range of compositions where the bandgap wavelength is greater than 1.3 μm for the wells and less than 1.2 μm for the barriers, corresponding to high tension wells and comparatively low compressed barriers. So, we select one of many possible solutions: $Al_{0.04}Ga_{0.58}In_{0.38}As$ which has a bandgap wavelength of 1.3 μm (1.1% tensile strain) for the wells, and $Al_{0.42}In_{0.58}As$ which has a bandgap wavelength of 0.96 μm (0.3% compressive strain) for the barriers. Since the

selected tensile strain in the wells is more than three times the compressive strain, we choose the barriers to be 3× thicker than the wells to partially compensate the strain mismatch.

The transition wavelength is also dependent on the carrier concentration in quantum well structures. The peak of the gain spectrum can blueshift or redshift as a function of the QW carrier density. The frequency of the gain peak as a function of carrier density is determined by two effects: band filling and bandgap shrinkage. The former causes a blueshift in the gain peak with increasing carrier density because injected carriers fill the lowest energy states of the bands first, such that transitions between the conduction and valence bands occur at increasingly higher photon energies. The latter results from many-body effects. At high concentrations, the carriers interact via Coulombic repulsion causing a decrease in electron energy in the conduction band and an increase in hole energy in the valence band. Therefore, the gain peak will experience a redshift. Because of these two effects, there is a net increase or decrease in the wavelength of the gain peak as the carrier density changes. Band filling scales linearly with carrier density whereas bandgap shrinkage scales with the cube root of the carrier density [19], so at low carrier densities (less than $\sim 5 \times 10^{18}$ cm^{-3}) the former dominates. The carrier density eventually saturates to its value at the lasing threshold, so the band filling effect also saturates, such that bandgap shrinkage becomes dominant. Both effects are considered in our simulations. The bandgap (ΔE_g) shrinkage at high carrier densities is modelled as $\Delta E_g = -\xi N^{1/3}$ where ξ is a fitting parameter. To our knowledge, there is no data available for the fitting parameter in the case of AlGaInAs in the literature and very little for InGaAsP (10^{-8} [31] and 3.2×10^{-8} [32] eV.cm). Thus, we set $\xi = 10^{-8}$ eV.cm in our simulations.

Another important effect is self-heating. It is known that temperature elevation in MQWs affects key device parameters, including optical gain. In our simulations, we include heating in the proposed p-i-n diode and the effects of a temperature rise in the QWs on the material gain. We use a finite-element mesh in two dimensions to evaluate the thermal response to Joule and recombination heating under electrical drive. We implement a coupled electro-thermal simulation to estimate the thermal response to increasing bias voltage and injected current. In our setup, we assume that the ridge is surrounded by SU-8 polymer which passivates the ridge in practice. The electrical simulation parameters are discussed in Section III-D. The thermal parameters of the materials used in the simulation are listed in Table II. These parameters are taken from [14], [33], [34], [35] with interpolation of binary constituents.

We set Neumann boundary conditions on all the boundaries except the bottom edge of the substrate. The bottom boundary is fixed to a temperature of 300 K, acting as a heat sink. The steady-state simulation results are presented in Fig. 5. Fig. 5 (a) shows the highest temperature in the diode *vs*. input power. The slope gives the thermal resistance of 107 °C/W, defined as $\Delta T / P_{dis}$ [36], where ΔT is the temperature change and P_{dis} the dissipated power, taken as the input DC power calculated from the V-I characteristics of Section III-D.

TABLE II

THERMAL PARAMETERS OF THE MATERIALS IN OUR STRUCTURE

Material	Specific Heat (J/Kg.K)	Thermal Conductivity (W/m.K)	Density (g/cm^3)
Au	385	397	8.93
InP	322	68	4.81
$Al_{0.42}In_{0.58}As$	413	50.2	4.866
$Al_{0.04}Ga_{0.58}In_{0.38}As$	367	38	5.41
$In_{0.53}Ga_{0.47}As$	360.16	50	5.503
SU-8	1500	0.2	1.17

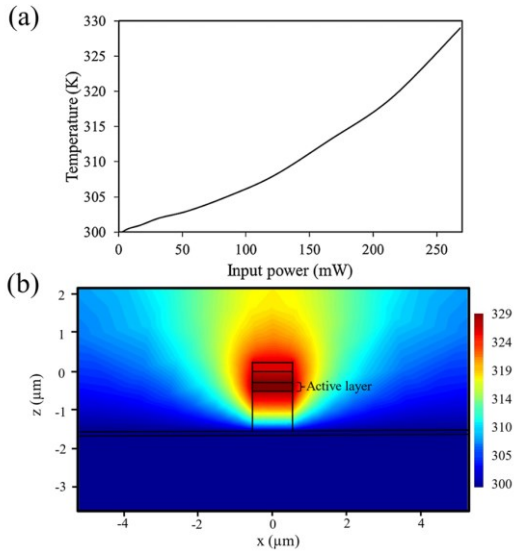

Fig. 5. (a) Highest temperature in the device versus the power consumption. (b) 2D temperature profile of the device at input power of ∼ 250 mW.

Fig. 5(b) plots the temperature distribution over the diode cross-section at an input power of 250 mW. The maximum temperature rise of 29 K occurs in the QWs mainly due to the recombination heat.

After many numerical calculations of the TM material gain, involving different quantum well thicknesses, we picked a well thickness of 6 nm to maximize the peak gain shift *vs*. carrier density. To take heating into account, we assumed a thermal bandgap reduction of 0.334 meV/K [37] for all barriers and wells. Fig. 6 shows the TM material gain of the active region *vs*. frequency for various average carrier densities in the MQW region, assuming a null carrier density in the barriers. The blue curves show the material gain in an isothermal situation, where heating is not considered. The red curves factor in heating effects as the carrier density increases. The dashed lines follow the gain peak for both cases. In general, as the QW carrier density increases, the blue shift due to band filling dominates, but becomes less significant as the temperature of the QWs increases. We henceforth include heating effects.

The thickness and refractive indices of the QWs and barriers designed are presented in Table I. The active region consists of eleven 6-nm-thick $Al_{0.04}Ga_{0.58}In_{0.38}As$ QWs, each of tensile

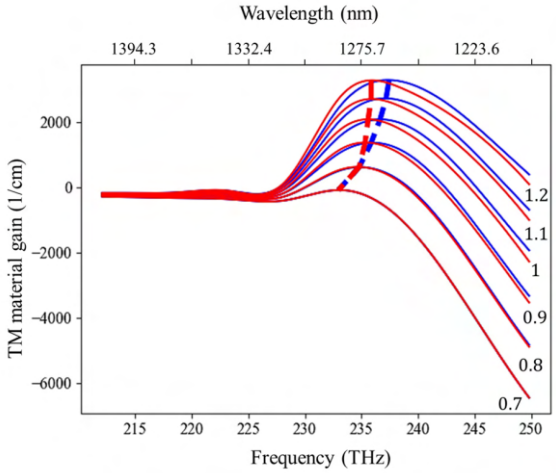

Fig. 6. TM material gain spectrum for various carrier densities as labelled ($\times 10^{18}$ cm^{-3}). Red curves take self-heating into account while blue curves do not. The dashed line follows the gain peak.

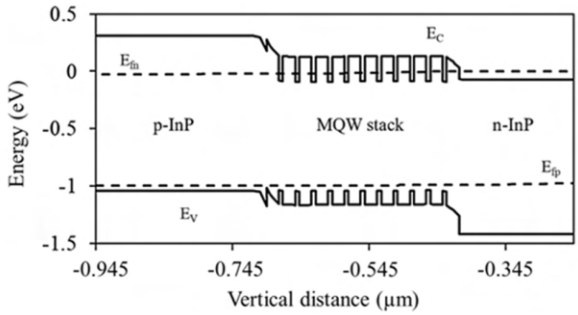

Fig. 7. Energy band diagram of MQW region along with InP claddings near threshold. Solid lines show conduction (E_c) and valence (E_v) band edges, and dashed lines show electron (E_{fn}) and hole (E_{fp}) Fermi levels.

strain of 1.1%. To partially compensate the strain, the 18-nm-thick $Al_{0.42}In_{0.58}As$ barriers each produce a compressive strain of 0.3%. In our modeling, a 0.1 ps intraband relaxation time was assumed, causing spectral broadening of the gain.

For the AlGaInAs material system, the band discontinuity ratio between conduction band edge (E_C) and the valence band edge (E_V) of $\Delta E_C/\Delta E_V = 0.7/0.3$ is typically assumed [37], [38], [39]. At the heterojunction of wells and barriers we assume in our simulations that $\Delta E_C = 0.218$ and $\Delta E_V = 0.122$, which is extracted from work functions of binary constituents of AlGaInAs. The MQW energy band diagram is shown in Fig. 7. The strong barrier in the MQW region in the conduction band will help prevent electron leakage at high temperatures.

Majority of quaternary parameters Q_{ijkl} used in the simulations, such as band deformation potentials, elastic stiffness coefficients, and Luttinger parameters are estimated via the interpolation of binary constituents using:

$$Q_{Al_xGa_yIn_{1-x-y}As} = xQ_{AlAs} + yQ_{GaAs} + (1-x-y)Q_{InAs} \quad (4)$$

where the corresponding binary alloy parameters Q_{ij} are extracted from [40] and [41].

D. Laser Characteristics

In an FP laser, the overlap of the peak of the gain spectrum with the cavity modes determines the wavelength of a lasing mode. As the mode loss (*i.e.*, imaginary part of effective index) increases, a higher current (carrier density) must be injected into the active region to compensate for the loss. Therefore, by injecting different current levels, the lasing frequency changes with the frequency of the gain peak.

As we saw earlier, the frequency of material gain peak varies with carrier density. Therefore, the cavity mode that overlaps best with the peak gain frequency will lase, leading to tuning by mode hopping. By properly choosing the cavity length, the lasing wavelengths will occur at desired wavelengths. In addition, the length of the laser should be kept relatively short to ensure a large spacing between modes, thereby ensuring a high side-mode suppression ratio (SMSR). We picked a cavity length of $L = 100$ μm to satisfy these conditions. V_g can be increased as high as 3.8 V, limited by the breakdown voltage of HfO_2, to perturb the ITO's complex permittivity.

The lasing characteristics were modeled by Lumerical INTERCONNECT, which uses a traveling wave laser model to capture the time evolution of the average carrier density as the propagating light interacts with the gain material.

The dominant nonradiative recombination current is the Auger effect. In this process, the excess energy released from an electron-hole recombination is given to a third carrier. The Auger recombination rate increases at higher carrier concentrations because it is determined by energy exchange between charge carriers. We expect that the recombination rate will be proportional to n^2p for electron-electron-hole processes and to np^2 for electron-hole-hole process, where n and p are electron and hole concentrations, respectively. So, the Auger recombination rate can be defined as $R_{Auger} = CN^3$ where C is the Auger coefficient dependent on the material and N is the carrier density. After reviewing previous reports [37], [38] and comparing them to interpolated data calculated via (4), we chose the Auger coefficient for $Al_{0.04}Ga_{0.58}In_{0.38}As$ to be 10^{-28} cm^{6}s^{-1}at room temperature.

Trap-assisted Shockley-Read-Hall (SRH) nonradiative recombination is less important but still considered. A SRH lifetime of 20 ns is assumed for electrons and holes in the QWs.

The radiative recombination rate is dominated by spontaneous recombination rate, which is obtained from the integral of the spontaneous emission spectrum. The surface recombination can become important due to the narrow width of the ridge. We assume a surface recombination velocity of 10^5 cm/s for InP in our simulations [42].

The mobility of carriers in wells and barriers were derived from binary materials using (4) because experimental data does not exist in the literature for our AlGaInAs compositions.

The simulated light-current-voltage (LIV) characteristics are shown in Fig. 8. The doping levels (presented in Table I) were optimized so that large currents can be injected under low applied voltage. The VI curve (dashed line) reveals a forward bias turn-on voltage of $V_P \sim 1$ V. The LI curves are shown for different gate voltages. The case $V_g = 3.7$ V corresponds to the situation where the hybrid TM mode has the highest

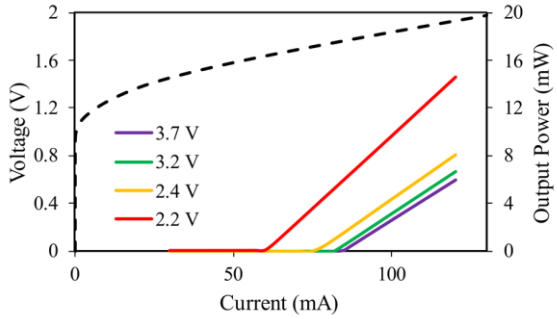

Fig. 8. Simulated VI curve (dashed line) and simulated LI curves (solid lines) for different V_g (legend).

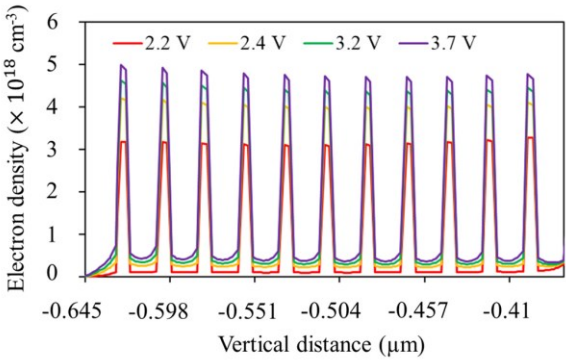

Fig. 9. Threshold electron density for different of gate voltages V_g (legend).

loss. Therefore, a larger threshold current is needed in this case (∼85 mA) for the onset of lasing. As V_g decreases to 2.2 V, the threshold current decreases to ∼60 mA. For $V_g <$ 2.2 V, the threshold current remains approximately the same as the imaginary effective index of the hybrid TM mode remains constant (*cf.* Fig. 3 (b)). We assumed facet reflectivies of 28% at both ends of the FP cavity, commensurate with air/InP interfaces. Our simulations show that the threshold current is highly dependent on the reflectivity of the facets, and can be reduced significantly by forming a high reflectance mirror on at least one end. For example, using an 80% reflectivity at one of the facets reduces the threshold current by ∼15 mA.

Fig. 9 gives the distribution of the electron concentration through the MQW stack near threshold for the same V_gs in Fig. 8. The average QW electron concentration increases from $\sim 3 \times 10^{18}\text{cm}^{-3}$ to 4.9×10^{18} cm^{-3} with V_g, which is consistent with average carrier densities assumed in Fig. 6. This increase causes an increase in Auger recombination as well as in spontaneous and SRH recombination, contributing to an increase in threshold current with gate voltage as shown in Fig. 8.

The simulated lasing spectra for a driving current at 100 mA are shown in Fig. 10 for the same cases of gate voltage used in Fig. 8 and 9. We assumed a cavity length of $L = 100$ μm in the simulations to produce a large spacing between cavity modes, leading to fewer modes overlapping with the gain spectrum and a higher SMSR. As observed from Fig. 10, the worst SMSR is 10.5 dB, corresponding to a gate voltage of $V_g = 3.7$ V. Simulations show that the SMSR increases as high as 20 dB as the mode loss decreases. The spacing

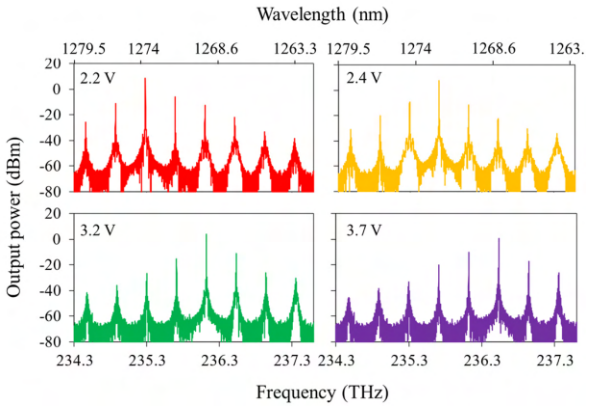

Fig. 10. Simulated lasing spectrum with a driving current of 100 mA for different cases of gate voltages V_g (shown in the insets).

between cavity modes is determined by [43]: $\Delta\upsilon = c/\left(2n_g L\right)$ where c is the speed of light in vacuum, n_g is the group index, and L is the physical length of the cavity. The group index is calculated in the vicinity of the lasing frequency as [43]: $n_g = n_{eff} + \omega dn_{eff}/d\omega$ (ω is the angular frequency) and taken to be locally weakly frequency dependent. The theoretical prediction of $\Delta\upsilon$ is about 430 GHz.

As can be seen in Fig. 10, discrete lasing wavelength tuning of up to 1.25 THz (∼7 nm) can be achieved. The tuning range is limited by the breakdown voltage of hafnia – a greater V_g if possible, would result in larger loss perturbation.

IV. Conclusion

We proposed a new approach based on loss perturbation to achieve laser tunability, representing a paradigm shift in the field of tunable lasers. The approach can be used at telecom wavelengths for two reasons: ITO has an ENZ region in this wavelength range, and III-V semiconductor materials have sufficient gain at telecom wavelengths to overcome all losses. The structure proposed consists of a p-i-n diode laser based on InP with an ITO/HfO_2/Au structure on top forming a MOS tuning capacitor. When the ITO is in the vicinity of its ENZ carrier density, the propagating hybrid plasmonic TM mode is significantly perturbed (complex effective index) which is exploited for laser tuning. Simulations yield a tuning range of over 7 nm in the O-band for a 100 μm long FP laser cavity.

References

[1] O. Reshef, I. De Leon, M. Z. Alam, and R. W. Boyd, "Nonlinear optical effects in epsilon-near-zero media," *Nature Rev. Mater.*, vol. 4, no. 8, pp. 535–551, Jun. 2019.

[2] N. Kinsey, C. DeVault, J. Kim, M. Ferrera, V. M. Shalaev, and A. Boltasseva, "Epsilon-near-zero AL-doped ZnO for ultrafast switching at telecom wavelengths," *Optica*, vol. 2, no. 7, pp. 616–622, 2015.

[3] M. Z. Alam, I. De Leon, and R. W. Boyd, "Large optical nonlinearity of indium tin oxide in its epsilon-near-zero region," *Science*, vol. 352, pp. 795–797, May 2016.

[4] A. Ciattoni, C. Rizza, and E. Palange, "Extreme nonlinear electrodynamics in metamaterials with very small linear dielectric permittivity," *Phys. Rev. A, Gen. Phys.*, vol. 81, no. 4, Apr. 2010, Art. no. 043839.

[5] C. Argyropoulos, P.-Y. Chen, G. D'Aguanno, N. Engheta, and A. Alù, "Boosting optical nonlinearities in ϵ-near-zero plasmonic channels," *Phys. Rev. B, Condens. Matter*, vol. 85, no. 4, Jan. 2012, Art. no. 045129.

[6] E. G. Carnemolla et al., "Giant nonlinear frequency shift in epsilon-near-zero aluminum zinc oxide thin films," in *Proc. Conf. Lasers Electro-Opt. (CLEO)*, vol. 7, May 2018, pp. 1–2.
[7] A. Capretti, Y. Wang, N. Engheta, and L. D. Negro, "Enhanced third-harmonic generation in Si-compatible epsilon-near-zero indium tin oxide nanolayers," *Opt. Lett.*, vol. 40, no. 7, pp. 1500–1503, 2015.
[8] R. Amin et al., "Low-loss tunable 1D ITO-slot photonic crystal nanobeam cavity," *J. Opt.*, vol. 20, no. 5, Apr. 2018, Art. no. 054003.
[9] V. E. Babicheva, A. Boltasseva, and A. V. Lavrinenko, "Transparent conducting oxides for electro-optical plasmonic modulators," *Nanophotonics*, vol. 4, no. 1, pp. 165–185, Jan. 2015.
[10] G. Sinatkas, T. Christopoulos, O. Tsilipakos, and E. E. Kriezis, "Comparative study of silicon photonic modulators based on transparent conducting oxide and graphene," *Phys. Rev. A, Gen. Phys. Appl.*, vol. 12, no. 6, Dec. 2019, Art. no. 064023.
[11] L. A. Coldren, G. A. Fish, Y. Akulova, J. S. Barton, L. Johansson, and C. W. Coldren, "Tunable semiconductor lasers: A tutorial," *J. Lightw. Technol.*, vol. 22, no. 1, pp. 193–202, Jan. 2004.
[12] A. C. Lesina, D. Goodwill, E. Bernier, L. Ramunno, and P. Berini, "Tunable plasmonic metasurfaces for optical phased arrays," *IEEE J. Sel. Topics Quantum Electron.*, vol. 27, no. 1, pp. 1–16, Jan. 2021.
[13] D. Costantini et al., "A hybrid plasmonic semiconductor laser," *Appl. Phys. Lett.*, vol. 102, no. 10, Mar. 2013, Art. no. 101106.
[14] D. R. Lide, *CRC Handbook of Chemistry and Physics*, vol. 85. Boca Raton, FL, USA: CRC Press, Jun. 2004.
[15] E. D. Palik, *Handbook of Optical Constants of Solids*, vol. 3. New York, NY, USA: Academic, 1998.
[16] D. L. Wood et al., "Optical properties of cubic Hafnia stabilized with yttria," *Appl. Opt.*, vol. 4, no. 10, pp. 604–607, Feb. 1990.
[17] B. R. Bennett, R. A. Soref, and J. A. Del Alamo, "Carrier-induced change in refractive index of InP, GaAs and InGaAsP," *IEEE J. Quantum Electron.*, vol. 26, no. 1, pp. 113–122, Jan. 1990.
[18] A. V. Ivanov et al., "Refractive indices of solid AlGaInAs solutions," *Quantum Electron.*, vol. 37, no. 6, pp. 545–548, Jun. 2007.
[19] J.-P. Weber, "Optimization of the carrier-induced effective index change in InGaAsP waveguides-application to tunable Bragg filters," *IEEE J. Quantum Electron.*, vol. 30, no. 8, pp. 1801–1816, Aug. 1994.
[20] (2022). *Lumerical is Now Part of the Ansys Family*. [Online]. Available: https://www.lumerical.com/
[21] G. K. Shirmanesh et al., "Dual-gated active metasurface at 1550 nm with wide (> 300°) phase tunability," *Nano Lett.*, vol. 18, no. 5, pp. 2957–2963, Mar. 2018.
[22] A. Olivieri, C. Chen, S. Hassan, E. Lisicka-Skrzek, R. N. Tait, and P. Berini, "Plasmonic nanostructured metal–oxide–semiconductor reflection modulators," *Nano Lett.*, vol. 15, no. 4, pp. 2304–2311, Apr. 2015.
[23] G. Sinatkas and E. E. Kriezis, "Silicon-photonic electro-optic phase modulators integrating transparent conducting oxides," *IEEE J. Quantum Electron.*, vol. 54, no. 4, pp. 1–8, Aug. 2018.
[24] M. Shabaninezhad, L. Ramunno, and P. Berini, "Tunable plasmonics on epsilon-near-zero materials: The case for a quantum carrier model," *Opt. Exp.*, vol. 30, no. 26, pp. 19–46501, Dec. 2022.
[25] P. Berini, "Figures of merit for surface plasmon waveguides," *Opt. Exp.*, vol. 14, no. 26, pp. 13030–13042, 2006.
[26] R. F. Oulton, V. J. Sorger, D. A. Genov, D. F. P. Pile, and X. Zhang, "A hybrid plasmonic waveguide for subwavelength confinement and long-range propagation," *Nature Photon.*, vol. 2, pp. 496–500, Jul. 2008.
[27] P. Berini and I. D. Leon, "Surface plasmon-polariton amplifiers and lasers," *Nature Photon.*, vol. 6, pp. 16–24, Jan. 2012.
[28] S. Saeidi et al., "Nonlinear photonics on-a-chip in III-V semiconductors: Quest for promising material candidates," *Appl. Optics*, vol. 56, no. 19, pp. 5532–5541, Jul. 2017.
[29] J. Decobert, N. Lagay, C. Cuisin, B. Dagens, B. Thedrez, and F. Laruelle, "MOVPE growth of AlGaInAs–InP highly tensile-strained MQWs for 1.3 μm low-threshold lasers," *J. Cryst. Growth*, vol. 272, nos. 1–4, pp. 543–548, Dec. 2004.
[30] D. Costantini, A. Bousseksou, M. Fevrier, B. Dagens, and R. Colombelli, "Loss and gain measurements of tensile-strained quantum well diode lasers for plasmonic devices at telecom wavelengths," *IEEE J. Quantum Electron.*, vol. 48, no. 1, pp. 73–78, Jan. 2011.
[31] J. Piprek, P. Abraham, and J. E. Bowers, "Self-consistent analysis of high-temperature effects on strained-layer multiquantum-well InGaAsP-InP lasers," *IEEE J. Quantum Electron.*, vol. 36, no. 3, pp. 366–374, Mar. 2000.
[32] M. J. Connelly, "Band-gap shrinkage calculations and analytic model for strained bulk InGaAsP," *Mater. Res. Exp.*, vol. 2, no. 2, Feb. 2015, Art. no. 026201.
[33] J. El-Ali, I. R. Perch-Nielsen, C. R. Poulsen, D. D. Bang, P. Telleman, and A. Wolff, "Simulation and experimental validation of a SU-8 based PCR thermocycler chip with integrated heaters and temperature sensor," *Sens. Actuators A, Phys.*, vol. 110, nos. 1–3, pp. 3–10, Feb. 2004.
[34] L. J. Guerin et al., "Simple and low cost fabrication of embedded micro-channels by using a new thick-film photoplastic," in *Proc. Int. Solid State Sensors Actuators Conf.*, vol. 2, Jun. 1997, pp. 1419–1422.
[35] S. Adachi, *Physical Properties of III-V Semiconductor Compounds*. Hoboken, NJ, USA: Wiley, 1992.
[36] R. McKenna et al., "Spatially resolved self-heating and thermal impedance of laser diodes using CCD-TR imaging," *OSA Continuum*, vol. 4, no. 4, pp. 1271–1281, Apr. 2021.
[37] J. Piprek, M. Manish, and V. Jayaraman, "Design and optimization of high-performance 1.3-μm VCSELs," *Proc. SPIE*, vol. 5349, pp. 375–384, Jun. 2004.
[38] S. R. Selmic et al., "Design and characterization of 1.3-/spl mu/m AlGaInAs-InP multiple-quantum-well lasers," *IEEE J. Sel. Top. Quantum Electron.*, vol. 7, no. 2, pp. 340–349, Mar. 2001.
[39] R. F. Kazarinov and G. L. Belenky, "Novel design of AlGaInAs-InP lasers operating at 1.3 μm," *IEEE J. Quantum Electron.*, vol. 31, no. 3, pp. 423–426, Mar. 1995.
[40] S. Kasap and P. Capper, *Springer Handbook of Electronic and Photonic Materials*. Cham, Switzerland: Springer, 2017.
[41] I. R. Vurgaftman, R. J. Meyer, and L. R. Ram-Mohan, "Band parameters for III-V compound semiconductors and their alloys," *J. Appl. Phys.*, vol. 89, no. 11, pp. 5815–5875, 2001.
[42] T. J. Coutts and M. Yamaguchi, "Indium phosphide based solar cells: A critical review of their fabrication, performance and operation," in *Current Topics in Photovoltaics*, vol. 3. New York, NY, USA: Academic, 1998, p. 79.
[43] G. P. Agrawal and N. K. Dutta, *Semiconductor Lasers*. New York, NY, USA: Van Norstrand Reinhold, 1993, pp. 30–135.

Shayan Saeidi received the B.Sc. degree in electrical engineering from Tehran Polytechnic in 2015 and the M.Sc. degree from the University of Ottawa, where he is currently pursuing the Ph.D. degree in electrical engineering.

In 2018, he successfully defended his thesis on nonlinear effects on III-V semiconductor compounds. He joined ArtIC Photonics Inc., Ottawa, in 2018, where he was involved in research and development of DFB lasers for optical communication systems. He received NSERC Canada Graduate Scholarship—Doctoral in 2022. His main research interests include InP-based photonic integration.

Pierre Berini (Fellow, IEEE) received the B.E.Sc. and B.Sc. degrees in electrical engineering and computer science from the University of Western Ontario, Canada, and the M.Sc.A. and Ph.D. degrees in electrical engineering from the École Polytechnique de Montréal, Canada.

He is currently a Distinguished University Professor in electrical engineering and physics, the University Research Chair of Surface Plasmon Photonics, the Director of the Centre for Research in Photonics, University of Ottawa (30 PIs), and the Director of the uOttawa Nanofab (>70 users). He was the Founder and the CTO of a venture capital financed company and he collaborates on an ongoing basis with industry. He has received an NSERC Steacie Fellowship, an NSERC Discovery Accelerator, a Premier of Ontario Research Excellence Award (PREA), the University of Ottawa Young Researcher of the Year Award, an URSI Young Scientist Award, and a George S. Glinski Award for Excellence in Research. He is also a Canada Foundation for Innovation Researcher. He is a fellow of the OSA, APS, Canadian Academy of Engineering, and Royal Society of Canada. He has published 12 book chapters, approximately 600 scientific and technical papers in peer-reviewed periodicals and conference proceedings. He is an inventor or co-inventor on 24 patents. He was an Associate Editor of *Optics Express* and a Managing Editor of *Nanophotonics*. He is currently an Associate Editor of *Optica*. He contributes on an ongoing basis to the organization of several international conferences in photonics. His research interests span many areas of optics and photonics, with surface plasmons, metasurfaces, and their applications being of interest.

3.3 Conclusion

Although we introduced a completely new concept for a tunable laser, it comes with its own advantages and limitations. In terms of advantages, compared with the devices in Chapter 2, which require multiple tuning elements and several vital sections (see Table 1.1), this design relies on only a single tuning section, making its characterization significantly simpler. Its cavity length is also only about 100 μm, much shorter than the devices discussed earlier. This greatly improves wafer-level device density and reduces overall fabrication cost.

The main limitations relate to the input/output power and waveguide losses. The device consumes more power due to its higher threshold current, and its performance metrics, including SMSR and linewidth, are generally inferior to those in Table 1.1. The SMSR is lower because the device operates as a Fabry-Perot cavity, and the linewidth is broader due to the shorter photon lifetime. The tuning range is also narrower. However, this is not a major drawback since it still covers at least four CWDM channels, which already support a wide range of applications.

Despite these trade-offs, when comparing performance requirements for datacom systems, this device appears better suited for sensing applications, where the parameters listed in Table 1.1 are less critical. In the next chapter, we employ a similar device specifically for sensing purposes.

Chapter 4

Hybrid Semiconductor Plasmonic Lasers for Biochemical Sensing: Theory and Design

4.1 Contribution Statement

This project was conducted in collaboration with the National Research Council of Canada (NRC), specifically with the research group led by Dr. Schmid and Dr. Cheben. The core concept was originally developed by myself and my supervisor, Prof. Berini. Regular meetings with the NRC team have been instrumental in shaping the direction of the research, particularly as we advanced toward the fabrication phase.

I was primarily responsible for the development and implementation of the optimization algorithms, as well as conducting the simulations and creating the figures included in the manuscript. I also took the lead in drafting the initial version of the manuscript.

Related conference publications arising from this work are listed below:

- S. Saeidi, *et al*. "Theoretical Exploration of Biosensing Using Hybrid Semiconductor Plasmonic Lasers." *Integrated Photonics Research, Silicon and Nanophotonics. Optica Publishing Group, 2024.*
- S. Saeidi, *et al*. " InP-Based Laser Diode for Plasmonic Biosensing." *Integrated Photonics Research, Silicon and Nanophotonics. Optica Publishing Group, 2025.*

4.2 Article

IEEE PHOTONICS JOURNAL, VOL. 17, NO. 2, APRIL 2025 0600112

Hybrid Semiconductor Plasmonic Lasers for Biochemical Sensing: Theory and Design

Shayan Saeidi, Jens H. Schmid, *Member, IEEE*, Pavel Cheben, *Fellow, IEEE*, and Pierre Berini, *Fellow, IEEE*

***Abstract*—An electrically driven InP-based Fabry-Perot biochemical sensing laser is proposed and analyzed. The design incorporates a sensing area on top of the laser to alter its characteristics and operates in a hybrid plasmonic-semiconductor lasing mode. Our device is designed for an etch-free III-V (InP) based stack, where lateral confinement of the hybrid mode is ensured by a thin gold (Au) strip on a thin indium tin oxide (ITO) strip. We optimize the waveguide geometry to produce maximum sensitivity while having compensable loss. Our investigation centers on three laser characteristics that are affected by the sensing fluid and that could serve as measurands: lasing wavelength, threshold current, and power-current slope efficiency. We determine the sensitivity of each measurand, assess the potential noise sources, and the limit of detection (LoD) associated with them. Our calculations indicate that the proposed biosensor can achieve LoDs as low as 10^{-5} RIU when employing the threshold current as the measurand.**

***Index Terms*—Biochemical sensors, Fabry-Perot laser, plasmonics, semiconductor lasers.**

I. Introduction

REAL-TIME biochemical sensing techniques utilizing Surface Plasmon Resonance (SPR) have gained considerable popularity due to their high sensitivity and label-free detection capabilities. These techniques can be implemented by exciting surface plasmons using a prism [1], [2], [3] or along waveguides [4], [5]. The fundamental principle involves the interaction of incident light with a metal waveguide, on which surface plasmons—oscillations of electrons at the metal surface – are excited. This interaction results in a surface wave having an electric field that extends into the sensing solution. Any changes in the solution affect the surface plasmon characteristics, enabling the detection of biomolecular interactions.

A recent innovation in surface plasmon sensors involves adding multifunctionality by using the metal surface for a second transduction method, such as electrochemical detection, resulting in multimodal biosensors [6], [7]. We extend this approach by addressing significant challenges in surface plasmon sensing: propagation loss, which limits both resonance linewidth [1], [2], [8] and sensing length [4], [9], and the coupling of a light source. Our proposed solution consists of a hybrid plasmonic semiconductor laser that serves as a biosensor. This design not only compensates for surface plasmon loss but also supports a plasmonic lasing mode, using the metal waveguide as a contact, the lasing waveguide, and the biosensing surface. By driving it electrically via the metal contact, we pump a PIN InP-based heterostructure to achieve high transverse-magnetic (TM) gain. This approach enhances sensitivity and eliminates the need for an external optical source, thereby reducing both the size and cost of the biosensor.

The structure of this paper is organized as follows: In Section II, we present the concept and its model. Section III is dedicated to modal analysis on the waveguide, including its optimization and an analysis of the optimized laser structure, focusing on modeling the active region and the electrical characteristics. In Section IV, we review three distinct sensing methodologies and evaluate the optimized laser structures within the context of each method. The limit of detection for each sensing scheme is then discussed in Section V. Our work achieves a detection limit as low as 10^{-5} RIU, which is competitive for a high-performance biosensor [10], [11]. Although smaller limits, such as [12], [13], have also been reported, the novelty of our approach lies in the compactness of the device, which eliminates the need for an external optical pump, and the use of an etch-free III-V stack. Finally, Section VI provides the conclusion.

II. Concept and Model

Fig. 1 illustrates the cross-section of the proposed Fabry-Perot laser, with different segments described in Table I. The structure contains an active layer based on intrinsic multiple-quantum wells (MQWs) sandwiched between a p-doped AlGaInAs layer at the bottom and an n-doped InGaAsP layer on the top. The design of the MQW region is discussed in Section III-C. A dielectric mode is confined within the MQW layer due to the higher refractive index of the latter relative to the surrounding layers. The lower-cladding high-index AlGaInAs layer (Fig. 1, layer 7), is employed to improve the confinement of the mode to the MQW layer. The gold (Au) layer on top is essential for lateral confinement of the hybrid mode. The strength of the plasmonic or dielectric character of the mode is determined by the thickness of the layers separating the MQW region and the top metal. Layer 5 in Fig. 1 is kept relatively thin, allowing the

Received 10 October 2024; revised 4 January 2025; accepted 17 January 2025. Date of publication 21 January 2025; date of current version 17 February 2025. This work was supported in part by the National Research Council Canada under Grant 200987 and in part by the Natural Sciences and Engineering Research Council of Canada under Grant 210396. *(Corresponding author: Shayan Saeidi.)*

Shayan Saeidi is with the School of Electrical Engineering and Computer Science, Nexus for Quantum Technologies Institute, University of Ottawa, Ottawa, ON K1N6N5, Canada, and also with the KVector Dynamics, Ottawa, ON K2B8E1, Canada (e-mail: ssaeidi@uottawa.ca).

Jens H. Schmid and Pavel Cheben are with the National Research Council of Canada, Ottawa, ON K1A 0R6, Canada.

Pierre Berini is with the School of Electrical Engineering and Computer Science, the Department of Physics, and Nexus for Quantum Technologies Institute, University of Ottawa, Ottawa, ON K1N 6N5, Canada.

Digital Object Identifier 10.1109/JPHOT.2025.3532399

0600112 IEEE PHOTONICS JOURNAL, VOL. 17, NO. 2, APRIL 2025

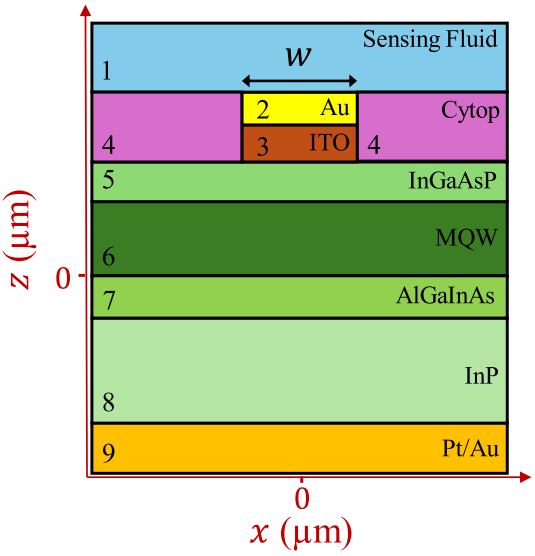

Fig. 1. Cross-sectional schematic of the proposed biosensor laser, with each segment detailed in Table I.

TABLE I
LAYERS OF THE LASER STRUCTURE OF FIG. 1

Layer	Material	Ref. Index	Thick-ness (μm)	Descrip-tion
1	Fluid	n_c	2	Sensing fluid
2	Au	0.13+0.83j	t_2	Top contact
3	ITO	1.71+0.04j	t_3	n-contact
4	Cytop	1.35	t_2+t_3	Isolator
5	InGaAsP	3.27	0.037	n-Upper Clad
6	AlInAs (x15 barrier)	3.57	0.018	MQW
	AlGaInAs (x14 well)	3.3	0.006	
7	AlGaInAs	3.35	0.2	p-Lower Clad
8	InP	3.2	300	p-Substrate
9	Pt/Au	-	-	Bottom Contact

separation thickness to be optimized solely based on layer 3, while still being thick enough to maintain good confinement of the dielectric mode in the MQW region. A detailed discussion of the waveguide design and its optimization is provided in Section III-A. Sensing fluid is dispensed on top of the Au waveguide and interacts with the hybrid mode. Cytop is used to isolate the rest of the laser from the fluid.

Electrical injection to excite the MQW layer is achieved by applying a voltage between the bottom Pt/Au metal stack and the gold layer on top. Platinum (Pt) is utilized to establish a reliable ohmic contact to p-type InP and also serves as an adhesion layer between InP and Au. For the top contact, we use indium tin oxide (ITO) due to its significant n-type doping, which enhances the current flow within the diode. Additionally, ITO's excellent adhesion properties to Au further justify its selection as a contact layer.

The refractive indices listed in Table I are measured at 1280 nm. A positive sign of the imaginary part of the refractive index indicates loss. The refractive indices of Au, Cytop, and InP are taken from [14], [15] and [16], respectively. The refractive index of InGaAsP and its dependency on doping are calculated from [17]. The refractive indices of the AlGaInAs layers are calculated using the formulation in [18]. The permittivity of ITO as a function of frequency $\varepsilon(\omega)$ is calculated using the Drude model:

$$\varepsilon(\omega) = \varepsilon_\infty - \omega_p^2 / \left(\omega^2 + i\zeta\omega\right) \tag{1}$$

in which ε_∞ is the high-frequency permittivity and ζ is the electron damping term. The plasmonic frequency ω_p is:

$$\omega_p = \sqrt{\frac{Ne^2}{\varepsilon_0 m_n^*}} \tag{2}$$

where m_n^* (= $0.35m_e$ [19]) is the effective electron mass with m_e being the free electron mass, N is the carrier density, e is the electron charge, ε_0 is the vacuum permittivity. These parameters are measured using in-house ellipsometry, with the derived refractive index provided in Table I.

III. RESULTS

In this section, we review various aspects of our laser design, including the structure of the active region, waveguide geometry, and electro-thermal mechanisms. The simulation results presented in this paper are obtained using Ansys Lumerical simulators [20].

A. Waveguide Modes

Plasmonic waveguides face a trade-off between mode confinement and propagation losses due to significant absorption in the metal [9]. Considering the overall device structure, a configuration supporting hybrid plasmonic-dielectric modes [21], [22] is suitable in this context. We utilize hybrid TM mode, resulting from the coupling between a dielectric mode propagating within the active region and a surface plasmon polariton mode on the metal surface. This TM mode naturally arises within a specific range of thickness of the layers separating the MQW layer and the top metal contact, i.e., layers 3 and 5 in Fig. 1. If the separation is small, the mode is predominantly confined to the metal surface. Conversely, if the separation is large, only the dielectric mode exists in the active region. Within the appropriate range of thicknesses, a hybrid mode effectively combines both plasmonic and dielectric characteristics, allowing for optimal mode overlap with the active layer and metal surface.

The width of the ridge plays an important role in determining which mode polarization is confined. Previous studies have

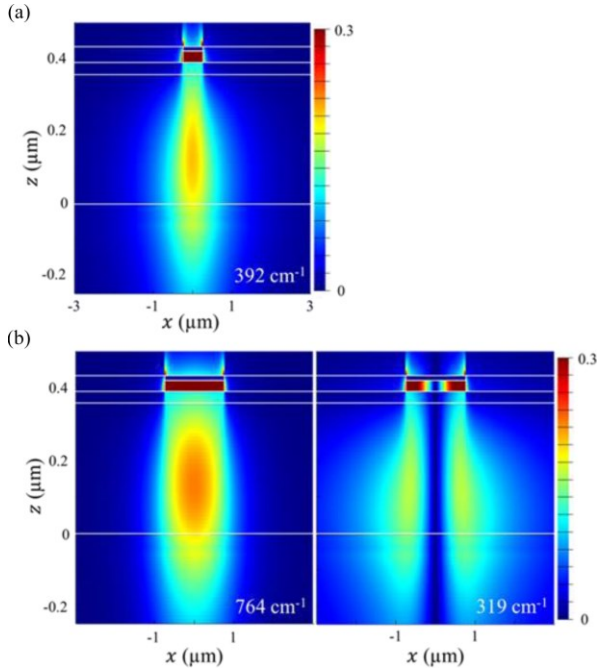

Fig. 2. Electric field magnitude of hybrid modes, normalized to unity, for n_c = 1.316 with (a) w = 0.5 μm, t_2 = 14 nm, t_3 = 30 nm, and (b) w = 1.5 μm, t_2 = 13 nm, t_3 = 30 nm. The color bar is capped to a maximum value of 0.3 for clarity, resulting in saturation in the plasmonic region of the modes.

shown that the transverse-electric (TE) mode loses its confinement more rapidly than the TM mode with decreasing ridge width [23], [24].

Adjusting separation layer thicknesses and the ridge width directly affects the modal gain:

$$g_{\text{modal}} = \Gamma g_{\text{mat}} \tag{3}$$

where Γ represents the fraction of modal power overlapping with the gain region, and g_{mat} is the gain provided by the active material, which will be discussed in Section III-C. In our simulations, w, t_2, and t_3 are selected to ensure that the TE mode remains unconfined, thereby enabling lasing exclusively in the hybrid TM mode.

Fig. 2(a) shows the hybrid mode profile for w = 0.5 μm, t_2 = 14 nm, t_3 = 30 nm, indicating that only the fundamental mode is supported. As w increases, the waveguide can support higher order modes. For instance, Fig. 2(b) shows the fundamental and second order modes for w = 1.5 μm, t_2 = 13 nm, t_3 = 30 nm. n_c is set to 1.316 for both cases, representing water on the top surface. Numbers at the bottom of the figure panels indicate the mode loss, calculated as:

$$\alpha_{\text{mode}} = 2k\kappa_{\text{eff}} \tag{4}$$

where k is the vacuum wavenumber and κ_{eff} is the imaginary part of the effective index of the mode. The higher order modes have lower loss, due to their smaller overlap with the top metal. In general, Γ is only slightly lower for higher-order modes compared to the fundamental mode. Consequently, the material gain required to counteract the losses is consistently lower for

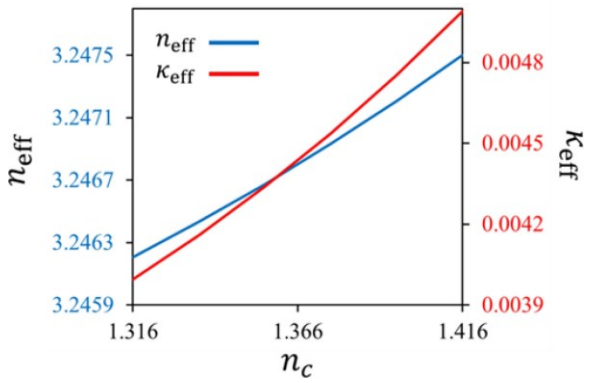

Fig. 3. Real (n_{eff}) and imaginary (κ_{eff}) part of effective index of the fundamental hybrid mode with varying n_c for w = 0.5 μm, t_2 = 14 nm, t_3 = 30 nm.

higher-order modes. For example, in Fig. 2(b), Γ is 0.13 for the fundamental mode and 0.11 for the second-order mode. This results in g_{mat} of 5877 cm^{-1} and 2900 cm^{-1} for the fundamental and second-order mode, respectively. This behavior is generally true for all waveguide geometries: in waveguides that support more than one mode, all modes exhibit similar confinement in the active region, while higher-order modes show reduced confinement in the top metal. Thus, the higher-order mode requires less material gain to overcome the losses, making it the dominant lasing mode. In our optimization procedure, we only consider the sensitivity of the dominant lasing mode, i.e., the highest supported hybrid mode.

The sensitivity of our laser is influenced significantly by the variation in the effective index of the propagating mode in response to changes in n_c. Fig. 3 shows the real and imaginary parts of the effective index of the fundamental mode supported by the structure of Fig. 2(a), as n_c ranges from 1.316 (the refractive index of water) to 1.416, which is a typical range for biochemical fluids. A near linear relationship is observed. This linear behavior is consistent across all modes, irrespective of the waveguide geometry. We utilize the slope of this linear relationship (bulk sensitivity) as a key parameter for device optimization. Another important factor is the loss associated with the dominant mode. The confinement factor Γ is approximately 0.1 for all modes and g_{mat} can reach up to ~5000 cm^{-1} (see Section III-C). Consequently, our gain system cannot compensate for mode losses exceeding 500 cm^{-1}. This agrees with previously reported data for similar hybrid laser systems [25].

In our optimization procedure, we sweep t_2 and t_3 from 10 to 40 nm in steps of 5 nm, and w from 0.5 to 4 μm in steps of 0.5 μm. Fig. 4(a), (b), and (c) show $\Delta n_{\text{eff}}/\Delta n_c$, $\Delta \kappa_{\text{eff}}/\Delta n_c$, and α_{mode} for different geometries, respectively. It is evident that as loss increases, i.e., the plasmonic character of the mode becomes stronger than the dielectric part, the modal sensitivity increases. Another observation from Fig. 4 is that the modal loss (and consequently, its sensitivity) significantly increases when t_2 varies from 15 to 10 nm. In contrast, any mode with $t_2 > 15$ nm remains relatively insensitive, while at $t_2 \approx 10$ nm, the mode becomes very lossy. Such a sudden change is not observed while changing t_3 or w. Fig. 5 shows the same parameters as Fig. 4 but

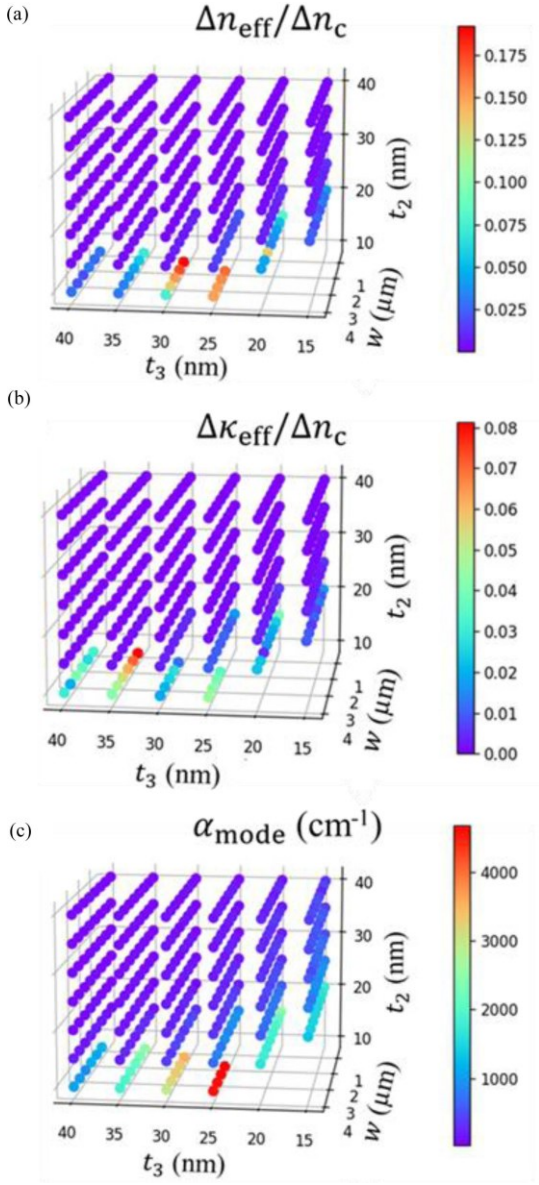

Fig. 4. Sensitivity of the (a) real and (b) imaginary parts of the effective index, and (c) mode loss of the propagating mode, to changes in n_c for different waveguide geometries. Here, t_2, t_3, and w represent the thickness of the Au layer, the thickness of the ITO layer, and the ridge width, respectively.

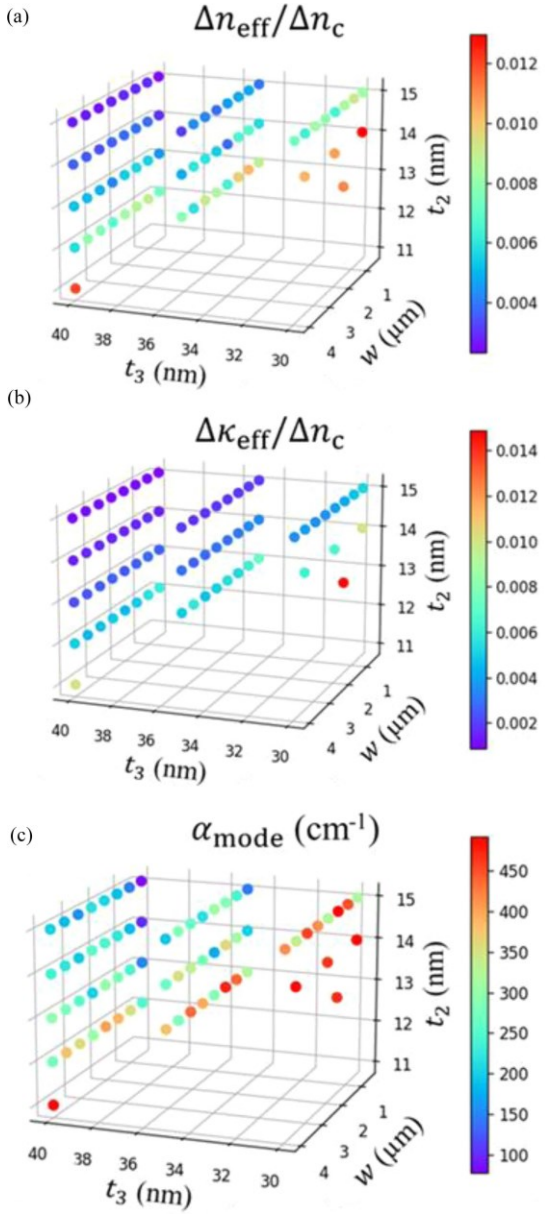

Fig. 5. Same description as Fig. 4. Geometries with losses exceeding 500 cm^{-1} have been filtered out.

with t_2 varying from 10 to 15 nm in steps of 1 nm. All modes with losses higher than 500 cm^{-1} are not shown for clarity, therefore all data points correspond to a lasing mode. It can be observed that the highest n_{eff} sensitivity and the maximum κ_{eff} sensitivity correspond to two different geometries. Therefore, we select these two geometries as our optimized structures and evaluate the sensitivity of the first lasing mode, i.e., the mode with lowest loss, throughout the remainder of the paper. The electric field profiles associated with the optimized structures, hereinafter referred to as Structures 1 and 2, were presented earlier in the paper in Fig. 2(a) and (b, right panel), respectively. The dimensions of these structures are given in Table II. The effective index of these

TABLE II
PARAMETERS OF THE OPTIMIZED STRUCTURES (DIMENSIONS ARE IN NM)

Structure	w	t_2	t_3	a	b	c	d
1	500	14	30	0.012	3.229	0.009	-0.009
2	1500	13	30	0.011	3.223	0.014	-0.016

modes can be modeled as a linear function of n_c (*cf.* Fig. 3):

$$n_{eff} = an_c + b \quad (5a)$$

$$\kappa_{eff} = cn_c + d \quad (5b)$$

where a, b, c, and d are coefficients, specified in Table II.

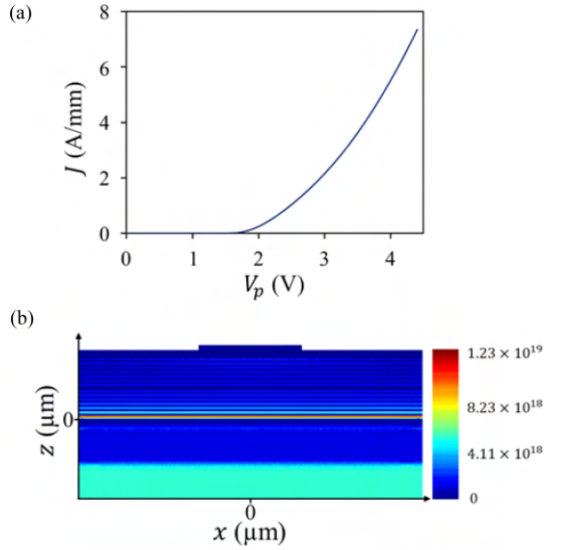

Fig. 6. (a) Simulated J-V curve. (b) 2D hole density distribution (cm^{-3}) at $V_P = 2.5$ V.

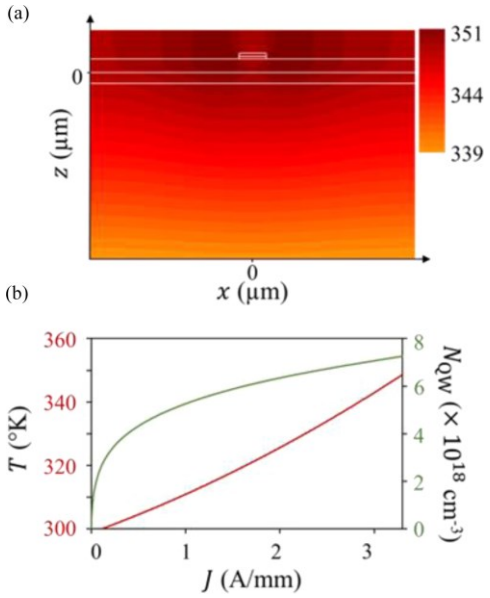

Fig. 7. (a) 2D temperature profile of the laser at $J = 3$ A/mm. (b) Temperature in the MQW region and average carrier density in QWs as a function of current density.

B. Electro-Thermal Simulations

To determine the electrostatic potential and carrier density distribution of the laser while accounting for self-heating effect, we solve the drift-diffusion equations together with Poisson's and the heat transport equations over the laser's cross-section. By implementing a coupled electro-thermal simulation at steady-state, we can estimate the thermal response to increasing bias voltage and injected current. We use a two-dimensional finite-element mesh window, with Neumann boundary conditions applied to all simulation boundaries, except for the bottom border. At this boundary, we apply the DC voltage V_p, while the top contact (Layer 2 of Fig. 1) is grounded. We also enforce a constant temperature of 300 K at the bottom boundary, acting as a heat sink implying efficient heat dissipation. Given the similarity between both optimized structures and their expected similar electro-thermal responses, we only investigate Structure 2. The electrical and thermal parameters of the materials used in the simulation are taken from [14], [15], [26], [27].

Fig. 6(a) illustrates the current density *vs*. voltage curve (J-V), where the current flows from the p region to the n region, passing through the intrinsic active layer. The J-V curve shows a turn-on bias voltage of around 1.7 V. Fig. 6(b) shows the hole density distribution over the simulation window at $V_p = 2.5$ V. As shown, the carrier density is laterally distributed in the active layer, indicating lateral leakage current. This occurs because there is no potential barrier in the lateral direction, allowing carriers to transport across the device. Given that the optical mode is confined solely under the ridge, this leakage suggests that only a small portion of the generated current contributes to modal gain. A conventional solution to create lateral carrier confinement is to etch a mesa into the active region [28]. However, this approach entails a more complex fabrication process and necessitates the passivation of the aluminum-based QWs to prevent exposure to air and subsequent oxidation. In this paper, we prioritize an etch-free III-V stack, and therefore avoid using a mesa in our modeling.

The current in the diode increases because of the rising carrier density in the QWs. This increase also leads to a higher built-in electric field and elevated temperature due to recombination heat and Ohmic losses. Fig. 7(a) illustrates the temperature distribution over the diode cross-section at $J = 3$ A/mm. The maximum temperature rise is observed at sharp corners of the top metal contact due to significant electric field in those regions. Moving away from the ridge in the *x*-direction, the electric field, and consequently the temperature, decrease. The temperature drops faster in the *-z* direction, because of the bottom boundary condition. The optical mode is confined under the ridge, where it interacts with the material gain. Therefore, the temperature rise in that region needs to be considered when calculating the gain, which will be discussed in the next sub-section. Fig. 7(b) shows the average temperature under the ridge T and the average QW carrier density N_{QW} as a function of current density.

Fig. 7(b) exhibits a linear rise of temperature with current density, and a logarithmic variation of N_{QW} with J. The latter is because as current increases, the number of injected carriers increases, but the rate of increase in carrier density gradually slows down due to factors like carrier recombination. At the transparency carrier density N_{tr}, the gain of the semiconductor material equals the optical losses. This is typically where the carrier density starts to approach saturation. From the curve, we can estimate the N_{tr} to be around 3×10^{18} cm^{-3}.

C. MQW Gain

Near-infrared diode lasers typically operate in the TE polarization due to the higher achievable gain in III-V semiconductor compounds for this polarization. However, the active region in

our model features an InP-based laser diode with high TM gain, essential for lasing in the targeted hybrid TM mode. Previous research indicates that tensile-strained AlGaInAs quantum wells yield greater TM gain compared to TE [29], [30]. Therefore, we have designed our active layer utilizing tensile-strained AlGaInAs MQWs.

AlGaInAs compounds exhibit optical gain within the O-band and are commonly used in laser diodes with emission wavelengths around 1300 nm, hence our laser is designed to operate near this wavelength. To select the appropriate composition for wells and barriers, it is essential to consider wells with high tensile strains to achieve higher TM gain. For a stable MQW structure, the strain in the wells and barriers should approximately balance each other. It is established that the product of the strain and thickness of the well should approximately equal the product of the strain and thickness of the barrier [31], assuming the wells are under tensile strain and the barriers are under compressive strain.

Another criterion is the tuning range of the peak gain wavelength. The peak of the gain spectrum can blueshift or redshift as a function of carrier density in the QWs. This shift is influenced by the band filling effect and bandgap shrinkage. We aim to achieve a high tuning range to ensure that our laser's wavelength is sensitive to the injected current. We have extensively discussed the material selection process for the MQW in previous work [32]. Here we adopt the same material composition, i.e., $Al_{0.04}Ga_{0.58}In_{0.38}As$ for wells and $Al_{0.42}In_{0.58}As$ for barriers. After extensive numerical modeling, we use 14 tensile-strained wells and 15 compressive-strained barriers, with thicknesses of 6 and 18 nm, respectively, to maximize the material TM gain and have a high peak gain shift as a function of injected carrier density.

Based on the data plotted in Fig. 7(b), we proceed to calculate the material gain of our system considering self-heating effects. Fig. 8 illustrates the TM and TE material gain of the active region as a function of wavelength for various average carrier densities within the MQW region. This computation assumes a zero-carrier density within the barriers and includes a thermal bandgap reduction of 0.334 meV/K [33] within the wells and barriers. The findings indicate a notably higher TM material gain in this system. The dashed curve in Fig. 8(a) traces the gain peak as a function of carrier density. Band filling increases linearly with carrier density, while bandgap shrinkage follows a cube root relationship [17]. Therefore, at low densities, band filling dominates, causing a blue shift. At higher densities, band gap shrinkage and temperature rise effects cause a red shift.

IV. Sensitivity

In this section, we examine our optimized structures, focusing on the sensitivity of the dominant mode and its impact on various laser characteristics. We theoretically evaluate three specific characteristics of the laser, demonstrating the extent to which each characteristic varies with n_c.

A. Laser Wavelength

To calculate the laser's wavelength as a function of n_c, we start by finding the threshold gain required for compensating all losses within the laser. The threshold gain g_{th} is:

$$g_{th}\Gamma = \alpha_{\text{mirror}} + \alpha_{\text{mode}} \tag{6}$$

where α_{mirror} is the loss from facets of the cavity:

$$\alpha_{\text{mirror}} = \frac{1}{L}\ln\frac{1}{R} \tag{7}$$

in which R is the reflectance of the facets. We consider that the facets are cleaved and exposed to air, therefore the effect of n_c on R is negligible. Using (5b), we rewrite (6) in terms of n_c:

$$g_{th} = \frac{1}{\Gamma L}\ln\frac{1}{R} + 2\frac{2\pi}{\Gamma\lambda_0}(\sigma n_c + d) \tag{8}$$

From Fig. 8(a), we identify the peak of the gain curves as a function of wavelength λ_{peak}. The gain peak is taken as the threshold gain g_{th}, and the dependence of g_{th} on λ_{peak} is fit as:

$$\lambda_{peak} = \zeta_1 {g_{th}}^3 + \zeta_2 {g_{th}}^2 + \zeta_3 g_{th} + \zeta_4 \tag{9}$$

where $\zeta_1 = -1.5833 \times 10^{-25}$ m^4, $\zeta_2 = 2.4093 \times 10^{-19}$ m^3, $\zeta_3 = -9.4626 \times 10^{-14}$ m^2, $\zeta_4 = 1.286 \times 10^{-6}$ m, and g_{th} is defined by (8). The lasing wavelength λ_{laser} corresponds to the cavity mode closest to λ_{peak}. We can find the cavity mode number m using:

$$m = \text{round}\left\lfloor\frac{2n_{\text{eff}}L}{\lambda_{\text{peak}}}\right\rfloor \tag{10}$$

in which m is an integer, L is the length of the cavity, and n_{eff} is given by (5a). Finally, one can write the laser's wavelength λ_{laser} using (6) to (10):

$$\lambda_{\text{laser}} = \frac{2n_{\text{eff}}L}{m} \tag{11}$$

Fig. 9(a) shows λ_{laser} as a function of n_c for a 1 mm long laser cavity based on the optimized structures, with n_c ranging

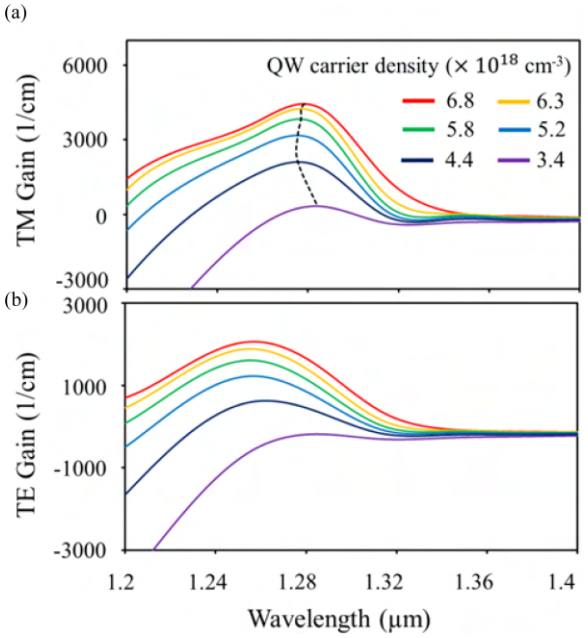

Fig. 8. (a) TM and (b) TE material gain spectra for various QW carrier densities. The dashed curve in (a) follows the gain peak.

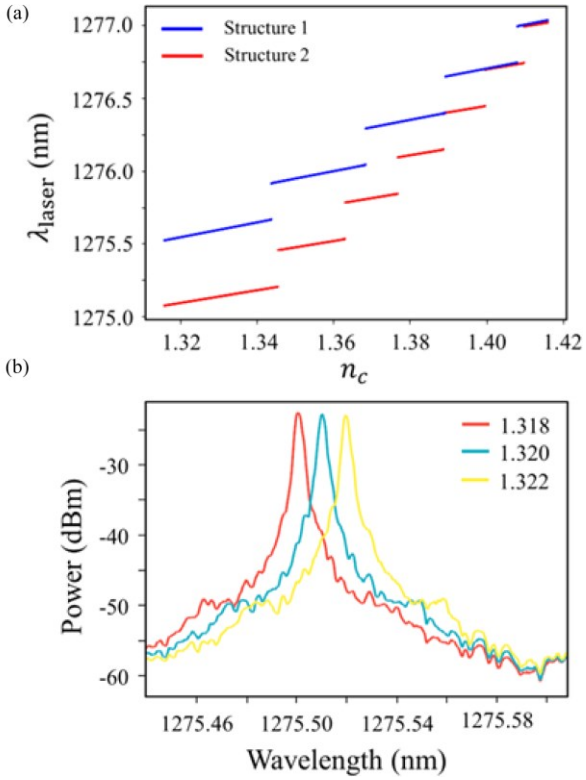

Fig. 9. (a) Laser wavelength as a function of n_c for the optimized structures. (b) Simulated lasing spectra of Structure 1 (1 mm long) with a driving current of 700 mA for different values of n_c.

from 1.316 to 1.416. Two types of wavelength dependence on n_c can be observed. The first is continuous tuning, which occurs when the lasing cavity mode shifts slightly with changes in n_c. The second is mode hopping, which is observed when the change in n_c is large enough that the cavity mode closest to the peak wavelength, changes. The slope of each line represents the sensitivity of lasing wavelength ΔS_λ to the change in n_c. As shown in Fig. 9(a), the slope is steeper during mode hopping. In practice, changes in n_c are typically small, and for a 1 mm long laser, mode hopping should not occur. If the laser cavity is long enough, mode hopping can become predominant, resulting in higher sensitivity. However, longer lasers significantly increase the threshold current and cost. Therefore, we evaluate the sensitivity based on the slope associated with a unique lasing mode for 1-mm-long lasers based on Structures 1 and 2, yielding ΔS_λ of 5.09 and 4.36 nm/RIU, respectively.

Fig. 9(b) shows the spectra of laser Structure 1 at a bias current of 700 mA for three different values of n_c, calculated using Lumerical's Interconnect. The lasing wavelength shift is evident for a 2×10^{-3} RIU change in n_c.

An important parameter to evaluate a wavelength-interrogated biosensor, is its Figure of Merit (FOM), which can be calculated from the ratio of the sensitivity to the full width at half maximum (FWHM) of the lasing peak:

$$\text{FOM} = \frac{\Delta S_\lambda}{\text{FWHM}} \tag{12}$$

in which the FWHM can be calculated using the Schawlow-Townes estimation [34]:

$$\text{FWHM} = \frac{\pi h \upsilon (\delta\upsilon)^2}{P_{out}} \tag{13}$$

where h is Planck's constant, υ is the resonant frequency, $\delta\upsilon$ is the cavity resonator's FWHM, which is related to the photon lifetime τ_p, and therefore the loss of the cavity, by:

$$\delta\upsilon = \frac{1}{2\pi\tau_p} = \frac{v_g(\alpha_{\text{mirror}} + \alpha_{\text{mode}})}{2\pi} \tag{14}$$

v_g in the above is the group velocity, which can be obtained via dispersive modal analysis. P_{out} in (13) is the optical output power. To estimate the FOM, we calculate P_{out} at 100 mA above threshold (as discussed in Section IV-C relative to (17)).

For a 1 mm long Structure 1, the FWHM is ~11 pm, calculated using Eqs. 12-14. Such a narrow peak demonstrates a high potential for accurate sensing. The resulting FOM is ~450 RIU^{-1}, which is comparable to the performance of other biosensors [35], [36].

The sensitivity ΔS_λ does not depend on cavity length because the mode number m increases with length, which keeps the L/m ratio in (11) nearly constant. However, the FOM increases for shorter cavity lengths. For instance, the FOM for lengths of 0.5 and 2 mm are ~850 and 250 RIU^{-1}, respectively, for Structure 1. In comparison, Structure 2 exhibits FOM values of ~1300 and 370 RIU^{-1} for the same lengths. Consequently, shorter lasers demonstrate superior performance as biosensors when using wavelength interrogation.

B. Threshold Current

We observed that the imaginary part of effective index, and consequently the mode loss, is significantly affected by the change in n_c. Therefore, the g_{th} is influenced by change in n_c, as shown in (8). One of the measurable characteristics of a laser which is directly related to g_{th}, is the threshold current I_{th}. In this sub-section, we investigate the dependence of I_{th} on n_c. We first estimate the threshold carrier density N_{th} [37]:

$$N_{th} = \frac{g_{th}}{a_0} + N_{tr} \tag{15}$$

in which N_{tr} is the transparency carrier density and a_0 is a fitting parameter. These parameters can be extracted from Fig. 8(a). I_{th} is given as [37]:

$$I_{th} = \left(AN_{th} + BN_{th}^2 + CN_{th}^3\right)\frac{q}{\eta_i} \cdot w \cdot t_{QW} \cdot L \tag{16}$$

where t_{QW} is the thickness of the QWs and η_i is the injected current efficiency. A, B and C represent the coefficients corresponding to nonradiative Shockley-Read-Hall (SRH), radiative bimolecular, and nonradiative Auger processes, respectively. The primary nonradiative recombination mechanism is Auger recombination. During this process, the excess energy from an electron-hole recombination is transferred to a third carrier. The rate of Auger recombination rises with increasing carrier concentrations due to the energy exchange between charge carriers. The Auger coefficient C is set to 10^{-42} $\text{m}^6 \cdot \text{s}^{-1}$, which

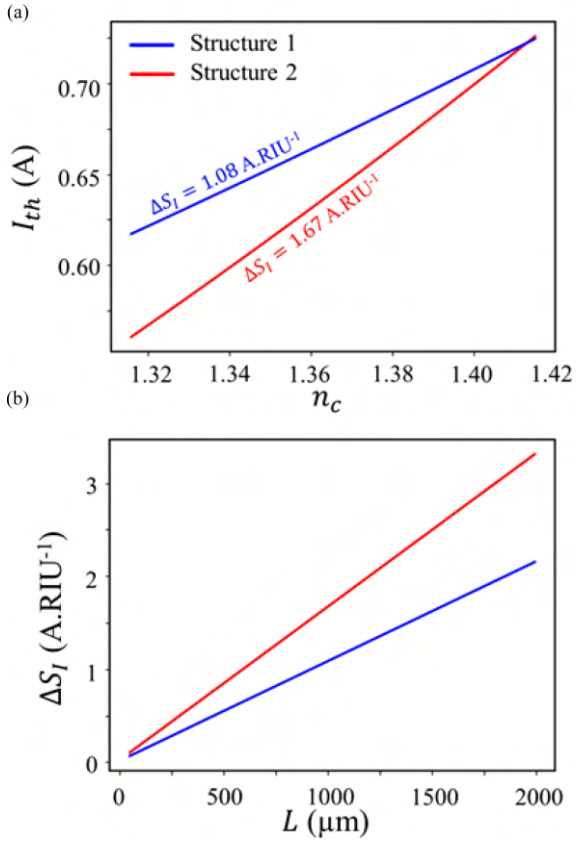

Fig. 10. (a) Threshold current as a function of n_c for the optimized structures (1 mm long). (b) Sensitivity ΔS_I as a function of length for the optimized structures.

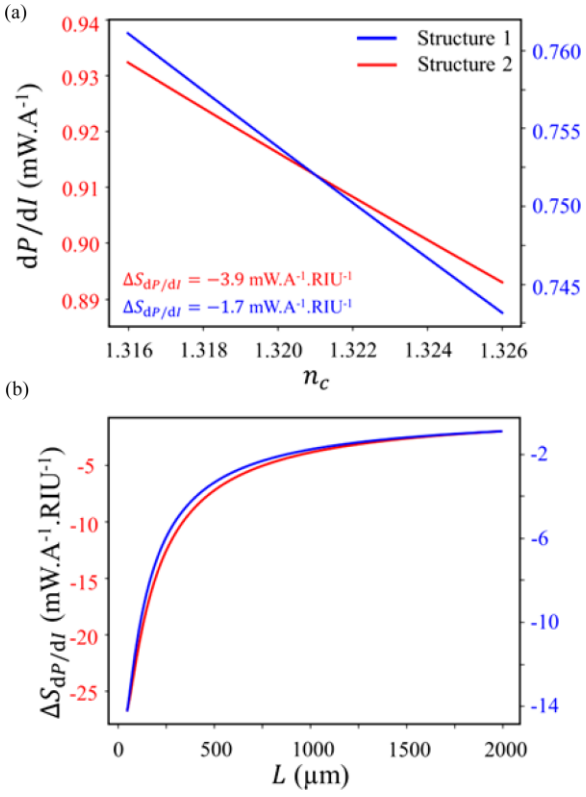

Fig. 11. (a) Slope efficiency as a function of n_c for the optimized structures (1 mm long). (b) Sensitivity $\Delta S_{dP/dI}$ as a function of length for the Structures 1 and 2 (blue and red curves, respectively).

is consistent with similar gain materials [33], [38]. The non-radiative SRH coefficient A is set to 10^8 s^{-1} [39], [40]. The radiative recombination rate B is primarily determined by the spontaneous recombination rate, which is derived by integrating the spontaneous emission spectrum, and set to 5×10^{-17} m^3 s^{-1}.

Our simulations in Section III-B and Fig. 6(b) show that η_i is about 5%. This value is estimated from ratio of the current passing through the optical mode area to the total current flowing between the contacts. The weak carrier confinement, surprisingly, works in favor of the sensitivity of I_{th} to n_c, as they are inversely proportional. A laser with high η_i (~100%) will be 20 times less sensitive to n_c than ours of η_i ~ 5%.

Fig. 10(a) shows I_{th} as a function of n_c for a 1 mm long laser for the optimized structures. The slope of these curves (ΔS_I) represents the sensitivity of I_{th} to n_c, as labeled on the curves. Fig. 10(b) shows ΔS_I as a function of L. It is apparent that increasing L works in favor of ΔS_I, but requires a higher injected current. For a 1 mm long laser, I_{th} is around 600 mA. From Fig. 6(a), we can see that such a current can be achieved by applying voltage bias of ~3 V.

C. Slope Efficiency

Another important characteristic of a laser is its output power P_{out}, i.e., the optical power emitted through one facet of the laser cavity, assuming both facets have identical reflectivity. For currents above threshold, P_{out} can be described by

$$P_{out} = \eta_o \eta_i \frac{h\nu}{q} (I - I_{th}) \cdot 0.5 \tag{17}$$

where I is the bias current. The output coupling efficiency η_o is the fraction of photons leaving the cavity from the end facets:

$$\eta_o = \frac{\alpha_{mirror}}{\alpha_{mirror} + \alpha_{mode}} \tag{18}$$

The slope efficiency above threshold, dP/dI, using (17), is:

$$\frac{dP}{dI} = \eta_o \eta_i \frac{h\nu}{2q} \tag{19}$$

Fig. 11(a) shows the slope efficiency as a function of n_c for a 1 mm long laser for the optimized structures. The sensitivity $\Delta S_{dP/dI}$ is the slope of dP/dI, indicated at the bottom. Fig. 11(b) shows $\Delta S_{dP/dI}$ as a function of length. The sensitivity decreases as the laser lengthens. This is because the mirror loss approaches zero exponentially with increasing cavity length, as indicated by (7). Consequently, $d\eta_o/dn_c$ decreases, leading to a corresponding reduction in $\Delta S_{dP/dI}$.

This interrogation scheme would require inexpensive interrogation optics and electronics. A straightforward method to experimentally monitor the slope efficiency is to superimpose an AC modulation onto the DC bias current driving the laser and monitor the corresponding amplitude modulation. The output

power, using the Taylor expansion around the operating current I_{DC}, can be described by:

$$P_{\text{out}}(I) = P_{\text{out}}(I_{DC}) + \frac{dP}{dI}\Big|_{I=I_{dc}} (I_{AC}\sin\omega t) \quad (20)$$

where I_{AC} is the amplitude of the AC current. This relationship indicates that the amplitude of the AC component of the power-current relation is directly proportional to the slope efficiency, making this interrogation method straightforward to implement.

V. Limit of Detection

So far, we have evaluated three distinct biosensing schemes. A direct comparison of these schemes would be complicated due to differences in read-out mechanisms and units of measurement. A parameter commonly used to assess the performance of sensor schemes across technologies is the smallest detectable change in n_c under ideal experimental conditions, known as the Limit of Detection (LoD), expressed in RIU.

The detection of changes in n_c is fundamentally constrained by the relative magnitude of the noise compared to the change in signal. In an experimental setup, noise can arise from multiple sources such as measurement equipment, physical or chemical phenomena within the sensor, and environmental perturbations. Here we estimate different noise contributions and incorporate it into LoD calculations. However, it is emphasized that while theoretical estimates provide valuable insight, they must eventually be validated experimentally. We define the LoD as [41], [42]:

$$\text{LoD} = \frac{2\sigma}{\Delta S} \quad (21)$$

in which σ is the noise and ΔS the signal modulation as discussed in the previous section.

One established approach to account for different sources of noise involves Langevin methods, which essentially reduce the problem to evaluating the spectral density of the fluctuating variable. Langevin methods use differential equations to model random fluctuations and determine the spectral density of the noise. These methods are extensively discussed in literature, e.g., in [43], and we adopt the same approach to determine the influence of noise on the LoD for different sensing schemes discussed in the previous section.

A. Laser Wavelength

When considering a wavelength-interrogated biosensor, as discussed in Section IV-A, a spectrometer or an Optical Spectrum Analyzer (OSA) is employed to extract the wavelength spectrum of the laser. For the latter, the limiting factor is the minimum wavelength step that the OSA can measure, i.e., its resolution. A typical resolution of an OSA is approximately $\sigma_{\lambda,\text{Res}} = 2.2$ pm [44], [45].

It is also important to account for the noise arising from the laser's internal sources. A primary source of such noise is the resonance wavelength drift $\sigma_{\lambda,T}$ induced by temperature fluctuations δT. This effect can be described by [46]:

$$\sigma_{\lambda,T} = \frac{\lambda}{n_g}\cdot\sqrt{n_{\text{eff}}.\alpha_{\text{sub}} + \frac{dn_{\text{eff}}}{dT}}\cdot\delta T \quad (22)$$

where λ is the resonant wavelength and n_g is the group index of the waveguide. The thermal expansion coefficient of the substrate material, denoted as α_{sub}, is $5\times10^{-6}\,\text{K}^{-1}$ [47]. Given that the thickness of the other layers is negligible in comparison to that of the substrate, their contributions to thermal expansion are disregarded. We assume that the thermo-optic coefficient (TOC) of the III-V compound materials used in our system is $\sim10^{-4}\ \text{K}^{-1}$ [48]. The TOC of tin oxide films is lower, in the range of $10^{-5}\ \text{K}^{-1}$ [49], which we assumed for our ITO layer in simulations. For gold, the TOC is taken as $5\times10^{-4}\,\text{K}^{-1}$ and $1\times10^{-3}\,\text{K}^{-1}$ for the real and imaginary parts of its refractive index, respectively [50]. Using these parameters, we calculated $(dn_{\text{eff}})/dT$ by mode-solving and considered these values in our noise estimation.

A typical temperature fluctuation δT of $\pm$ 0.02 K is common for semiconductor lasers when using a thermoelectric cooler [51]. Substituting this value in (22), it yields $\sigma_{\lambda,T} = 0.8$ pm of instability in the lasing wavelength for both Structures 1 and 2 due to thermal fluctuations.

Other noise sources produce a negligible contribution to instability of the laser's wavelength, and mainly impact the diode's current and output optical power. These sources will be addressed later in this section. Upon comparing $\sigma_{\lambda,T}$ and $\sigma_{\lambda,\text{Res}}$, it is evident that $\sigma_{\lambda,\text{Res}}$ is predominant, and consequently, it should be incorporated into the LoD calculation as described by (21). This consideration yields LoD values of 3.1×10^{-4} and 3.6×10^{-4} RIU for Structures 1 and 2, respectively. However, measurement methods like heterodyne and self-heterodyne techniques, as well as fitting approaches, can be utilized to improve resolution [52], [53], [54], and thus, sensitivity. In Section IV-A, we demonstrated that the signal ΔS_λ is independent of the laser's length. Additionally, the laser length has a negligible effect on wavelength drift characteristics. As a result, the LoD of the optimized structures remains constant regardless of the laser's length.

B. Threshold Current

Fluctuations in the drive current supplied to the laser diode can introduce noise. According to the datasheet of a standard source meter, e.g., [55], for a current of 1 A, the peak-to-peak noise current is $\sim$25 μA. Therefore, the corresponding root-mean-square (RMS) noise current, $\sigma_{I,\text{source}}$, is $\sim$8.8 μA.

We also examine two other sources of noise: shot noise and thermal noise.

Shot noise is important in lasers and photodiodes, arising from the inherent randomness of photon – electron hole pair conversions, which occur at discrete times. This type of noise becomes significant at large injected currents, which is relevant in our case. The RMS shot noise current generated by discrete random generation events is given by [43]:

$$\sigma_{I,q} = \sqrt{2eI\Delta f} \quad (23)$$

where Δf is the detection bandwidth. Typically, a bandpass filter is used to limit the range of measured frequencies, and therefore noise. A multimeter is typically used for measuring DC current, which has a narrow bandwidth of approximately 10 Hz [55]. For

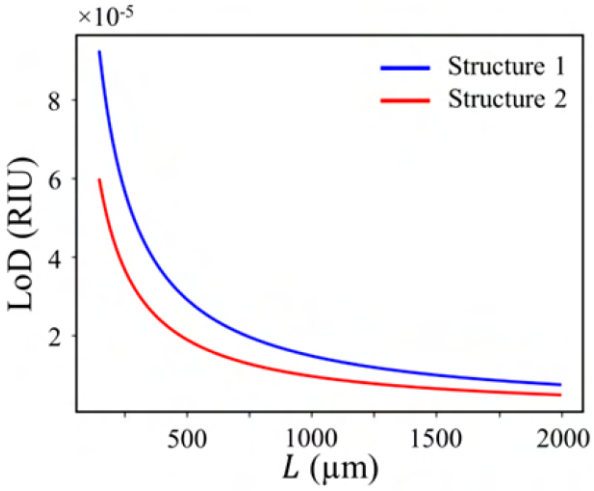

Fig. 12. LoD as a function of laser cavity length for the optimized structures, based on the sensitivity of the threshold current to n_c.

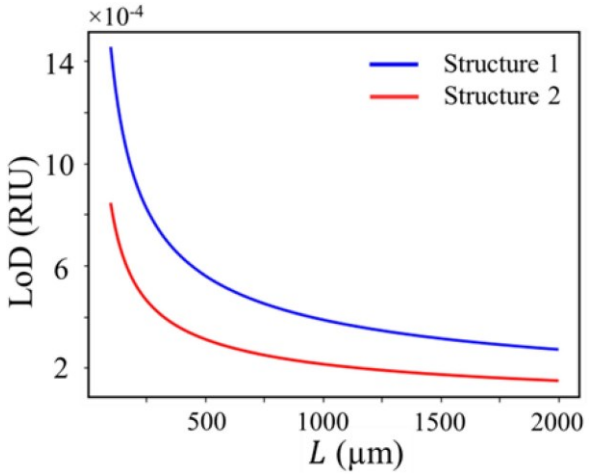

Fig. 13. LoD as a function of laser cavity length of the optimized structures, based on the sensitivity of the slope efficiency to n_c.

a 1 mm long laser, as in Section IV-B, the bias current is ~0.8 A, which leads to shot noise of ~2 nA.

The random thermal motion of the carriers within the device, including the junction region and Ohmic contacts, give rise to a noise current. We model their aggregate effects as a noisy resistance R_s. This resistance can be determined from the slope of the VJ curve shown in Fig. 6(a), and through electrical simulations across the ohmic contacts at the interfaces of layers 8/9 and 2/3, as depicted in Fig. 1. The spectral density of the thermal noise current is given in [56], from which the RMS value is calculated as follows:

$$\sigma_{I,T} = \sqrt{\frac{2h\upsilon}{R_s}\coth\frac{h\upsilon}{2k_B T}\Delta f} \tag{24}$$

where, k_B is the Boltzmann constant, and T is the temperature at the bias current, shown in Fig. 7(b). For a 1 mm long laser and a Δf of 10 Hz, $\sigma_{I,T}$ is ~3 nA. Comparing the noise current sources, $\sigma_{I,\text{source}}$ dominates and should be considered in LoD calculations. Using (21) and the ΔS values derived in Fig. 10(b), we determine the LoD for different laser lengths, as shown in Fig. 12. In general, the LoD is in the range of 10^{-5} RIU, and decreases with length.

C. Slope Efficiency

Random carrier recombination and photon generation produce instantaneous fluctuations in photon density. These fluctuations lead to variations in the output power, i.e., intensity noise ($\sigma_{P,IN}$), described by:

$$\sigma_{P,IN} = \sqrt{2S_{\delta P}(\omega)\Delta f} \tag{25}$$

The detection bandwidth of a typical filter in the O-band is $\Delta f \approx 200$ GHz [57]. The spectral density of the output power $S_{\delta P}(\omega)$ above threshold is given by [43]:

$$S_{\delta P}(\omega) = h\upsilon P_o\left[\frac{a_1 + a_2\omega^2}{\omega_R{}^4}|H(\omega)|^2 + 1\right] \tag{26}$$

in which P_o is the power output from the laser's facet, and

$$a_1 = \frac{8\pi\Delta\upsilon P_o}{h\upsilon\tau_{\Delta N}{}^2} + \eta_o\omega_R{}^4\left[\frac{I + I_{th}}{I - I_{th}} - 1\right] \tag{27a}$$

$$a_2 = \frac{8\pi\Delta\upsilon P_o}{h\upsilon} - 2\eta_o\omega_R{}^2\frac{\Gamma a_p}{a_N} \tag{27b}$$

where a_N and a_p represent the derivative of the material gain with respect to the carrier and photon densities, respectively. $\tau_{\Delta N}$ is the differential carrier lifetime, $\Delta\upsilon$ is twice the FWHM defined by (13), η_o is given by (18), and $H(\omega)$ is the modulation transfer function:

$$H(\omega) = \frac{\omega_R{}^2}{\omega_R{}^2 - \omega^2 + j\omega\gamma} \tag{28}$$

where γ is the damping factor, $\omega_R = \sqrt{\Gamma v_g a_N \eta_i (I - I_{th})/qV}$ is the relaxation resonance frequency, and V denotes the volume of the active region. The parameters required to estimate $\sigma_{P,IN}$ are derived partly from our calculations presented earlier in the paper and partly from [43]. For a 1 mm long laser and at bias current of 100 mA above I_{th}, $\sigma_{P,IN} \sim 2.2\,\mu$W is approximately the same for both optimized structures. This noise is significantly higher than the noise of a typical optical power meter (e.g., 100 pW from [58]), and should be considered in LoD calculations.

To estimate the noise of the slope efficiency (in W/A) we must combine noise contributions from output optical power and the bias current, as both contribute to the noise of the slope efficiency. We assume that the optical power and bias current noise sources are uncorrelated and combine these sources using the error propagation formula [59]:

$$\sigma_{dP/dI} = \sqrt{\left(\frac{\sigma_{P,IN}}{I}\right)^2 + \left(\frac{P_o\sigma_{I,T}}{I^2}\right)^2} \tag{29}$$

For a 1 mm long laser operating just above the threshold, $\sigma_{dP/dI}$ is ~0.4 μW/A for both optimized structures. This results in LoDs of 3.8×10^{-4} for Structure 1 and 2.1×10^{-4} RIU for

Structure 2. Fig. 13 shows the LoD as a function of laser cavity length for the optimized structures, using the slope efficiency as the sensing parameter.

VI. Conclusion

In summary, we proposed and investigated a novel electrically driven Fabry-Perot biosensor laser operating in a plasmonic-dielectric hybrid mode, with compelling sensing characteristics. The laser uses an InP-based semiconductor gain medium to overcome losses induced by plasmonic absorption. Through optimization of the waveguide geometry, we achieve maximal perturbation in both the real and imaginary parts of the mode effective index in response to changes in sensing medium (n_c), thereby enhancing the laser's sensitivity. We analyzed the laser's characteristics in optimized geometries, focusing primarily on their suitability for biosensing applications. Potential noise sources were evaluated and utilized to estimate the limit of detection of three different sensing schemes, namely monitoring the emission wavelength, the threshold current and the slope efficiency. Our findings indicate that tracking the threshold current yields the most promising results for biosensing applications. This study highlights the potential of using simple etch-free III-V Fabry-Perot lasers for high-performance biochemical sensing.

References

[1] J. Homola, *Surface Plasmon Resonance Based Sensors*. Berlin, Germany: Springer, 2006.
[2] H. H. Nguyen et al., "Surface plasmon resonance: A versatile technique for biosensor applications," *Sensors*, vol. 15, no. 5, pp. 10481–10510, May 2015.
[3] X. Yang et al., "Optical property and adsorption isotherm models of glucose sensitive membrane based on prism SPR sensor," *Sens. Actuators. B Chem.*, vol. 237, pp. 150–158, Dec. 2016.
[4] L. Liu, Z. Han, and S. He, "Novel surface plasmon waveguide for high integration," *Opt. Exp.*, vol. 13, no. 17, pp. 6645–6650, Aug. 2005.
[5] A. Khan et al., "Mach-Zehnder refractometric sensor using long-range surface plasmon waveguides," *Appl. Phys. Lett.*, vol. 103, no. 11, Sep. 2013, Art. no. 111108.
[6] M. Khodami et al., "Fabrication of Bloch long range surface plasmon waveguides integrating counter electrodes and microfluidic channels for multimodal biosensing," *J. Microelectromech. Syst.*, vol. 30, no. 5, pp. 686–695, Jul. 2021.
[7] Z. Hirbodvash et al., "Infrared surface plasmons on a Au waveguide electrode open new redox channels associated with the transfer of energetic carriers," *Sci. Adv.*, vol. 8, no. 20, May 2022, Art. no. eabm9303.
[8] E. K. Keshmarzi, R. N. Tair, and P. Berini, "Single-mode surface plasmon distributed feedback lasers," *Nanoscale*, vol. 10, no. 13, pp. 5914–5922, 2018.
[9] P. Berini, "Figures of merit for surface plasmon waveguides," *Opt. Exp.*, vol. 14, no. 26, pp. 13030–13042, 2006.
[10] S. Singh et al., "Theoretical analysis of sensitivity enhancement of surface plasmon resonance biosensor with zinc oxide and blue phosphorus/MoS_2 heterostructure," *Optik*, vol. 244, Oct. 2021, Art. no. 167618.
[11] S. Sharma and A. Kumar, "Design of a biosensor for the detection of dengue virus using 1D photonic crystals," *Plasmonics*, vol. 17, no. 2, pp. 675–680, Apr. 2022.
[12] J. Leuermann et al., "Optimizing the limit of detection of waveguide-based interferometric biosensor devices," *Sensors*, vol. 19, no. 17, Aug. 2019, Art. no. 3671.
[13] A. B. González-Guerrero et al., "Trends in photonic lab-on-chip interferometric biosensors for point-of-care diagnostics," *Anal. Methods*, vol. 8, no. 48, pp. 8380–8394, 2016.
[14] D. R. Lide, *CRC Handbook of Chemistry and Physics*, vol. 85, Boca Raton, FL, USA: CRC Press, Jun. 2004.
[15] Asahi Glass Company, "Cytop technical brochure," 2024. [Online]. Available: https://www.agcce.com/cytop-technical-information/
[16] E. D. Palik, *Handbook of Optical Constants of Solids*, vol. 3, New York, NY, USA: Academic, 1998.
[17] J.-P. Weber, "Optimization of the carrier-induced effective index change in InGaAsP waveguides-application to tunable Bragg filters," *IEEE J. Quantum Electron.*, vol. 30, no. 8, pp. 1801–1816, Aug. 1994.
[18] A. V. Ivanov et al., "Refractive indices of solid AlGaInAs solutions," *Quantum Electron.*, vol. 37, no. 6, pp. 545–548, Jun. 2007.
[19] G. K. Shirmanesh et al., "Dual-gated active metasurface at 1550 nm with wide (> 300°) phase tunability," *Nano Lett.*, vol. 18, no. 5, pp. 2957–2963, Mar. 2018.
[20] "Lumerical is now part of the Ansys family," 2025. [Online]. Available: https://www.lumerical.com/
[21] M. Z. Alam, J. S. Aitchison, and M. Mojahedi, "A marriage of convenience: Hybridization of surface plasmon and dielectric waveguide modes," *Laser Photon. Rev.*, vol. 8, no. 3, pp. 394–408, May 2014.
[22] P. Berini and I. D. Leon, "Surface plasmon-polariton amplifiers and lasers," *Nat. Photon.*, vol. 6, pp. 16–24, Jan. 2012.
[23] S. Saeidi et al., "Nonlinear photonics on-a-chip in III–V semiconductors: Quest for promising material candidates," *Appl. Opt.*, vol. 56, no. 19, pp. 5532–5541, Jul. 2017.
[24] K. Dolgaleva et al., "Compact highly-nonlinear AlGaAs waveguides for efficient wavelength conversion," *Opt. Exp.*, vol. 19, no. 13, pp. 12440–12455, Jun. 2011.
[25] D. Costantini et al., "A hybrid plasmonic semiconductor laser," *Appl. Phys. Lett.*, vol. 102, no. 10, Mar. 2013, Art. no. 101106.
[26] S. Adachi, *Physical Properties of III–V Semiconductor Compounds*. Hoboken, NJ, USA: Wiley, 1992.
[27] J. F. Shackelford, *CRC Materials Science and Engineering*. Boca Raton, FL, USA: CRC Press, Dec. 200.
[28] D. Pasquariello, E. S. Bjorlin, D. Lasaosa, Y.-J. Chiu, J. Piprek, and J. E. Bowers, "Selective undercut etching of InGaAs and InGaAsP quantum wells for improved performance of long-wavelength optoelectronic devices," *J. Lightw. Technol.*, vol. 24, no. 3, pp. 1470–1477, Mar. 2006.
[29] J. Decobert et al., "MOVPE growth of AlGaInAs–InP highly tensile-strained MQWs for 1.3 μm low-threshold lasers," *J. Cryst. Growth*, vol. 272, no. 1–4, pp. 543–548, Dec. 2004.
[30] D. Costantini, A. Bousseksou, M. Fevrier, B. Dagens, and R. Colombelli, "Loss and gain measurements of tensile-strained quantum well diode lasers for plasmonic devices at telecom wavelengths," *IEEE J. Quantum Electron.*, vol. 48, no. 1, pp. 73–78, Jan. 2012.
[31] G. Patriarche, A. Ougazzaden, and F. Glas, "Inhibition of thickness variations during growth of InAsP/InGaP and InAsP/InGaAsP multiquantum wells with high compensated strains," *Appl. Phys. Lett.*, vol. 69, no. 15, pp. 2279–2281, Oct. 1996.
[32] S. Saeidi and P. Berini, "Tunable hybrid plasmonic semiconductor laser based on loss perturbation," *IEEE J. Quantum Electron.*, vol. 59, no. 2, Apr. 2023, Art. no. 1100108.
[33] J. Piprek, M. Manish, and V. Jayaraman, "Design and optimization of high-performance 1.3-μm VCSELs," *Phys. Simul. Optoelectron. Devices XII*, vol. 5349, pp. 375–384, Jun. 2004.
[34] A. L. Schawlow and C. H. Townes, "Infrared and optical masers," *Phys. Rev.*, vol. 112, no. 6, Dec. 1958, Art. no. 1940.
[35] A. B. Socorro-Leránoz et al., "Trends in the design of wavelength-based optical fibre biosensors (2008–2018)," *Biosensors Bioelectron., X*, vol. 1, Jun. 2019, Art. no. 100015.
[36] S. Kumar et al., *Optical Fiber-Based Plasmonic Biosensors: Trends, Techniques, and Applications*. Boca Raton, FL, USA: CRC Press, Dec. 2022.
[37] G. P. Agrawal and N. K. Dutta, *Semiconductor Lasers*. New York, NY, USA: Reinhold, 1993.
[38] S. R. Selmic et al., "Design and characterization of 1.3-/spl mu/m AlGaInAs-InP multiple-quantum-well lasers," *IEEE J. Sel. Top. Quantum Electron.*, vol. 7, no. 2, pp. 340–349, Mar./Apr. 2001.
[39] J. Minch et al., "Theory and experiment of InGaAsP and InGaAlAs long-wavelength strained quantum—Well lasers," *IEEE J. Quantum Electron.*, vol. 35, no. 5, pp. 771–782, May 1999.
[40] T. J. Houle et al., "Characterization of the temperature sensitivity of gain and recombination mechanisms in 1.3-/spl mu/m AlGaInAs MQW lasers," *IEEE J. Quantum Electron.*, vol. 41, no. 2, pp. 132–139, Feb. 2005.
[41] X. Zhou, L. Zhang, and W. Pang, "Performance and noise analysis of optical microresonator-based biochemical sensors using intensity detection," *Opt. Exp.*, vol. 24, no. 16, pp. 18197–18208, Aug. 2016.
[42] Í. Molina-Fernández et al., "Fundamental limit of detection of photonic biosensors with coherent phase read-out," *Opt. Exp.*, vol. 27, no. 9, pp. 12616–12629, Apr. 2019.
[43] L. A. Coldren, S. W. Corzine, and M. L. Mashanovitch, *Diode Lasers and Photonic Integrated Circuits*. Hoboken, NJ, USA: Wiley, 2012.

[44] VIAVI Solutions Inc., 2021. [Online]. Available: https://www.viavisolutions.com/en-us/literature/osa-610b-high-resolution-osa-400g-flex-grid-nyquist-dwdm-data-sheets-en.pdf
[45] ProFiber Networking, 2016. [Online]. Available: https://www.profiber.eu/files/produkty/meracia%20technika_opticke_komunikacie/opticke_spektralne_analyzatory_OSA/Yenista_OSA_20_Optical_Spectrum_Analyzer/OSA20_DS_1-5v1-4_A4.pdf
[46] J. Teng et al., "Athermal silicon-on-insulator ring resonators by overlaying a polymer cladding on narrowed waveguides," *Opt. Exp.*, vol. 17, no. 17, pp. 14627–14633, Aug. 2009.
[47] T. Soma, J. Satoh, and H. Matsuo, "Thermal expansion coefficient of GaAs and InP," *Solid State Commun.*, vol. 42, no. 12, pp. 889–892, Jun. 1982.
[48] D. Melati et al., "Wavelength and composition dependence of the thermo-optic coefficient for InGaAsP-based integrated waveguides," *J. Appl. Phys.*, vol. 120, no. 21, Dec. 2016, Art. no. 213102.
[49] D. Ristić et al., "Thermo optical coefficient of tin-oxide films measured by ellipsometry," *J. Appl. Phys.*, vol. 118, no. 21, Dec. 2015, Art. no. 215306.
[50] H. Reddy et al., "Temperature-dependent optical properties of gold thin films," *Opt. Mater. Exp.*, vol. 6, no. 9, pp. 2776–2802, Sep. 2016.
[51] Y. Zhao et al., "High-precision semiconductor laser current drive and temperature control system design," *Sensors*, vol. 22, no. 24, Dec. 2022, Art. no. 9989.
[52] H. Tsuchida, "Simple technique for improving the resolution of the delayed self-heterodyne method," *Opt. Lett.*, vol. 15, no. 11, pp. 640–642, Jun. 1990.
[53] M. A. Tran, D. Huang, and J. E. Bowers, "Tutorial on narrow linewidth tunable semiconductor lasers using Si/III-V heterogeneous integration," *APL Photon.*, vol. 4, no. 11, Nov. 2019.
[54] Z. Zheng et al., "Comparison of different linewidth measuring methods for narrow linewidth laser," *Sensors*, vol. 23, no. 1, pp. 122–132, Dec. 2022.
[55] Tektronix Company, "SourceMeter specifications," 2024. [Online]. Available: https://www.tek.com/en/documents/specification/models-2400-2401-2400-lv-and-2400-c-sourcemeter-specifications
[56] Y. Yamamoto and S. Machida, "High-impedance suppression of pump fluctuation and amplitude squeezing in semiconductor lasers," *Phys. Rev. A.*, vol. 35, no. 12, Jun. 1987, Art. no. 5114.
[57] OZ Optics Ltd., "Bandwidth tunable filter specifications," 2021. [Online]. Available: https://www.ozoptics.com/ALLNEW_PDF/DTS0144.pdf
[58] Keysight Technologies, "Optical power head specifications," 2017. [Online]. Available: https://www.keysight.com/us/en/product/81623B/germanium-optical-power-head.html
[59] J. Tellinghuisen, "Statistical error propagation," *J. Phys. Chem. A.*, vol. 105, no. 15, pp. 3917–3921, Apr. 2001.

Chapter 5

Edge-Emitting LED Refractometer

This chapter was initially intended to present the fabrication and characterization of a biosensing laser, building upon the discussions in the previous chapter. However, due to unforeseen issues during the fabrication process and time constraints within the research timeline, the complete realization of the device was not possible. The validated and completed portions of the fabrication procedure are documented in detail in Appendix A. Consequently, this chapter focuses instead on a different active device designed for refractometric applications, which lays the groundwork for future improvements and potential biosensing implementations.

This chapter presents an article that describes the design and modeling of a light-emitting diode (LED) structure, followed by describing the fabrication process and experimental measurements.

5.1 Contribution Statement

The epitaxial wafer and LED design were carried out by me under the supervision of Prof. Berini. The device fabrication was performed by me together with D. Sekhar and H. Choi (2nd and 3rd authors). Experimental measurements were conducted by me with the assistance of L. Mayoral (4th author), all under the supervision of Dr. Berini. The progress at various stages of the project was regularly discussed with P. Cheben and J. Schmid (5th and 6th authors), who's constructive feedback was very valuable.

5.2 Article

Edge-Emitting LED Refractometer

SHAYAN SAEIDI,[1,2,*] DEEPTHI SEKHAR,[1,2] HYUNG WOO CHOI,[1,2] LUIS A. MAYORAL ASTORGA,[1,2] PAVEL CHEBEN,[3] JENS H. SCHMID,[3] PIERRE BERINI[1,2,4]

[1]*School of Electrical Engineering and Computer Science, University of Ottawa, ON K1N6N5, Canada*
[2]*Nexus for Quantum Technologies Institute, University of Ottawa, ON K1N6N5, Canada*
[3]*National Research Council of Canada, Ottawa, ON K1A 0R6, Canada.*
[4]*Department of Physics, University of Ottawa, ON K1N6N5, Canada*
*ssaei014@uottawa.ca

Received XX Month XXXX; revised XX Month, XXXX; accepted XX Month XXXX; posted XX Month XXXX (Doc. ID XXXXX); published XX Month XXXX

We report a compact light-emitting diode (LED) on InP in edge-emitting configuration for refractometric sensing. The device features a p-i-n structure with active AlGaInAs quantum wells, where the reflectance at the LED facets is influenced by the refractive index of the surrounding fluid. This index-dependent reflectance modulates the output power, enabling refractive index sensing using a standard photodetector operating in the O-band. We developed a theoretical model for the sensor and assessed experimentally the detection limit for two different scenarios, namely using the LI curve slope and the output power as the measurand.

Label-free refractometry has well-established applications in biology, medicine, and the food and beverage industries [1-3]. Refractometric sensors rely on the detection of refractive index changes using light. Typically, such sensors involve a photonic chip, where the output light is monitored for its sensitivity to refractive index variations. Such chips are commonly based on surface plasmons, which are valued for their high sensitivity and strong molecular binding capability [4, 5], or on silicon-on-insulator (SOI) platform, such as Mach–Zehnder interferometers [6-8] and ring resonators [9-11]. Regardless of the platform, these systems typically require an external light source or a spectrometer for detection. In this work, we present a compact, low-cost, and easy-to-fabricate LED-based refractometer that circumvents the need for bulky and expensive optical components.

The proposed LED features a broad cavity with one facet cleaved for light emission and the other modified to form a trench that holds the sensing fluid. Under electrical injection, the output power is influenced by the reflectance of both cavity facets. By monitoring this output power, refractive index variations in the sensing fluid can be detected.

Our device is based on a multilayer p-doped InP substrate incorporating AlGaInAs multiple quantum wells (MQWs), selected for their high material gain and thermal stability [12]. Fig. 1(a) shows a 3D schematic of the epitaxial structure, in which the MQW core is sandwiched between a p-doped lower cladding and an n-doped upper cladding layer. The III–V wafer was grown by metal-organic chemical vapor deposition (MOCVD) [13]. The epitaxial layer structure is summarized in Table 1. For the bottom electrical contact, a palladium/gold (Pd/Au) stack was deposited as palladium forms a reliable ohmic contact with p-type InP (30 nm of Pd deposited by e-beam evaporation, followed by 100 nm of Au by thermal evaporation). The top contact consists of a titanium/gold/titanium (Ti/Au/Ti) trilayer: the bottom Ti layer ensures adhesion and contact to the n-type upper cladding, the Au layer ensures excellent electrical conductivity, and the top Ti layer serves as a hard cap suitable for probing (3 nm of Ti was deposited by electron-beam evaporation for the bottom layer, followed by 100 nm of Au by thermal evaporation, and 50 nm of Ti by electron-beam evaporation). The wafer was then cleaved into individual pieces using an automated wafer cleaver. Three trenches were subsequently fabricated using Zeiss Orion system equipped with focused ion beam (FIB) to electrically and optically isolate the active region from the rest of the sample and to define the LED cavity, with the cleaved facet acting as the optical output interface. The FIB milling was performed under optimized parameters, including an acceleration voltage of 30 kV, a beam current of 300 pA, a dwell time of 1 µs per spot, and a dose of 1 nC/cm^2. The trenches have a depth and width of ~1 µm. Fig. 1(b) shows a top-view SEM image of the edge-emitting LED, highlighting the three isolation trenches and the cleaved front facet. The cavity has a width of 75 µm and a length of 125 µm (facet to facet). These dimensions were chosen to facilitate electrical probing.

Table 1. Layer structure on the InP wafer for the fabricated LED.

Layer	Refractive index at 1300 nm	Thickness (nm)	Doping (cm^{-3})
p-InP Substrate	3.204	-	2×10^{18}
p-$Al_{0.33}Ga_{0.14}In_{0.53}As$	3.35	50	10^{17}
14× $Al_{0.04}Ga_{0.58}In_{0.38}As$	3.57	6	-
15× $Al_{0.41}Ga_{0.02}In_{0.57}As$	3.3	18	-
InP	3.204	7	-
n-$In_{0.9}Ga_{0.1}As_{0.22}P_{0.78}$	3.27	30	2×10^{18}

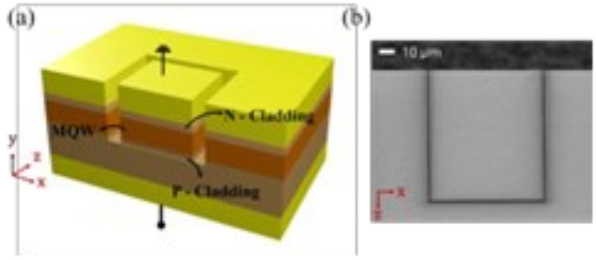

Fig. 1. (a) 3D illustration of the proposed edge-emitting LED. (b) Top-view SEM image of the fabricated device.

Fig. 2(a) shows the refractive index distribution of the device layers (real part only), and Fig. 2(b) shows the simulated fundamental transverse electric (TE) mode, obtained using an in-house finite-difference mode solver (similar to the approach discussed in [14]). Due to the large lateral width, the waveguide supports multiple transverse modes, all with similar effective indices and overlap with the active region (approximately 11%). As a result, the output power represents the combined contribution of all guided modes. The effective index of the fundamental mode in the unbiased (passive) LED structure was calculated to be 3.24 + i·0.00045. This value is later used in our LED model to estimate the facet reflectance and the external quantum efficiency. The non-negligible imaginary component arises from absorption in the top metal stack.

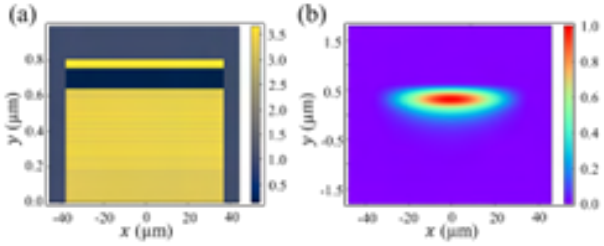

Fig. 2. (a) Refractive index distribution (real part) across the LED cross-section, with the multilayer region corresponding to the MQW active core. (b) Simulated intensity profile of the fundamental TE mode.

The reflection from the back facet is governed by thin-film interference effect, where multiple reflections within the trench lead to constructive or destructive interference depending on the refractive index and thickness of the trench. The facet reflectance, R_2, can be calculated using the transfer matrix method (TMM) [15]. Denoting the refractive index of the medium in the trench as n_{trench}, the facet reflectance for $n_{\text{trench}} = 1$ (air, no fluid) and $n_{\text{trench}} = 1.319$ (corresponding to deionized water [16]) is calculated via the TMM to be $R_2 = 0.66$ and 0.09, respectively, at $\lambda_0 = 1250$ nm, where the material gain is highest.

To characterize the LED, we measured its light-current-voltage (LIV) characteristics, as shown in Fig. 3. The output optical power was monitored using a Ge photodiode sensor with sensitivity in the O-band. A source-meter was used to supply current and record the diode voltage. All measurements were carried out under pulsed operation with the chip mounted on a temperature-controlled stage to minimize heating effects. The device exhibits a turn-on voltage of approximately 0.5 V and a dynamic resistance of 7 Ω at an operating current of 100 mA. The light–current (LI) curves are shown for two cases: for the trench filled with air ($n_{\text{trench}} = 1$) and with deionized (DI) water ($n_{\text{trench}} = 1.319$). For the latter, a droplet of DI water was applied to the device, affecting both facets. The LI measurements were repeated multiple times, and the results were consistent across trials, confirming the reproducibility of the device response. The sensitivity of the LI curve to the surrounding fluid is clearly observed.

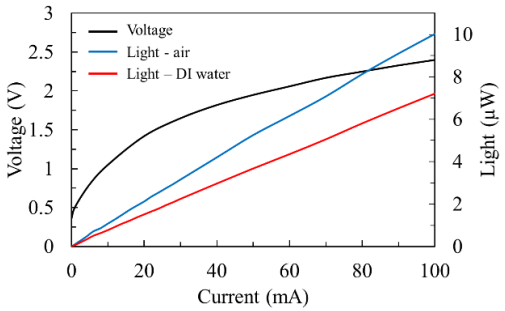

Fig. 3. Measured VI and LI curves for air-covered and DI water-covered facets.

Before analyzing the sensitivity in more detail, we first compare the results with theoretical expectations. The output power of an LED as a function of current increases linearly and is given by [17]:

$$P = \eta_{ex} \frac{h\nu}{q} I \tag{1}$$

where h is Planck's constant, ν is the optical frequency, q is the electron charge, η_{ex} is the external quantum efficiency, and I is the injection current. The external quantum efficiency is the product of three factors:

$$\eta_{ex} = \eta_i \eta_r \eta_o \tag{2}$$

where η_i is the current injection efficiency, η_r is the radiative recombination efficiency, and η_o is the optical out-coupling efficiency. Among these, only η_o depends on the front and back facet reflectances as well as the cavity length. The remaining parameters remain constant regardless of the presence or absence of fluid in the trench. The optical out-coupling efficiency is calculated using:

$$\eta_o = \frac{\alpha_m}{\alpha_m + \alpha_i} \tag{3}$$

where α_i is the internal cavity loss and α_m is the mirror loss. Based on mode simulations, the internal loss α_i is around 50 cm^{-1}. The mirror loss α_m is given by:

$$\alpha_m = \frac{1}{4L} \ln\left(\frac{1}{R_1 R_2}\right) \tag{4}$$

where L is the cavity length (125 μm), and R_1 and R_2 are the front and back facet reflectances, respectively. For the case without fluid, $R_1 = 0.28$ and $R_2 = 0.66$. When deionized (DI) water is present, R_1 and R_2 drop to 0.17 and 0.09, respectively,

based on TMM calculations. The ratio of the slopes in the LI curves is equal to the ratio of the out-coupling efficiencies:

$$\frac{dP/dI_{\text{air}}}{dP/dI_{\text{DI water}}} = \frac{\eta_{o,\text{air}}}{\eta_{o,\text{DI water}}} \approx 1.3 \quad (5)$$

This theoretical value agrees well with the measured slope ratio, which is ~1.3. From the measured LI data, the product $\eta_i \eta_r$ for our material system is determined as 2.5×10^{-4}. Since the term $h\nu/q$ is known, the model can be used to predict the output power and slope for different cavity lengths or surrounding fluids, enabling performance estimates for alternative device designs.

As discussed earlier, two indicators can be used to quantify the sensitivity, one is the slope of the LI curve, and the other is the output power at a specific operating current. For the latter, the power sensitivity increases with higher injection currents, as observed from Fig. 3. However, we limited the current to 100 mA to avoid saturation of the LI curve due to thermal effects. Therefore, 100 mA was chosen as the operating point for reference. Below, we evaluate both of these measurands.

The slope sensitivity, S_{slope}, to the medium's refractive index can be determined from Fig. 3 as:

$$S_{\text{slope}} = \frac{dP/dI_{\text{air}} - dP/dI_{\text{DI water}}}{n_{\text{air}} - n_{\text{DI water}}} \approx 95 \frac{\mu\text{W}}{\text{A RIU}} \quad (6)$$

To assess this value, it is necessary to consider the noise in the system and determine the limit of detection (LoD), which is the smallest detectable change in refractive index for our device. The noise in the slope measurement, σ_{slope}, is estimated by calculating the standard deviation of the power residuals (power deviations from the fitted LI line), normalized by current [18]:

$$\sigma_{\text{slope}} = \sqrt{\frac{\sum (P_i - \hat{P}_i)^2}{(N-2)\sum (I_i - \bar{I})^2}} \quad (7)$$

where P_i is the measured optical power at each current point I_i, $\hat{P}_i$ is the corresponding value on the fitted line, $\bar{I}$ is the average of the current spanning the LI line, and N is the number of data points. Using this method, the slope noise was found to be approximately 0.4 μW/A. The LoD, defined as twice the noise-to-signal ratio, is given by:

$$\text{LoD} = \frac{2\sigma}{S} \quad (8)$$

This yields an LoD of approximately 8×10^{-3} RIU when using the slope as the measurand.

When considering the output power at 100 mA as the measurand, the main contribution to the noise comes from the photodetector. In our setup, the observed noise in the measured power is approximately 0.01 μW. The corresponding power sensitivity S_P is approximately 8.8 μW/RIU. According to Eq. 8, this results in an LoD of approximately 2×10^{-3} RIU, which is four times lower than the slope-based approach. This suggests that using output power as the measurand provides improved sensitivity.

Using the theoretical model with our experimentally measured noise contributions, we evaluated the performance of the same LED structure by varying the cavity length L. Fig. 4 shows the predicted LoD as a function of cavity length, ranging from 30 to 200 μm, for both measurands. A minimum length of 30 μm was chosen to ensure sufficient area for probing using standard needle probes. In this analysis, the noise contributions were assumed constant and independent of cavity length.

The results clearly show that the LoD increases with cavity length, indicating that longer devices degrade sensitivity. Across all lengths, the power measurand consistently outperforms the slope-based one. This suggests that shorter cavities and higher operating currents are favorable for achieving better detection limits. For example, if the device is appropriately cooled, allowing the injection current to increase without thermal saturation (*e.g.*, up to 200 mA) and using a cavity length of 30 μm, the predicted LoD could be reduced to approximately 5×10^{-4} RIU. Furthermore, by employing lower-noise measurement equipment or using bandwidth-limited detection under AC modulation, the LoD can be further decreased, likely by one order of magnitude, improving the overall performance of the refractometric system.

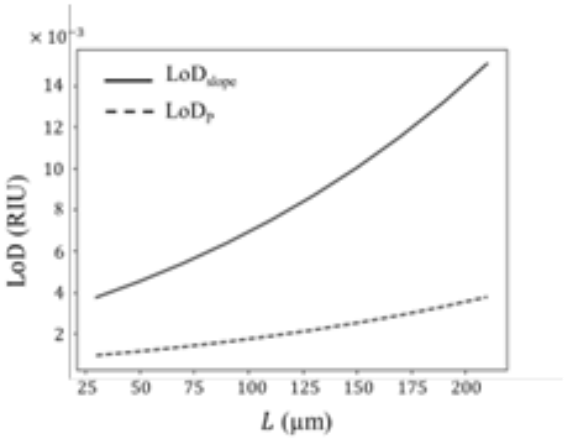

Fig. 4. Modeled LoD when using the LI slope (solid line) or the output power at 100 mA (dashed line) as the measurand.

In conclusion, we proposed, designed and experimentally demonstrated a compact edge-emitting LED for liquid refractometry. The prototype device was fabricated using InP epitaxy, metal deposition and FIB milling, though it can be readily adapted for wafer-scale production using standard photolithography and etching techniques. We assessed experimentally the detection limit of the device and suggested avenues for further improvement through enhancements in the experimental setup and device design.

Funding. National Research Council of Canada under the Quantum Sensors Program (QSP 005).

Acknowledgment. S. Saeidi thanks F. Wu and M. Wehbe for providing access to their wafer cleaver and for assistance with cleaving.

Disclosures. The authors declare no conflicts of interest.

Data availability. Data underlying the results presented in this paper are not publicly available at this time but may be obtained from the authors upon reasonable request.

References

1. R. Chandrasekar, Z. J. Lapin, A. S. Nichols, *et al*., Opt. Eng. **58**(2), "Photonic integrated circuits for Department of Defense-relevant chemical and biological sensing applications: state-of-the-art and future outlooks," 020901-020901 (2019).
2. S. Sun, L. Wu, Z. Geng, *et al*., Laser Photonics Rev. **17**(6), "Refractometric imaging and biodetection empowered by nanophotonics," 2200814 (2023).
3. A. Kovacs, A. Ivanov, U. Mescheder, In IEEE SENSORS, "Refractometer using photonic crystals for fermentation process characterization," 1-4 (2015).
4. A. Khan, O. Krupin, E. Lisicka-Skrzek, P. Berini, Appl. Phys. Lett. **103**(11), "Mach-Zehnder refractometric sensor using long-range surface plasmon waveguides," 111108 (2013).
5. H. H. Nguyen, J. Park, S. Kang, *et al*., Sens. **15**(5), "Surface plasmon resonance: a versatile technique for biosensor applications," 10481-10510 (2015).
6. B. J. Luff, J. S. Wilkinson, J. Piehler, *et al*., J. Lightwave Technol. **16**(4), "Integrated optical mach-zehnder biosensor," 583 (1998).
7. Q. Liu, X. Tu, K. W. Kim, *et al*., Sens. Actuators, B Chem. **188**, "Highly sensitive Mach–Zehnder interferometer biosensor based on silicon nitride slot waveguide," 681-688 (2013).
8. A. Densmore, D. X. Xu, P. Waldron, *et al*., IEEE Photonics Technol. Lett. **18**(23), "A silicon-on-insulator photonic wire based evanescent field sensor," 2520-2522 (2006).
9. T. C. Oates, L. W. Burgess, Anal. Chem. **84**(18), "Sensitive refractive index detection using a broad-band optical ring resonator," 7713-7720 (2012).
10. G. Voronkov, A. Zakoyan, V. Ivanov, *et al*., Sens. **22**(23), "Design and modeling of a fully integrated microring-based photonic sensing system for liquid refractometry," 9553 (2022).
11. S. Janz, D. X. Xu, M. Vachon, *et al*., Opt. Express **21**(4), "Photonic wire biosensor microarray chip and instrumentation with application to serotyping of Escherichia coli isolates," 4623-4637 (2013).
12. S. R. Selmic, T. M. Chou, J. P. Sih, *et al*., IEEE J. Sel. Top. Quantum Electron. **7**(2), "Design and characterization of 1.3 μm AlGaInAs-InP multiple-quantum-well lasers.," 340-349 (2001).
13. LandMark Optoelectronics Corporation, "https://www.lmoc.com.tw/".
14. M. J. Beaubien , and A. Wexler, T-MTT. **16**(12), "An Accurate Finite-Difference Method for Higher Order Waveguide Modes," 1007-1017 (1968).
15. P. Yeh, Wiley Series in Pure and Applied Optics, "Optical Waves in Layered Media," (2005).
16. D. J. Segelstein, Diss. "The complex refractive index of water," University of Missouri - Kansas City, (1981).
17. L. A. Coldren, S. W. Corzine, M. L. Mashanovitch, John Wiley & Sons., "Diode lasers and photonic integrated circuits," (2012).
18. D. C. Montgomery, E. A. Peck, G. G. Vining, John Wiley & Sons., "Introduction to linear regression analysis," (2021).

Chapter 6

Strong and Short Bragg Waveguide Gratings with Trapezoidal-Shaped Grooves

6.1 Contribution Statement

This project was motivated by work conducted at Banyan Photonics Inc. and benefited from technical discussions and input provided by members of the Banyan team, as well as from regular guidance by Prof. Pierre Berini.

The problem formulation and model selection were carried out by me together with Banyan under the direction of F. Wu (second author). Model verification was performed by me and Chris (third author). The optimization, simulations, and conclusions were done by me with continuous feedback from Banyan and Prof. Berini. I also prepared the figures and wrote the initial draft of the manuscript.

6.2 Article

JOURNAL OF LIGHTWAVE TECHNOLOGY, VOL. 39, NO. 13, JULY 1, 2021 4395

Strong and Short Bragg Waveguide Gratings With Trapezoidal-Shaped Grooves

Shayan Saeidi, Fang Wu, Christopher Watson, Yury Logvin, and Pierre Berini, *Fellow, IEEE, Fellow, OSA*

***Abstract*—In this study, we evaluate strong Bragg waveguide gratings formed of trapezoidal-shaped grooves, as typically produced in surface-etched structures, and we propose optimal groove shapes. We begin by validating our modelling approach, which is based on the finite-difference time-domain method, through comparisons with coupled mode theory applied to rectangular gratings. We then compute the reflectance, transmittance and loss of trapezoidal gratings as a function of Bragg order, and of the top and bottom widths of the grooves. Simulations reveal that the highest reflectance peaks are achieved for widths that are about λ/8, regardless of the Bragg order. We find that the characteristics of trapezoidal-grooved gratings are strongly dependent on the bottom width of the grooves, and that a very high reflectance can be achieved by carefully tailoring this width. We also calculate the coupling coefficients of infinitely long optimized structures, finding that they decrease with increasing Bragg order. Our results are of interest in the design of strong short gratings etched in the surface of semiconductor waveguides.**

***Index Terms*—Bragg gratings, finite-difference time-domain, integrated optics, lasers, photonics, semiconductors, waveguide.**

I. Introduction

PHOTONIC integration is the dominant technology for optical networks and high bandwidth communications because of its low cost and high reliability [1],[2]. Indium Phosphide (InP) based photonic integration, offering the capability of monolithic integration with lasers and amplifiers, has consistently attracted significant attention, especially for ultra high speed optical communications. Distributed feedback (DFB) lasers and distributed Bragg-reflector (DBR) lasers, either as edge or as surface emitters, are critical components in optical communications [3]. Diffraction gratings embedded into a slab waveguide, known as Bragg waveguide gratings, form the basis of such lasers by providing the reflection or distributed feedback required to form the cavity that sustains oscillation. A typical fabrication method consists of burying the grating layer into the slab waveguide, which requires the interruption of epitaxial growth to form the grating, then completing the upper layers via epitaxial overgrowth [4].

Alternatively, surface grating lasers are generating interest as they avoid epitaxial overgrowth. In such structures, the grating is formed in the upper layer of the epitaxial system. Typically, such surface-etched gratings provide strong coupling due to the high index contrast between the grating grooves and the upper layer, however radiation loss must be carefully managed. There are two types of structures that are widely used: one type has grating grooves formed along the top of the ridge (surface etched), whereas the second type has grating grooves positioned laterally alongside the ridge (laterally-coupled gratings) [5]–[7]. The latter require a narrow ridge to improve the weak overlap of the fundamental mode with the laterally-coupled grating.

In this paper, we investigate first and higher-order (second and third) surface-etched Bragg waveguide gratings. First-order gratings typically offer the lowest radiation loss and highest reflection, but higher-order gratings are also of interest due to their relaxed fabrication requirements. Specifically, high-resolution lithography processes can be avoided by using higher-order Bragg gratings, due to their larger period [8]. Furthermore, higher-order gratings may be preferable in some applications. For example, the radiation field in second and higher-order gratings is used as a mechanism for mode selection, making them suitable in out-couplers, edge- and surface- emitting lasers [9]–[12].

As the grooves are etched, depending on the etch process, the sidewall angle could be positive, vertical, or negative, as illustrated in Fig. 1(a). To design and optimize the performance of surface-etched gratings, such trapezoidal grooves are typically approximated as rectangular grooves of width equal to the bottom width of the trapezoidal groove [13]. While the effect of groove shape on grating performance has been discussed previously [14]–[18], a systematic study of gratings formed of trapezoidal-shaped grooves is missing from the literature. In this paper, we focus on grating grooves with inward and vertical sidewalls due to their prevalence in manufacturing.

It is not trivial to investigate the effects of groove profile on grating performance as the geometry is complex and radiation loss must be carefully handled. For numerical and analytical simulations of such structures, a variety of modelling approaches based on entirely different principles exist.

Manuscript received December 22, 2020; revised March 9, 2021 and April 9, 2021; accepted April 15, 2021. Date of publication April 19, 2021; date of current version July 2, 2021. *(Corresponding author: Shayan Saeidi).*

Shayan Saeidi is with ArtIC Photonics Inc., Ottawa, ON K2K 2A1, Canada, and also with the School of Electrical Engineering and Computer Science and the Centre for Research in Photonics, University of Ottawa, Ottawa, ON K1N 6N5, Canada (e-mail: shayan.saeidi@articphotonics.com).

Fang Wu, Christopher Watson, and Yury Logvin are with ArtIC Photonics Inc., Ottawa, ON K2K 2A1, Canada (e-mail: fang.wu@articphotonics.com; chris.watson@articphotonics.com; yury.logvin@articphotonics.com).

Pierre Berini is with the School of Electrical Engineering and Computer Science, the Department of Physics, Centre for Research in Photonics, University of Ottawa, Ottawa, ON K1N 6N5, Canada (e-mail: pberini@uottawa.ca).

Color versions of one or more figures in this article are available at https://doi.org/10.1109/JLT.2021.3074137.

Digital Object Identifier 10.1109/JLT.2021.3074137

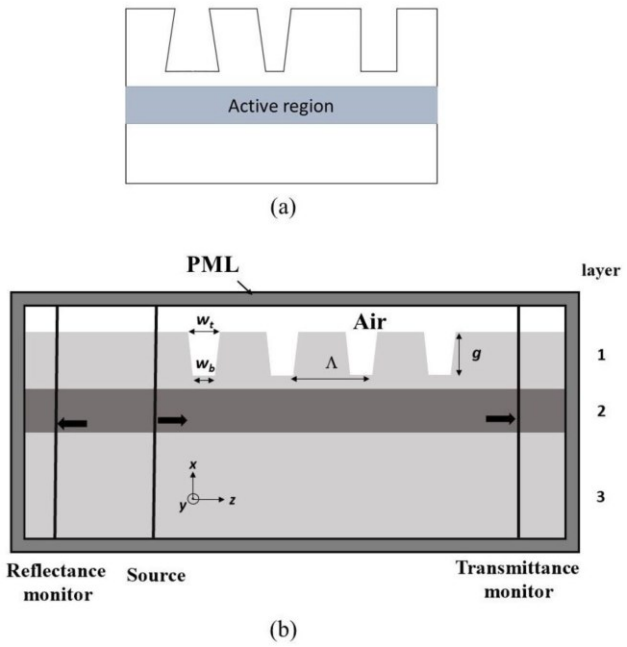

Fig. 1. (a) Schematics of the cross-section of a surface grating with outward, inward-tapered and vertical sidewalls (From left to right). (b) Grating structure and computational model of interest.

One of the well-established and widely-used methods for modeling grating structures relies on coupled mode theory (CMT). In this method, which was initially established by Kogelnik *et al.* [19] then improved by Streifer *et al.* [20], the mode field is expressed as infinite sums of partial waves in Floquet form. The resulting modified coupled-mode equations not only characterize the contra-directional propagating waves interacting with a grating but also describe the radiated waves. In this method, the permittivity perturbation directly dependent on the grating profile is expanded in a Fourier series. Therefore, accurate simulations can be done if sufficiently precise analytical functions describe grating groove profiles.

Other methods are mainly based on the direct solution of Maxwell's equations. Among these, the finite-difference time-domain (FDTD) method is well-known for the calculation of electromagnetic fields in structures of high geometric complexity. Good mutual agreement between the FDTD method and other methods applied to model gratings (*e.g.*, method of lines, bi-directional mode expansion, propagation method) was reported by Čtyroký *et al.* [21].

This paper is organized as follows. In Section II, the FDTD simulation setup and the trapezoidal grating structures of interest are introduced. In Section III, the reliability of our approach is verified by comparing results for rectangular-grooved gratings to those obtained via Streifer's modified CMT. In Section IV, we report results for rectangular-grooved gratings of the first, second and third Bragg orders. Then we consider trapezoidal-grooved gratings of the same orders and optimize their geometry. We complete our study by calculating coupling coefficients for infinitely-long optimized structures. Our results are summarized and conclusion given in Section V.

TABLE I
PROPERTIES OF STUDIED MULTILAYER GRATING STRUCTURE

Layer	Description	Thickness (nm)	Refractive Index
1	Top Cladding	400	3.204
2	QW stack with SC	350	3.33
3	Bottom Cladding	2000	3.204

II. SIMULATION SETUP AND GRATING STRUCTURE

The parametrized grating structure, along with the simulation setup, are sketched in Fig. 1(b). In this figure, W_t and W_b represent the top and bottom widths of each groove, respectively, g denotes the groove depth, and Λ denotes the grating pitch. We only consider real refractive indices, neglecting gain or absorption in the materials, in order to unambiguously account for loss by coupling to radiation modes (scattering). The details of each layer (thickness, refractive index) are given in Table I. Layer 2 represents the active layer which consists of quantum wells (QWs), barriers, and separate confinement (SC) layers.

To reduce the computational effort, we treat the structure as invariant in the y direction, thus simplifying to 2D. We used a commercial implementation of the FDTD method (Lumerical) to carry out the simulations, previously shown to be accurate in modelling similar structures [22]. This FDTD implementation is grid-based and the mesh step size strongly affects accuracy. To save computational time while maintaining good accuracy, a non-uniform mesh was used in the grating region with a minimum step size of 0.2 nm. Perfectly matched layers (PMLs) were used to line dielectric wall boundary conditions terminating the computational domain to minimize reflections.

The fundamental TE mode of the slab waveguide is used as the source and is launched in the z-direction in the input slab waveguide towards the input of the grating. This mode has only one electric field component in the y-direction. To carry out the simulations, a short TE mode pulse (few fs) of corresponding broad frequency content is launched. The time evolution of the fields is calculated at each discrete spatial grid point along with the Fourier transform of the resulting time series. The TE mode reflectance (R) and transmittance (T) of the grating are then computed on the input and output sides, respectively. The reflectance and transmittance monitors are located before the source and after the gratings, so they do not catch any forward and backward propagating waves, respectively. Fig. 1(b) illustrates the location of these ports. Mode expansion at the reflectance and transmittance ports is used to determine reflectance and transmittance specific to the TE mode by taking the overlap integral of the local modal field with the total field distribution calculated by FDTD. The loss of the grating (L) is then obtained as:

$$L = 1 - R - T \tag{1}$$

The Bragg wavelength λ_B is intended to be around 1300 nm. Using:

$$M\lambda_B = 2n_{eff}\Lambda \tag{2}$$

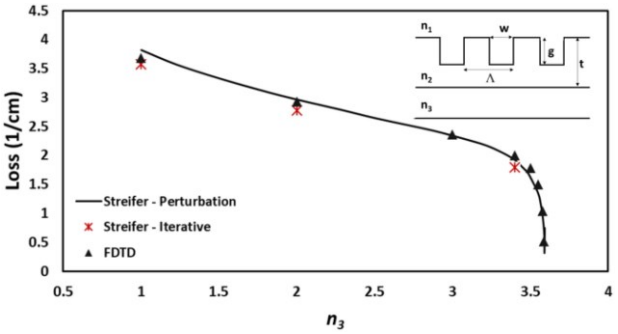

Fig. 2. Comparison of radiation loss as a function of n_3 for the perturbative and iterative solutions [23], and the FDTD method. The characteristics of the rectangular-grooved grating, shown in inset, are: $n_1 = 3.4$, $n_2 = 3.6$, $g = 0.2$ μm, $t = 1$ μm, $\Lambda = 0.21$ μm, and $w = 0.0525$ μm.

leads to a period Λ of about 400 nm for a grating order $M = 2$, using an effective index (n_{eff}) for the TE mode that varies between 3.230 for the thin slab where the whole period is etched and 3.258 for the thick slab where the entire waveguide remains un-etched. Therefore, for a fixed period, the Bragg wavelength varies correspondingly between 1292 and 1304 nm in each simulation. The total length of the grating is set to 30 μm during the optimization procedure in order to reduce the simulation time. Longer lengths will produce a stronger reflectance, but the optimized groove widths are expected remain the same.

The simulated Bragg wavelength is slightly higher than expected due to numerical dispersion in the FDTD mesh (the speed of light in the meshed medium departs slightly from that in the physical medium). We implemented a non-uniform mesh across the grating region to set a balance between minimizing numerical dispersion and computational requirements.

III. Verification of the Simulation Setup

We verify the reliability of our computational method by calculating the radiation loss from a rectangular-grooved grating, as studied by Streifer *et al.* [23], and shown in the inset of Fig. 2. The operating mode is the fundamental TE mode of the corresponding slab waveguide, and the free-space wavelength is 880 nm which falls on the long-wavelength side of the Bragg wavelength. At this wavelength, the grating reflection is negligible, implying that the incident power is either transmitted or lost due to radiation. The total radiation loss can be calculated via (1), using the reflectance and transmittance associated with the TE mode only.

Fig. 2 shows the radiated power as a function of the refractive index of the substrate n_3, for the fundamental TE mode, computed using three different methods. Despite the many differences between the FDTD method and the CMT-based perturbative and iterative solutions [23], the results are in very good agreement. Interestingly, applying the CMT equations to strong gratings (at the left tail of the curve) produces very similar results to the FDTD.

Another coefficient useful to assess the performance of gratings is the coupling coefficient, which describes the coupling strength per unit of length between the forward and backward propagating modes. Streifer *et al.* [20] carried out a perturbation analysis to express the coupling coefficient for the TE mode. In such an analysis, the perturbation in the refractive index of the grating region is expanded in terms of Fourier coefficients which depend on the geometry of the grooves. Therefore, this method can be valid for any groove shape as long as analytical functions can describe the groove profile.

TABLE II
Comparison of Coupling Coefficient Calculations Using Two Methods. Details of the Model Are Given in [20]

Grating order	$\|\kappa\|$ (1/cm) Streifer *et al.* [20]	$\|\kappa\|$ (1/cm) FDTD
1	99.89	105
2	31.91	30
3	16.43	15

This contra-directional coupling between two modes can occur only over a narrow range of wavelengths, occurring in the Bragg regime. This behaviour resembles the scattering of electrons at the edge of Brillouin zones which leads to the appearance of forbidden energy gaps. This bandgap can be described by [24]:

$$(\Delta\omega)_{gap} = \frac{2\,|\kappa|\,c}{n_{eff}} \tag{3}$$

where $|\kappa|$ is the coupling coefficient, n_{eff} is the effective index of the mode, c is the speed of light in free space, and $(\Delta\omega)_{gap}$ is the width of the energy gap with $\omega = 2\pi c/\lambda_0$ (λ_0 denotes the wavelength of operation in vacuum). It is important to note that (3) is only valid when the frequency dependence of n_{eff} is neglected. We analyzed a single period of gratings bounded by Bloch boundary conditions to simulate an infinitely long grating. Monitoring the electric field in the frequency domain at the band edge (where the wavevector equals to π/Λ) gives information about the width of the bandgap and the mid-gap frequency. By substituting $(\Delta\omega)_{gap}$ into (3), we can calculate the coupling coefficient for an infinitely long grating. Using this approach, in combination with the FDTD method, a three-layer slab waveguide with symmetric triangular gratings, as described in detail at [20], is modelled. The resulting coupling coefficients are calculated for first, second, and third-order gratings. Table II shows a comparison between the calculations using the FDTD method and CMT-based methods for the same problem. As can be observed, the results are in excellent agreement.

IV. Results

A. Rectangular-Grooved Gratings

Initially, we compute the reflectance, transmittance, and radiation loss responses of first to third order gratings for benchmark rectangular-shaped designs, and we discuss and interpret the results. The gratings considered have the following dimensions (Fig. 1(b)): $W_t = W_b = 60$ nm , $g = 350$ nm, $\Lambda = 200,\ 400,\ 600$ nm for first, second and third order gratings, and a length of 30 μm.

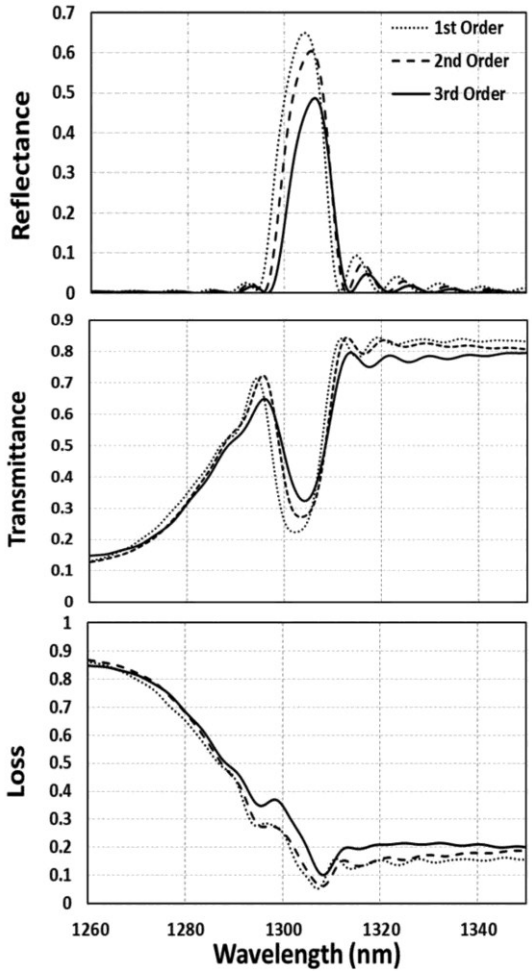

Fig. 3. Comparison of reflectance, transmittance, and loss for first to third order gratings with W_t and W_b fixed at 60 nm. The characteristics of the groove profiles are: $W_t = W_b = 60$ nm, $g = 350$ nm, $\Lambda = 200, 400, 600$ nm for first, second and third order gratings, and a length of 30 μm.

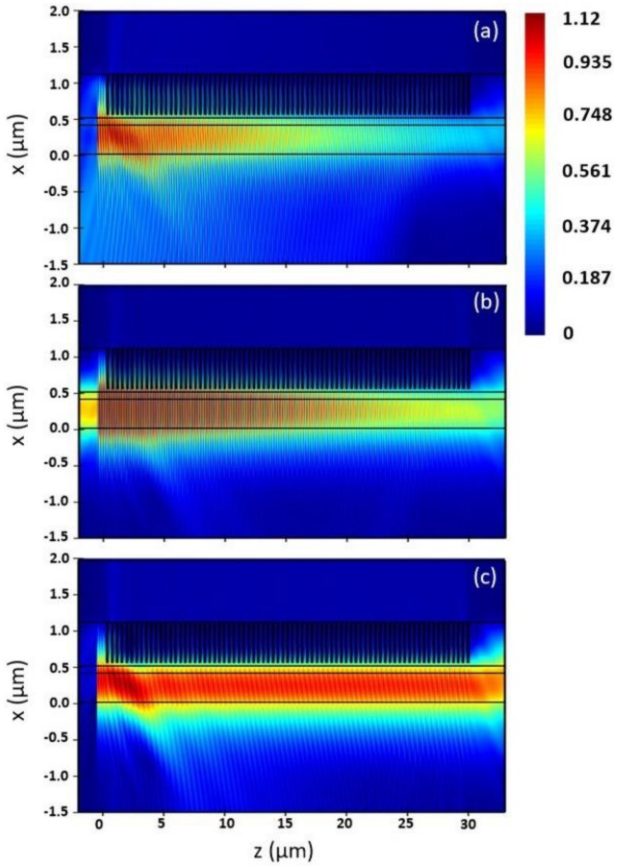

Fig. 4. Electrical field distribution over the second order grating structure, at (a) $\lambda_0 = 1260$ nm, (b) $\lambda_0 = 1305$ nm (Bragg wavelength), and (c) $\lambda_0 = 1370$ nm. The grating design is the same as in Fig. 3.

Fig. 3 shows the spectral characteristics of the three grating designs for the fundamental TE mode. The Bragg wavelengths show a good uniformity between the gratings with a slight shift as the grating order increases. This shift is due to the change in the effective index of each design. Another observation is that the gratings behave similarly at off-resonance wavelengths regardless of their order. On the long wavelength side of the Bragg wavelength, the curves exhibit an oscillatory behaviour that may correspond to Fabry-Perot resonances in a finite-length grating [21]. This oscillation will be more pronounced when the grating length increases, as the reflection at the grating ends increases. Near the long-wavelength edge of the bandgap, the gratings produce the lowest loss. As the wavelength decreases, the loss increases through the bandgap and keeps growing with roughly the same slope with decreasing wavelength. This behaviour can also be observed in transmittance curves, where the transmittance is lower on the short wavelength side of the bandgap than on its longer wavelength side. This is caused by the coupling of the propagating fundamental mode into the radiative modes of the structure at short wavelengths [25].

To better understand the behaviour of these gratings, we plot in Fig. 4 the electric field distribution over the grating structure, at three different wavelengths, for the case of the second order grating. The excitation of fundamental TE mode occurs slightly before $z = 0$ μm. The bright areas above and below the grating represent light scattered into the air and substrate, respectively. We note that the power radiated into the substrate is much larger than the power radiated in air because the substrate has a higher refractive index. Comparing Fig. 4(a) to 4(c), which correspond to the shorter- and longer-wavelength regions of the bandgap, respectively, reveals that the scattered power is larger at shorter wavelengths, in agreement with the loss curves of Fig. 3. Most of the scattered light originates at the input of the grating, due to mode mismatch between the input waveguide and the grating region. Fig. 4(b) shows the electric field distribution near the Bragg wavelength where strong reflectance occurs. The grating experiences the lowest loss in this wavelength region.

B. *Trapezoidal-Grooved Gratings*

We investigated the performance of trapezoidal-grooved gratings by sweeping over the parameters W_t and W_b, and computing

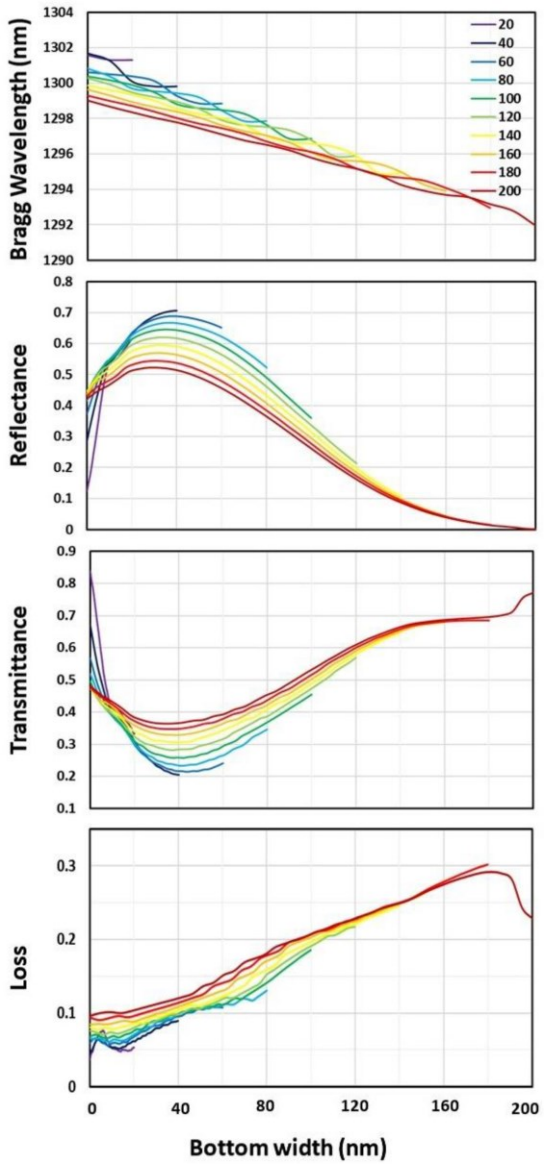

Fig. 5. Bragg wavelength, reflectance, transmittance and loss at the Bragg wavelength for first order gratings as a function of the bottom width (W_b) for several top widths (W_t) as shown in the legend (nm). The other characteristics of the groove profiles are: $g = 350$ nm, $\Lambda = 200$ nm.

the response of first, second and third order gratings. The location of the bandgap stays roughly constant, varying by less than 10 nm throughout the simulations due to the dependence of the mode effective index on the groove profile.

Fig. 5 summarizes the performance of first-order gratings in terms of bandgap location (Bragg wavelength), reflectance, transmittance, and loss, as a function of W_b for different values of W_t. The performance was determined at the Bragg wavelength, where the reflectance is highest and the transmittance is lowest. Steps of 20 nm were used for W_t, and W_b was made to vary for each W_t such that the groove shape changes from symmetric triangular ($W_b = 0$) to rectangular ($W_b = W_t$). We observe that the loss increases with both widths, although more significantly with the bottom width. We also observe that the reflectance and transmittance depend more strongly on the bottom width, which is unsurprising as the bottom of the groove interacts more strongly with the mode. This observation is instructive from a fabrication standpoint because high-performance gratings can be achieved at 50% duty cycle at the top by tailoring the bottom width (masks of duty cycle close to 50% tend to be easiest to fabricate). We also note, generally, that it is important for the bottom width to be narrow. The gratings providing maximum reflectance and minimum loss are clustered near $W_b = 40$ nm, irrespective of the grating top width. The highest reflectance and lowest transmittance occur for $W_t = W_b = 40$ nm, so the best grating is rectangular-grooved.

Figs. 6 and 7 summarize the performance of second and third order gratings, respectively. The highest reflectance of the second and third-order structures is achieved for approximately the same widths as the first order gratings. As for the second-order gratings, the largest loss occurs slightly beyond $W_b/\Lambda = 0.5$, because as the grooves widen, the effective index in the grating region decreases, as well as the penetration of the field into the grating [23]. In the case of the third-order gratings, the losses are much more sensitive to W_b, but the highest loss occurs near $W_b/\Lambda = 0.5$ as in the second order structures. Another noticeable point that emerges by comparison is the similar fabrication tolerance that each grating order provides. Using the full-width at half maximum (FWHM) of the reflectance curves as the tolerance gauge, each grating order offers about 100 nm of tolerance in dimensioning the bottom width.

The Bragg wavelength in all three grating orders decreases as the widths increase. This can be explained by the fact that n_{eff} of the fundamental TE mode decreases as the groove widths increase, which leads to a reduction of the Bragg wavelength according to (2).

The optimum geometry of the grooves is taken as the dimensions that produce the strongest back-reflection, not necessarily the lowest loss. The minimum loss occurs when the gratings tend to vanish. Thus, the optimum geometries consist of rectangular grooves of widths $W_b = W_t = 40$, 50 and 60 nm for first, second and third order gratings, respectively. On average, setting W_b to $\lambda/8$ (λ denotes the wavelength in the medium) produces the best performance for any value of W_t. It is important to emphasize that rectangular grooves are difficult to achieve in practice. However, one can achieve similar performances with trapezoidal grooves by setting only the bottom width around the optimum value as selected from such plots.

The coupling coefficients of corresponding gratings of infinite length can be calculated using Bloch boundary conditions, as discussed in Section III. Table III summarizes the calculations for optimized first, second and third order gratings. The values obtained are high, which is mainly due to the high-index contrast that exists in these gratings. As the grating order increases, the number of radiating waves increases as well, and the coupling coefficient κ decreases. It should be noted that although in practice the grating length is finite, approximating to infinite length still provides accurate information about the width of the bandgap and its location (simulations of long finite devices are computationally intensive).

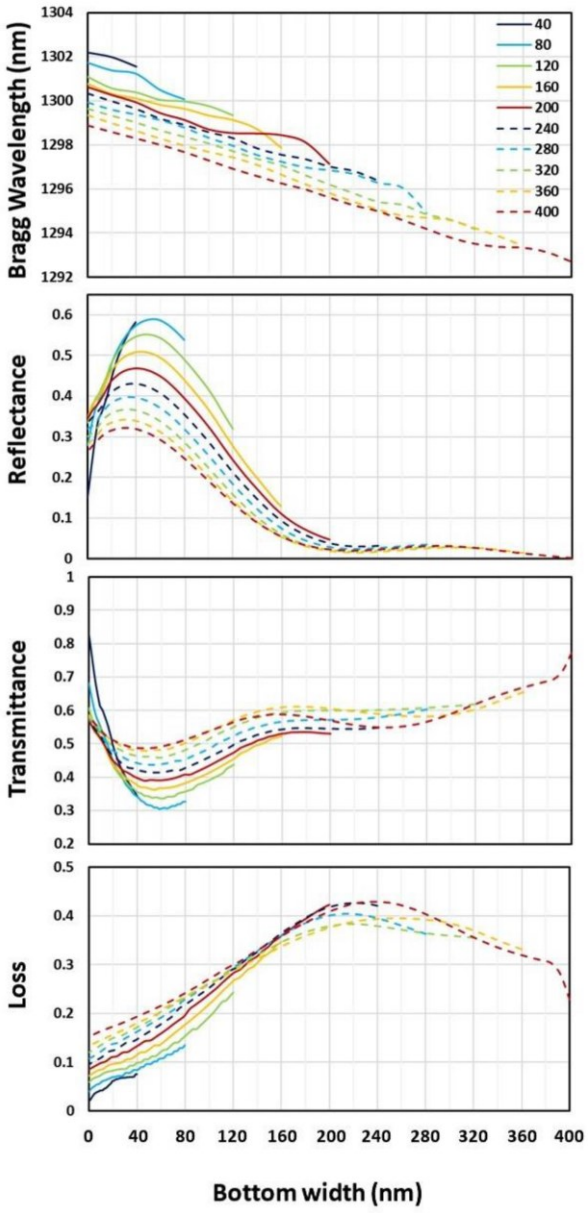

Fig. 6. Bragg wavelength, reflectance, transmittance and loss at the Bragg wavelength for second order gratings as a function of the bottom width (W_b) for several top widths (W_t) as shown in the legend (nm). The other characteristics of the groove profiles are: $g = 350$ nm, $\Lambda = 400$ nm.

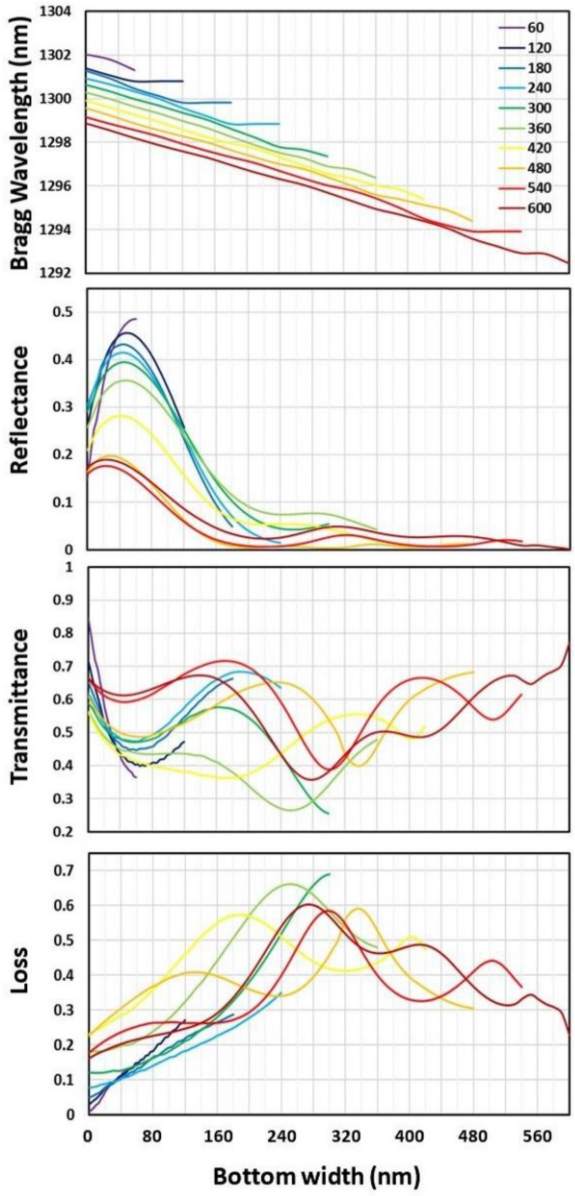

Fig. 7. Bragg wavelength, reflectance, transmittance and loss at the Bragg wavelength for third order gratings as a function of the bottom width (W_b) for several top widths (W_t) as shown in the legend (nm). The other characteristics of the groove profiles are: $g = 350$ nm, $\Lambda = 600$ nm.

TABLE III
VALUES OF COUPLING COEFFICIENT FOR FIRST THROUGH THIRD ORDER BRAGG GRATINGS

Grating order	W_t (nm)	W_b (nm)	$\|\kappa\|$ (1/cm)
1	40	40	416.67
2	50	50	369.22
3	60	60	321.4

V. CONCLUSION

Strong first, second and third order Bragg gratings formed of (presumed etched) trapezoidal grooves in a semiconductor waveguide were investigated and optimized using the 2D FDTD method. Our modelling approach agrees very well with the modified CMT method described in the literature. The reflectance and transmittance spectra of the gratings show increasing loss by scattering on the short-wavelength side of the bandgap, but comparatively lower and constant loss on the long-wavelength side. The effects of varying the top and bottom widths of trapezoidal grooves was explored. We have shown that by simply

adjusting the angle of the sidewalls in the grooves and controlling the bottom width, one can achieve a performance close to optimal. Calculations show that the best grating performance is obtained for bottom widths near $\lambda/8$, (*e.g.*, $\sim$50 nm). The highest reflectance peaks are obtained for rectangular grooves of width $W_t = W_b = 40$, 50 and 60 nm, for first to third order gratings, respectively. It is also found that the radiation loss increases monotonically with increasing groove width in first order gratings. However, this is not the case for second and third order gratings as the highest loss is produced for groove widths that are slightly larger than half of the period. Strong coupling coefficients were achieved for optimized and infinitely long structures. Our results are of interest in the design of strong short gratings etched into semiconductor waveguides.

REFERENCES

[1] M. Smit, K. Williams, and J. V. D. Tol, "Past, present, and future of InP-based photonic integration," *APL Photon.*, vol. 4, no. 5, May 2019, Art. no. 05091.

[2] S. Arafin and L. A. Coldren, "Advanced InP photonic integrated circuits for communication and sensing," *IEEE J. Sel. Top. Quantum Electron.*, vol. 24, no. 1, pp. 1–12, Sep. 2017.

[3] D. Botez and M. Ettenberg, "Comparison of surface-and edge-emitting LED's for use in fiber-optical communications," *IEEE Trans. Electron. Devices*, vol. 26, no. 8, pp. 1230–1238, Aug. 1979.

[4] J. T. Andrews *et al.*, "Buried grating distributed feedback laser at lambda = 1.51 mu m," in *Proc. 3rd Int. Conf. Indium Phosphide Related Mater.*, Apr. 1991, pp. 106–109.

[5] K. Pimenov *et al.*, "Analysis of high-order surface etched gratings for longitudinal mode selection in DFB lasers," in *Proc. IEEE Numer. Simul. Optoelectron. Devices*, Sep. 2010, pp. 49–50.

[6] R. R. Millet *et al.*, "Simulation analysis of higher order laterally-coupled distributed feedback lasers," *IEEE J. Quantum Electron.*, vol. 44, no. 12, pp. 1145–1151, Nov. 2008.

[7] A. Laakso *et al.*, "Laterally-corrugated ridge-waveguide distributed feedback lasers at 980 nm," *Opt. Quantum. Electron.*, vol. 41, no. 1, pp. 11–16, Jan. 2009.

[8] J. Fricke *et al.*, "Properties and fabrication of high-order Bragg gratings for wavelength stabilization of diode lasers," *Semicond. Sci. Technol.*, vol. 27, no. 5, Apr. 2012, Art. no. 055009.

[9] H. Wenzel *et al.*, "A comparative study of higher order Bragg gratings: Coupled-mode theory versus mode expansion modeling," *IEEE J. Quantum Electron.*, vol. 42, no. 1, pp. 64–70, Dec. 2005.

[10] T. Masood *et al.*, "Single-frequency 1310-nm AlGaInAs-InP grating-outcoupled surface-emitting lasers," *PTL*, vol. 16, no. 3, pp. 726–728, Mar. 2004.

[11] A. M. Shams-Zadeh-Amiri *et al.*, "Amplified-spontaneous-emission spectrum of the radiation field in surface-emitting DFB lasers," *J. Lightw. Technol.*, vol. 24, no. 4, pp. 1824–1833, Apr. 2006.

[12] A. M. Shams-Zadeh-Amiri *et al.*, "Second-and higher-order resonant gratings with gain or Loss-part 1: Green's function analysis," *IEEE J. Quantum Electron.*, vol. 36, no. 12, pp. 1421–1430, Dec. 2000.

[13] H. Wenzel *et al.*, "High-power distributed feedback lasers with surface gratings: Theory and experiment," *IEEE J. Sel. Top. Quantum Electron.*, vol. 21, no. 6, pp. 352–358, May 2015.

[14] W. Streifer, D. R. Scifres and R. D. Burnham, "Coupling coefficients for distributed feedback single-and double-heterostructure diode lasers," *IEEE J. Quantum Electron.*, vol. 11, no. 11, pp. 867–873, Nov. 1975.

[15] A. Takemoto *et al.*, "1.3-mu m distributed feedback laser diode with a grating accurately controlled by a new fabrication technique," *J. Lightw. Technol.*, vol. 7, no. 12, pp. 2072–2077, Dec. 1989.

[16] H. Ghafouri-Shiraz and B. S. K. Lo, "Computation of coupling coefficient contours for a five-layer trapezoidal grating structure," *Opt. Laser Technol.*, vol. 26, no. 1, pp. 45–48, Jan. 1994.

[17] H. Abiri *et al.*, "Optimization of first-order and second-order trapezoidal gratings used in DFB and DBR lasers," in *Proc. 8th Phys. Simul. Optoelectron. Devices*, 2000, pp. 853–861.

[18] J. Fricke *et al.*, "Surface Bragg gratings for high brightness lasers," in *Proc. 19th Novel -Plane Semicond. Lasers*, 2020, Art. no. 113011H.

[19] H. Kogelnik and C. V. Shank, "Coupled-wave theory of distributed feedback lasers," *J. Appl. Phys.*, vol. 43, no. 5, pp. 2327–2335, May 1972.

[20] W. Streifer, D. R. Scifres, and R. D. Burnham, "Coupled wave analysis of DFB and DBR lasers," *IEEE J. Quantum Electron.*, vol. 13, no. 4, pp. 134–141, Apr. 1977.

[21] J. Čtyroký *et al.*, "Bragg waveguide grating as a 1D photonic band gap structure: COST 268 modelling task," *Opt. Quantum Electron.*, vol. 34, no. 5/6, pp. 455–470, May 2002.

[22] W. Sun *et al.*, "Analysis of high-order slotted surface gratings by the 2D finite-difference time-domain method," *J. Lightw. Technol.*, vol. 35, no. 1, pp. 96–102, Nov. 2016.

[23] W. Streifer, D. R. Scifres, and R. D. Burnham, "Analysis of grating-coupled radiation in GaAs: Gaalas lasers and waveguides-I," *IEEE J. Quantum Electron.*, vol. 12, no. 7, pp. 422–428, Jul. 1976.

[24] A. Yariv, "Coupled-mode theory for guided-wave optics," *IEEE J. Quantum Electron.*, vol. 9, no. 9, pp. 919–933, Sep. 1973.

[25] S. Jetté-Charbonneau *et al.*, "Demonstration of Bragg gratings based on long ranging surface plasmon polariton waveguides," *Opt. Exp.*, vol. 13, no. 12, pp. 4674–4682, Jun. 2005.

Chapter 7

Dirac Gratings

7.1 Contribution Statement

This project was conducted in collaboration with the research group led by Dr. Schmid and Dr. Cheben at the NRC. The theoretical framework was initially developed by me and my supervisor, Prof. Pierre Berini. Through regular meetings with the NRC team, we reviewed and refined the modeled structures, some of which were later included in the final manuscript.

I developed the core concept of the paper and was primarily responsible for establishing the theoretical foundation and performing the simulations. I also wrote the initial draft of the manuscript.

Related conference publication arising from this work is listed below:

- S. Saeidi, *et al*. " Exploring Dirac Gratings in Silicon Photonics." *2025 Photonics North (PN)*. IEEE, 2025.

7.2 Article

Research Article Vol. 31, No. 19 / 11 Sep 2023 / Optics Express 31200
Optics EXPRESS

Dirac gratings

SHAYAN SAEIDI,[1,2,*] PAVEL CHEBEN,[3] JENS H. SCHMID,[3] AND PIERRE BERINI[1,2,4,5]

[1]School of Electrical Engineering and Computer Science, University of Ottawa, Ottawa ON K1N 6N5, Canada
[2]Nexus for Quantum Technologies Institute, University of Ottawa, Ottawa ON K1N 5N6, Canada
[3]National Research Council of Canada, Ottawa, ON K1A 0R6, Canada
[4]Department of Physics, University of Ottawa, Ottawa, ON K1N 6N5, Canada
[5]pberini@uottawa.ca
[*]ssaeidi@uottawa.ca

Abstract: We propose the concept of a Dirac grating, where periodic permittivity perturbations approach a train of Dirac functions. We show that Dirac gratings can yield identical spectral characteristics for higher-order gratings compared to first-order gratings of the same length. Using an inverse Fourier transform technique, we design different types of Dirac gratings, including structures operating at the exceptional point where parity-time symmetry breaks down, producing unidirectional reflectance. We employ analytical and numerical techniques to validate our theory by modelling practical examples of Dirac gratings implemented in dielectric stacks and silicon nanophotonic waveguides.

1. Introduction

Bragg gratings have been used extensively over many decades as photonic bandgap structures in optical fibers or in photonic integrated circuits, as filtering elements, or in distributed-feedback lasers [1–5]. They have been theoretically investigated using analytical methods such as coupled-mode theory (CMT), which is accurate for weak gratings and simple perturbation profiles that can be described by analytical functions [6]. In CMT a Fourier representation is used to describe the permittivity perturbation along the grating. The non-uniform permittivity along the waveguide generally consists of real and imaginary index perturbations, which induce coupling between different modes. In Bragg gratings, such coupling is contra-directional, and the strength is typically defined by coupling coefficients [7]. More recently, numerical techniques such as finite-difference time-domain (FDTD) and eigenmode expansion (EME) methods were employed to model complex Bragg gratings [8,9]. The common drawback of such numerical methods is computational expense.

Electromagnetic inverse scattering techniques provide a wide range of design possibilities for gratings. These mathematical methods allow the definition of a structure, such as its refractive index or shape, by analyzing the scattering of waves. Multiple approaches are used to solve inverse scattering problems, including layer-peeling and layer-adding [10–13], genetic algorithms [14], simulated annealing [15,16], spectral techniques [17,18], and other optimization approaches. These methods typically solve equations iteratively that link the computed scattering data to the unknown properties of the medium or structure. The ultimate objective is to identify the design that best corresponds to the measured scattering data.

In this paper we exploit the discrete Fourier transform (DFT) representation of a permittivity perturbation and find a direct relationship between its Fourier coefficients and the Bragg grating's reflectance spectrum. We then show that by applying the inverse discrete Fourier transform (IDFT) to a desired or prescribed spectral response, the permittivity profile can be determined.

#494372 https://doi.org/10.1364/OE.494372
Journal © 2023 Received 27 Apr 2023; revised 17 Aug 2023; accepted 19 Aug 2023; published 6 Sep 2023

Research Article Vol. 31, No. 19 / 11 Sep 2023 / Optics Express 31201
Optics EXPRESS

This method offers a simple and efficient approach to Bragg grating design, provided that the phase and amplitude of the grating's spectral response are known.

Using the IDFT method, we then arrive at a novel type of grating, which we refer to as Dirac gratings. These gratings are characterized by sharp periodic perturbations in the permittivity along the propagation axis, and they have a near-zero duty cycle. Notably, Dirac gratings may exhibit order-independent performance, meaning that the spectral response is identical for higher-order gratings compared to first-order gratings of the same length. Other types of Dirac gratings can be designed, including odd-equal Diracs where only odd order gratings reflect light (inspired by quarter-wavelength gratings), and exceptional point Dirac gratings with unidirectional reflectance. These findings have significant implications for the design and fabrication of optical gratings for various applications.

This paper is structured as follows: In Section II, we derive analytically the coupling coefficients of coupled-mode theory using the DFT amplitudes representing a spatial permittivity perturbation. We introduce the concept of Dirac gratings by demonstrating that under specific conditions the reflectivity is independent of the order of the grating. In Section III, we employ the IDFT to arrive at perturbation profiles for various designs of Dirac gratings. In Section IV, we evaluate the performance of these gratings through the analytical Transfer Matrix Method (TMM) and the numerical Eigenmode Expansion (EME) method. Finally, we provide concluding remarks in Section 5.

2. Fourier and coupling coefficients

A Bragg grating with a rectangular profile can be mathematically modeled as a rectangular pulse train, where the relative permittivity changes between high and low values within each period. The rectangular pulse train is described by (1) and sketched in Fig. 1.

$$\varepsilon(z) = \begin{cases} \varepsilon_2, & z \le d \cdot \Lambda \\ \varepsilon_1, & d \cdot \Lambda < z < \Lambda \\ \varepsilon(z \pm q\Lambda), & q \in \mathbb{Z}\ (integers) \end{cases} \tag{1}$$

ε_1 and ε_2 are the relative permittivities of each region within a period and $\Delta\varepsilon = \varepsilon_1 - \varepsilon_2$ is the relative permittivity contrast, Λ is the period, d is the duty cycle defined as the fraction of a period where the permittivity is high, and N is the number of periods. The relative permittivities can be complex but are sketched here as real for simplicity. The direction of propagation is along the z axis. Equation (1) may model a dielectric stack under plane wave excitation, or a structural perturbation along a waveguide in which case ε_1 and ε_2 are effective relative permittivities of waveguide sections.

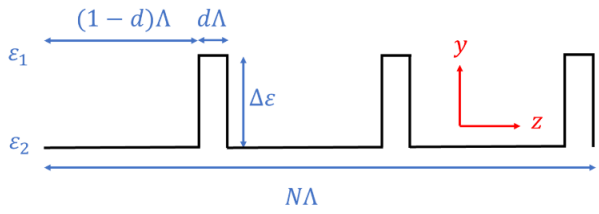

Fig. 1. Relative permittivity distribution described by (1).

Research Article Vol. 31, No. 19 / 11 Sep 2023 / Optics Express 31202
Optics EXPRESS

2.1. Spectral representation

Generally, we can apply the DFT to derive the spectral-domain representation of the discretized form of Eq. (1) [19]:

$$F_k = \sum_{m=0}^{\xi-1} f_m e^{-2\pi j \frac{mk}{\xi}} \qquad k = -\frac{\xi}{2}, \ldots, 0, \ldots, \frac{\xi}{2} - 1 \tag{2}$$

where F_k is the Fourier coefficient of the k-th spectral component, f_m is the m-th spatial sample of $\varepsilon(z)$, ξ is the number of spatial samples ($\xi \gg N$), and $j = \sqrt{-1}$. Here f_m and F_k are dimensionless coefficients. We re-write the Fourier coefficients (2) in terms of $H = e^{-2\pi j/\xi}$, then simplify the resulting geometric series:

$$\begin{aligned}
F_k &= f_0 + f_1 H^k + \ldots + f_{\xi-1} H^{(\xi-1)k} \\
&= \varepsilon_1 + \varepsilon_1 H^k + \ldots + \varepsilon_1 H^{\left(d\frac{\xi}{N}-1\right)k} + \varepsilon_2 H^{d\frac{\xi}{N}k} + \ldots + \varepsilon_2 H^{\left(\frac{\xi}{N}-1\right)k} \\
&+ \varepsilon_1 H^{\frac{\xi}{N}k} + \ldots + \varepsilon_1 H^{\left((d+1)\frac{\xi}{N}-1\right)k} + \varepsilon_2 H^{(d+1)\frac{\xi}{N}k} + \ldots + \varepsilon_2 H^{\left(\frac{2\xi}{N}-1\right)k} + \ldots \\
&+ \varepsilon_1 H^{\frac{N-1}{N}\xi k} + \ldots + \varepsilon_1 H^{\left((d+N-1)\frac{\xi}{N}-1\right)k} + \varepsilon_2 H^{(d+N-1)\frac{\xi}{N}k} + \ldots + \varepsilon_2 H^{(\xi-1)k} \\
&= \left(\frac{1 - H^{\frac{d\xi k}{N}}}{1 - H^k}\right)\left(\varepsilon_1 + \ldots + \varepsilon_1 H^{\frac{(N-1)\xi k}{N}}\right) \\
&+ \left(\frac{1 - H^{\frac{(1-d)\xi k}{N}}}{1 - H^k}\right)\left(\varepsilon_2 H^{\frac{d\xi k}{N}} + \ldots + \varepsilon_2 H^{(d+N-1)\frac{\xi k}{N}}\right) \\
&= \left(\frac{\varepsilon_1\left(1 - H^{\frac{d\xi k}{N}}\right) - \varepsilon_2\left(H^{\frac{\xi k}{N}} - H^{\frac{d\xi k}{N}}\right)}{1 - H^k}\right)\left(\frac{1 - H^{\xi k}}{1 - H^{\frac{\xi k}{N}}}\right)
\end{aligned} \tag{3}$$

The Fourier coefficients F_k which have the largest magnitude are denoted $\mathcal{F}_M$ and they occur for $k = MN$ where M is an integer. They are identified directly from the last equality of Eq. (3), after resubstituting H by $e^{-2\pi j/\xi}$:

$$\mathcal{F}_M = \frac{(1 - e^{-2\pi jMd})(\varepsilon_1 - \varepsilon_2)}{1 - e^{-\frac{2\pi j}{\xi}MN}} \cdot \frac{1 - e^{-2\pi jMN}}{1 - e^{-2\pi jM}} = \frac{N(1 - e^{-2\pi jMd})(\varepsilon_1 - \varepsilon_2)}{1 - e^{-\frac{2\pi j}{\xi}MN}} \tag{4}$$

We can re-write (4) in terms of trigonometric functions:

$$\mathcal{F}_M = \frac{1}{2}N\Delta\varepsilon(1 - e^{-2\pi jMd})\left(1 - j\cot\left(\frac{\pi MN}{\xi}\right)\right) \tag{5}$$

or:

$$\mathcal{F}_M = N\Delta\varepsilon\frac{\sin(\pi Md)}{\sin\left(\frac{\pi MN}{\xi}\right)}e^{j\pi M\left(\frac{N}{\xi}-d\right)} \tag{6}$$

When the number of samples ξ is sufficiently large to ensure $\xi \gg \pi MN$, the expression for $|\mathcal{F}_M|$ reduces to:

$$|\mathcal{F}_M| \cong \left|\frac{\xi\Delta\varepsilon}{M\pi}\sin(\pi Md)\right| \tag{7}$$

It is observed that $|\mathcal{F}_M|$ is directly proportional to ξ. To remove this dependence, we normalize $|\mathcal{F}_M|$ by dividing by ξ:

$$|\overline{\mathcal{F}_M}| \cong \left|\frac{\Delta\varepsilon}{M\pi}\sin(\pi Md)\right| \tag{8}$$

Research Article Vol. 31, No. 19 / 11 Sep 2023 / Optics Express 31203
Optics EXPRESS

which retains the implied unit in the spectral domain representation as the inverse of the implied unit of the original function [20] (here both are dimensionless). From the above we observe that $|\overline{\mathcal{F}_M}|$ is periodic in M, but of amplitude that decreases as M increases.

2.2. Coupling coefficients

The expression for the coupling coefficient, $\kappa_{\pm k}$, that results from coupled mode theory (CMT) applied to a weak waveguide grating, is given by [21]:

$$\kappa_{\pm k} = \frac{{\beta_0}^2}{2\beta} \frac{\int F_{\pm k}(x,y)|U(x,y)|^2 dA}{\int |U(x,y)|^2 dA} \tag{9}$$

where β is the propagation constant of the waveguide mode, β_0 is the free-space propagation constant, $U(x,y)$ is the spatial profile of the waveguide mode, and $F_{\pm k}(x,y)$ represents the k-th Fourier expansion functions of the permittivity perturbation along the waveguide. For a weakly guided mode (plane-wave like), the field dependencies in the x-y plane are negligible, so $\kappa_{\pm k}$ simplifies to:

$$\kappa_{\pm k} = \frac{{\beta_0}^2}{2\beta} F_{\pm k} \tag{10}$$

where $F_{\pm k}$ are Fourier coefficients (Eq. (2)). It is evident that $|\kappa_{\pm k}|$ will be strongest when $|F_{\pm k}|$ is largest, i.e., for the set $|\overline{\mathcal{F}_M}|$:

$$|\kappa_M| = \frac{{\beta_0}^2}{2\beta} |\overline{\mathcal{F}_M}| \cong \frac{{\beta_0}^2}{2\beta} \left| \frac{\Delta\varepsilon}{M\pi} \sin(\pi M d) \right| \tag{11}$$

where the second equality arises by substituting Eq. (8), assuming $\xi \gg \pi MN$. Introducing $\bar{n}$ as the effective refractive index of the waveguide mode ($\bar{n} = \beta/\beta_0$) and λ_0 as the free-space wavelength, Eq. (11) can be rewritten as:

$$|\kappa_M| \cong \left| \frac{\Delta\varepsilon}{M\lambda_0\bar{n}} \sin(\pi M d) \right| \tag{12}$$

The strongest coupling coefficient also occurs at the Bragg wavelength λ_B [22]. So, by substituting $\lambda_0 = \lambda_B$ and using the Bragg equation, $\lambda_B = 2\bar{n}\Lambda/M$, Eq. (12) becomes:

$$|\kappa_{M,B}| \cong \left| \frac{\Delta\varepsilon}{2\bar{n}^2\Lambda} \sin(\pi M d) \right| \tag{13}$$

This expression for the coupling coefficient (Eq. (13)) is consistent with the literature [21–24], indicating that the integer M, first introduced here in Eq. (4) to identify the largest Fourier coefficients, also corresponds to the grating order in the Bragg equation. We also note that $\bar{n}$ is sometimes taken as the effective refractive index of the waveguide mode averaged over a period, or for a dielectric stack as the refractive index averaged over a period.

To operate at the same Bragg wavelength at order M, it is necessary to increase the pitch by a factor of M, resulting in a reduction of $|\kappa_M|$ (Eq. (13)). The reflectance of an M-th order Bragg grating following CMT is given by [21]:

$$R_M = |\tanh(\kappa_{-M} L)|^2 \tag{14}$$

Thus, conventionally, increasing M decreases the reflectance if the length of the grating, L, remains constant.

Research Article Vol. 31, No. 19 / 11 Sep 2023 / Optics Express 31204
Optics EXPRESS

2.3. Limit of small duty cycle: Dirac gratings

If the duty cycle, d, is small enough for $\pi M d \rightarrow 0$, then Eqs. (8), (11) and (12) simplify, respectively, to:

$$|\overline{\mathcal{F}_M}| \cong |d\Delta\varepsilon| \quad \text{and} \quad |\kappa_M| \cong \frac{{\beta_0}^2}{2\beta}|d\Delta\varepsilon| = \left|\frac{\pi d\Delta\varepsilon}{{}_0\bar{n}}\right| \tag{15}$$

from which it is observed that $|\kappa_M|$ and consequently R_M (Eq. (14)) are independent of grating order. We refer to these gratings as Dirac gratings because a Bragg grating with narrow-width perturbations, or equivalently a small duty cycle d, resembles a series of Dirac delta functions. An attribute of Dirac gratings is that higher order gratings can replace lower order ones while maintaining the same performance for the same grating length.

Equation (15) shows that for the same material system, i.e., fixed $\Delta\varepsilon$, Dirac gratings yield a weaker $|\kappa_M|$ compared to a conventional first order grating due to the small d. However, a high reflectance can be maintained by increasing L to compensate for the small κ_{-M} (Eq. (14)). For example, for a first order quarter-wavelength grating, the coupling coefficient is $|\kappa_1| \cong |\Delta\varepsilon/\lambda_0\bar{n}|$ according to Eq. (12), which is $1/\pi d$ times larger than that of a Dirac grating (Eq. (15)). Thus, for a Dirac grating to produce the same reflectance as the corresponding quarter-wavelength grating, L should be $1/\pi d$ times longer.

We observed that the reflectance at λ_B, given by Eq. (14), depends on κ_{-M} and $\overline{\mathcal{F}_M}$, as revealed by (11). Therefore, the behavior of R_M is dependent on the Fourier amplitudes F_M. The Fourier amplitudes can thus be prescribed, and the IDFT applied to determine the required permittivity modulation in the spatial domain. These observations motivate the development of a design technique based on the IDFT. In the next section, we will use this technique to explore intricate Dirac grating designs.

3. IDFT design and Dirac gratings

Initially we use the IDFT to verify that a Dirac grating has a reflectance response independent of grating order, $M = 1,\ 2,\ 3, \ldots,$. To verify this, we set the magnitude of the spectral components $|F_k|$ to the same arbitrary constant, e.g., unity, for $k = MN$, and zero elsewhere, as shown in Fig. 2(a), and their phase to zero so that the incident and reflected waves are in phase at the Bragg wavelength.

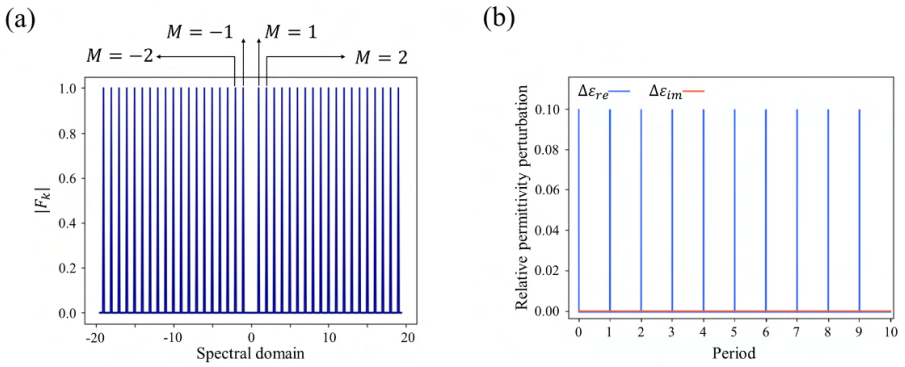

Fig. 2. (a) Desired distribution of $|\mathcal{F}_k|$ in the spectral domain for order independent reflectance. (b) Spatial permittivity profile of the corresponding Dirac grating over ten periods.

Research Article Vol. 31, No. 19 / 11 Sep 2023 / Optics Express 31205
Optics EXPRESS

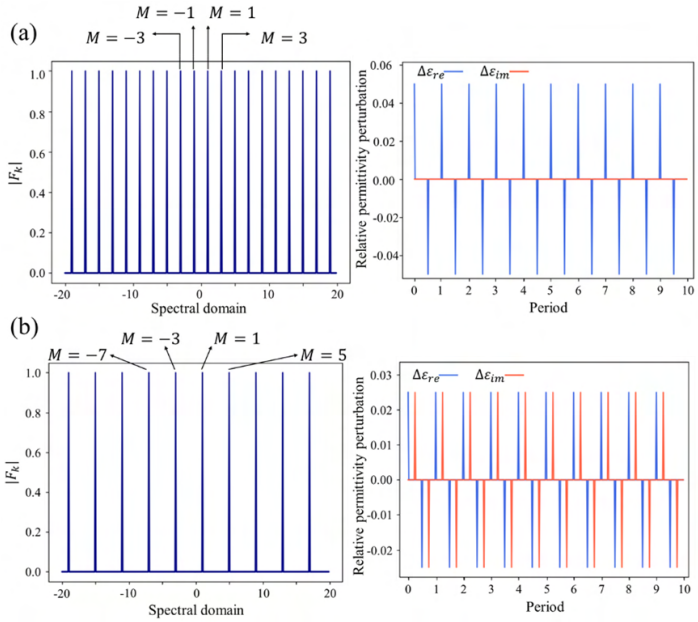

Fig. 3. Left panels: Desired distribution of $|F_k|$ in the spectral domain. Right panels: Spatial permittivity profile of the corresponding Dirac gratings over ten periods. (a) Odd equal-order grating, and (b) exceptional point grating.

Applying the IDFT [19] to a discrete spectral distribution, F_k, leads to the required permittivity perturbation in the spatial domain, described by the samples f_m:

$$f_m = \frac{1}{\xi} \sum_{k=-\xi/2}^{\xi/2-1} F_k e^{2\pi j \frac{mk}{\xi}} \qquad m = 0, 1, \ldots, \xi - 1 \tag{16}$$

Note that the magnitude of the resulting samples (Eq. (16)) depends on the magnitude chosen for $|F_k|$ and on ξ.

The permittivity modulation resulting from the spectral distribution of Fig. 2(a) is shown in Fig. 2(b), where the horizontal axis is normalized so that a period is equal to unity. We observe that the real part of the permittivity modulation, $\Delta\varepsilon_{re}$, required to implement the grating consists of Dirac-like peaks, whereas the imaginary part of the permittivity modulation is zero ($\Delta\varepsilon_{im} = 0$), which follows our definition of Dirac gratings and Eq. (15).

Other types of Dirac gratings can be envisioned and designed using the IDFT. The conventional quarter-wavelength grating is of particular interest in semiconductor laser design because it can act as an efficient and high-reflectance mirror while also being relatively easy to fabricate. For the case of Bragg gratings formed as a quarter-wavelength stack ($d = 0.5$), from Eq. (8) it follows that $|\overline{\mathcal{F}_M}|$ vanishes for $d = 0.5$ and even M, while for odd M:

$$|\overline{\mathcal{F}_M}| = |\frac{\Delta\varepsilon}{M\pi}| \tag{17}$$

This implies that the coupling coefficient (12) and the reflectance (14) are zero for even orders and non-zero for odd orders. Inspired by the conventional quarter-wavelength stack, we set as an alternative design in Fig. 3(a) (left panel) the odd spectral components $|\mathcal{F}_M|$ to unity and the even

Research Article Vol. 31, No. 19 / 11 Sep 2023 / Optics Express 31206
Optics EXPRESS

ones to zero. We then find the permittivity profile by applying the IDFT, yielding a Dirac-like profile involving sharp positive and negative perturbations occurring at specific points along the grating length, as shown in Fig. 3(a) (right panel). We term this design an odd equal-order grating.

In Fig. 3(b), a Dirac grating is designed to produce unidirectional reflection, which means that light is reflected from one grating port but not from the other. This is achieved by ensuring that the spectral representation of the permittivity perturbation has odd orders occurring at only one spectral location such that the spectrum is single-sided, as shown in the left panel of Fig. 3(b). Such gratings are known as exceptional point gratings where parity-time symmetry breaks down [25–27]. The required permittivity modulation shown in the right panel of Fig. 3(b) exhibits even and odd symmetries for the real and imaginary parts of the refractive index, respectively, in agreement with the literature [28].

The IDFT approach can be extended to create gratings with arbitrary reflectance responses, resulting in a complex permittivity profile. Our findings are consistent with the findings of [29], which showed that the reflection spectrum of weak gratings is the Fourier transform of the refractive index profile.

4. Modelling of Dirac gratings

Dirac gratings theoretically require infinitesimally narrow perturbations, which could be practically implemented as thin layers in a dielectric stack, or as short discontinuities in waveguide geometry along the propagation direction, such that the effective index perturbation resembles, e.g., the profile of Fig. 2(b). In this section, we investigate analytically the limit up to which the length of the perturbations can be increased while retaining the properties of a Dirac grating. Additionally, we further validate the concept of Dirac gratings by modelling the performance of two example structures using the TMM and EME method.

4.1. Upper limit of duty cycle

As described in Section 2, a Dirac grating is formed when the duty cycle d is small, such that the small-angle approximation for the sine function in Eq. (12) holds. This sine function can be expressed using the Maclaurin series expansion as follows [30]:

$$\sin(\pi Md) = (\pi Md) - \frac{(\pi Md)^3}{3!} + \frac{(\pi Md)^5}{5!} - \dots \tag{18}$$

It is evident from the above that the second and subsequent terms can be disregarded for sufficiently small arguments. To obtain Fourier coefficients (coupling coefficients and a reflectance) that are equal for all grating orders to within a specified error ζ, then using Eq. (18), the upper limit for the duty cycle, d_{max}, should respect:

$$(\pi Md_{max}) - \frac{(\pi Md_{max})^3}{3!} + \dots = (1-\zeta)(\pi Md_{max}) \tag{19}$$

which yields:

$$d_{max} \approx \frac{\sqrt{6\zeta}}{\pi M} \tag{20}$$

It can be observed that d_{max} depends solely on ζ and M. For instance, if the designer aims to achieve order-independency for orders up to 100 with an error less than 2%, the maximum allowed duty cycle is $d_{max} \approx 0.001$. So, the designer faces a trade-off between the error (ζ) and fabrication-related considerations including the grating period ($M\Lambda$) and the smallest feature size ($d_{max}\Lambda$). The other grating parameters such as index contrast and grating length do not play a defining role in realizing a Dirac grating.

Research Article Vol. 31, No. 19 / 11 Sep 2023 / Optics Express 31207
Optics EXPRESS

4.2. Dirac dielectric stack and TMM analysis

We employ the TMM to investigate a dielectric stack composed of Si/SiO_2 multilayers on a Si substrate, as an order-independent Dirac grating (following Fig. 2). The simulation setup, along with the multilayer stack considered, are illustrated in Fig. 4. In this figure, $M\Lambda$ is the pitch and L_D is the length of each perturbation approximating Dirac peaks (Dirac length). The duty cycle $d = L_D/M\Lambda$ is the ratio of the Dirac length to the pitch. The refractive indices of Si and SiO_2 were taken as $n_0 = 3.47$ and $n_1 = 1.44$, respectively, [31] for operation near $\lambda_0 = 1550$ nm. To ensure that the first order ($M = 1$) Bragg reflection occurs near 1550 nm, we set Λ to 225 nm.

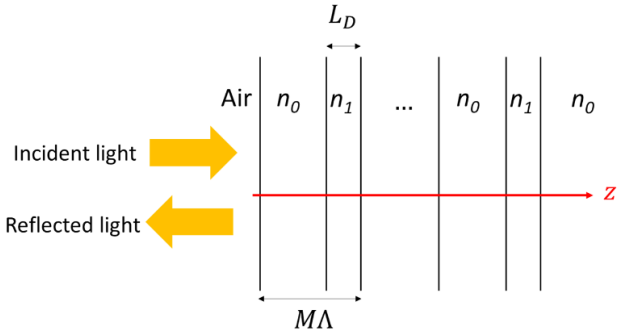

Fig. 4. Schematic of the periodic multilayer stack of pitch $M\Lambda$, used in TMM calculations. The grating is bounded by two semi-infinite layers - a Si substrate of index n_0 and air of index 1.

The reflectance response R was computed for several grating orders and different values of d while maintaining the total stack thickness fixed to 10.8 μm, which holds $N = 48$ periods for $M = 1$. Figure 5(a) plots the reflectance at λ_B as a function of duty cycle d for four different grating structures, corresponding to $M = 1$, 2, 4, and 8. We fixed d when comparing different orders to verify the order independent performance predicted by (14) and (15). Figure 5(a) reveals two key observations. First, the Dirac stack indeed exhibits order-independent performance, as the reflectance response remains constant for different orders at the same d. Second, the order-independent behavior is not significantly affected by L_D values up to 2.5% of the pitch. Thus, in a dielectric stack, thin slabs of finite thickness are good approximations to a Dirac function.

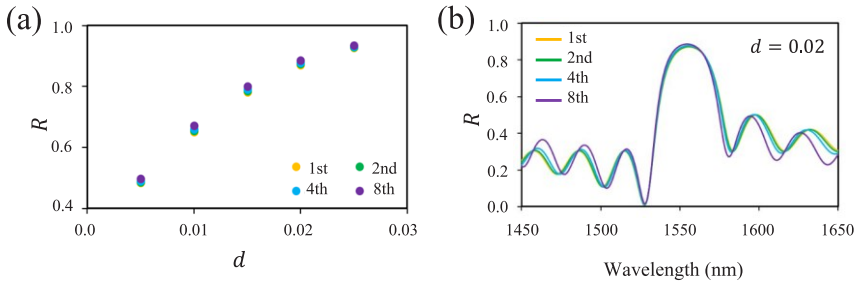

Fig. 5. (a) Reflectance near the Bragg wavelength as a function of d for several grating orders. (b) Comparison of reflectance responses for several grating orders (shown in legend) for $d = 0.02$, calculated via the TMM. The grating length is fixed to 10.8 μm for all orders.

Research Article Vol. 31, No. 19 / 11 Sep 2023 / Optics Express 31208
Optics EXPRESS

Figure 5(b) compares the reflectance responses of different gratings for $d = 0.02$. For the case where $d = 0.02$, the SiO_2 and Si thicknesses are 4.5 and 220.5 nm, respectively, for 1st order, and 36 and 1764nm, respectively for 8th order. Both designs produce the same reflectance for the same total stack thickness (10.8 μm). Furthermore, the reflectance responses of Fig. 5(b) exhibit good agreement with one another, not only in terms of the reflectance values at λ_B but also in terms of the width of the reflection band. The TMM simulations thus provide confirmation of the effectiveness of Dirac gratings.

The order-independence of the spectral responses can be explained phenomenologically as follows. The Dirac-like perturbations have a short length L_D so they may be viewed as scatterers as long as they remain shorter than the wavelength. As the grating pitch is increased from Λ to $M\Lambda$, the perturbation length must also be increased from L_D to ML_D in order to maintain the duty cycle d constant. The M-times longer perturbation produces M-times stronger scattering, such that for gratings of the same length but different orders, the reflectance response remains identical even though the M-th order grating has M-times fewer scatterers compared to the first-order grating. So, the integrated effect of the scatterers in both cases remains identical.

The fabrication of a Dirac grating as a dielectric stack requires precise control of the refractive index and thickness of individual layers, which must also be uniform and of high quality (low roughness, particles and defects). Semiconductor deposition tools readily offer the required control and quality in material, via physical or chemical vapour deposition [32].

4.3. *Dirac waveguide grating and EME analysis*

The example waveguide assumed in this section is a Silicon-on-Insulator (SOI) strip-loaded waveguide as shown in Fig. 6(a). The details of each layer (thickness, refractive index) are given in Table 1. The refractive indices of Si and SiO_2 were extracted from [31]. The waveguide is taken as lossless and passive, i.e., the imaginary parts of the refractive indices are zero. The top view of the parameterized grating structure is shown in Fig. 6(b), where $M\Lambda$ is the pitch and L_D is the length of the Dirac peaks. Λ is assumed to be 280 nm such that the first order λ_B occurs at ~1550 nm. Figure 6(c) shows the electric field profile of the fundamental transverse-electric (TE) mode for the two ridge widths used within each period.

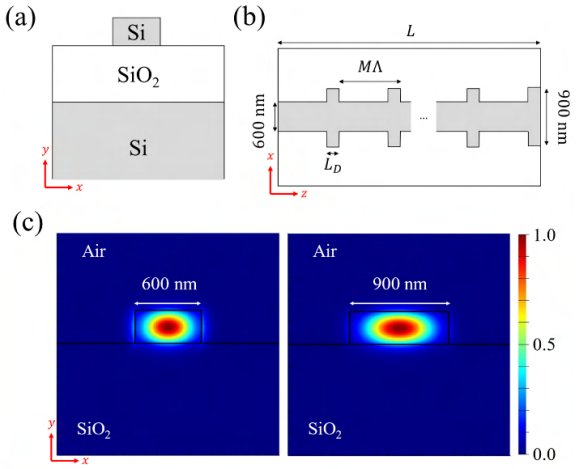

Fig. 6. (a) 1D cross section of the assumed strip-loaded waveguide. (b) Schematic of the Dirac waveguide grating. (c) Electric field profiles of the fundamental mode for the two ridge widths used in (b).

Research Article Vol. 31, No. 19 / 11 Sep 2023 / Optics Express 31209
Optics EXPRESS

Table 1. Properties of the multilayer grating structure at 1550 nm

Layer Description	Material	Thickness (nm)	Refractive Index
Core	Si	300	3.47
Insulator	SiO_2	2000	1.44
Substrate	Si		3.47

We now use the EME method to model the grating structure. The EME method is rigorous, modelling the response of the 3D structure, including any scattering losses due to mode mismatch along a grating. The simulations were carried out using the EME solver in Lumerical Mode [33]. The fundamental TE mode was selected as the input source.

Similarly to the previous section, we vary the parameter $d = L_D/M\Lambda$ and the grating order M, and we compute the reflectance response for a constant grating length set to $L = 560$ µm, i.e., $N = 2000$ for $M = 1$. Figure 7(a) plots the reflectance at λ_B *vs.* d for four different orders. It is apparent that for d>0.01, the performance is not independent of order as different reflectance values are produced for the same grating length. This contrasts with Fig. 5(a), where a stronger grating maintained order-independence for larger d. Additionally, the EME method considers radiation loss, which means that the reflectance might diverge for duty cycles smaller than expected based on Eq. (20). In this example, the upper limit for the duty cycle should be 0.013 according to Eq. (20) for $\zeta = 10\%$, whereas the EME simulations show d<0.01. The structural parameters for $d = 0.005$ for the 20th order grating are: $M\Lambda = 5.6$ µm and $L_D = 28$ nm, whereas the structural parameters for the first order grating are: $M\Lambda = 0.28$ µm and $L_D = 1.4$ nm. The former which has only 100 periods produces almost the same performance as the latter which has 2000 periods.

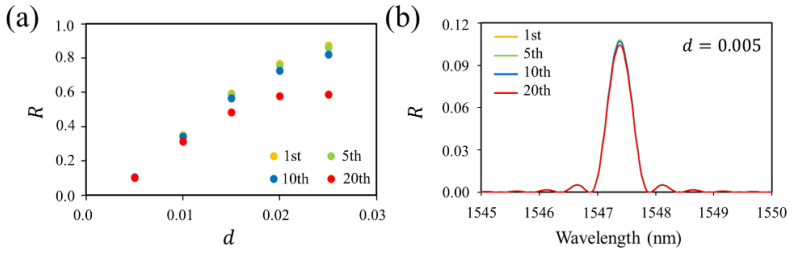

Fig. 7. (a) Reflectance near the Bragg wavelength as a function of d for several grating orders. (b) Comparison of reflectance responses for several grating orders (shown in legend) for $d = 0.005$, calculated via the EME method. The grating length is fixed to 560 µm for all cases.

Figure 7(b) shows the wavelength response of the reflectance R computed using the EME of the four grating designs for the case $d = 0.005$. It is clear that despite very different orders, the gratings share almost identical wavelength responses, thereby confirming order-independent behavior for Dirac waveguide gratings.

The fabrication of a Dirac waveguide grating shares similar considerations as a dielectric stack, in that precise control of material properties and quality are required. Additionally, high-resolution lithography is required to define the waveguides and the Dirac perturbations of length L_D, as well as an etching process that produces vertical and smooth sidewalls. High-resolution features can be accessed via electron beam or helium ion beam lithography [34], and the latter by reactive ion etching.

Research Article Vol. 31, No. 19 / 11 Sep 2023 / Optics Express 31210
Optics EXPRESS

5. Conclusion

We demonstrated theoretically that the reflectance of a grating, which depends on the coupling coefficient κ_{-M}, is proportional to the Fourier coefficients of the largest magnitude in the discrete spectral representation of a permittivity perturbation. Based on this observation, we introduced a design technique whereby a desired spectral response is inverse Fourier transformed to produce the corresponding permittivity perturbation in space. The approach is general and can be used to design gratings of arbitrary reflectance response. The outcome is a complex permittivity profile of the desired Bragg grating. This method provides an efficient way to design devices for a variety of purposes, such as generating frequency combs, single-frequency lasers, unidirectional lasers (e.g., exceptional point gratings), of arbitrary permittivity profile.

Using this technique, we arrived at the concept of a Dirac grating, where (strong or weak) periodic perturbations of vanishing duty cycle approach a train of Dirac functions. Such gratings produce interesting spectral responses, such as order-independent performance for the same grating length. We provided practical design examples based on a dielectric stack and on an SOI waveguide. The analytical TMM and numerical EME methods were used to verify the performance on these examples and verify the concept of Dirac gratings. Apart from their interesting behavior, Dirac gratings have practical significance in that higher order gratings can be used in place of lower order gratings while maintaining the same performance for the same grating length.

Funding. National Research Council Canada; Natural Sciences and Engineering Research Council of Canada.

Disclosures. The authors declare no conflicts of interest.

Data availability. Data underlying the results presented in this paper are not publicly available at this time but may be obtained from the authors upon reasonable request.

References

1. A. Yariv, "Coupled-mode theory for guided-wave optics," IEEE J. Quantum Electron. **9**(9), 919–933 (1973).
2. L. A. Coldren, G. A. Fish, Y. Akulova, J. S. Barton, L. Johansson, and C. W. Coldren, "Tunable semiconductor lasers: A tutorial," J. Lightwave Technol. **22**(1), 193–202 (2004).
3. A. Othonos, "Fibre Bragg gratings," Rev. Sci. Instrum. **68**(12), 4309–4341 (1997).
4. J. Wang and L. R. Chen, "Low crosstalk Bragg grating/Mach-Zehnder interferometer optical add-drop multiplexer in silicon photonics," Opt. Express **23**(20), 26450–26459 (2015).
5. R. Kashyap, *Fiber Bragg Gratings* (Academic Press, 2009).
6. W. Streifer, D. R. Scifres, and R. D. Burnham, "Coupling coefficients for distributed feedback single-and double-heterostructure diode lasers," IEEE J. Quantum Electron. **11**(11), 867–873 (1975).
7. M. C. Parker, R. J. Mears, and S. D. Walker, "High refractive index contrast Bragg gratings: an accurate Fourier transform theory," in *Bragg Gratings, Photosensitivity, and Poling in Glass Waveguides* (Optica Publishing Group, 2001) BThC10.
8. J. Čtyroký, S. Helfert, R. Pregla, P. Bienstman, R. Baets, R. De Ridder, R. Stoffer, G. Klaasse, J. Petráček, P. Lalanne, and J. P. Hugonin, "Bragg waveguide grating as a 1D photonic band gap structure: COST 268 modelling task," Opt. Quantum Electron. **34**(5-6), 455–470 (2002).
9. S. Saeidi, F. Wu, C. Watson, Y. Logvin, and P. Berini, "Strong and short Bragg waveguide gratings with trapezoidal-shaped grooves," J. Lightwave Technol. **39**(13), 4395–4401 (2021).
10. R. Feced, M. N. Zervas, and M. A. Muriel, "An efficient inverse scattering algorithm for the design of nonuniform fiber Bragg gratings," IEEE J. Quantum Electron. **35**(8), 1105 (1999).
11. D. Pereira-Martín, J. M. Luque-González, J. G. Wangüemert-Pérez, A. Hadij-ElHouati, Í. Molina-Fernández, P. Cheben, J. H. Schmid, S. Wang, N. Y. Winnie, J. Čtyroký, and A. Ortega-Moñux, "Complex spectral filters in silicon waveguides based on cladding-modulated Bragg gratings," Opt. Express **29**(11), 15867–15881 (2021).
12. T. Zhu, Y. Hu, P. Gatkine, S. Veilleux, J. Bland-Hawthorn, and M. Dagenais, "Arbitrary on-chip optical filter using complex waveguide Bragg gratings," Appl. Phys. Lett. **108**(10), 101104 (2016).
13. H. Li and Y. Sheng, "Direct design of multichannel fiber Bragg grating with discrete layer-peeling algorithm," IEEE Photonics Technol. Lett. **15**(9), 1252–1254 (2003).
14. J. Skaar and K. M. Risvik, "A genetic algorithm for the inverse problem in synthesis of fiber gratings," J. Lightwave Technol. **16**(10), 1928–1932 (1998).
15. H. Szu and R. Hartley, "Fast simulated annealing," Phys. Lett. A **122**(3-4), 157–162 (1987).
16. A. V. Buryak, K. Y. Kolossovski, and D. Y. Stepanov, "Optimization of refractive index sampling for multichannel fiber Bragg gratings," IEEE J. Quantum Electron. **39**(1), 91–98 (2003).

Research Article Vol. 31, No. 19 / 11 Sep 2023 / Optics Express 31211
Optics EXPRESS

17. R. Blanchard, S. Menzel, C. Pflügl, L. Diehl, C. Wang, Y. Huang, J. H. Ryou, R. D. Dupuis, L. Dal Negro, and F. Capasso, "Gratings with an aperiodic basis: single-mode emission in multi-wavelength lasers," New J. Phys. **13**(11), 113023 (2011).
18. S. Chakraborty, O. P. Marshall, Md. Khairuzzaman, C. W. Hsin, H. E. Beere, and D. A. Ritchie, "Longitudinal computer-generated holograms for digital frequency control in electronically tunable terahertz lasers," Appl. Phys. Lett. **101**(12), 1 (2012).
19. W. H. Press, *Numerical Recipes: The Art of Scientific Computing*, 3rd edition (Cambridge University Press, 2007).
20. J. Ahrens, C. Andersson, P. Höstmad, and W. Kropp, "Tutorial on Scaling of the Discrete Fourier Transform and the Implied Physical Units of the Spectra of Time-Discrete Signals," Audio Engineering Society Convention **148**, 1 (2020).
21. G. P. Agrawal and N. K. Dutta, *Long-wavelength Semiconductor Lasers* (Van Nostrand Reinhold, 1986).
22. B. P. Pal, *Guided Wave Optical Components and Devices: Basics, Technology, and Applications* (Academic Press, 2010).
23. N. Matuschek, F. X. Kartner, and U. Keller, "Exact coupled-mode theories for multilayer interference coatings with arbitrary strong index modulations," IEEE J. Quantum Electron. **33**(3), 295–302 (1997).
24. H. A. Haus, *Waves and Fields in Optoelectronics* (Prentice-Hall, 1984).
25. L. Feng, M. Ayache, J. Huang, Y. L. Xu, M. H. Lu, Y. F. Chen, Y. Fainman, and A. Scherer, "Nonreciprocal light propagation in a silicon photonic circuit," Science **333**(6043), 729–733 (2011).
26. B. Qi, H. Z. Chen, L. Ge, P. Berini, and R. M. Ma, "Parity–time symmetry synthetic lasers: Physics and devices," Adv. Opt. Mater. **7**(22), 1900694 (2019).
27. T. Hao and P. Berini, "Directional coupling with parity-time symmetric Bragg gratings," Opt. Express **30**(4), 5167–5176 (2022).
28. C. Hahn, E. K. Keshmarzi, S. H. Song, C. H. Oh, R. N. Tait, and P. Berini, "Unidirectional Bragg gratings using parity-time symmetry breaking in plasmonic systems," IEEE J. Sel. Top. Quantum Electron. **22**(5), 48–59 (2016).
29. M. Verbist, D. Van Thourhout, and W. Bogaerts, "Weak gratings in silicon-on-insulator for spectral filters based on volume holography," Opt. Lett. **38**(3), 386 (2013).
30. M. L. Boas, *Mathematical Methods in the Physical Sciences* (John Wiley & Sons, 2006).
31. E. D. Palik ed., *Handbook of Optical Constants of Solids* (Academic Press, 1998).
32. N. R. Fong, M. Menotti, E. Lisicka-Skrzek, H. Northfield, A. Olivieri, N. Tait, M. Liscidini, and P. Berini, "Bloch long-range surface plasmon polaritons on metal stripe waveguides on a multilayer substrate," ACS Photonics **4**(3), 593–599 (2017).
33. Lumerical is Now Part of the Ansys Family (2023), https://www.lumerical.com/.
34. S. Rashid, J. Walia, H. Northfield, C. Hahn, A. Olivieri, A. C. Lesina, F. Variola, A. Weck, L. Ramunno, and P. Berini, "Helium ion beam lithography and liftoff," Nano Futures **5**(2), 025003 (2021).

Chapter 8

Finite-Difference Coupled-Mode Analysis of Waveguide Gratings And Their Optimization for Single-Mode DFB Lasers

8.1 Contribution Statement

This project originated in Prof. Dolgaleva's group, building on the prior work of Tuhin Paul and Boris Rosenstein (third and fourth authors), and was initially led by Sina Aghili (second author). I joined the project due to my background in grating design and programming. The theoretical foundation and methodology presented in the paper were developed primarily through close collaboration between Aghili and me, under the supervision of Prof. Dolgaleva, Prof. Berini, and Dr. Tolstikhin.

I developed the finite-difference based simulation algorithm, carried out the optimization of our studied example, conducted several key simulations, generated the figures for the manuscript, and wrote the initial draft of the paper, except for Section 2. B.

8.2 Article

438 Vol. 42, No. 2 / February 2025 / Journal of the Optical Society of America B Research Article

Journal of the Optical Society of America B OPTICAL PHYSICS

Finite-difference coupled-mode analysis of waveguide gratings and their optimization for single-mode DFB lasers

Shayan Saeidi,[1,2,3,*] Sina Aghili,[1,2,3] Tuhin Paul,[4] Boris Rosenstein,[1] Valery Tolstikhin,[5] Pierre Berini,[1,2,4] and Ksenia Dolgaleva[1,2,4]

[1]School of Electrical Engineering and Computer Science, University of Ottawa, Ottawa, Ontario K1N 6N5, Canada
[2]Nexus for Quantum Technologies Institute, University of Ottawa, Ottawa, Ontario K1N 6N5, Canada
[3]KVector Dynamics, Ottawa, Ontario K2B8E1, Canada
[4]Department of Physics, University of Ottawa, Ottawa, Ontario K1N 6N5, Canada
[5]Intengent Inc., Ottawa, Ontario K2K2X3, Canada
*shayan.saeidi@kvectordynamics.com

Received 9 September 2024; revised 1 December 2024; accepted 3 January 2025; posted 3 January 2025; published 31 January 2025

This study presents a semi-numerical algorithm based on the coupled-mode theory combined with finite differencing to assess the performance of one-dimensional trapezoidal waveguide gratings, as well as arbitrarily shaped ones. Our approach not only surpasses traditional finite-difference time-domain (FDTD) and finite-element method (FEM) solvers in computational efficiency but also provides insightful information on DFB stack design by including partially confined radiative waves. We apply this method to investigate fifth-order trapezoidal waveguide gratings and optimize groove profiles in the context of a single-mode DFB laser, demonstrating its potential for rapid design and analysis in photonics applications.

https://doi.org/10.1364/JOSAB.541856

1. INTRODUCTION

Since their introduction, waveguide Bragg gratings (WBGs) have played a vital role in the development of active and passive photonic devices. WBGs function by selectively reflecting certain wavelengths of light in accordance with the grating's periodicity. Distributed-feedback (DFB) and distributed Bragg reflector (DBR) cavity lasers, grating couplers, and filters are just a few of their many applications in optical tele- and datacom, sensing, microwave photonics, and more [1–3].

Conventionally, the coupled-mode theory (CMT) was extensively employed to investigate the performance of WBGs because it provides an effective way to model light interaction in these gratings by emphasizing the coupling between waves propagating in opposite directions. In this method, both fundamental forward- and backward-propagating contra-guided waves were considered in the calculation of the coupling coefficient—an essential parameter for evaluating WBG efficiency [4,5]. Streifer *et al*. significantly improved upon the CMT by incorporating all interacting waves, including guided modes, partially confined radiative modes (also termed partial waves), and diffracted waves [6]. Streifer's method was superseded by the numerical methods, which facilitate the modeling of WBGs with arbitrary-shaped corrugations [7–9]. However, the primary challenge associated with numerical methods is the long simulation time required, resulting in high computational expense.

Here, we report a newly developed semi-numerical algorithm to calculate the coupling coefficient of any arbitrary grating, resting on the CMT formulation introduced by Streifer *et al.* [6]. Our algorithm yields precise solutions for geometries of greater complexity than those examined by Streifer while requiring minimal computational resources, yielding results in significantly reduced computational time compared to mainstream numerical methods. The numerical algorithm is implemented in Python and available in Ref. [10].

The remaining of the paper is organized as follows. In Section 2, we present three methodologies for determining the coupling coefficient of a WBG: (A) the approach proposed and used in this paper, termed the finite-difference coupled-mode theory (FD CMT); (B) a numerical scheme based on the finite-element method (FEM); and (C) that using the finite-difference time-domain (FDTD) method. Subsequently, a comparative analysis of the results is reported in Section 3. In Section 4, we analyze a fifth-order grating, explain the rationale for this choice, and discuss the optimization of the WBG profile for single-mode operation in a DFB laser (DFBL). Finally, a conclusion is given in Section 5.

Research Article Vol. 42, No. 2 / February 2025 / Journal of the Optical Society of America B 439

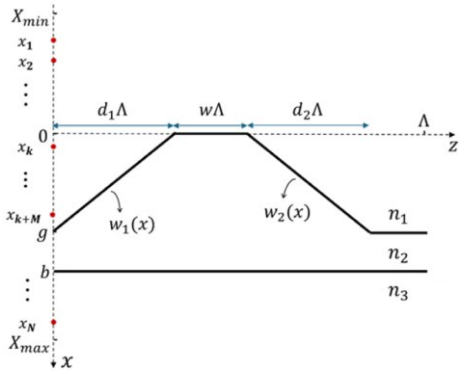

Fig. 1. Single period of the studied grating structure.

2. METHODS

A. Finite-Difference Coupled-Mode Theory

1. *Finite-Difference Solution for Fundamental and Partial Waves*

Figure 1 shows a three-layer slab waveguide featuring an embedded grating at the interface between its core and cover layers. In the real waveguide structure, it could be related to, the embedded WBG would be formed by patterned etching and blanket overgrowth, a standard process used in fabrication of the DFBLs, allowing for a certain degree of flexibility in terms of the grating pitch, shape, and depth.

Referring to the near-infrared spectral range, e.g., communication O- or C-band important for applications, the first-order grating would require such a lithography with well below 100 nm resolution, which is not commonly available in the photonic fabs. An alternative would be the higher-order grating, typically third or fifth order (depending on the etching process), implementable with a more accessible I-line stepper (365 nm wavelength).

Following Streifer's notation, the main transverse electric field component of the fundamental TE mode $\varepsilon_0(x)$ at the Bragg wavelength $\lambda_B = 2n_{\text{eff}}\Lambda$ is described by the Helmholtz equation:

$$\frac{d^2\varepsilon_0(x)}{dx^2} + \left[k_0{}^2 n^2(x) - \beta_0{}^2\right]\varepsilon_0(x) = 0, \tag{1}$$

where $k_0 = 2\pi/\lambda_B$ is the free-space wavenumber, $\beta_0 = 2\pi n_{\text{eff}}/\lambda_B$ is the propagation constant of the TE mode, and n_{eff} is its effective index. For the remainder of this paper, we will follow the time-harmonic form $\exp(-j\omega t)$ and consider only the TE mode.

The refractive index $n(x)$ equals n_1, n_2, and n_3 in the cover ($x < 0$), core ($g < x < b$), and substrate ($x > b$) regions, respectively. In the grating region ($0 < x < g$), the refractive index varies with both x and z. However, due to its periodicity in z, the z dependence can be expressed through a Fourier series, reducing the refractive index to a function of x alone. The details of this approach are provided in Ref. [6]. Therefore, in the grating region, the refractive index $n(x)$ is represented as

$$n_g(x) = \sqrt{n_2{}^2 + \frac{\left(n_1{}^2 - n_2{}^2\right)\left[w_2(x) - w_1(x)\right]}{\Lambda}}, \tag{2}$$

where the groove's profile is characterized by the functions $w_1(x)$ and $w_2(x)$, which are, in general, arbitrary. In this paper, we assume these functions to be linear, resulting in a trapezoidal profile. This choice allows for direct comparison with the results reported by Streifer *et al*. [11] and better aligns with DFB laser fabrication methods, as etching processes often produce grooves with linearly sloped walls.

To calculate the effective index of the waveguide with grating, n_{eff}, we employ a method similar to that described in Ref. [12]. We first discretize the grating region into a series of grids along the x axis. Figure 2(a) illustrates the 1D refractive index profile of the structure along the x axis (green lines), where according to Eq. (2), $n_g{}^2(x)$ varies linearly in the grating region ($0 < x < g$). We discretize the refractive index distribution $n_g{}^2(x)$ into M + 1 (M is an integer) equally spaced grids. The divisions between grids are identified by black dots in Fig. 2(a), each located at x_{k+v} ($v = 1, 2, \ldots, M$). At each division point, two distinct slab waveguides are constructed. An example for $x = x_{k+v}$ is shown in Fig. 2(a): the first waveguide (shown by red lines) incorporates the cover layer extending into the grating region with a thickness x_{k+v}. Beyond this point, another layer extends continuously to the core with the refractive index of $n(x_{k+v})$. The second waveguide (shown by blue lines) includes the core layer extending into the grating region with a thickness of $g - x_{k+v}$. Another layer extends from $x = x_{k+v}$ to the cover at $x = 0$, with the refractive index of $n(x_{k+v})$.

It is straightforward to calculate the effective refractive index of each slab waveguide, as described, e.g., in Ref. [13]. Figure 2(b) shows the effective index of these two waveguides (red and blue curves) as a function of x_{k+v} for grating System 1, described in Table 1. The n_{eff} of grating System 1 is taken as the average of these values and is found to be 3.5797, which shows excellent agreement with Ref. [11]. We used intervals of $x_{k+v} - x_{k+v-1} = 10$ nm in this calculation. Smaller intervals yield more accurate results but increase computation time. It is crucial to choose intervals small enough for n_{eff} to converge, as inaccurate values can significantly impact subsequent calculations.

After finding n_{eff} and β_0, the mode functions are expressed analytically within each layer. The first-order perturbation for the partial wave $\varepsilon_m(x)$ is defined by the solution of this equation [6,11]:

$$\frac{d^2\varepsilon_m^{(i)}(x)}{dx^2} + \left[k_0{}^2 n^2(x) - \beta_m{}^2\right]\varepsilon_m^{(i)}(x) = -k_0{}^2 A_{m-i}(x)\,\varepsilon_0(x), \tag{3}$$

where $\beta_m = \beta_0 + 2\pi m/\Lambda$ represents the propagation constant of the partial wave of order $m (m \neq i)$; $A_q(x)$ is the qth Fourier coefficient of the grating; and i denotes the forward ($i = 0$) or backward ($i = p$) propagation direction of the wave, with $p = -P$, where P is the grating order. $A_q(x)$ is zero everywhere except for the grating layer, where it equals

$$A_q(x) = \frac{n_f{}^2 - n_c{}^2}{j2\pi q}\left[e^{-\frac{j2\pi q w_2(x)}{\Lambda}} - e^{-\frac{j2\pi q w_1(x)}{\Lambda}}\right]. \tag{4}$$

Since Eq. (3) represents an inhomogeneous Helmholtz equation, numerical methods are preferable for its solution, especially for arbitrarily shaped grating profiles. Using our discretization of the structure along the x axis, we

440 Vol. 42, No. 2 / February 2025 / Journal of the Optical Society of America B Research Article

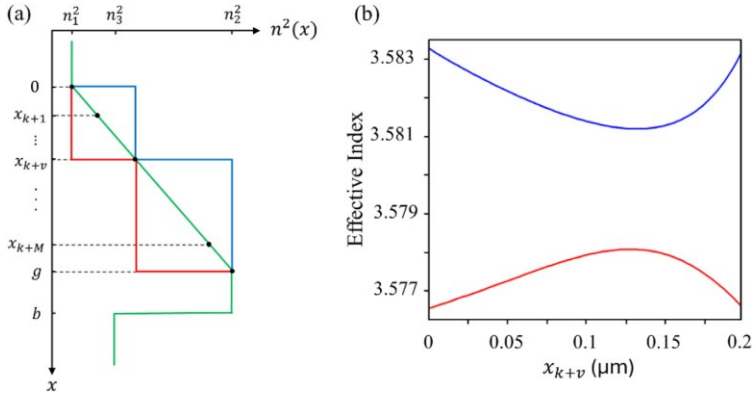

Fig. 2. (a) Refractive index distribution over the x axis, shown by the green lines. The grating layer is discretized into $M+1$ grids, where the division of grids is identified by black dots at x_{k+v} for $v = 1, \ldots, M$. Two waveguides are generated at each dot, shown by the red and blue lines. (b) Effective index of the waveguides depicted by the red and blue lines in (a), as a function of x_{k+v}.

Table 1. Parameters of the Grating System 1

Parameter	w	d_1	d_2	n_1	n_2	n_3	g	b	Λ	λ_B
Value	0	0.25	0.75	3.4	3.6	3.4	0.2 μm	1 μm	237.5 nm	850 nm

rewrite the left-hand side of Eq. (3) using a central difference approximation:

$$\varepsilon_m^{(i)\prime\prime}(x) \approx \frac{\varepsilon_m^{(i)}(x+h) - 2\varepsilon_m^{(i)}(x) + \varepsilon_m^{(i)}(x-h)}{h^2}, \tag{5}$$

where

$$h = \frac{X_{\max} - X_{\min}}{N-1}. \tag{6}$$

Here, N is the total number of grids used in the discretization, and $X_{\min}$ and $X_{\max}$ are the boundaries of the simulation window. Thus, we transform the differential equation given by Eq. (3) into N linear equations of the form

$$\frac{\varepsilon_{m\,l+1}^{(i)} - 2\varepsilon_{m\,l}^{(i)} + \varepsilon_{m\,l-1}^{(i)}}{h^2} + \left({k_0}^2 n^2(x_l) - {\beta_m}^2\right)\varepsilon_{m\,l}^{(i)} = -{k_0}^2 A_{m-i}(x_l)\,\varepsilon_0(x_l), \tag{7}$$

where $1 \le l \le N$ (x_ls are shown in Fig. 1). There are N equations with $N+2$ unknowns, including $\varepsilon_{m\,0}^{(i)}$ and $\varepsilon_{m\,N+1}^{(i)}$, which can be eliminated by substituting appropriate boundary conditions to terminate the computational domain at $X_{\min}$ and $X_{\max}$.

Given our emphasis on modeling partial waves (radiative modes), we apply radiative boundary conditions at $X_{\min}$ and $X_{\max}$ by defining plane waves propagating outward from the domain in the $\pm x$ directions at these locations. These conditions provide two additional equations, which allow us to relate $\varepsilon_{m\,0}^{(i)}$ and $\varepsilon_{m\,N+1}^{(i)}$ to the fields within the domain. The radiative boundary conditions are defined as follows:

$$\varepsilon_{m\,1}^{(i)} = \varepsilon_{m\,0}^{(i)} e^{-jk_1 h}, \tag{8a}$$

$$\varepsilon_{m\,N}^{(i)} = \varepsilon_{m\,N+1}^{(i)} e^{-jk_N h}, \tag{8b}$$

where $k_1 = \sqrt{{k_0}^2 {n_1}^2 - {\beta_m}^2}$ and $k_N = \sqrt{{k_0}^2 {n_3}^2 - {\beta_m}^2}$ are the transverse components of the plane waves' wavenumbers.

2. Computing Streifer's Coefficients

Once the $\varepsilon_m^{(i)}$ are determined, the partial wave parameters $\zeta_{1,\ldots,4}$ introduced by Streifer *et al.* [6] can be readily calculated. These parameters, extensively discussed in Refs. [6,11], are summarized as follows:

$$\zeta_1 = \sum_{\substack{q=-\infty \\ q\neq 0,-p}}^{\infty} \eta_{q,-q}^{(0)}, \tag{9a}$$

$$\zeta_2 = \sum_{\substack{q=-\infty \\ q\neq 0,-p}}^{\infty} \eta_{q,-q}^{(p)}, \tag{9b}$$

$$\zeta_3 = \sum_{\substack{q=-\infty \\ q\neq 0,p}}^{\infty} \eta_{q,p-q}^{(p)}, \tag{9c}$$

$$\zeta_4 = \sum_{\substack{q=-\infty \\ q\neq 0,p}}^{\infty} \eta_{q,p-q}^{(0)}, \tag{9d}$$

where

$$\eta_{r,s}^{(i)} = \frac{{k_0}^2}{2\beta} \frac{\int_0^g A_r(x)\,\varepsilon_0(x)\,\varepsilon_s^{(i)}(x)\,dx}{\int_{-\infty}^{\infty} {\varepsilon_0}^2(x)\,dx}, \tag{9e}$$

$$\kappa_p = \frac{{k_0}^2}{2\beta} \frac{\int_0^g A_p(x)\,{\varepsilon_0}^2(x)\,dx}{\int_{-\infty}^{\infty} {\varepsilon_0}^2(x)\,dx}. \tag{9f}$$

Here κ_p is the coupling coefficient. In general, including more partial terms improves the accuracy of the results, though at the cost of increased computational time. However, per our experience, the partial terms have negligible effect when $|q| > P$ ($q \neq 0$). The coupling coefficient of the higher-order grating, incorporating contributions from partial terms $\zeta_{1,\ldots,4}$, can be

Research Article Vol. 42, No. 2 / February 2025 / Journal of the Optical Society of America B 441

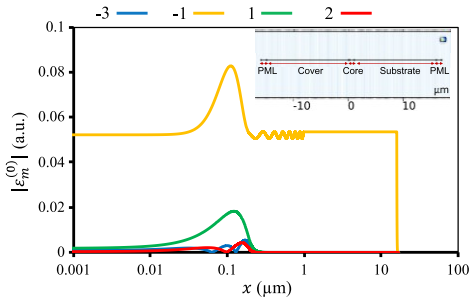

Fig. 3. Dominant orders of partial waves (legends show the order m). The inset presents the geometry of System 1, rigorously discretized by the FEM solver.

described using an effective coupling coefficient [14]:

$$\kappa_{\text{eff}} = \sqrt{(\kappa_p{}^* + \zeta_2)(\kappa_p + \zeta_4)}. \tag{10}$$

B. Finite-Element Method

We use the commercial FEM software, COMSOL v6.1 [15], to analyze an example triangular-profiled grating, labeled System 1 and described in Table 1. FEM solvers enable numerical calculations of n_{eff}, $\varepsilon_0(x)$, and $\varepsilon_m^{(i)}(x)$ through a multistep modeling process.

First, a wave equation study using the RF module is implemented to solve Eq. (1) numerically. The refractive indices and geometrical parameters of a WBG aligned with System 1 are defined. The inset of Fig. 3 shows the 1D configuration of the system as defined in the Geometry section of COMSOL. The simulation box is large enough and surrounded by perfectly matched layer (PML) boundary conditions to prevent reflections from the walls. Using the computed values of n_{eff} and $\varepsilon_0(x)$, we implement a general type of partial differential equation (PDE) from the Mathematics module,

$$\nabla \cdot \left(-c\nabla\varepsilon_m^{(i)}(x)\right) + a\varepsilon_m^{(i)}(x) = f, \tag{11}$$

to numerically calculate the partial waves. Equation (11) is defined by

$$c = -1/S(x), \tag{12}$$

$$a = \left(\beta_0^2 - \beta_m^2\right) S(x), \tag{13}$$

$$f = -k_0^2 A_{m-i}(x)\,\varepsilon_0(x)\,S(x), \tag{14}$$

where c, a, and f are the diffusion coefficient, the absorption coefficient, and the source term, respectively. The PML correction factor is

$$S(x) = 1 + i\frac{\sigma(x)}{\sqrt{|\beta_0^2 - \beta_m^2|}}, \tag{15}$$

where $\sigma(x)$ is the stretching factor [16].

Figure 3 shows the E-field distribution of the dominant orders of partially radiative waves across the waveguide in the forward setup ($i = 0$). The sudden drop of the fields at 15 μm is due to enforcing PML boundaries. It is obvious that the partial waves can constructively or destructively interact with guided modes while decaying as they approach the modified absorber walls. At the end of this step, one can recall Eqs. (9) and (10) to calculate the effective coupling coefficient of System 1.

C. Finite-Difference Time-Domain

Due to the periodic modulation in gratings, a range of wavelengths surrounding the Bragg wavelength λ_B will not be transmitted at the output of the gratings. This range is termed the stopband, and its width is referred to as the bandwidth. The bandwidth of a grating can be theoretically obtained using the CMT as [17]

$$\Delta\lambda = \frac{{\lambda_B}^2}{L n_{\text{group}}}\sqrt{1 + \left(\frac{L|\kappa_{\text{eff}}|}{\pi}\right)^2}, \tag{16}$$

where n_{group} represents the group index. According to Eq. (16), we can calculate the coupling coefficient by knowing the bandwidth.

One can utilize the FDTD technique to carry out this calculation. By modeling a finite-length grating bounded by PML conditions and launching the fundamental mode of the unperturbed waveguide at the input of the grating, the reflectance and transmittance of the waveguide mode can be computed. This is achieved by implementing frequency-domain monitors located at the input and output of the grating, respectively. Such simulations have been elaborated [18,19].

However, simulations of finite-length gratings are computationally expensive and time-consuming. A more efficient FDTD approach has been reported [20], wherein an infinitely long grating is modeled by simulating only one unit cell and applying Bloch boundary conditions along the propagation axis. We use this technique in the commercial software Lumerical FDTD [21] to determine $\Delta\lambda$ and subsequently calculate $|\kappa_{\text{eff}}|$ using Eq. (16). The fundamental mode of the slab waveguide serves as the source for our simulations. A mode pulse of a few femtoseconds (consecutively, with a broad spectrum) is launched into the grating. This pulse propagates to the output boundary, and due to the periodicity of the system, re-enters from the input boundary. This process repeats until the simulation time finishes or the energy within the simulation window reaches a predefined threshold. A frequency-domain monitor, positioned perpendicularly to the propagation direction within the simulation window, captures the wave spectrum transmitted through the system. The normalized square of the transmitted field, or transmittance, is illustrated in Fig. 4 for the grating System 1 for various simulation durations. It is evident that as the simulation time increases, the width of the peaks narrows, and the peaks become more distinguishable. Weak gratings have narrow bandwidths, and their peaks are closer to each other, therefore requiring more simulation time.

The bandwidth and the Bragg wavelength can be determined from the positions of these two peaks. By reformulating Eq. (16) with the length approaching infinity, the magnitude of the coupling coefficient can be deduced from

$$|\kappa_{\text{eff}}| = \frac{\Delta\lambda\pi\, n_{\text{group}}}{{\lambda_B}^2}. \tag{17}$$

442 Vol. 42, No. 2 / February 2025 / Journal of the Optical Society of America B Research Article

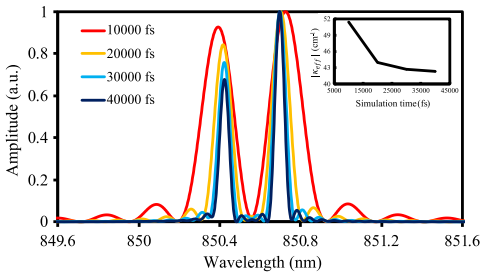

Fig. 4. Transmittance for different simulation times (from Lumerical FDTD). The inset shows calculated $|\kappa_{\text{eff}}|$ as a function of the simulation time.

The inset of Fig. 4 plots the variation of $|\kappa_{\text{eff}}|$ as a function of the simulation time. For materials with the refractive indices that are weakly dependent on the wavelength (such as III–V semiconductors in the infrared), n_{group} can be replaced by n_{eff} (as was done in this calculation). The convergence becomes evident with increasing simulation time, suggesting that short simulation times may yield inaccurate results.

3. COMPARISON OF METHODS

In this section, the coupling coefficients of the fundamental mode obtained by FD CMT, FEM, and FDTD are compared to each other and to the data reported in Ref. [13] for the grating structure of System 1, as a function of d_1 ($d_2 = 1 - d_1$). In FDTD simulations, we used 40,000 fs for the simulation time with a time step of 0.015 fs and a uniform mesh size of 3 nm. The FD CMT and FEM simulations were conducted with $-8 < q < 7$ and a mesh size of 3 nm for discretization. This mesh size was selected to ensure the convergence, as discussed later in this section.

Figures 5(a) and 5(b) plot $|\kappa_{\text{eff}}|$ and $\angle\kappa_{\text{eff}}$, respectively, as functions of d_1. Overall, good agreement exists between all three methods. The $|\kappa_{\text{eff}}|$ is minimum when the grating is symmetric and reaches its maximum at $d_1 = 0.15$ and 0.85. This triangled grating exhibits a small phase regardless of d_1, suggesting minimal radiation loss. The highest phase is achieved where $|\kappa_{\text{eff}}|$ is minimum. An important feature of a grating having a large phase of κ_{eff} is its ability to increase mode selectivity. This aspect will be discussed further in Section 4.

Table 2 compares the computational times of the three methods for the grating System 1. The computational power remains consistent across all cases, on an Intel Core i7-10700 CPU at 2.9 GHz processor and 32 GB of RAM. The efficiency of the FD CMT compared to other methods is remarkable.

Table 2. Comparison of Computing Time of Different Simulation Methods

Method	FD CMT	FEM	FDTD
Computing time (s)	~10	~900	~600

The primary reason for the FD CMT's superior efficiency over the FEM lies in how each solver handles meshing. The FD CMT applies boundary conditions primarily at the edges of the overall problem domain to enforce physical constraints. In contrast, the FEM discretizes problem by thousands of free triangular elements, solving the solution within each element and ensuring convergence via regular iterative refinement. Meanwhile, the FDTD, being an inherently time-domain solver, requires both spatial and temporal stepping, which makes it a time-consuming method.

For the FEM, note that the actual simulation time is significantly longer than the listed computational time due to the need for identical data mapping between different modules in COMSOL.

Figure 6(a) illustrates the convergence of $|\kappa_{\text{eff}}|$ for each method as the mesh size is reduced from 45 nm. The FDTD method decreases in steps of 3 nm, while the FEM method is refined in steps of 10 nm. The FD CMT method is shown with continuous lines refined in 1 nm steps. Other simulation settings are as discussed above. In the smaller mesh size range (down to 10 nm), all the methods converge to the same value. However, as the mesh grid size increases, both the FDTD and FD CMT methods yield similar results due to their identical meshing principles along with a decrease in the simulation time. In contrast, the FEM shows better overall convergence owing to the higher accuracy of finite-element meshing, albeit at the cost of longer simulation times.

Figure 6(b) shows the convergence of $|\kappa_{\text{eff}}|$ as a function of the number of partial modes included in the FD CMT simulation. The partial modes, represented on the horizontal axis, are symmetrically distributed with respect to $q = 0$, excluding $q = 0$ itself. For example, including two modes corresponds to q ranging from -1 to 1. A value of 0 on the horizontal axis indicates that no partial mode is included. As discussed in Section 2.A.2, $|\kappa_{\text{eff}}|$ converges when the summations in Eq. (9) incorporate partial waves for $|q| > P$ (here, $P = 2$).

4. OPTIMIZATION OF THE WBG FOR A SINGLE-MODE DFBL

In the DFBL design, commonly used first-order gratings have the advantage that guided waves are decoupled from partial

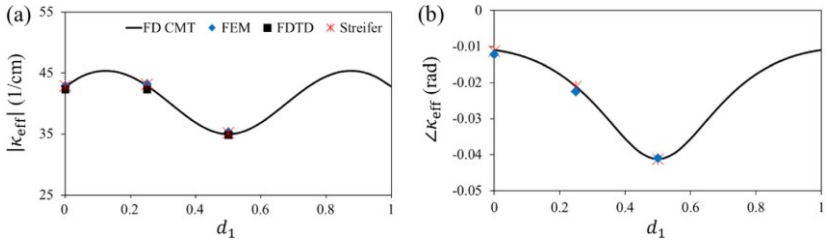

Fig. 5. Comparison of the (a) amplitude and (b) phase of the effective coupling coefficient κ_{eff} obtained using different methods.

Research Article Vol. 42, No. 2 / February 2025 / Journal of the Optical Society of America B 443

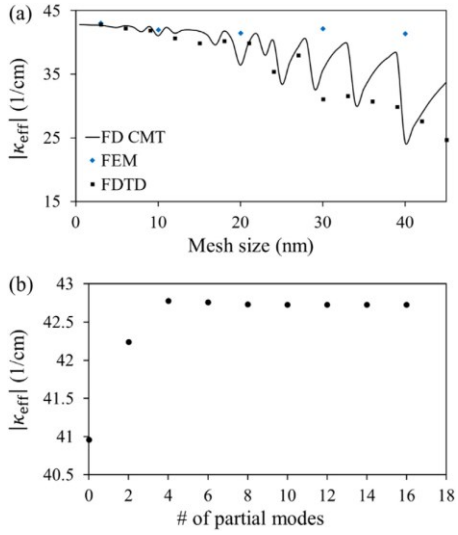

Fig. 6. (a) Coupling coefficient $|\kappa_{\text{eff}}|$ as a function of the mesh size used in FD CMT, FEM, and FDTD. (b) $|\kappa_{\text{eff}}|$ as a function of the number of partial modes included in the FD CMT.

waves, so no radiation loss occurs in this case. This minimizes the threshold current and maximizes the slope efficiency, but it makes the laser susceptible to mode hopping due to the degeneracy of the longitudinal modes. In a DFBL with a higher-order grating, the radiation loss associated with the resonant coupling between guided and partial waves increases the threshold current and reduces the slope efficiency, but it has the advantage of breaking longitudinal mode degeneracy [22–25]. To demonstrate the mode selectivity in higher-order gratings, we optimize a fifth-order grating in this section for the single-mode operation. We chose a fifth-order grating for three reasons: first, while second- and third-order gratings have been extensively studied [8,9,23,25,26] and fourth-order to some extent [27,28], fifth-order gratings remain relatively unexplored. Second, in the O-band, a fifth-order grating has a pitch of ∼1 μm, which is well-suited for fabrication using inexpensive photolithography techniques, e.g., based on a mask aligner. Third, fifth-order gratings inherently have many radiative modes, making them good candidates to test the accuracy of our FD CMT scheme.

Table 3 describes the parameters of the model structure depicted in Fig. 1 used for an illustration of how the WBG could be optimized for a single-mode DFBL operation. It is representative of an InP-based DFBL with the overgrown WBG. By varying the values of w and d ($= d_1 = d_2$), the trapezoid grating profile may be changed to rectangular or triangular. Varying g adjusts the depth of the grating. The optimization procedure is as follows: we vary w from 0 to 1 (in a step size of 0.02) and d from 0 to $(1 - w)/2$ (in a step size of 0.02). Increasing d further will make the groove profile resemble an outward trapezoid, which is unlikely to occur in fabrication. Therefore, we excluded such cases from our analysis.

We vary g from 0.25 to 0.75 μm in a step of 0.25 μm. The optimization goal for such a structure is to achieve a single-mode spectrum while maintaining a high coupling coefficient magnitude. The coupling strength of a grating is commonly assessed

Table 3. Parameters of the Grating System 2

Parameter	n_1	n_2	n_3	P	b	λ_B
Value	3.2	3.3	3.2	5	1 μm	1300 nm

using the product of the coupling coefficient and the length, denoted $|\kappa_{\text{eff}}|L$. A strong grating is characterized by $|\kappa_{\text{eff}}|L > 1$, indicating that for a typical laser length of 1 mm, the value of $|\kappa_{\text{eff}}|$ should be at least 10 cm^{-1}. Thus, in our optimization algorithm, we assume a 1 mm long laser and only consider the geometries that result in $|\kappa_{\text{eff}}|$ values greater than 10 cm^{-1}. We select the one with the largest phase from the resulting geometries to achieve single-mode performance.

Figures 7(a) and 7(b) depict the amplitude and phase, respectively, of the coupling coefficient at a wavelength of 1300 nm computed using the algorithm discussed in Section 2.A. The data points with $|\kappa_{\text{eff}}| < 10\ \text{cm}^{-1}$ are omitted for clarity. The simulation was conducted with the following settings: $X_{\min} = -3$ μm, $X_{\max} = 3$ μm, $-7 < q < 7$, and a step size of 3 nm for the discretization.

Upon initial observation, it is evident that the amplitude peaks coincide with minima in phase, and conversely, minimum amplitudes correspond to larger phase values. Deeper gratings generally exhibit higher amplitude and phase. It is important to note that the selection of groove shapes should be tailored to the specific application, as different applications may require different characteristics. However, in our case, we prioritize gratings with the largest phase.

Radiating waves interact with the contradirectional guided waves in a grating structure, partially coupling back into the laser waveguide. This interaction decreases or increases the guided wave intensity, effectively inducing additional loss or gain to the guided wave. From Fig. 7(b), we see that the sign of the phase of the coupling coefficient depends on the grooves' profile and can be either positive or negative, corresponding to partial gain or loss coupling, respectively. To achieve natural single-mode behavior in DFBLs, it is desirable to have a phase of large magnitude. According to Fig. 7(b), the largest phase is achieved at $w = 0.04$, $d = 0.32$, and $g = 0.75$ μm, corresponding to our optimized design.

To evaluate the lasing condition of the WBGs, we need to solve the coupled wave equations for the forward R and backward S traveling waves [11]:

$$\frac{dR}{dz} - (\alpha + i\delta + i\zeta_1)R = i\left(\kappa_p^* + \zeta_2\right)S, \tag{18a}$$

$$-\frac{dS}{dz} - (\alpha + i\delta + i\zeta_1)S = i\left(\kappa_p + \zeta_4\right)R, \tag{18b}$$

where $\delta = \beta - \beta_0$ represents the Bragg detuning parameter and α represents the sources of loss and gain, expressed as

$$\alpha = \Gamma g_{\text{mat}} - \alpha_{\text{sca}} - \alpha_{\text{abs}}, \tag{19}$$

where α_{abs} denotes the mode's loss due to material absorption, here assumed to be 0. The term α_{sca} refers to the scattered loss, represented by the normalized radiated power of partial waves escaping from the cavity and dissipating in the cover and substrate regions [6]:

444 Vol. 42, No. 2 / February 2025 / Journal of the Optical Society of America B Research Article

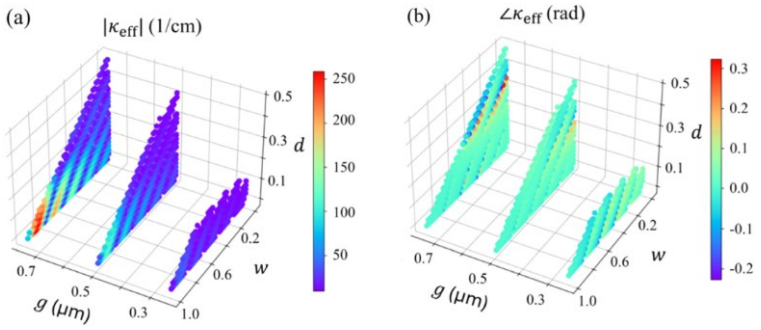

Fig. 7. (a) Amplitude and (b) phase of the effective coupling coefficient, κ_{eff}, as a function of d, w, and g.

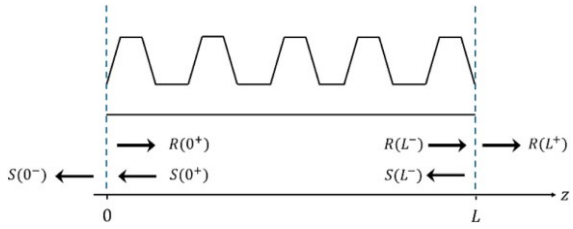

Fig. 8. Schematic of a DFB longitudinal cross section with forward R and backward S traveling waves.

$$\alpha_{sca} = \sum_m \mathrm{Re}\left\{\sqrt{k_0^2 n_c^2 - \beta_m^2}|\varepsilon_m(0)|^2 + \sqrt{k_0^2 n_s^2 - \beta_m^2}|\varepsilon_m(b)|^2\right\} \Big/ \left(\beta_0 \int_{-\infty}^{\infty} |\varepsilon_0(x)|^2 dx\right). \quad (20)$$

For our optimized structure, α_{sca} is 8.14 cm^{-1}. The term Γg_{mat} represents the modal gain, where Γ is the fraction of mode power overlapping with the gain region and g_{mat} is the material gain. The parameters α and δ are inherently coupled and typically solved numerically as pairs. We find these pairs numerically, based on the formulation discussed in Ref. [29]. To do so, we first define our boundary conditions. In our DFB structure, we assume that the facets at $z = 0$ and $z = L$ are cleaved and have the reflectivity of r, i.e., $R(0^+) = r\,S(0^+)$ and $S(L^-) = r\,R(L^-)$, as illustrated in Fig. 8. Figure 9 presents the paired eigenvalues, δ and α, at $L = 1$ mm and $r = 0.28$ (which is a typical value for an air/III–V material interface). These eigenvalue pairs determine the threshold characteristics of all potential lasing modes.

From Fig. 9, the shorter wavelength side of λ_B (right side of $\delta = 0$) exhibits the lowest threshold gain ($\alpha_{th} = 1.23\ cm^{-1}$), indicating it is the lasing mode. This notable disparity in threshold gain between this mode and its adjacent modes ensures a pronounced single-mode behavior and effective suppression of side modes. By substituting this value into Eq. (19), we find that this laser requires a modal gain Γg_{mat} of 9.37 cm^{-1} to reach the threshold gain. g_{mat} depends on the material system of the active region and the carrier injection level. For a typical III–V gain medium with multiple quantum wells, g_{mat} can reach values beyond 1000 cm^{-1}. Γ is highly dependent on the waveguide geometry and typically is around 0.1 [30,31].

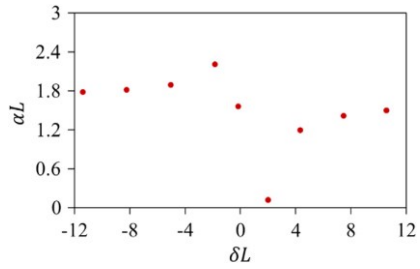

Fig. 9. Threshold characteristics of all potential lasing modes of System 2 for a cavity length of $L = 1$ mm and $r = 0.28$.

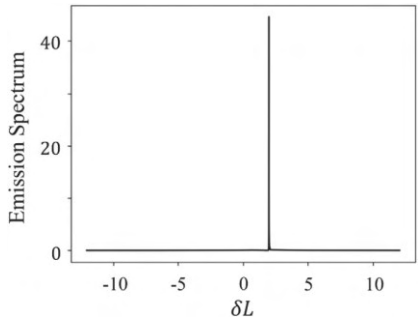

Fig. 10. Subthreshold emission spectrum of the optimized DFB structure with a groove profile defined by $w = 0.04$, $d = 0.32$, and $g = 0.75$ μm.

Figure 10 presents the emission spectrum derived using the analytic method described in Ref. [32], with α being just below the α_{th}. The spectrum reveals a pronounced natural single-mode behavior at $\delta L \approx 2$, consistent with the observations in Fig. 9.

5. CONCLUSION

We developed a semi-numerical algorithm based on the previously established coupled-mode theory to investigate waveguide gratings. We achieved excellent agreement with other numerical methods offered by commercial software packages. Our approach exhibits significantly faster computational performance, making it suitable for optimizing devices with extensive parameter sweeps. Leveraging this method, we investigated a generic InP-based grating and optimized it for single-mode

DFB operation, which is crucial for applications that demand a stable and high-quality signal output. The optimization, involving over 2000 different geometries using the FD CMT, would have been impractical to complete within a comparable timeframe using the FEM or FDTD.

Disclosures. The authors declare no conflicts of interest.

Data availability. Data underlying the results presented in this paper are not publicly available at this time but may be obtained from the authors upon reasonable request.

REFERENCES

1. L. A. Coldren, P. A. Verrinder, and J. Klamkin, "A review of photonic systems-on-chip enabled by widely tunable lasers," IEEE J. Quantum Electron. **58**, 6300110 (2022).
2. K. A. Williams, E. A. J. M. Bente, D. Heiss, *et al.*, "InP photonic circuits using generic integration," Photonics Res. **3**, B60–B68 (2015).
3. M. J. R. Heck, J. F. Bauters, M. L. Davenport, *et al.*, "Ultra-low loss waveguide platform and its integration with silicon photonics," Laser Photonics Rev. **8**, B60–B68 (2014).
4. H. Kogelnik and C. V. Shank, "Coupled-wave theory of distributed feedback lasers," J. Appl. Phys. **43**, 2327–2335 (1972).
5. A. Yariv, "Coupled-mode theory for guided-wave optics," IEEE J. Quantum Electron. **9**, 919–933 (1973).
6. W. Streifer, D. R. Scifres, and R. D. Burnham, "Analysis of grating-coupled radiation in GaAs:GaAlAs lasers and waveguides-I," IEEE J. Quantum Electron. **12**, 422–428 (1976).
7. J. Ctyroký, S. Helfert, R. Pregla, *et al.*, "Bragg waveguide grating as a 1D photonic band gap structure: COST 268 modelling task," Opt. Quantum Electron. **34**, 455–470 (2002).
8. H. Wenzel, R. Guther, A. M. Shams-Zadeh-Amiri, *et al.*, "A comparative study of higher order Bragg gratings: coupled-mode theory versus mode expansion modeling," IEEE J. Quantum Electron. **42**, 64–70 (2005).
9. R. R. Millet, K. Hinzer, T. J. Hall, *et al.*, "Simulation analysis of higher order laterally-coupled distributed feedback lasers," IEEE J. Quantum Electron. **44**, 1145–1151 (2008).
10. KVector, "Dynamics Grating Solver," https://kvectordynamics.com/grating-solvers/.
11. W. Streifer, D. R. Scifres, and R. D. Burnham, "Coupled wave analysis of DFB and DBR lasers," IEEE J. Quantum Electron. **13**, 134–141 (1977).
12. J. P. Donnelly and S. D. Lau, "Generalized effective index series solution analysis of waveguide structures with positionally varying refractive index profiles," IEEE J. Quantum Electron. **32**, 1070–1079 (1996).
13. L. Shen and Z. Wang, "Guided modes in a four-layer slab waveguide with dispersive left-handed material," J. Electromagn. Anal. Appl. **2**, 264–269 (2010).
14. C. H. Chen, L. H. Chen, and Q. M. Wang, "Coupling coefficients of gain-coupled distributed feedback lasers with absorptive grating," Electron. Lett. **32**, 1288–1290 (1996).
15. COMSOL Multiphysics, https://www.comsol.com/.
16. A. Taflove, A. Oskooi, and S. G. Johnson, *Advances in FDTD Computational Electrodynamics: Photonics and Nanotechnology* (Artech House, 2013).
17. D. C. Flanders, H. Kogelnik, R. V. Schmidt, *et al.*, "Grating filters for thin-film optical waveguides," Appl. Phys. Lett. **24**, 194–196 (1974).
18. W. Sun, Q. Lu, W. Guo, *et al.*, "Analysis of high-order slotted surface gratings by the 2D finite-difference time-domain method," J. Lightwave Technol. **35**, 96–102 (2016).
19. S. Saeidi, F. Wu, C. Watson, *et al.*, "Strong and short Bragg waveguide gratings with trapezoidal-shaped grooves," J. Lightwave Technol. **39**, 4395–4401 (2021).
20. X. Wang, Y. Wang, J. Flueckiger, *et al.*, "Precise control of the coupling coefficient through destructive interference in silicon waveguide Bragg gratings," Opt. Lett. **39**, 5519–5522 (2014).
21. "Lumerical is now part of the Ansys family," 2023, https://www.lumerical.com/.
22. T. Makino and J. Glinski, "Effects of radiation loss on the performance of second-order DFB semiconductor lasers," IEEE J. Quantum Electron. **24**, 73–82 (1988).
23. R. Kazarinov and C. Henry, "Second-order distributed feedback lasers with mode selection provided by first-order radiation losses," IEEE J. Quantum Electron. **21**, 144–150 (1985).
24. V. Tolstikhin, C. Watson, K. Pimenov, *et al.*, "Laterally coupled DFB lasers for one-step growth photonic integrated circuits in InP," IEEE Photonics Technol. Lett. **21**, 621–623 (2009).
25. K. Pimenov, C. Watson, Y. Logvin, *et al.*, "Analysis of high-order surface etched gratings for longitudinal mode selection in DFB lasers," in *Numerical Simulation of Optoelectronic Devices* (2010), pp. 49–50.
26. L. Zhang and D. A. Ackerman, "Second- and third-order harmonic distortion in DFB lasers," IEEE J. Quantum Electron. **31**, 1974–1980 (1995).
27. J. Kinoshita, "Analysis of radiation mode effects on oscillating properties of DFB lasers," IEEE J. Quantum Electron. **35**, 1569–1583 (1999).
28. A. Akrout, K. Dridi, and T. J. Hall, "Dynamic analysis of high-order laterally coupled DFB lasers using time-domain traveling-wave model," IEEE J. Quantum Electron. **48**, 1252–1258 (2012).
29. G. P. Agrawal and N. K. Dutta, *Semiconductor Lasers* (Van Norstrand Reinhold, 1993).
30. S. R. Selmic, T.-M. Chou, J. Sih, *et al.*, "Design and characterization of 1.3-/spl mu/m AlGaInAs-InP multiple-quantum-well lasers," IEEE J. Sel. Top. Quantum Electron. **7**, 340–349 (2001).
31. J. Piprek, P. Abraham, and J. E. Bowers, "Self-consistent analysis of high-temperature effects on strained-layer multiquantum-well InGaAsP-InP lasers," IEEE J. Quantum Electron. **36**, 366–374 (2000).
32. T. Makino and J. Glinski, "Transfer matrix analysis of the amplified spontaneous emission of DFB semiconductor laser amplifiers," IEEE J. Quantum Electron. **24**, 1507–1518 (1988).

Chapter 9

Conclusion and Future Work

This thesis has explored a range of laser systems with novel structural concepts, focusing on both theoretical modeling and practical considerations. We began with the development of a plasmonic-semiconductor laser, demonstrating its potential for wavelength tuning in telecommunications and biosensing applications. Furthermore, we introduced mathematical frameworks and computational models for grating-based devices, highlighting their significance in DFB laser design. A particularly innovative contribution of this work is the introduction of the Dirac Grating, a novel concept with promising implications for future photonic devices. Although the constraints of time limited the fabrication and experimental realization of all these devices, this thesis has provided rigorous modeling approaches and design guidelines that prioritize practical feasibility and pave the way for future experimental validation. Let us briefly review the key contributions of this work and outline possible directions for future research.

9.1 Thesis Summary

The thesis began with a comprehensive overview of existing tunable diode lasers, most of which rely on complex multi-segment structures or grating-based mechanisms. This review set the foundation for introducing a fundamentally different approach: a Fabry–Pérot diode laser that employs hybrid plasmonic-semiconductor structures to achieve tunability.

These hybrid devices offer the unique advantage that the high optical gain of the biased semiconductor can compensate for the inherent absorption losses of the plasmonic component, enabling efficient mode propagation. Using this concept, we theoretically demonstrated two devices: a tunable diode laser with a 7 nm tuning range in the O-band, and a highly sensitive diode laser capable of detecting refractive index changes as small as 10^{-5} RIU. While both designs were explored through modeling, only the latter device was selected for fabrication efforts. Although fabrication could not be completed due to time constraints, the process and methodology have been thoroughly documented in Appendix A for future reference.

In continuation of the sensing work, we modeled, fabricated, and demonstrated an edge-emitting LED functioning as a refractometer. The device was realized using the same epi-wafer design described in the previous section. Focused ion beam (FIB) milling was employed to create trenches at sides of the LED to hold the sensing fluid. The presence of the fluid modifies the facet reflectance, thereby altering the device's performance. This effect enables the LED to operate as a novel, simple, and low-cost refractometer.

Furthermore, we investigated waveguide Bragg gratings (WBGs), which hold significant importance in the integrated photonics industry. A comparative study was conducted on surface-etched WBGs, focusing on both first-order and higher-order gratings, and evaluating their reflective strength across various grating profiles. Special attention was given to trapezoidal grating shapes due to their relevance in practical fabrication processes. Simulations were performed using a FDTD setup, which was first validated against an improved version of coupled-mode theory that accounts for all radiated waves, a critical consideration for accurately modeling higher-order gratings. For a selected benchmark case, we identified an optimized grating profile that achieved maximal reflectance with minimal loss when light was injected into the waveguide.

Perhaps one of the most interesting contributions of this thesis is the introduction of Dirac gratings. These gratings are characterized by very small duty cycles, resulting in an index perturbation that closely resembles a Dirac delta function, hence the name. A key feature of Dirac gratings is that their coupling coefficient, and thus their spectral response, is independent of the grating order. This means that longer-pitch gratings can effectively replace shorter-pitch counterparts within the same cavity length without significant degradation in spectral performance. Even the loss remains essentially the same in both cases because the cavity length and the strength of the scatterers (i.e., the perturbation) are unchanged. As a result, the photon lifetime, and therefore the experienced loss, remains the same. This order-independence was demonstrated both analytically and through inverse design techniques based on Fourier transform. Additionally, a threshold criterion was established to define how narrow the perturbation must be for a grating to qualify as "Dirac-like." Unfortunately, the fabrication and experimental validation were not possible within the limited timeframe of this work, but the mathematical results are promising and lay the groundwork for future experimental and design investigations.

As a continuation of the grating-related studies, we developed an algorithm based on an improved version of coupled-mode theory (CMT), which we termed Finite-Difference Coupled-Mode Theory (FD CMT). CMT remains the only method that allows direct analytical calculation of the coupling coefficient in grating structures, something numerical techniques such as FDTD and EME cannot directly provide. FD CMT bridges this gap by formulating a semi-numerical method grounded in CMT. Unlike traditional CMT, our approach is not constrained by the geometric complexity of the grating profile, enabling broader applicability. Validation against full-wave numerical methods showed excellent agreement, with the added advantage that our approach was more than 50 times faster. This tool offers strong potential for efficient and accurate design of DFB lasers and shows potential for its future commercialization.

In conclusion, this thesis touched on different topics, but they all connected back to the broader goal of designing and analyzing photonic structures in III–V and plasmonic platforms. Whether through tunability, sensing, or grating engineering, each chapter explored how optical modes can be controlled to achieve useful functionality. With growing demands in communication and sensing, these ideas may help point toward future device directions.

9.2 Future Work

This thesis covered a diverse range of devices and applications, many of which offer multiple directions for future exploration. A particularly novel device investigated here was the hybrid semiconductor-plasmonic laser. While the modeled tunable laser demonstrated promising characteristics, its power consumption remained relatively high, limiting its practicality for datacom applications. Future research could focus on optimizing the device design, as numerous structural and material parameters could be explored to improve efficiency and make the laser more attractive for industrial applications.

In this hybrid laser work, only a Fabry-Perot cavity design was implemented. More advanced cavity architectures, such as grating-based distributed feedback (DFB) structures, were investigated (though not included in this thesis) but were not pursued due to fabrication challenges within the timeframe of the project. Future work could aim to realize hybrid plasmonic-semiconductor DFB lasers. A DFB configuration can significantly enhance the performance of this type of laser for both datacom and sensing applications. The sharper linewidth of the laser mode is an obvious benefit, as it makes the wavelength sensitivity much higher, for example, in sensing applications. Furthermore, developing reliable fabrication processes for such devices could itself constitute a substantial research effort.

From a broader perspective, hybrid semiconductor-plasmonic lasers remain relatively underexplored and therefore present many opportunities for novel applications. One promising direction involves programmable laser architectures. As demonstrated in Chapter 3, the high index modulation achievable in such systems could enable grating configurations where each period is individually controlled, allowing user-defined functionality.

In addition to sensing, plasmonic modes offer potential advantages due to their small mode areas, which can support very high modulation speeds. Leveraging these properties in hybrid semiconductor-plasmonic lasers could enable directly modulated laser sources, which would be of significant interest for telecommunications applications.

The ideas outlined above are potential development paths rather than firm research directions, as a detailed literature review on these specific applications was beyond the scope of this thesis.

In Chapter 5, we demonstrated an LED-based refractometer. This device could be further developed into a broad-area laser, where the higher output power might improve the sensitivity of the measured signal. Several approaches could be considered to achieve this. One possibility is redesigning the cavity, for example by etching and tapering the active region toward the facet to reduce its size, thereby lowering the threshold current and enabling lasing more efficiently. A tapered output facet could also facilitate efficient coupling of the mode into a fiber, allowing the spectral sensitivity of the output light to be measured. However, this requires passivation, as etching the gain medium causes oxide formation. Alternatively, improvements in the experimental setup, such as minimizing environmental noise or operating

the device in a temperature-controlled chamber to reduce self-heating, could enhance sensitivity and potentially allow lasing in the current device configuration.

The remainder of this thesis focused on waveguide Bragg gratings. An obvious follow-up would be the fabrication and experimental demonstration of Dirac gratings, which could be easily realized using Si-based DBR reflectors. Additionally, III-V-based DFB lasers employing Dirac configurations could be explored and modeled. Other grating-based devices, such as grating couplers, could also be investigated in their Dirac forms, potentially leading to new functionalities and applications.

We eventually developed a finite-difference algorithm to solve the coupled-mode theory (CMT) for waveguide gratings. This algorithm is computationally efficient and capable of handling gratings with complex groove profiles, allowing simulations from device-level design to spectral response characterization for both DBR and DFB structures. This work has focused on 1D gratings, an obvious extension would be to generalize the algorithm to 2D gratings. In addition, like conventional CMT, the current algorithm is limited to weak gratings. By generalizing its formulation to account for the dependence of the mode profile on the propagation axis, it is possible to overcome this limitation. Such an improvement could make this method a strong and computationally efficient alternative to the widely used, but time-consuming, finite-difference time-domain (FDTD) method.

Appendix A

Fabrication and Testing of Hybrid Biosensor Laser

This appendix outlines the fabrication process and testing of the hybrid plasmonic-semiconductor laser, based on the device introduced in Chapter 4, which remained incomplete. Fig. A.1 presents a three-dimensional illustration of the laser structure. The laser consists of several main components. The device is made of a III-V multi-layer wafer, which forms the active region. On top of the epi-layers, the waveguide ridge is formed using indium-tin oxide (ITO). Top and bottom metallic contacts are implemented to enable diode biasing. Additionally, a layer of Cytop, a polymer material, is applied to electrically isolate the contacts from the wafer and to form a microfluidic chamber, where a sensing droplet can be placed above the waveguide region.

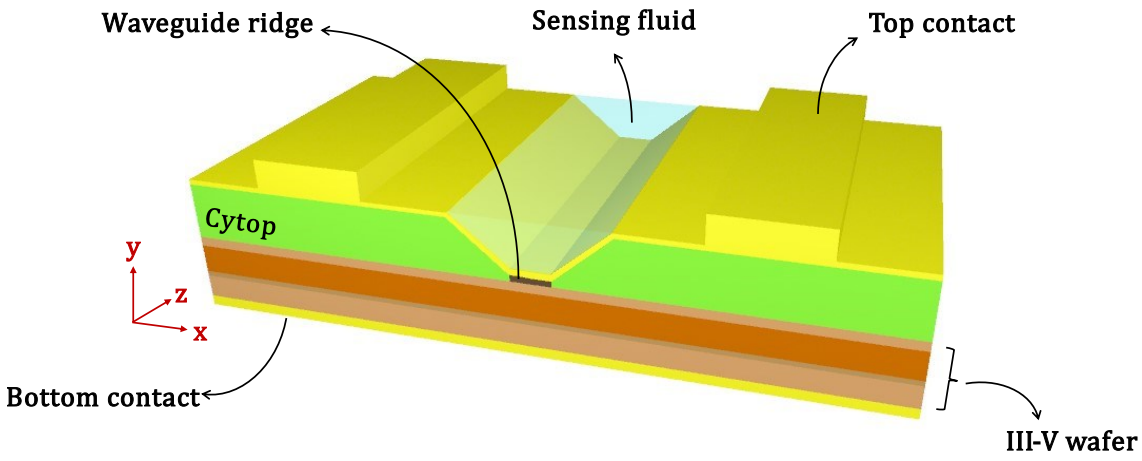

Fig. A.1 3D schematic of the proposed hybrid biosensor laser.

Fig. A.2 illustrates the three photolithography masks used in the fabrication process. Mask #1 defines the laser ridges, as well as the streets and avenues that separate the individual dies. Mask #2 is used to define the contact pads, also incorporating the streets and avenues. Mask #3 defines the N-contact metallization for each device, including separation between devices within a die, along with streets and avenues. All three masks feature alignment marks within each die. Masks #1 and #2 are dark-field masks, while Mask #3 is a bright-field mask. Mask #1 was fabricated at the Photronics Inc. [1], whereas Masks #2 and #3 were fabricated at the University of Alberta [2]. The layout for all three masks was designed using Design Workshop

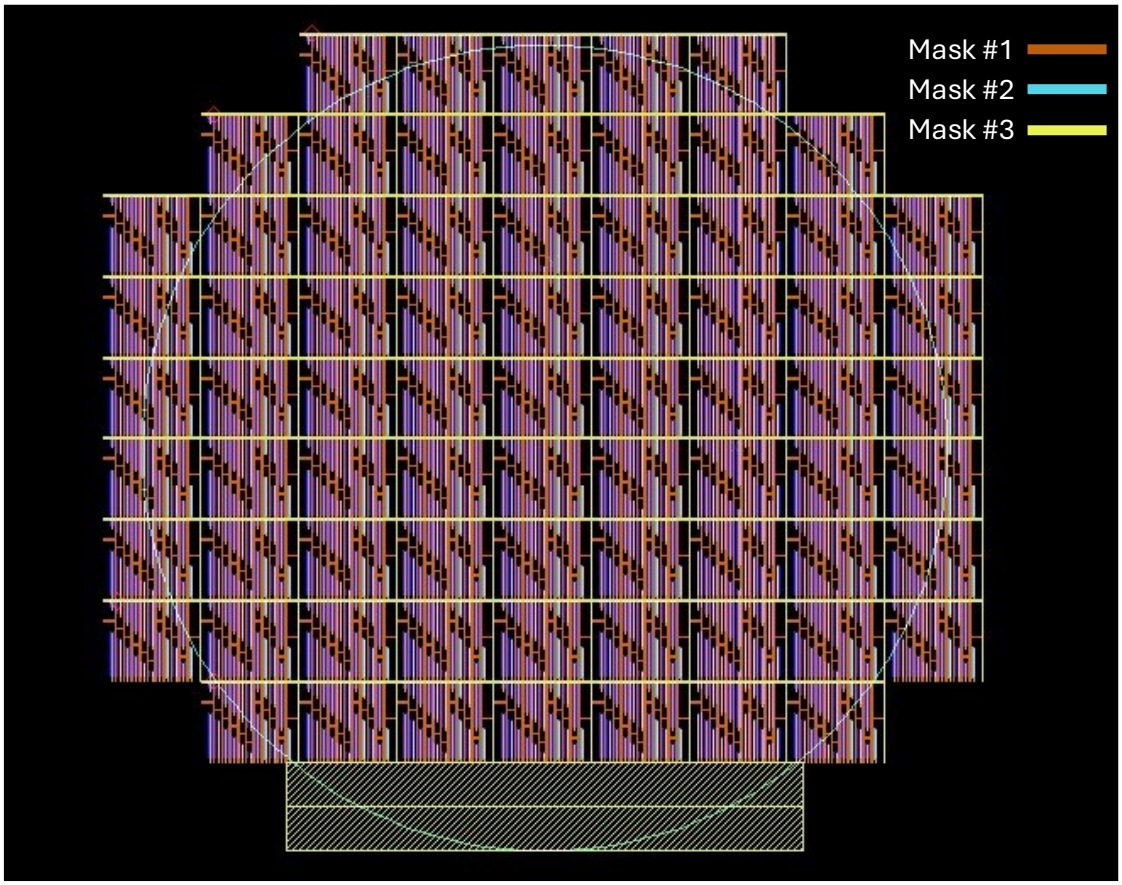

Fig. A.2 The mask layouts used throughout the fabrication process. The blue circle represents a 2-inch wafer.

200 (DW200) [3]. The wafer contains approximately 50 dies, each containing 21 lasers with varying designs, differing in length and width.

The wafer was custom-grown on a p-doped InP substrate, which is relatively uncommon among commercial epitaxial growth providers, as n-doped InP is typically preferred probably because of its better compatibility with ohmic contacts. However, for this device, a p-type substrate was necessary since the top layer must be n-doped, to accommodate the integration of n-doped ITO on the surface. The wafer was grown by LandMark Optoelectronics Inc. [4] using metal-organic chemical vapor deposition (MOCVD). The epitaxial layer structure was designed based on simulations conducted using Lumerical's MQW Solver [5] and is discussed in Chapters 3 and 4. A summary of the epitaxial layer design is provided in Table A.1.

Table A.1: Epitaxial layer description

No.	Material	Thickness (nm)	Doping Level (cm^{-3})
0	P-InP Substrate		$2\sim8\times10^{18}$
1	P-InP Buffer Layer	200	10^{18}
2	P-$Al_{0.33}In_{0.53}Ga_{0.14}As$	50	10^{17}

3	14×U-$Al_{0.04}In_{0.38}Ga_{0.58}As$ (QW –1.1% T.S.) 15×U-$Al_{0.41}In_{0.57}Ga_{0.02}As$ (Barrier +0.3% C.S.)	6 / 18	-
4	U-InP	7	-
5	N-$In_{0.9}Ga_{0.1}As_{0.219}P_{0.781}$	30	2×10^{18}

A.1 Fabrication Process flow

Fig. A.3 illustrates the overall fabrication process flow of our hybrid biosensor laser (HBL) device. The device was fabricated on a 2-inch wafer grown by MOCVD. The following sections describe the steps that were carried out prior to the termination of the process.

A.1.1 Surface Preparation

Prior to any processing steps, the wafer was cleaned to remove the native oxide layer from the InGaAsP surface. This was done by placing the wafer in a solution of hydrofluoric acid (HF) and deionized water (DI) in a 1:20 ratio for 1 minute. After the etch, the wafer was rinsed in DI water and dried using a nitrogen blow.

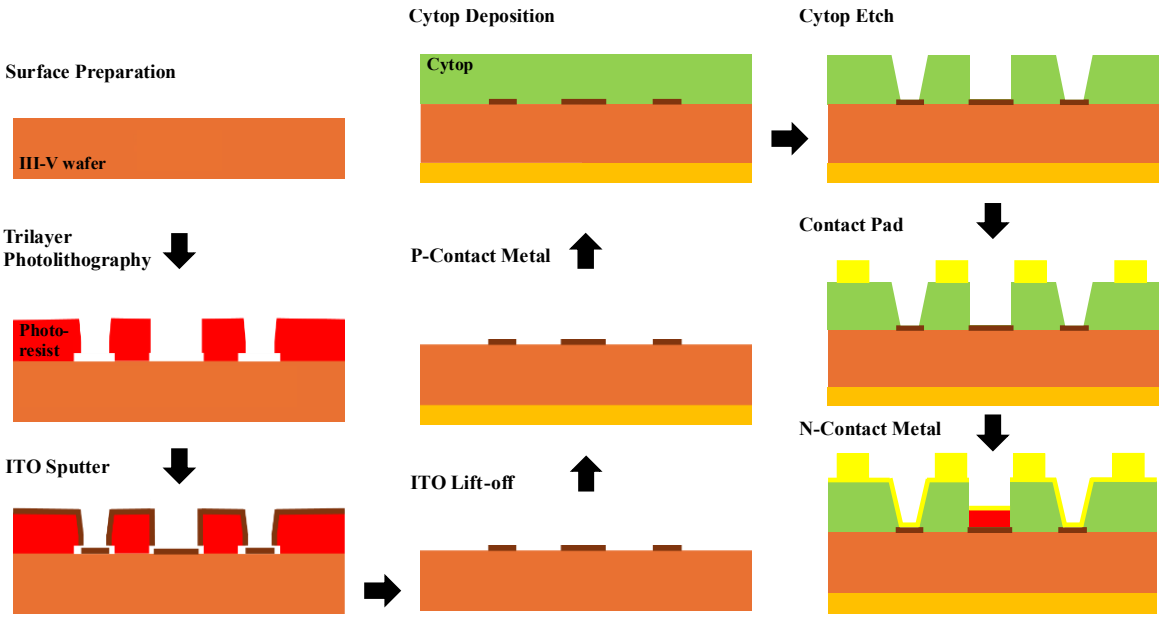

Fig. A.3 Summary of HBL fabrication flow.

A.1.2 Trilayer Photolithography

In this step, we prepared the wafer for patterning the indium-tin oxide (ITO) regions using a trilayer photolithography process, which provides high-resolution features with vertical sidewalls, as described in [6].

The process began by placing the wafer in a hexamethyldisilazane (HMDS) oven at 100 °C for approximately 18 minutes to promote adhesion of the resist layers. Next, the first layer of photoresist, LOR1A, was spin-coated using the multi-step spin profile described in [6], followed by a bake on hotplate at 185 °C for 4 minutes. The second layer, BARC (bottom anti-reflective coating), was spin-coated using the same settings. After spin-coating, the wafer was allowed to rest for 1 minute and then baked at 185 °C for another minute. The third and final layer, SPR955, was also spin-coated using the same spinner program. This was followed by a 1-minute relaxation time and a final bake at 90 °C for 5 minutes.

After coating the photoresist layers, the photolithography Mask #1 was used for exposure. This was done using the Mask Aligner with an exposure dose of 95 mJ/cm². Following the exposure, a post-exposure bake was carried out at 120 °C for 5 minutes.

The wafer was then developed using MF24 developer for 1 minute and 10 seconds. During development, ultrasonic agitation was applied for 30 seconds to help remove the top photoresist layer (SPR955) and clearly define the pattern. Next, reactive ion etching (RIE) was used to remove the BARC layer. This was done using oxygen gas with a flow rate of 10 sccm, a power of 50 W, and a chamber pressure of 4 Pa for 4 minutes and 10 seconds. Finally, the wafer was dipped again in MF24 developer for 10 seconds to develop the LOR1A layer and create an undercut profile.

Fig. A.4 An optical microscope image of a region on the wafer at the end of Step A.1.2, showing the developed photoresist patterns after the first photolithography process.

A microscope image of the sample at this stage is shown in Fig. A.4. The image displays the alignment marks, as well as a waveguide structure, which is intended to form the laser cavity.

A.1.3 ITO Sputter & Lift-off

A 30 nm layer of n-doped ITO was deposited onto the wafer using a sputtering system at the Carleton University. After deposition, the lift-off process was carried out by placing the wafer in a Remover 1165 bath on a hotplate at 50 °C, with the lid closed to ensure effective removal of excess ITO.

Following lift-off, the wafer was annealed using rapid thermal annealing (RTA) at 350 °C in an oxygen environment for 30 minutes to improve the material quality of the ITO. This process was also performed on a blank wafer, which was later used for optical characterization of the ITO film using ellipsometry. The measured data was used to refine the optical parameters in subsequent modeling and simulations.

A microscope image of the main wafer at this stage is shown in Fig. A.5(a). Several waveguides were characterized using atomic force microscopy (AFM), and a 3D surface

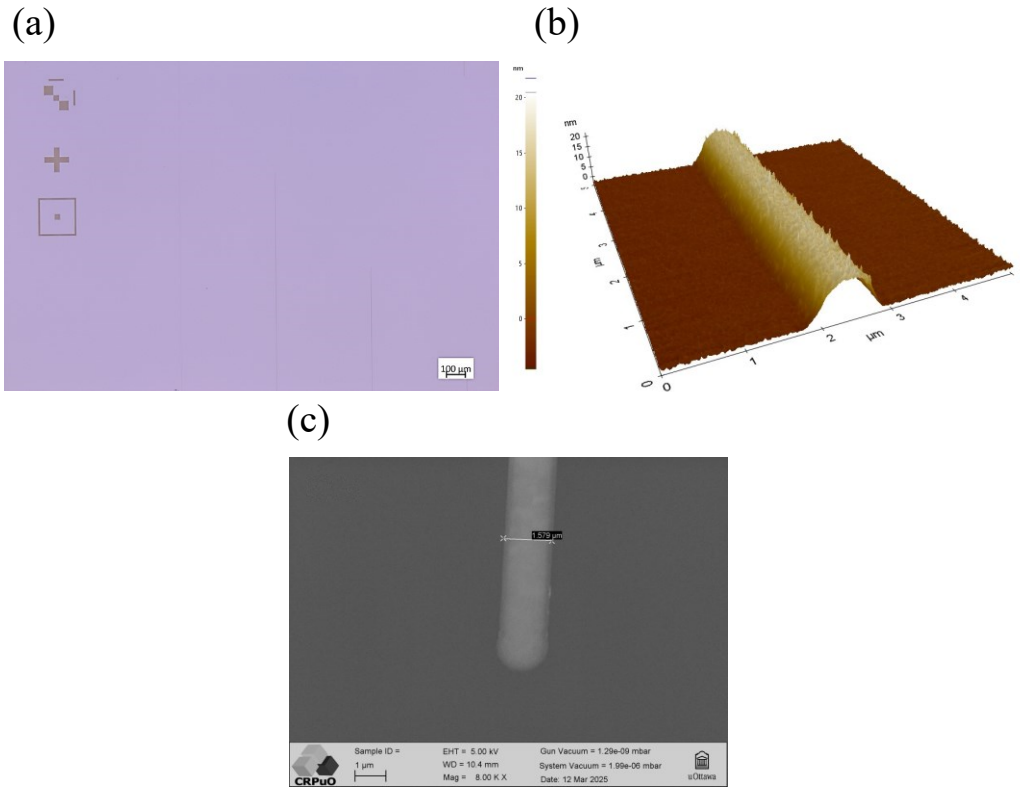

Fig. A.5 (a) Optical microscope image, (b) AFM image, and (c) SEM image of a region on the wafer at the end of Step A.1.3, showing the patterned ITO waveguide ridges.

profile of one of them is presented in Fig. A.5(b). The measured root mean square (RMS) roughness of the ridge was approximately 1.7 nm. The ITO thickness was found to be around 24 nm, about 20% less than the target value, which is likely due to changes during the RTA step. Additionally, the waveguide width was approximately 0.5 μm wider than the original design, and the ridge corners appeared slightly rounded. These deviations are attributed to the undercut formed in the LOR1A layer, which allowed sputtered ITO to deposit along the sidewalls. The overall waveguide profile was confirmed by scanning electron microscopy (SEM), as shown in Fig. A.5(c).

A.1.4 P-Contact metal

To proceed with metal deposition on the backside of the wafer, a protective layer of SPR955 photoresist was spin-coated and baked on a hotplate. This layer served to shield the front-side patterns during the backside metallization process. A bilayer of palladium (Pd) and gold (Au), with thicknesses of 30 nm and 100 nm respectively, was evaporated on the backside of the wafer. Palladium was chosen for its ability to form a good ohmic contact with the p-doped InP substrate, while the gold layer on top facilitates electrical probing. Following deposition, the SPR955 layer was removed using a Remover 1165 bath. Finally, RTA was performed at 350 °C in an oxygen for 4 minutes to improve the quality of the ohmic contact.

A.1.5 Cytop Deposition

Cytop deposition began with spin-coating an AP3000 adhesion promoter, followed by a layer of Cytop Grade A. The process followed the detailed procedure described in [7] and included an overnight curing step.

Due to the tendency of Cytop to accumulate more thickly at the wafer edges during spin-coating, a metallic disc was used to selectively expose only the outer edge of the wafer. This allowed edge bead removal using RIE with oxygen at a flow rate of 10 sccm, power of 150 W, and a chamber pressure of 4 Pa for 4 minutes. This step improves the uniformity of the surface and enhances the resolution of subsequent photolithography steps. Since Cytop is highly hydrophobic, surface roughening, known as ashing, was performed to improve photoresist adhesion in later steps. This was done using RIE under the same gas flow and pressure conditions, but with a reduced power of 75 W for only 10 seconds.

Fig. A.6 shows the wafer at this stage. The ITO patterns, which define the die separations, are visible to the naked eye.

A.1.6 Cytop Etch

To expose the waveguide ridges beneath the Cytop layer, the wafer was first placed in an HMDS oven at 100 °C to promote resist adhesion. A single layer of SPR955 photoresist was

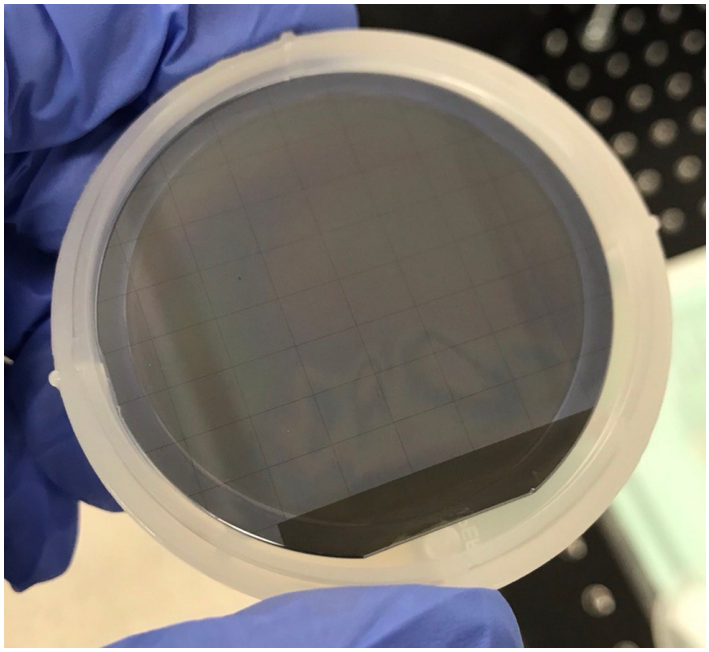

Fig. A.6 Image of the wafer at the end of Step A.1.5, showing the unpatterned Cytop layer covering the ITO structures.

then spin-coated, followed by a soft bake at 90 °C for 5 minutes. It is important to note that Cytop has a glass transition temperature near 100 °C; therefore, any baking at or above this temperature must be avoided to prevent deformation or flow of the Cytop layer.

The same photolithography mask used during the ITO patterning step was reused for alignment. UV exposure was carried out using the Mask Aligner at a dose of 95 mJ/cm². The wafer was then developed in MF24 developer for 1 minute and 10 seconds, including 30 seconds of sonication to assist in pattern development. Precise alignment was critical in this step, as the existing ITO patterns needed to match the new openings in the Cytop layer.

Reactive ion etching was then performed with oxygen at a flow rate of 10 sccm, power of 150 W, pressure of 4 Pa, and a duration of 4 minutes and 10 seconds. A relatively high power was intentionally used to produce angled sidewalls in the etched Cytop. Based on prior experiments, lower RIE power results in more vertical sidewalls, which were not desired in this case. At 150 W, the etch rate of Cytop is approximately 600 nm/min, while SPR955 etches at about 250 nm/min. The chosen etch duration ensured complete removal of the Cytop in the exposed areas without fully etching through the SPR955, preserving the integrity of the remaining surface.

Fig. A.7(a) presents microscope images showing good alignment between the Cytop openings and the underlying ITO patterns. Fig. A.7(b) shows an AFM scan of the Cytop profile over a waveguide ridge, indicating successful patterning. However, the RMS surface roughness of the exposed ITO increased to approximately 4 nm from its original value of around 2 nm, likely due to mechanical surface effects introduced during the RIE process.

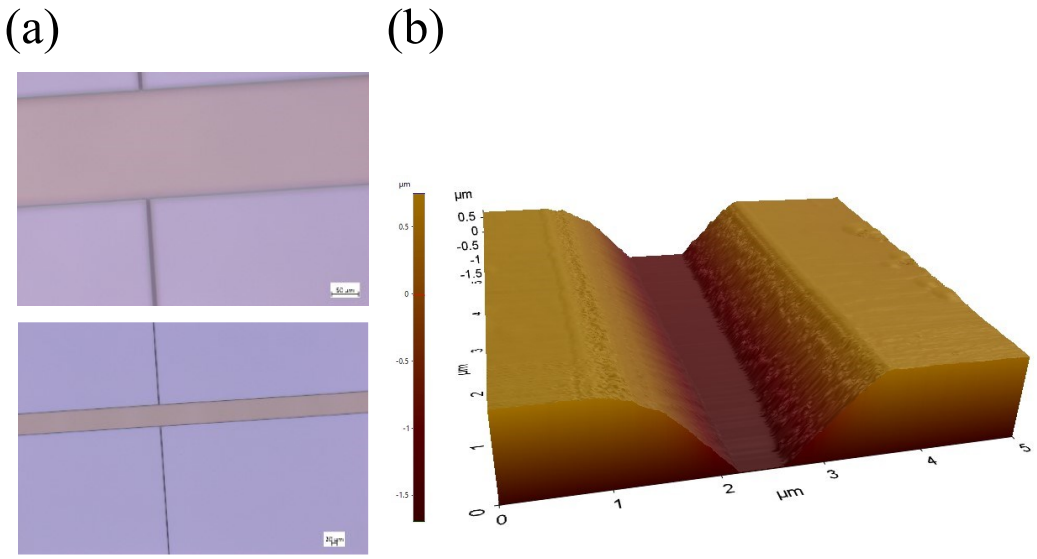

Fig. A.7 (a) Optical images of the wafer and (b) AFM scan at the end of Step A.1.6, showing the patterned Cytop layer and its surface profile over the waveguide region.

A.1.7 Contact Pads

To define the contact pad regions, a single layer of SPR955 photoresist was spin-coated and baked at 90 °C for 5 minutes. The second photolithography mask was then used for UV exposure at a dose of 95 mJ/cm², followed by development in MF24 developer, using the same procedure as in previous steps. Microscope images at this stage, shown in Fig. A.8, clearly display the opened pad regions prepared for metal deposition.

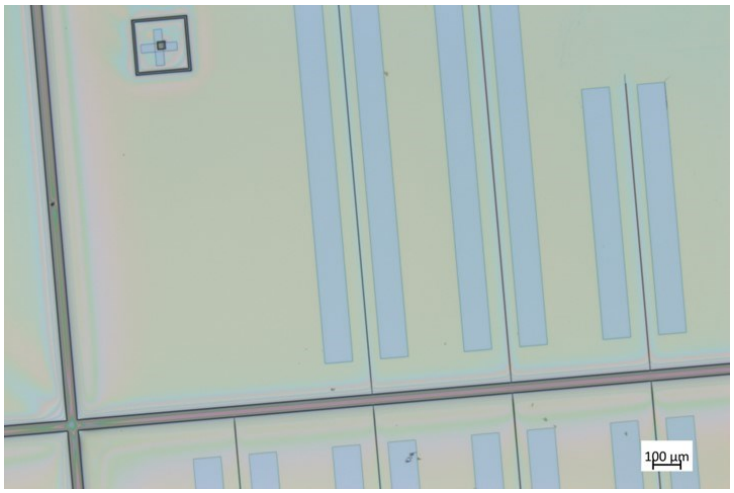

Fig. A.8 Optical microscope images of the wafer, showing the opened regions for contact pads after photolithography, prior to metal deposition.

Gold/titanium contact metal was then evaporated, with layer thicknesses of 100 nm and 50 nm, respectively. Gold was selected for its strong adhesion to Cytop, and titanium was used as a capping layer due to its greater hardness, which improves mechanical durability for electrical probing.

Following metal deposition, lift-off was performed using Remover 1165. However, at this stage, the Cytop layer was unintentionally and completely removed from the InGaAsP surface, along with the patterned structures it supported. This issue revealed that Cytop does not adhere well to InGaAsP. Unfortunately, this behavior had not been observed in prior trials because earlier process tests were conducted on silicon substrates, where Cytop adhesion was found to be reliable. Due to limitations in the number of available III-V wafers, no preliminary adhesion tests had been carried out on InGaAsP before this step.

A.2 Re-modeling the HBL

To address the critical issue encountered in the previous step (the delamination of Cytop from the InGaAsP surface), a viable solution would be to use an alternative polymer or a different adhesion promoter compatible with InGaAsP. However, exploring these options would require an extended period of process optimization and testing, which was not feasible within the time constraints of this PhD project.

As an alternative, the device was re-designed to bring the contact pads directly into contact with the semiconductor surface, eliminating the need for the Cytop layer. The ITO waveguide ridges are heavily n-doped, with a doping level approximately 100 times higher than the surrounding InGaAsP. By leveraging this doping contrast, the design assumes that current will preferentially flow beneath the ITO ridges, enabling a degree of lateral current confinement even without the original insulating layer.

Given that most fabrication steps had already been completed by this stage, this approach was considered the most practical solution. Fig. A.9 illustrates the revised design of the hybrid biosensor laser (HBL), in which the metal contact pads are placed directly on the exposed surface. The rest of this section describes the remaining processing steps.

A.2.1 Cleaning the surface

The first step in the revised process was to remove the remaining Cytop layer. This was done using a sequence of solvents: CT Solvent, isopropyl alcohol (IPA), acetone, and DI water, followed by a nitrogen blow-dry. To ensure complete removal of any residual polymer or surface contamination, a short RIE was performed with oxygen at 60 W for 10 seconds. AFM measurements indicated that the surface roughness at this stage was approximately 4 nm.

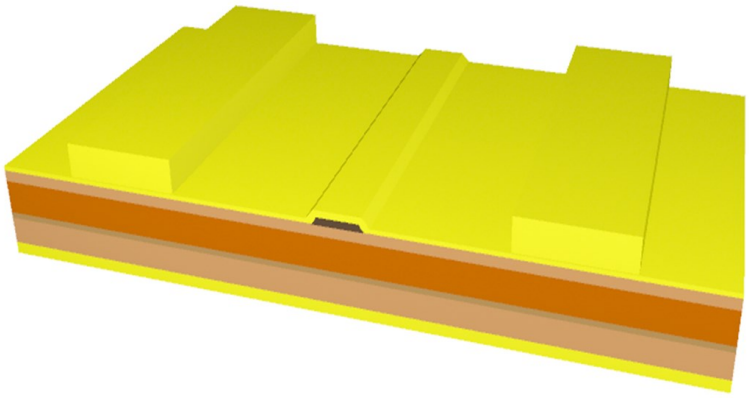

Fig. A.9 Schematic illustration of the adjusted HBL model, where the top contact pads are directly placed on the device surface due to the removal of the Cytop layer.

A.2.2 N-Contact Metal

The process began with surface preparation in an HMDS oven at 100 °C, followed by spin-coating a single layer of SPR955 photoresist and baking at 90 °C for 5 minutes. Mask #3 was then used for UV exposure at a dose of 95 mJ/cm². A post-exposure bake was performed at 120 °C for 5 minutes, and the pattern was developed in MF24 developer.

Next, a bilayer of titanium (Ti) and gold (Au) was deposited using electron beam and thermal evaporation, respectively. Ti (3 nm) was chosen for its good adhesion to InGaAsP and its ability to form an ohmic contact. A 17 nm gold layer was deposited on top, intended to serve as the plasmonic component of the laser for sensing applications. After deposition, lift-off was performed using Remover 1165.

Fig. A.10(a) shows microscope images of the wafer at this stage. The images display two back-to-back lasers on separate dies. Each laser is electrically isolated from adjacent devices by a defined gap.

A.2.3 Contact Pads

In the final fabrication step, the photolithography process was repeated as in the previous sections, with the exception that Mask #2 was used to define the contact pad regions. Following development, a 100 nm / 50 nm Au/Ti bilayer was deposited to form the electrical contact pads. The metal deposition and lift-off were performed using the same procedures described earlier in Section A.1.7.

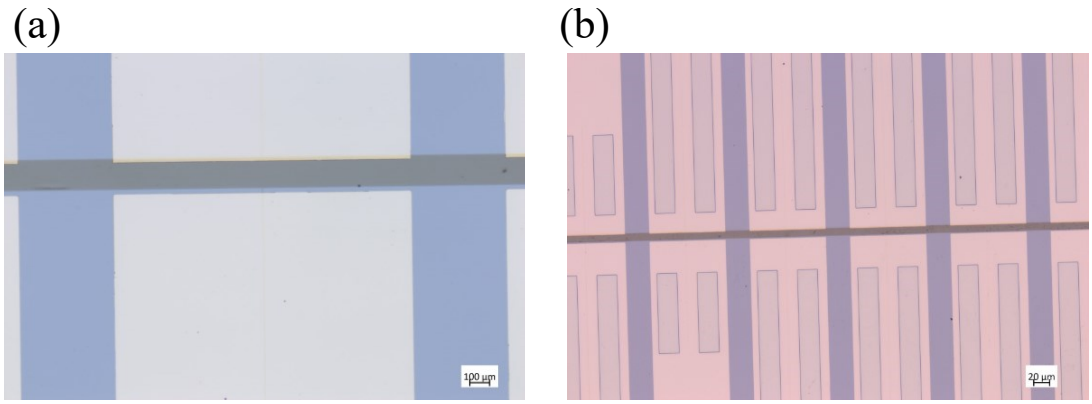

Fig. A.10 Optical microscope image of the (a) wafer at the end of Step A.2.2, showing completed N-contact metal structures and separation gaps between adjacent devices within a die, and (b) at the end of Step A.2.3, showing the final contact pad structures after metal deposition and lift-off.

Fig. A.10(b) shows microscope images of the wafer after this final step, with clearly defined contact pads in place.

This concludes the fabrication process. The wafer was then cleaved into individual dies using a Loomis Wafer Cleaver (LSD-155), with assistance from Banyan Photonics Canada. Fig. A.11 presents SEM images of a cleaved device at two magnifications: one showing the full laser cavity along with the N-contact pads on either side, and another highlighting the laser ridge.

A.3 Experimental Results

To characterize the fabricated device, electrical and optical measurements were performed. The device was mounted on a vacuumed holder to ensure mechanical stability. Two probes were used for electrical biasing: one probe contacted the metallic stage, which was electrically

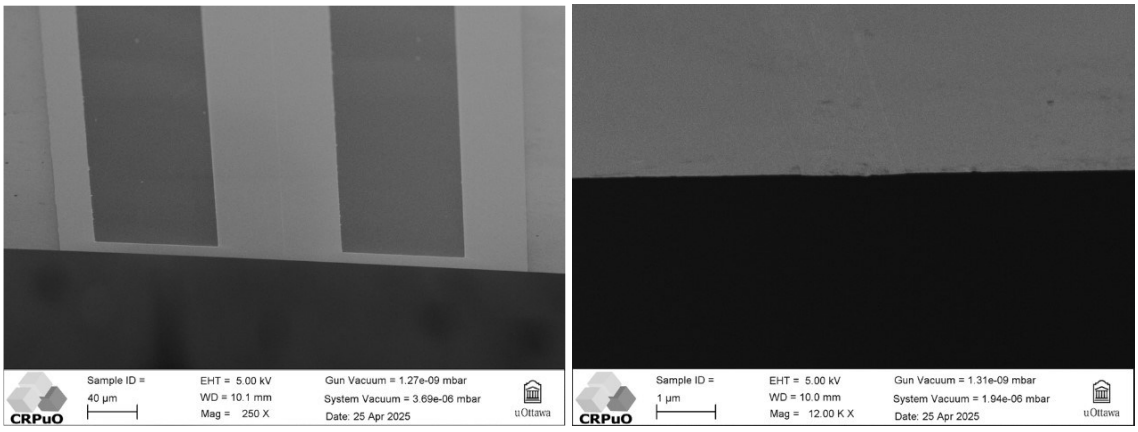

Fig. A.11 SEM images of a cleaved device: (left) showing the full laser cavity with adjacent N-contact pads, and (right) a close-up view of the laser ridge.

connected to the back-side metallization of the wafer, and the other probe contacted one of the top metal pads of the laser.

A source meter was used to inject current through the probes and simultaneously measure the voltage across them. As an initial test, the voltage-current (VI) characteristics of the device were measured to verify the integrity of the p–i–n junction. The resulting curve, shown in Fig. A.12(a), exhibits clear diode-like behavior under forward bias, with a threshold voltage of approximately 1.5 V.

For optical measurements, a fiber was positioned to collect emitted light from the device. Upon adjusting the fiber around different edges of the structure, it was observed that light was emitted from all sides of the device, rather than being confined to the waveguide ridge as originally designed. Notably, stronger emission was detected near the probed pad, indicating that the current was spreading laterally across the device rather than being laterally confined under the ITO ridge. As a result, even with increasing injection current, the collected optical power remained low. Fig. A.12(b) shows a representative light–current (LI) curve, which does

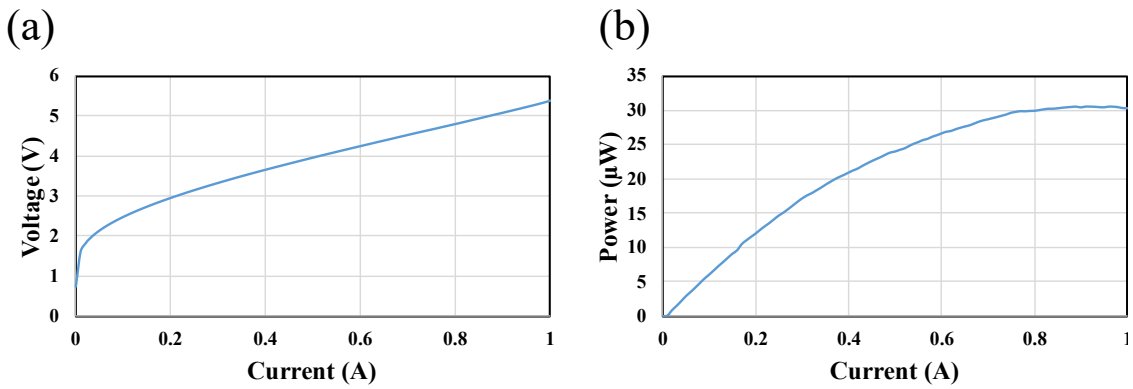

Fig. A.12 (a) VI characteristic of the device, showing diode-like behavior with a threshold voltage around 1.5 V. (b) LI curve indicating no clear lasing threshold, with maximum collected power below 30 µW at 1A injection.

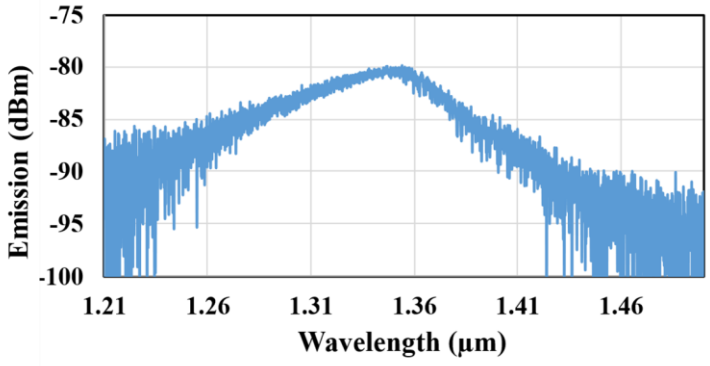

Fig. A.13 Emission spectrum of the device.

not exhibit a clear lasing threshold, confirming the lack of effective optical confinement and lasing behavior in the current design.

Fig. A. 13 shows the emission spectrum of the device, with the peak intensity observed around 1350 nm. It can be seen that the low emission power, the presence of multiple unintended optical paths within the structure, and multi-transverse mode nature of laser, prevent clean mode formation.

A.4 Conclusion

In summary, the original HBL laser design could not be fully realized, primarily due to the lack of current confinement. As a result, an alternative design, based on the device described in this appendix, was developed and is further discussed in Chapter 5.

References

1. Photronics Inc. "https://www.photronics.com/" [Online].
2. University of Alberta, Nanofab Mask Fabrication "https://www.nanofab.ualberta.ca/services/mask-fabrication/" [Online].
3. Design Workshop Technologies dw-2000, "https://www.designw.com/EDA-Overview.php" [Online].
4. LandMark Optoelectronics Corporation, https://www.lmoc.com.tw/ [Online].
5. Lumerical is now part of Ansys, https://www.ansys.com/products/optics [Online].
6. H. Northfield, *et al*. "Tri-layer contact photolithography process for high-resolution lift-off." *Microelectronic Engineering* 241 (2021): 111545.
7. M. Khodami, *et al*. "Reactive ion etching of cytop and investigation of residual microstructures." *Journal of Microelectromechanical Systems* 29.2 (2020): 228-235.